Understanding the mechanisms of aortic dissection : finite element modeling and in situ experimentation with X-ray tomography

Joseph Brunet

N° d'ordre NNT: 2021LYSEM010

THÈSE de DOCTORAT DE L'UNIVERSITÉ DE LYON
opérée au sein de
École des Mines de Saint-Étienne

École Doctorale N° 488
(Sciences, Ingénierie, Santé)

Spécialité de doctorat: Mécanique et Ingénierie

Soutenue publiquement le 05/03/2021, par:
Joseph BRUNET

Comprendre les mécanismes de dissection aortique: modélisation éléments finis et expérimentation in situ sous tomographie RX

—

Understanding the mechanisms of aortic dissection: finite element modeling and in situ experimentation with X-ray tomography

---

Devant le jury composé de:

Famaey, Nele	Professeure	KU, Leuven	Présidente du Jury
Deplano, Valérie	Directeur de Recherche CNRS	IRPHE, Marseille	Rapporteure
Orgéas, Laurent	Directeur de Recherche CNRS	UJF, Grenoble	Rapporteur
Trachet, Bram	Docteur	Université de Ghent	Examinateur
Molimard, Jérôme	Professeur	Mines Saint-Etienne	Directeur de thèse
Maire, Éric	Directeur de Recherche CNRS	INSA, Lyon	Co-directeur de thèse
Pierrat, Baptiste	Ingénieur de recherche	Mines Saint-Etienne	Encadrant
Adrien, Jérôme	Ingénieur de recherche CNRS	INSA, Lyon	Co-encadrant
Badel, Pierre	Docteur		Invité

Spécialités doctorales	Responsables :	Spécialités doctorales	Responsables
SCIENCES ET GENIE DES MATERIAUX	K. Wolski Directeur de recherche	MATHEMATIQUES APPLIQUEES	O. Roustant, Maître-assistant
MECANIQUE ET INGENIERIE	S. Drapier, professeur	INFORMATIQUE	O. Boissier, Professeur
GENIE DES PROCEDES	F. Gruy, Maître de recherche	SCIENCES DES IMAGES ET DES FORMES	JC. Pinoli, Professeur
SCIENCES DE LA TERRE	B. Guy, Directeur de recherche	GENIE INDUSTRIEL	N. Absi, Maitre de recherche
SCIENCES ET GENIE DE L'ENVIRONNEMENT	D. Graillot, Directeur de recherche	MICROELECTRONIQUE	Ph. Lalevée, Professeur

EMSE : Enseignants-chercheurs et chercheurs autorisés à diriger des thèses de doctorat (titulaires d'un doctorat d'État ou d'une HDR)

ABSI	Nabil	MR	Génie industriel	CMP
AUGUSTO	Vincent	CR	Image, Vision, Signal	CIS
AVRIL	Stéphane	PR2	Mécanique et ingénierie	CIS
BADEL	Pierre	MA(MDC)	Mécanique et ingénierie	CIS
BALBO	Flavien	PR2	Informatique	FAYOL
BASSEREAU	Jean-François	PR	Sciences et génie des matériaux	SMS
BATTON-HUBERT	Mireille	PR2	Sciences et génie de l'environnement	FAYOL
BEIGBEDER	Michel	MA(MDC)	Informatique	FAYOL
BLAYAC	Sylvain	MA(MDC)	Microélectronique	CMP
BOISSIER	Olivier	PR1	Informatique	FAYOL
BONNEFOY	Olivier	PR	Génie des Procédés	SPIN
BORBELY	Andras	MR(DR2)	Sciences et génie des matériaux	SMS
BOUCHER	Xavier	PR2	Génie Industriel	FAYOL
BRODHAG	Christian	DR	Sciences et génie de l'environnement	FAYOL
BRUCHON	Julien	MA(MDC)	Mécanique et ingénierie	SMS
CAMEIRAO	Ana	MA(MDC)	Génie des Procédés	SPIN
CHRISTIEN	Frédéric	PR	Science et génie des matériaux	SMS
DAUZERE-PERES	Stéphane	PR1	Génie Industriel	CMP
DEBAYLE	Johan	MR	Sciences des Images et des Formes	SPIN
DEGEORGE	Jean-Michel	MA(MDC)	Génie industriel	Fayol
DELAFOSSE	David	PR0	Sciences et génie des matériaux	SMS
DELORME	Xavier	MA(MDC)	Génie industriel	FAYOL
DESRAYAUD	Christophe	PR1	Mécanique et ingénierie	SMS
DJENIZIAN	Thierry	PR	Science et génie des matériaux	CMP
BERGER-DOUCE	Sandrine	PR1	Sciences de gestion	FAYOL
DRAPIER	Sylvain	PR1	Mécanique et ingénierie	SMS
DUTERTRE	Jean-Max	MA(MDC)		CMP
EL MRABET	Nadia	MA(MDC)		CMP
FAUCHEU	Jenny	MA(MDC)	Sciences et génie des matériaux	SMS
FAVERGEON	Loïc	CR	Génie des Procédés	SPIN
FEILLET	Dominique	PR1	Génie Industriel	CMP
FOREST	Valérie	MA(MDC)	Génie des Procédés	CIS
FRACZKIEWICZ	Anna	DR	Sciences et génie des matériaux	SMS
GARCIA	Daniel	MR(DR2)	Sciences de la Terre	SPIN
GAVET	Yann	MA(MDC)	Sciences des Images et des Formes	SPIN
GERINGER	Jean	MA(MDC)	Sciences et génie des matériaux	CIS
GOEURIOT	Dominique	DR	Sciences et génie des matériaux	SMS
GONDRAN	Natacha	MA(MDC)	Sciences et génie de l'environnement	FAYOL
GONZALEZ FELIU	Jesus	MA(MDC)	Sciences économiques	FAYOL
GRAILLOT	Didier	DR	Sciences et génie de l'environnement	SPIN
GROSSEAU	Philippe	DR	Génie des Procédés	SPIN
GRUY	Frédéric	PR1	Génie des Procédés	SPIN
HAN	Woo-Suck	MR	Mécanique et ingénierie	SMS
HERRI	Jean Michel	PR1	Génie des Procédés	SPIN
KERMOUCHE	Guillaume	PR2	Mécanique et Ingénierie	SMS
KLOCKER	Helmut	DR	Sciences et génie des matériaux	SMS
LAFOREST	Valérie	MR(DR2)	Sciences et génie de l'environnement	FAYOL
LERICHE	Rodolphe	CR	Mécanique et ingénierie	FAYOL
MALLIARAS	Georges	PR1	Microélectronique	CMP
MOLIMARD	Jérôme	PR2	Mécanique et ingénierie	CIS
MOUTTE	Jacques	CR	Génie des Procédés	SPIN
NAVARRO	Laurent	CR		CIS
NEUBERT	Gilles			FAYOL
NIKOLOVSKI	Jean-Pierre	Ingénieur de recherche	Mécanique et ingénierie	CMP
NORTIER	Patrice	PR1	Génie des Procédés	SPIN
O CONNOR	Rodney Philip	MA(MDC)	Microélectronique	CMP
PICARD	Gauthier	MA(MDC)	Informatique	FAYOL
PINOLI	Jean Charles	PR0	Sciences des Images et des Formes	SPIN
POURCHEZ	Jérémy	MR	Génie des Procédés	CIS
ROUSSY	Agnès	MA(MDC)	Microélectronique	CMP
ROUSTANT	Olivier	MA(MDC)	Mathématiques appliquées	FAYOL
SANAUR	Sébastien	MA(MDC)	Microélectronique	CMP
SERRIS	Eric	IRD		FAYOL
STOLARZ	Jacques	CR	Sciences et génie des matériaux	SMS
TRIA	Assia	Ingénieur de recherche	Microélectronique	CMP
VALDIVIESO	François	PR2	Sciences et génie des matériaux	SMS
VIRICELLE	Jean Paul	DR	Génie des Procédés	SPIN
WOLSKI	Krzystof	DR	Sciences et génie des matériaux	SMS
XIE	Xiaolan	PR0	Génie industriel	CIS
YUGMA	Gallian	CR	Génie industriel	CMP

Mise à jour : 30/08/2018

Remerciements - *Acknowledgments*

Je voudrais tout d'abord remercier l'ensemble des membres du jury pour avoir participé à ma soutenance. Je remercie en particulier Laurent Orgéas et Valérie Déplano d'avoir été les rapporteurs de mon manuscrit, vos commentaires m'auront apporté de nouvelles et nombreuses pistes de réflexion en plus de m'apporter un recul nécessaire sur mes travaux. Je remercie également Nele Famaey pour avoir si bien présidé ce jury. Merci aussi à Bram Trachet d'avoir accepté de faire partie du jury en tant qu'examinateur. Enfin merci à tous pour la discussion extrêmement intéressante qui a suivi la présentation.

Un immense merci à mon directeur de thèse, Pierre. Tu as été mon mentor tout au long de mon doctorat. Ta disponibilité et ta gentillesse m'ont permis de faire une thèse dont je suis très fier. Grâce à ton recul et ta curiosité j'ai toujours pu travailler en sachant où j'allais sans être dirigé de manière rigide et cela m'a fait mûrir plus que je ne l'aurais imaginé. J'espère que tu t'épanouiras dans ton nouveau métier (ce qui à l'air d'être complètement le cas de ce que j'en ai vu).
Un grand merci à Baptiste, mon encadrant. Tes connaissances dont j'ai très peu de fois atteint les limites m'ont débloqué des situations que je pensais désespérées. Tu m'as appris tellement de choses, de la mécanique expérimentale à la modélisation numérique. Tu as toujours été disponible lorsque que j'avais besoin d'aide et cela à grandement contribué à faire de cette thèse ce qu'elle est. J'espère que tu apprécieras la terrine de lapin ;).
Je vous remercie tous les deux du fond du coeur, vous avez été les meilleurs encadrants dont je puisse rêver, la team parfaite, vous m'avez tout appris en biomécanique. J'espère un jour m'élever à votre niveau. Encore une fois merci !

Je tiens aussi à remercier mes encadrants de Lyon, Eric Maire et Jérôme Adrien. Outre vos extraordinaires connaissances en tomographie qui ont été indispensables à ce travail, vous m'avez aussi apporté une formidable aide psychologique. Je ne compte plus le nombre de voyages infructueux à Lyon qui testaient mon mental. Votre bonne humeur et votre humour m'ont vraiment aidé à surmonter ces échecs et à persévérer.

Merci à Jérôme Molimard, mon directeur (temporaire) de thèse. Ta vision extérieur et tes commentaires pertinents m'ont aidé à prendre du recul sur mon travail et à l'améliorer. Tes conseils tout au long de mon doctorat m'ont été d'une grande utilité.

Je remercie Nicolas Curt sans qui cette thèse n'aurait pas été ce qu'elle est. Je ne sais pas comment on aurait pu construire les dispositifs expérimentaux sans toi. Tes connaissances et ta rigueur m'ont beaucoup apporté, je pense même être un peu plus ordonné que lors de mon arrivée (ce qui n'était pas gagné).

Je remercie chaleureusement Pierre-Yves Rohan. Lors de la première semaine du Master BME tu m'as mis en contact avec Pierre juste après que j'ai prononcé (un peu par hasard) le mot "cardio-vasculaire". Sans toi je n'aurais pas pu vivre cette formidable aventure.

Merci à tous les gens que j'ai rencontré pendant ces trois années et qui ont contribué de près ou de loin à ce travail scientifique. Merci à Stéphane Avril pour tes conseils toujours avisés, merci à Woo-Suck Han pour m'avoir permis de présenter mon travail plus d'une fois, merci à Norbert Laroche pour l'histologie. Un grand merci à Alberto Bravin et Michael Krisch de l'ESRF pour leur aide indispensable lors des essais au synchrotron. Merci à tout les autres que ma faible mémoire m'empêche de nommer ici.

Merci aux meilleurs des co-bureaux Nicolas, Joan et Claudie. Ça a été trois super années. Malgré quelques bruits intermittents qui venaient perturber notre concentration (je ne mettrais aucun nom), notre bureau était le meilleur des bureaux !

Merci aux Space Bros (Rossella, Maria, Nicolas, Joan), les premières personnes que j'ai rencontrées à Sainté. Le temps passé avec vous, à sortir, à s'amuser, à skier aussi, était vraiment cool. Dès que le covid sera passé, il va vraiment falloir qu'on se refasse un voyage en Italie avec restaurant illimité !

Merci à Sophie et Thierry d'avoir été mes colocs, ça a été un période vraiment sympa !

Merci aux anciens du CIS qui ont pavé le chemin avant moi, Boris, Cristina, Aymeric, Radha, Pierre, Mickael, Romain, Afafe, Roberto, Mohsen, et tous ceux que j'oublie. Merci à toi Fanette pour toutes ces soirées au Bul, promis dès que ça ré-ouvre on y fonce ! Merci aux docteurs ou futurs docteurs qui m'ont accompagné pendant ces trois ans de thèse: Cyriac, Ozge, Daniele, Jules, Hugo, Laure, Cindy, Carine, Salma, Corentin, Gökçe, Tristan, Madge, Ali, Daniele, Raja, et tous les autres...

Je remercie tous les membres de l'ASEC, la meilleure des teams, Marie, Yoann, Sophie, Aymeric, Momo. C'était vraiment cool d'organiser toutes ces soirées avec vous. Merci à Bastien et Floflo pour toutes ces soirées chez vous, vivement le prochain Gala ! Merci aussi à Baptiste pour ces discussions sur les zones cohésives et pour tes rhums arrangés, bonne chance pour la suite de ton doctorat ! Merci à Marion pour être aussi cool et pour toutes ces soirées passées avec Maud et toi. Merci à Brooks sans qui je n'aurais jamais pu faire mes expériences. Tu m'as appris tellement de choses et je t'en suis extrêmement reconnaissant.

Merci à ma stagiaire préférée Yasmine. Ta bonne humeur et ta volonté sont vraiment contagieuses. Bonne chance pour ton doctorat, tu vas tout démonter !

Merci à Françoise et Amélie pour votre gentillesse et pour votre efficacité. C'était vraiment agréable de travailler avec vous.

Grosse pensée à la Coloc de l'enfer avec tous les mamènes: Paulo, Chloé, Hugo, Diane, et Yasmine. Les soirées Chantier - Bul resteront toujours dans mon coeur. J'ai honnêtement vécu une des meilleures périodes de ma vie avec vous. Il faut absolument que l'on se refasse un week-end à Strasbourg tous ensemble !

Je remercie du fond du coeur tous les fratés de Savoie (il y en a trop pour les énumérer). Vous avez été ma bouffée d'oxygène lorsque rien n'allait, vous êtes ma deuxième famille. Le travail m'oblige à m'éloigner mais un jour je reviendrai et on passera nos journées au BdC tous ensemble.

Merci aux potes du Master Biomed et en particulier à l'Auberge (ils se reconnaîtront). C'est génial d'avoir gardé contact avec vous tous et de se revoir de temps en temps.

Merci aux potes des Arts et en particulier la Boquette des Riders, même si on est tous éparpillés ça fait vraiment plaisir de continuer à vous parler et de se revoir de temps en temps pour une soirée ou une rando. Vivien j'oublie pas la rando que l'on doit faire mais mes petits muscles ont peur de ce que tu va leur faire subir. Au passage, merci au grô Hugo, le bateau (j'apprécie mieux la vie depuis) puis le voyage au Népal ont été des expériences magiques ! Va falloir qu'on se refasse un truc dans le genre un de ces jours !

Merci à Gilbert de la boucherie Maison Didier, sans toi je n'aurais pas pu faire toutes ces expériences. Merci aussi à la Bergerie de la Combe aux Loups. Enfin merci à la boucherie Despi.

Un grand merci à ma famille de m'avoir soutenu pendant ces trois ans. Merci à toi Bernard de m'avoir conseillé et aidé tout au long de ma scolarité, sans toi je ne serais pas là où j'en suis (merci aussi pour la veste orange, elle m'aura servi autant au labo qu'en Asie). Merci au meilleur des petits frères, Théo, toujours partant pour me remonter le moral avec un tacos ! Merci à Lucile aussi, nouvelle dans la famille. Merci à mon père et ma mère de m'avoir soutenu en toute circonstance et d'avoir pris de votre temps pour me donner des (incroyables) coups de main quand ça n'allait pas. Je me rappelle, quand j'étais jeune je voulais être électricien comme toi Papa, tu m'as alors dit: "Fais autant d'études que tu peux fils, l'électricité je pourrai toujours te l'apprendre moi-même", ba voila je suis docteur Papa !!

Merci à Jean-Marc et Sylvie de m'avoir accueilli plusieurs fois pour de courtes vacances.

Un grand merci à Maud-ounette (Bonjour !!) qui m'a supporté pendant plusieurs années déjà. Nous sommes à la fois si semblables (vive le désordre) et si différents. Tu m'as soutenu et réconforté quand ça n'allait pas tout au long de ces 3 années. Merci beaucoup !!

Enfin merci à tout ceux que j'ai oublié, malgré le doctorat ma mémoire est toujours aussi peu fiable.

Contents

List of Figures

List of Tables

Introduction Générale - *General Introduction*

La dissection aortique est une maladie vasculaire grave caractérisée par un décollement des couches de la paroi artérielle. Dans la majorité des cas, une déchirure au niveau de la paroi interne de l'aorte est présente, permettant au sang sous pression de rentrer et de créer un faux chenal. La mortalité due à cette affection est particulièrement élevée et demande une intervention chirurgicale dans les délais les plus brefs. Bien que largement documentés cliniquement, les conditions et mécanismes à l'origine de cette maladie sont peu connus et de nombreuses questions restent sans réponses. De plus, un grand nombre de patients décèdent avant d'avoir atteint l'hôpital, il est donc nécessaire d'identifier les patients à risque. Pour cela une connaissance approfondie des phénomènes en jeu est nécessaire.

La dissection aortique peut être séparée en deux mécanismes : l'initiation et la propagation. Les interrogations sur cette maladie sont principalement centrées sur le premier de ces mécanismes. La chaîne d'événements menant à la dissection de la paroi est peu décrite, ce qui s'explique par le fait que la dissection est un phénomène rapide et difficilement observable. La grande majorité des observations cliniques sont réalisées *a posteriori* de la dissection, ce qui conduit à faire des hypothèses concernant son déroulement. Ainsi, de nombreuses interrogations subsistent concernant les fissures intimales : comment se forment-elles ? Quelle est leur forme et leur direction ? Pourquoi certaines se propagent et d'autres non ? Quelle est leur taille initiale et comment cette taille évolue-t-elle durant la propagation ? Un consensus semble exister sur la nécessaire dégénérescence de la paroi aortique conduisant à un affaiblissement de sa résistance face à la contrainte exercée par la pression sanguine. Cependant, le consensus s'arrête là et les pistes étudiées pour expliquer la formation et la propagation de la dissection aortique sont nombreuses.

Pour résoudre ces questions, de nombreux travaux se sont concentrés sur l'étude et la quantification du comportement de l'aorte à l'échelle macroscopique. Le comportement élastique de l'aorte a été étudié, ainsi que son comportement dans les différents modes de rupture. Cependant, la caractérisation mécanique macroscopique de la paroi aortique n'explique pas l'ensemble des phénomènes en jeu. En effet, la paroi aortique possède une structure en trois dimensions hétérogène et complexe. Il est donc essentiel d'étudier la dissection aortique à différentes échelles et faire le lien entre elles.

Un certain nombre d'études utilisent des modèles numériques pour mieux comprendre l'impact de certains composants micro-structurels sur l'initiation de la dissection aortique. Cependant, peu de données expérimentales permettent de comparer avec le réel les résultats obtenus et de valider ces modèles.

Les nouvelles avancées sur les techniques d'imagerie permettent de réaliser des études

approfondies au niveau de la structure de la paroi. Ainsi, de plus en plus de travaux combinent test mécanique et méthode d'imagerie afin de mieux comprendre l'influence de la microstructure sur le comportement global de la paroi aortique. Cela peut aussi permettre de quantifier les mécanismes observés afin de créer et/ou valider des modèles numériques.

Cette étude doctorale fait partie du projet de recherche AArteMIS, financé par le Conseil Européen de la Recherche (European Research Council, ERC). Elle est le résultat d'un travail conjoint entre :

- le Centre Ingénierie et Santé de l'École des Mines de Saint-Étienne, via le département STBio qui étudie la biomécanique des tissus mous,
- le laboratoire MaTéIS de l'INSA de Lyon grâce à qui nous avons pu réaliser les analyses de tomographie à rayon X.

Ce manuscrit est découpé de la façon suivante :

Le **Chapitre 1** présente le contexte clinique et scientifique de cette étude. Une revue de la littérature sur la caractérisation mécanique de l'aorte dans le cas de la dissection aortique et la modélisation des phénomènes liés à cette maladie est présentée. Enfin, les hypothèses et les objectifs de cette étude sont décrits.

Le **Chapitre 2** présente une étude basée sur le travail de Helfenstein-Didier et al. [89]. Un modèle reproduisant la rupture des différentes couches de la media lors d'un test uniaxial est élaboré. Par la suite, les propriétés matériaux et de rupture en mode I sont identifiées pour chaque échantillon par des méthodes inverses. Enfin, une étude de sensibilité sur un modèle éléments finis est réalisée afin d'étudier l'influence du cisaillement entre les lamelles médiales lors de la rupture de la paroi aortique.

Le **Chapitre 3** étudie plus en détail la délamination en mode II en réalisant un test *in situ* de traction sur des échantillons aortiques entaillés sous radiographie par rayons X. Par la suite, un modèle éléments finis est calibré sur les expériences afin de quantifier les propriétés de rupture en mode II dans les directions circonférentielle et longitudinale.

Le **Chapitre 4** présente une étude élément finis mené grâce à un modèle de dissection aortique. Cette simulation utilise la méthode des éléments finis étendues pour quantifier l'influence de plusieurs paramètres géométriques et mécaniques (la géométrie de la fissure, la contrainte résiduelle, les paramètres de rupture) sur l'initiation et la propagation d'une fissure dans la paroi aortique.

Le **Chapitre 5** présente deux études expérimentales. La première étude décrit une méthode expérimentale *in situ* associant un test de traction-gonflement avec de la microtomographie aux rayons X. Un dispositif de traction-gonflement s'adaptant à l'intérieur d'un tomographe a été développé. Une fissure est créée préalablement dans l'artère afin d'étudier sa propagation lors du gonflement. Cette expérience permet la reconstruction en 3D de la structure de l'échantillon à différentes pressions. Le protocole ainsi que les résultats de deux échantillons sont présentés. Dans la deuxième étude les propriétés mécaniques d'échantillons d'artères carotides communes sont caractérisées grâce à des tests uniaxiaux et des tests de pelage afin de comprendre pourquoi ces tissus sont plus résistants à la dissection que les tissus aortique.

Le **Chapitre 6** décrit une campagne expérimentale menée sur des aortes de lapin afin de quantifier l'influence de la géométrie et de la direction de la fissure intimale sur l'initiation

et la propagation de la dissection. La méthode de test *in situ*, décrite dans le chapitre 5, est utilisée et permet de caractériser la morphologie de l'aorte et de la fissure jusqu'à rupture. De plus, l'observation de la dissection en temps réel par images radiographiques permet une description complète des mécanismes intervenant dans la dissection aortique.

Enfin, une discussion synthétise l'ensemble des résultats, les limites de ces études, et les perspectives prévues pour l'avenir.

Chaque chapitre est précédé d'un résumé en français récapitulant les principales motivations du chapitre, ainsi que les résultats et conclusions.

Chapter I

Contexte - *Context*

This introductory chapter describes the clinical and scientific context of this study. An overview of the aortic anatomy followed by the aortic dissection and its management is presented. In a second part, the state of the art details the mechanical experiments and the computational modelling investigating aortic dissection. This section was published as a review paper in IEEE Review in Biomedical Engineering (jan. 2020); however, the text is shortened herein to avoid repetitions. In the last section of the chapter, the main hypothesis and objectives of the doctoral work are outlined.

Contents of the chapter

Résumé du chapitre

Le système artériel alimente le corps en oxygène et en nutriments, nécessaires à son fonctionner. La principale artère de ce système est l'aorte, elle est composée de plusieurs sections : l'aorte ascendante, la crosse aortique, l'aorte thoracique descendante, et enfin l'aorte abdominale. L'aorte est composée de trois couches principales, l'intima, la media, et l'adventitia. Chacune de ces couches a une fonction propre et permet à l'aorte de transporter le sang du cœur vers les artères plus petites de façon continue, tout en résistant à la contrainte mécanique induite par la pression sanguine. Une des maladies pouvant toucher l'aorte est la dissection aortique. Une fissure dans l'intima permet au sang de s'engouffrer dans la paroi aortique, entraînant une délamination des couches de la media. Cette condition s'avère souvent fatale si elle n'est pas prise en charge à temps. Les principaux facteurs de risques sont l'hypertension, l'athérosclérose, la bicuspidie valvulaire aortique, les troubles génétiques affectant les tissus conjonctifs. La prévention de cette maladie consiste à limiter les facteurs de risques, notamment l'hypertension, le tabac, et la dyslipidémie [1]. Les symptômes de la dissection aortique sont similaires à ceux d'autres maladies plus fréquentes comme l'infarctus du myocarde, ce qui peut souvent entraîner un délai dans la pose du bon diagnostic. Plusieurs techniques d'imagerie médicale comme le scanner permettent de confirmer le diagnostic. Différentes classifications existent concernant la dissection aortique, la plus utilisée étant le système de Stanford. Selon l'anatomie de la dissection et sa complexité, un traitement médical et/ou une intervention chirurgicale sont nécessaires.

L'état de l'art peut être divisé en deux parties : une partie expérimentale regroupant les essais mécaniques caractérisant les propriétés de l'aorte, et une partie regroupant les modèles mécaniques analysant les mécanismes à l'œuvre durant une dissection aortique. Les techniques d'imagerie en clinique et en recherche sont comparées en fonction de leur résolution, leur champ de vision, et leur particularités respectives (Table I.1). La caractérisation expérimentale s'appuie sur différents essais mécaniques : les tests uniaxiaux dans les différentes directions (radiale, circonférentielle, et longitudinale), les essais de peeling, les tests de cisaillement, et enfin les tests de traction-gonflement. Une partie spécifique est dédiée aux essais *in situ* qui combinent test mécanique et technique d'imagerie. Ce type d'expérimentation permet d'étudier l'évolution de la structure à différentes échelles (macro ou micro) durant une déformation mécanique.

Les approches pour modéliser les mécanismes de la dissection aortique sont variées. Les modèles se basant sur le calcul de la contrainte maximale dans la paroi aortique pour prédire la zone de rupture se sont révélés être des outils de prédiction limités. Les modèles étudiant la dissection aortique à l'échelle macroscopique et intégrant des mécanismes de rupture ont permis de modéliser des essais simples comme les tests uniaxiaux ou de pelage. Malgré les nombreuses informations apportées, ces modèles sont limités et ne permettent pas de représenter le comportement de l'aorte lors d'une dissection aortique. En effet, la paroi aortique possède une structure complexe et hétérogène, des modèles à une échelle plus petite sont nécessaires pour comprendre et quantifier l'influence et le comportement des différents composants. Les modèles multi-échelles relient la microstructure et la macrostructure afin de prendre en compte l'ensemble des paramètres intervenant lors de la rupture du tissu aortique, ainsi ils sont une solution pour palier ce problème d'échelle.

Dans la dernière partie de ce chapitre, les questions et objectifs de ce travail doctoral sont

1. Concentration trop importante de lipides dans le sang

présentés.

I.1 Anatomy pathophysiology

I.1.1 Arterial system and aorta

The arterial system is composed of a number of vessels which transport the blood from the heart to the capillaries network throughout the body (Figure I.1). The main function of the arteries is to carry oxygen and nutrients, and remove carbon dioxide and waste products. This system is categorized into two subsystems: pulmonic and systemic. Pulmonic arteries are low-pressure vessels that moves the deoxygenated blood from the heart to the lungs, whereas systemic arteries are high-pressure vessels that transport the oxygenated blood from the heart to the rest of the body. During the cardiac cycle, the arterial pressure varies between a minimum, called diastolic pressure, and a maximum, called systolic pressure. Arteries of the systemic circulation can be divided into two groups: elastic and muscular arteries. Elastic arteries include the aorta, main pulmonary artery, common carotids, and common iliacs, and muscular arteries include the coronaries, cerebrals, femorals, and renals. These two types of arteries differ in their microstructure and composition in term of relative amount of connective tissue and smooth muscle cell [102]. Another difference lies in their diameter, elastic arteries tend to have a large diameter and be closer to the heart, whereas muscular arteries have a smaller diameter and are located closer to the arterioles. Elastic arteries use their elastic properties to store elastic energy during systole and restore it during diastole, avoiding intermittent flow, this effect is called Windkessel effect. Conversely, with a relatively higher smooth muscle to elastin content, the muscular arteries are able to regulate the pressure and distribute the blood according to peripheral body needs by varying their diameter.

The aorta is the largest blood vessel in the body with a diameter varying between 16 mm to 35 mm under pressure depending on the location along the vessel and on the gender [9, 82]. The aorta is attached to the heart by a segment called the ascending aorta. This section arises from the left ventricle, initiating at the aortic valve. It has a total length of about 5 cm and is twisted around the pulmonary trunk. Both of these blood vessels are encompassed in a pericardial sheath. The ascending aorta merges into the aortic arch at the second sternocostal articulation and loops over the bifurcation of the pulmonary trunk and the left pulmonary artery. The brachiocephalic trunk, the left common carotid artery, and the left subclavian artery branch off the upper part of the aortic arch. Then, the aorta curves downward and descends vertically. At the lower border of the fourth thoracic vertebra the aortic arch ends and the descending aorta begins. This segment is divided into two sections separated by the diaphragm: the thoracic aorta and the abdominal aorta. The descending aorta has multiple branches which are either parietal or visceral branches. The abdominal aorta is approximately 13 cm long and ends by bifurcating into the two iliacs arteries.

I.1.2 Structure of the aorta

The aorta is composed of three layers. The innermost layer is the intima. It is composed of (i) a single and smooth layer of endothelial cells in contact with blood, called endothelium, underlying on (ii) a thin basal membrane (∼80 nm) and (iii) a sub-endothelial layer composed of smooth muscle cells, collageneous bundles and elastic fibrils [182, 67]. Subendothelial layer thickness depends on location, age and disease. Although the endothelium does not contribute significantly to the mechanical behaviour of the arterial wall, the subendothelial layer certainly does. Holzapfel et al. [94] demonstrated that in coronary

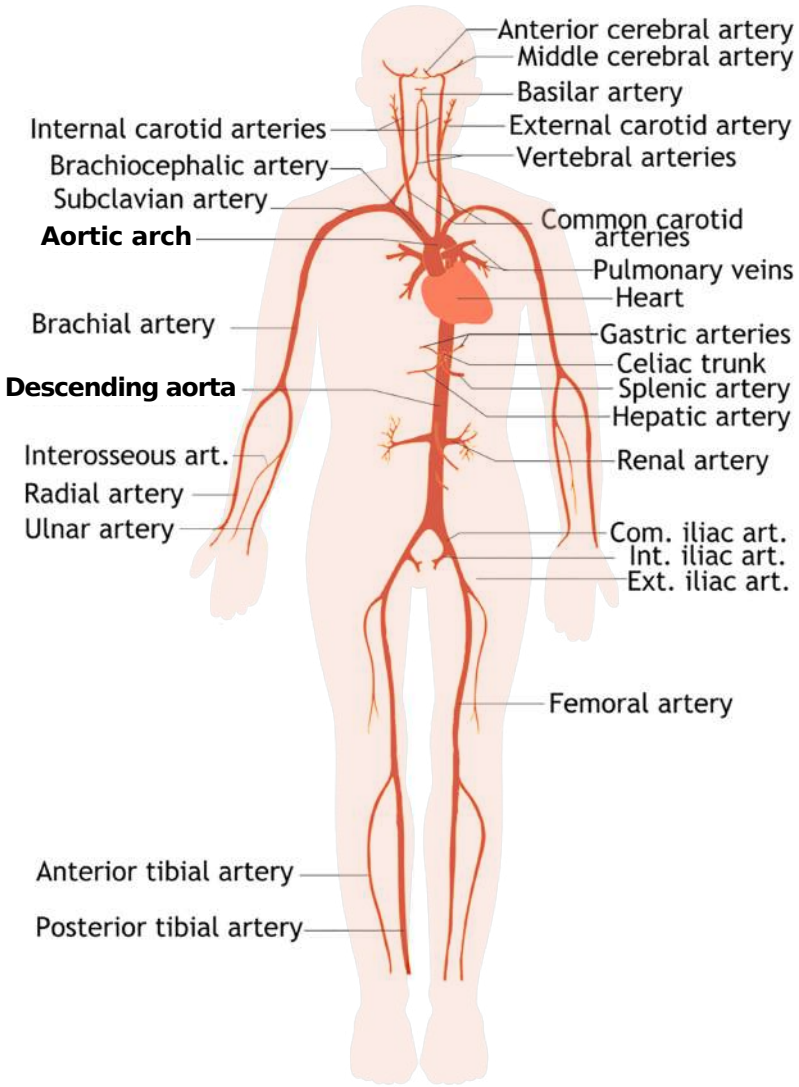

Figure I.1 – Human circulatory system with the principal systemic arteries. Modified from Qin et al. [105]

arteries the subendothelial layer exhibits a significant thickness, load-bearing capacity, and mechanical strength in comparison with the media and adventitia. The middle layer is the media. It is a complex structure consisting in several lamellar units called musculo-elastic fascicles, separated by elastin laminae. Each unit is mainly composed of elastin, type I and III collagen and smooth muscle cells [37, 132]. The media is separated from the intima by the internal elastic lamina and from the adventitia by the external elastic lamina. Due to its organization, similar to laminate composites, the media resists to relatively high loads in longitudinal and circumferential directions but is weaker in the radial direction [130]; hence, it is prone to dissection separation, a delamination event. The outermost layer is the adventitia. It is composed mainly of fibroblasts, fibrocytes, ground substance and type I collagen [132]. It is surrounded by connective tissue and the limit between the two is not clearly defined. The vasa vasorum, a network of vessels and capillaries in the adventitia and outer part of the media, provides blood supply and nourishment to the aortic wall. The adventitia has a significant role in the stability and ultimate strength of the artery. At the unloaded state, adventitial collagen is crimped, the consequence is that the media mainly contributes to the mechanical behaviour of the arterial wall at low pressure. However, at a

significant strain, collagen fibres are straightened and the arterial wall becomes extremely stiff, effectively preventing the artery from overstretching and rupture. Furthermore, the arterial wall is not stress-free without external loads, layer-specific residual stresses were evidenced [36] and shown to play an important role as pointed out by Holzapfel et al. [96]. In particular, it may homogenize the circumferential stress, thus diminishing the stress gradients through the aortic wall. A schematic of the aortic structure is presented Figure I.2.

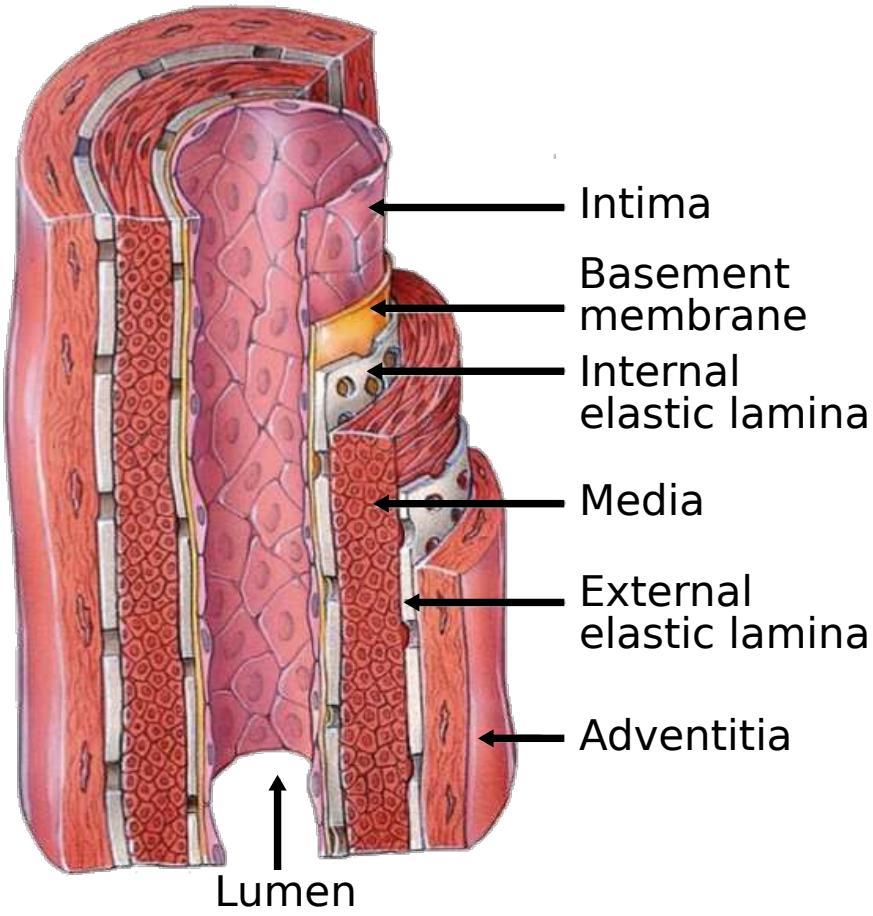

FIGURE I.2 – Structure of an elastic artery with the major histological components. Adapted from [8]

I.1.3 Aortic dissection

The aorta can be affected by several diseases, the most common are aortic aneurysm, aortic dissection and atherosclerosis. Aortic dissection is a sudden delamination of the aortic wall occurring in the medial layer. In the majority of cases, dissection is described as initiating with an intimal tear which then allows blood flowing in the media [230], although intramural haemorrhage can also lead to dissection [157, 231] (Figure I.3). Aortic dissection most often occurs in the ascending aorta (62%), along the right lateral wall, where the maximum shear stress caused by blood flow is located [156]. Another common site is below the ligamentum arteriosum (16%), in the descending thoracic aorta [187, 110]. The dissection can propagate either in the antegrade or retrograde direction [2] from the intimal tear or haemorrhage. This clinical description is based on the location of the

2. Forward and backward in the direction of blood flow, respectively

entry tear in the aortic wall in relation to the blood flow direction. Once the intimal entry (or tear) is formed, propagation starts, eventually creating an intimal flap. Two pathways for the blood are then present, the true lumen and the false lumen. This condition is extremely dangerous for the patient as it affects the mechanical integrity of the arterial wall, compromising its strength and hemodynamics due to the false lumen narrowing the true lumen, or occluding collateral vessels, which leads to a decrease in blood supply of tissues and organs.

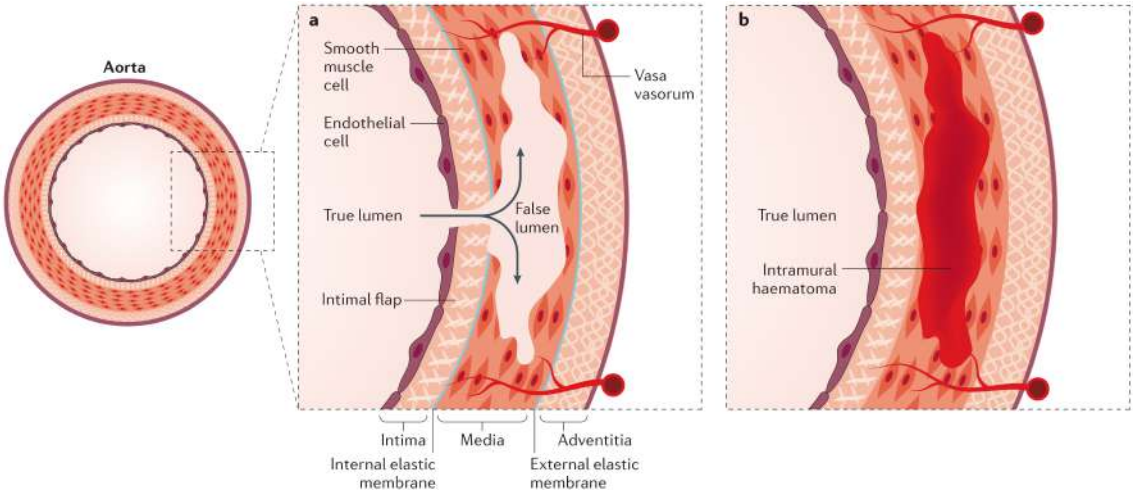

Figure I.3 – Aortic dissection propagating in the medial layer of the aortic wall. (a) An intimal tear is present and allows the blood to flow in the media creating a false lumen. (b) In some cases, an intramural haematoma caused by a rupture in the vasa vasorum can also progress in dissection. Reproduced from Nienaber et al. [156].

Aortic dissection requires rapid diagnosis and decision-making. The incidence of this pathology is 3–5 cases per 100,000 people per year, and 35 cases per 100,000 people per year among the 65-75 years of age. Risk factors include hypertension, atherosclerosis, bicuspid aortic valve, and genetic disorders that affect connective tissue like Marfan syndrome [156]. Without intervention, up to 90% of patients with acute aortic dissection die within weeks [117]. Aortic dissection can also be caused by traumas, for instance occurring in a car accident [156], or during catheter insertion [51, 75]. For example, balloon angioplasty can lead to several undesirable side effects including permanent damaging of the arterial wall caused by over-stretch and atherosclerotic plaque fracture [13].

I.2 Management of aortic dissection

I.2.1 Prevention

Hypertension is an important risk factor for aortic dissection and could be prevented by a careful control of the blood pressure. Smoking and dyslipidaemia [3] are also considered as preventable risk factors for aortic dissection.

I.2.2 Diagnosis

Aortic dissection diagnosis is complicated as the symptoms are similar to other more common diseases such as myocardial infarction. As a result, in more than 30% of cases the

3. Abnormal amount of lipids in the blood

treatment of a patient is delayed due to an incorrect diagnosis on first presentation [156], decreasing greatly his survival rate.

I.2.3 Screening

The different imaging modalities currently used in clinics when an aortic dissection is suspected are helical computed tomography (CT), transthoracic echocardiography (TTE), transesophageal echocardiography (TEE), and magnetic resonance imaging (MRI). In clinical management, imaging techniques are crucial in the treatment of aortic dissection. This disease can rapidly threaten the patient life; thus, time is essential in the confirmation of the diagnosis. Other goals are localization of the initial tear, assessment of the extent of the dissection, and finally, classification of the dissection (Fig. I.4) [155].

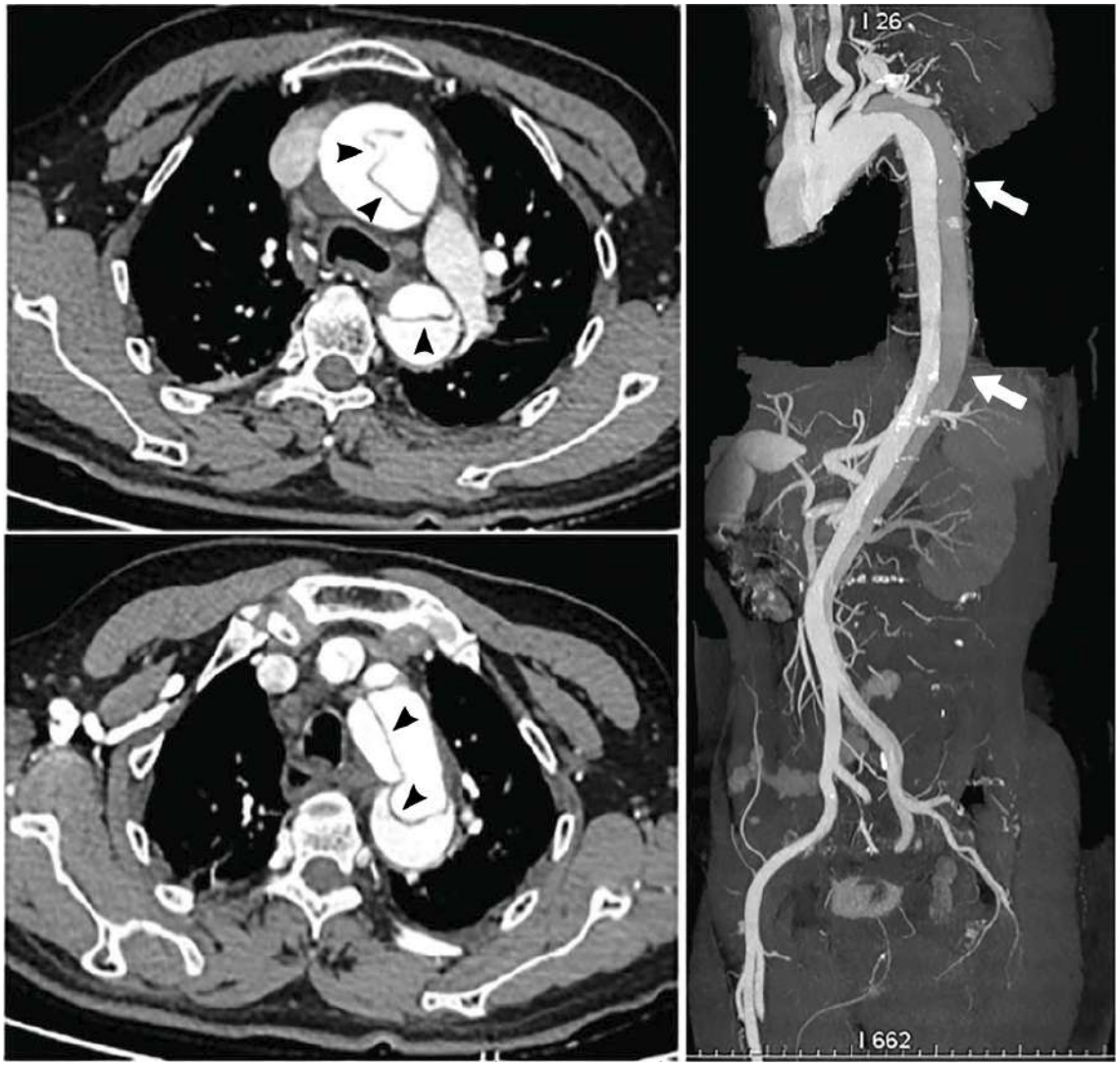

FIGURE I.4 – CT angiography of a patient with a type I aortic dissection originating in the ascending aorta and propagating to the aortic arch and descending aorta (black and white arrows). Modified from Qin et al. [177].

I.2.4 Classification

Several classification systems have been used to describe aortic dissection; however systems based on the anatomy of the dissection are increasingly being used as they allow a better

decision-making. Two anatomical classification systems are presented here: DeBakey and Stanford (Figure I.5 b,c,d). The DeBakey classification system is divided as follows:

- Type I: the dissection originates in the ascending aorta and propagates at least to the aortic arch.
- Type II: the dissection is limited to the ascending aorta only.
- Type III: the dissection originates distally to the subclavian artery in the descending aorta and the propagation either stops above the diaphragm (type IIIa) or extends beyong the diaphragm (type IIIb).

From a more practical perspective, the Stanford classification system distinguishes two groups:

- Group A: the dissection involves the ascending aorta. In most cases, this condition requires a surgical intervention. It includes DeBakey type I and type II.
- Group B: the dissection involves the descending aorta only. In this case, medical management is prefered over surgical management. It includes DeBakey type IIIa and type IIIb.

The Stanford classification is the most commonly used system in clinics as it simplifies the decision-making concerning the management of the patient. Nevertheless, it remains a tool and the final choice belongs to the clinician. For instance, a complicated Stanford type B dissection requires a surgical intervention. Complications include damaging of a vital organ, rupture of the aorta, retrograde dissection into the ascending aorta.

Highlights

- Aortic wall has a complex fibrous structure divided into 3 layers: intima, media, adventitia.
- Aortic dissection is a life-threatening disease with a high mortality rate.
- Location of the intimal tear determines the need for surgery. Thereby, understanding the apparition and propagation of initial tear is essential.

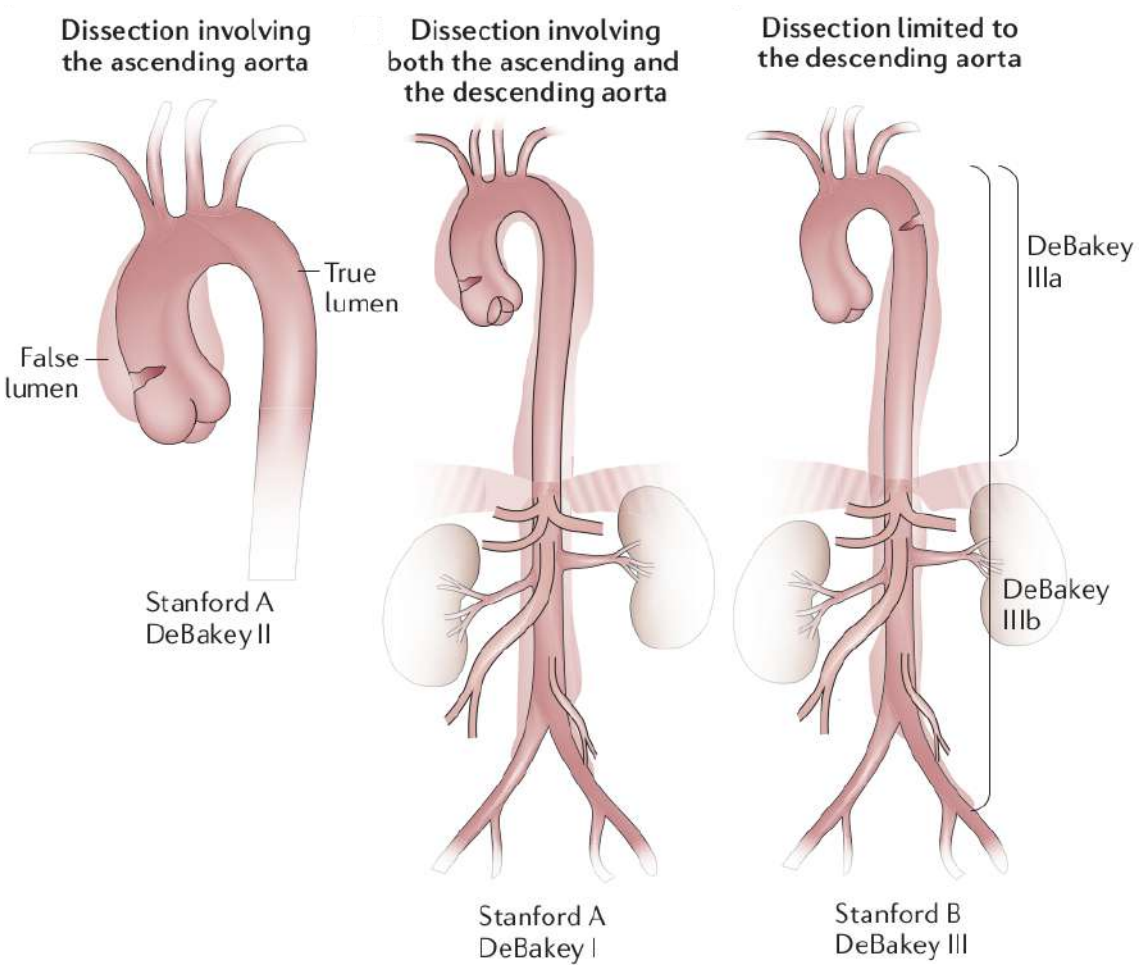

FIGURE I.5 – DeBackey and Stanford classifications systems. Modified from Nienaber et al. [156].

I.3 State of the art regarding current advances in the mechanical description and quantification of aortic dissection mechanisms

Extracted from the paper "Review of current advances in the mechanical description and quantification of aortic dissection mechanisms." published in IEEE Review in Biomedical Engineering (2020) [26]. The text is shortened herein to avoid repetitions.

I.3.1 Introduction

Because its immediate consequences are hemodynamics-related, existing aortic dissection was often studied from the perspective of fluid mechanics and fluid-structure interactions [48], the objective of such approaches being to determine which treatment would be the most appropriate for a given patient, with minimum potential complications. Various approaches were applied to investigate the effect of hemodynamics on aortic dissection. Thanks to advances in medical imaging such as 4D magnetic resonance imaging (MRI), blood flow velocity [207, 244] and arterial wall displacement [236] can be measured during the cardiac cycle which constitutes valuable input for such approaches. However, the accuracy is still not sufficient to assess the wall shear stress accurately [212], especially in aortic dissection where flow velocity gradients around the dissection are high, and the presence of an intimal flap makes it even more complex. To address this issue, computational fluid dynamics approaches coupled with patient-specific models were used [31, 109, 229, 210]. These models allowed obtaining local pressure and wall shear stress values. Yet, some assumptions on which they rely are questionable. A major one is to consider the aortic wall as rigid, while it is very compliant and its geometric variations may be substantial. A relevant approach, in that respect, is fluid-structure interaction modeling [68, 113, 4] which couples fluid and solid mechanics. Though very promising, these models involve many constitutive and numerical parameters, in addition to intrinsic complexity (example: remeshing issues when large transformations occur) [19]. Although the results of such investigations are crucial to improve clinical care and help in decision making for patients suffering from an already detected dissection, models related to hemodynamics will not be reviewed. Readers are referred to the work of Morris et al. [148] for further reading on these aspects.

The mechanical event of aortic dissection itself can be separated in two different mechanisms: initiation and propagation, the causes and most influential factors of which are not well understood. Rajagopal et al. [179] postulated that initiation of the aortic dissection can be related to systolic blood pressure, while pulse pressure and heart rate can influence its propagation. Osada et al. [165] observed that most aortic dissections developed in the outer third of the media, alongside the vasa vasorum, suggesting an important role of the vasa vasorum in initiation of aortic dissection. Recently, pooling of glycosaminoglycans/proteoglycans was identified as a possible cause for aortic dissection initiation by creating significant stress concentrations and intralamellar swelling in the arterial wall [101, 190, 3].

The various conclusions and hypotheses formulated based on these studies reveal a marked lack of understanding of the underlying mechanisms involved in aortic dissection initiation and propagation certainly due to the complexity and multiple causes involved. In particular, advanced mechanical analyses of the underlying mechanisms based on mechanical

experiments, as well as structural observations at the relevant scales combining mechanical loading and imaging, would deeply improve current knowledge of these life-threatening events and could improve clinical decision criteria. In this context, the objective of the present state of the art is to focus on previous works which address relevant aspects to these questions of initiation and propagation of aortic dissection. An overview of the experimental techniques will be addressed first. Then, modeling approaches will be presented along with their added value and limitations. This section will be concluded by open questions and perspectives.

I.3.2 Experimental approaches to dissection mechanics

Aortic dissection is a complex vascular event involving several phenomena at different scales. Experimental studies focusing on the mechanisms behind this phenomenon are still rare in the literature. A likely reason is that aortic dissection, and especially its initiation, is a dynamic, transient process which turns out to be difficult to observe or quantify due to its spontaneity and relative short duration. In addition, the complexity of the vascular wall micro-structure explains the difficulty of identifying the modes of rupture involved in aortic dissection.

In this regard, it must be mentioned that imaging techniques have been a prerequisite to any progress towards improved management and understanding of dissection. On both clinical and research sides, available imaging techniques present advantages and drawbacks, requiring compromises to be made according to each use. Acquisition time, field of view, resolution are typical features of interest in this context. Imaging techniques are essential to most of the research presented in this state of the art but all technical aspects and choice-making criteria are out of the present scope. Only a brief overview of the most common techniques, used in clinics and/or research works detailed herein, is provided in Table I.1. It should be emphasized that this comparison was made from a research point of view and not from a clinical one.

Animal tissues are extensively used for in-vitro mechanical testing (Section I.3.2.1), although human tissue has also been characterized. Porcine aortic tissue is usually regarded as a good candidate due to its anatomical similarity, although not identical [45], with human aortic wall [163]. However, the majority of porcine aortas are harvested on young healthy animals while aortic dissection occurs in cases of medial degeneration and hypertension [134]. On the other hand, mouse models have been widely used for in-vivo testing, as detailed in section I.3.2.2.

In the following, we report the work of several authors who performed experimental investigations aiming at describing and quantifying the mechanisms involved in aortic dissection. In brief, macro-scale investigations mainly provided global descriptive trends on dissection propagation, as well as quantitative energetic values involved in the delamination phenomena. On the other hand, experiments performed at lower scales were relevant in addressing more quantitative aspects related to elementary mechanisms possibly involved in the dissection sequence from initiation to a propagated dissection, towards a possible classification of these mechanisms. This section is divided into two parts, addressing respectively *in vitro* and *in vivo* investigations.

Imaging Technique	Spatial Resolution	Field of view	Advantages	Drawbacks	References
Clinical Computed Tomography (CT)*	$\sim$ 500 µm	Non limiting	Widely available	Contrast agent needed Ionizing radiation	[124, 100, 73]
Clinical MRI*	$\sim$ 1 mm	Non limiting	Great scale of view Good contrast	Long-time scan Lack of availability	[79, 124]
Clinical Echocardiography techniques*	$\sim$ 100 µm	Maximum depth: 100 mm	Great temporal resolution Portable Cheap	Operator-dependent	[137, 147]
Light-based histology	0.2 µm	In plane: $\sim$ 10 mm	Good resolution Wall scale	Tissue damaged	[15]
Electron-based histology	$\sim$ 5 nm	In plane: $\sim$ 10 µm	Extremely good resolution	Tissue damaged	[74, 160, 114]
High-resolution Ultrasound	30 - 100 µm	Maximum depth: 15 mm; lateral: $\sim$ 20 mm	Great temporal resolution Good field of view	Poor resolution	[63, 226, 133, 99]
Multiphoton microscopy	15 - 1000 nm	Maximum depth: $\sim$ 300 µm; lateral: $\sim$ 750 µm	Great resolution Intrinsic fluorescence of tissues	Limited field of view Poor penetration	[114, 78, 30]
X-ray computed tomography	0.150 - 4 µm	$\sim$ 1-10 mm^3	Good field of view Great resolution	Ionizing radiation Contrast agent needed	[158, 89, 235, 183]
Optical coherence tomography	1 - 10 µm	Maximum depth: 5 mm; lateral: $\sim$ 1 mm	Great resolution	Shadowing effect Poor penetration Low contrast	[1, 78, 5]

* Representative equipment used in standard clinical practices

TABLE I.1 – Comparison of the different imaging techniques currently used in clinics and research. Values present in this table are given as orders of magnitude of what can be accomplished with standard methods, lower resolutions can be achieved in special conditions. Spatial resolution and field of view correspond to a range of values found in the mentioned references for imaging arterial tissue.

I.3.2.1 *In vitro* characterizations

Fracture can happen following three modes: mode I is described by a normal opening with respect to the crack surface, mode II is described by shear sliding parallel to the crack surface but orthogonal to the leading edge, and mode III is described by shear sliding parallel to the crack surface and to the leading edge (Figure I.6). These modes can be mixed depending on, for instance, the external loading, the material properties, and the crack propagation. Though mode I is very likely to be dominant in an already opened dissection which propagates due to blood pressure, a detailed and accurate description of fracture modes and their ratios from early initiation to complete propagation of dissection remains an open question. The present subsection introduces studies that were performed to characterize these fracture modes in the context of arterial dissection.

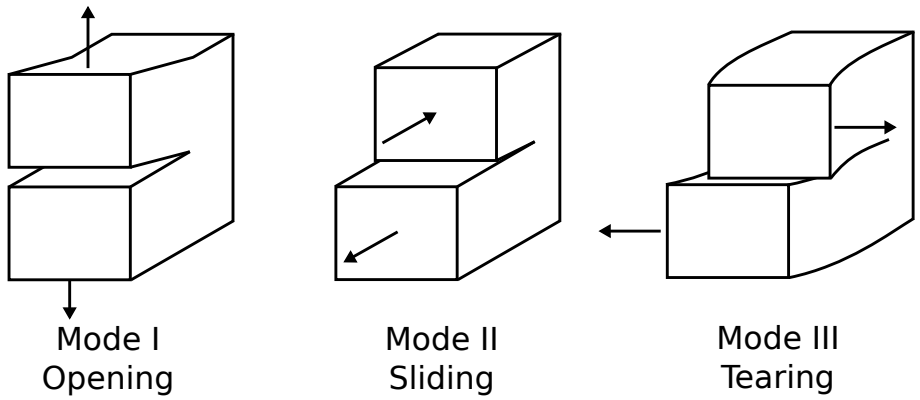

FIGURE I.6 – The three fracture modes: opening mode (mode I), sliding mode (mode II), and tearing mode (mode III).

Liquid infusion test

One of the first techniques used to study the mechanisms leading to dissection was developed by Roach and co-workers. A fluid was infused at a constant flow rate into the media using a thin needle, resulting in the progressive delamination of elastic laminae in the path of least resistance, while recording pressure and volume. In an early study, Carson et al. [28] assessed the strength of the media and its influence on the propagation of the dissection thanks to this technique. The test was done on 31 opened porcine upper descending thoracic aortas. The peak pressure to tear the aortic media was 77.2 ± 1.5 kPa (579 mmHg) which is a non-physiological blood pressure suggesting that the mechanical strength of the aortic wall has to be weakened for aortic dissection to initiate. The energy release rate required to propagate the dissection was 15.9 ± 0.9 mJ/cm^2, and the pressure required to propagate the dissection dropped down to a physiological range, which suggests a clear distinction between initiation and propagation events. Tiessen et al. [220] investigated the influence of several parameters on the propagation of dissection in 21 opened unpressurized human aortas. The peak pressure to tear the media was 79 ± 29 kPa and their results did not show any significant effect of age and tear depth on medial strength of human aorta. However, sex, location and atherosclerotic plaque formation did. Roach et al. [185] studied the influence of the location on the energy required to propagate the dissection in 17 opened porcine aortas. The energy release rates were 2.84 ± 1.19 mJ/cm^2 for the upper thoracic aorta, 2.90 ± 1.21 mJ/cm^2 for the lower thoracic aorta, 1.88 ± 0.89 mJ/cm^2 for upper abdominal aorta and 11.34 ± 4.05 mJ/cm^2 for lower abdominal aorta. It was also observed that the lower abdominal aorta tore at a lower pressure but

required higher energy to propagate the dissection. Observations with scanning electron microscopy (SEM) suggested a change in the elastin microstructure between the thoracic aorta and the abdominal aorta. This could explain the difference in values. Using the same technique, but with pressurized aortas under static conditions (i.e. no flow), Tam et al. [213] investigated the influence of tear depth on the propagation of the dissection in porcine thoracic aorta. Blebs were created in the media using saline solution and a circumferential slit was made on the intimal side to connect the true and false lumen. Then, the aortas were pressurized under no-flow conditions until propagation. Their results showed that propagation of the dissection occurred for tear (normalized) depth of 0.44 to 0.89 (with 1 being closest to the adventitial side). A positive correlation was found between the propagation pressure and the number of medial units remaining in the dissected wall. Conversely, but logically, inverse correlation was found between the propagation pressure and the tear depth. These correlations were not found in the previously detailed studies [28, 220] which may be explained by differences in the experimental methods and/or tissues.

Radial tensile test

An intuitive way to approach the mechanisms underlying aortic dissection is radial tensile testing aimed at directly studying medial separation. This mechanical test gives an indication about the interlamellar connection strength in the aortic wall, which is relevant in dissection propagation because it is likely to be driven by mode I fracture properties. To prepare the specimens for radial tensile test, the artery is opened longitudinally and a rectangular or cylindrical sample is cut out. Sandpaper and glue are commonly used to fix the sample in the testing machine and avoid slippage in the clamps. Maclean et al. [130] compared the response of upper and lower porcine thoracic aorta to radial stresses with the response to longitudinal and circumferential stresses. The elastic modulus was calculated for different values of strain, showing that, just before failing, it is significantly lower in radial direction (61.4 $\pm$ 4.3 kPa) than in longitudinal and circumferential directions (112.7 $\pm$ 9.2 kPa and 151.1 $\pm$ 8.6 kPa). Later, Sommer et al. [203] investigated the strength of the media of 8 human abdominal aortas using the same test. The radial failure stress was 140.1 $\pm$ 15.9 kPa. The stress-strain curves were divided in three parts: region S1 for elastic, S2 for damage accumulation and S3 for failure, with the behaviour of S1 being linear elastic unlike most biological tissues which exhibit a typical J-shaped curve. Furthermore, a peeling-like mechanism was observed during rupture, showing a lamellar decohesion process (Figure I.7). Another more recent study on human thoracic aortic tissue confirmed that the tensile strength could be ranked in decreasing order from circumferential, to longitudinal and radial direction [204]. This result could explain the fact that, once a tear is present, the dissection propagates generally in the tangential plane (either in longitudinal or circumferential direction).

Peeling test

Peeling is a mechanical test that was often used to study the propagation of dissection. While tensile tests in radial direction allow assessing the strength between layers of the aortic wall, the peeling test is more appropriate to measure the mode I energy release rate in the separation of layers [123]. To prepare the specimens for such a test, the artery is opened longitudinally and a rectangular strip is cut out. One end of the specimen is, then, split in the thickness to get two tongues that are respectively fixed in each clamp of the testing machine. Sandpaper or glue is also commonly used to avoid slippage in the clamps. A schematic of the experimental setup before and after the test is shown in Figure I.8.

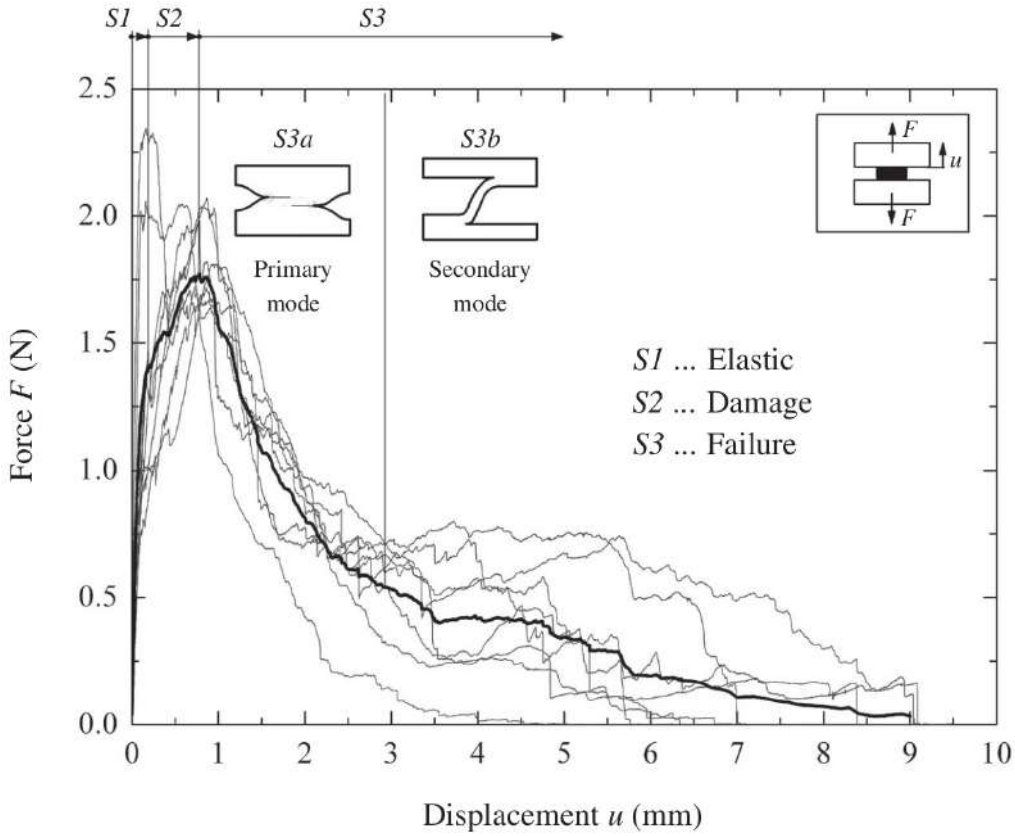

FIGURE I.7 – Force-displacement curves, from direct tension tests, of 8 samples of human abdominal aortas, with the thick curve representing the arithmetic mean response. The initial decohesion of the medial layers S3a is followed by a peeling-like failure mechanism S3b. Reproduced from Sommer et al. [203].

Force and displacement are measured throughout the test, allowing extraction of the mode I energy release rate (involved in dissection propagation). The advantage of peeling tests mainly lies in the control of fracture propagation, unlike direct tension tests or inflation tests where fracture is unstable. Sommer et al. [203] analyzed the dissection properties of the media of 12 human abdominal aortas using peeling tests. The dissection energy release rates were 5.1 $\pm$ 0.6 mJ/cm^2 in the circumferential direction and 7.6 $\pm$ 2.7 mJ/cm^2 in the longitudinal direction. This indicates a possible anisotropy of propagation properties, suggesting a preferred propagation of dissection in the circumferential direction. The authors suggested that, from a structure-to-mechanics point of view, this may be explained by the anisotropic arrangement of the different components like elastin, collagen fibres and smooth muscle cells, which may impact the fracture response as it does for the elastic response of such tissue. This is supported by the fact that peeling in the longitudinal direction generated a "rougher" surface compared to peeling in the circumferential direction. It is also interesting to note that the crack of the medial dissection was observed to spread over six or seven elastic lamina, hence not being confined to the same lamellae when propagating. Tong et al. [223] used the same methodology on 62 human carotid bifurcations to study their dissection behaviour. The dissection energy release rate required was lower in circumferential direction than in longitudinal direction and the surface generated by longitudinal peeling tests was "rougher" compared with the surface generated by the tests in the circumferential direction, consolidating the hypothesis of anisotropy of cohesive properties previously observed in Sommer et al. [203]. Also, the measured energy

release rate significantly varied with the location, higher energy is required to propagate a dissection in the common carotid artery than in the internal carotid artery. Pasta et al. [168] used peeling tests to compare the dissection behaviour of aneurysmal and non-aneurysmal human ascending thoracic aorta from bicuspid aortic valve (BAV) or tricuspid aortic valve (TAV) patients. The results exhibited a delamination strength significantly greater for non-aneurysmal samples than for aneurysmal samples, regardless of the valve morphology and testing direction. They also showed that, for aneurysmal samples, delamination strength of BAV samples was significantly lower than delamination strength of TAV samples for both directions. This demonstrates that patients with thoracic aneurysm have a greater risk of aortic dissection and that patients with BAV are more prone to aortic dissection than patients with TAV, in qualitative agreement with clinical experience. Considering that several studies reported structural differences between these categories of tissues [173, 174, 39], this conclusion raises the need to explore and understand the mechanisms involved at the microstructural level. A significant difference was also found between circumferential and longitudinal directions within non-aneurysmal specimens with higher delamination strength in longitudinal direction, like in Tong et al. [223]. However, this significant difference was not observed within aneurysmal specimens which suggested that the delamination behaviour of aneurysmal samples was isotropic.

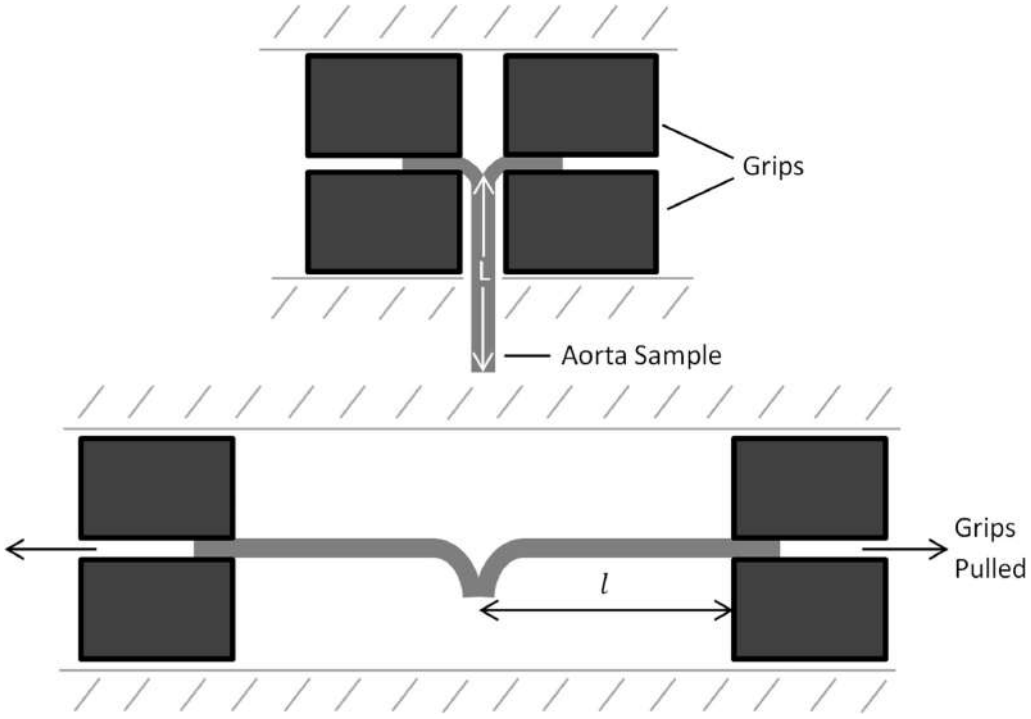

Figure I.8 – Experimental set up for peeling test, before the test and after the test. Reproduced from Noble et al. [159].

Tearing test

Also called trousers test, the tearing test is close to the peeling test in its implementation (the orientation of the sample is simply changed in the testing machine); however, the mechanisms of failure observed may be different as this test allows investigating mode III fracture. Purslow et al. [176] performed this experiment on descending thoracic aortas and showed that the failure stress is greater in the circumferential direction than in the longitudinal direction, and in both orientations the strength increased further away from

the heart. To date, further investigation is necessary to confirm the presence of mode III in aortic dissection.

Shear test

Several studies addressed shear testing on arterial wall to find its shear modulus. Vossoughi et al. [233] applied shear deformation on bovine aortic rectangular samples (hence deforming them in a parallelogram-like shape) and derived their shear modulus. Other studies used extension-inflation-torsion tests on human common carotid arteries [111] and porcine coronary artery [128] to also derive the shear modulus. However, these studies did not investigate rupture of the tissue under these testing conditions. In another approach, Haslach et al. [84] drew radial lines on ring-shaped samples of bovine descending aorta and observed that these lines, during inflation of the ring, actually curved due to non-uniform circumferential displacement. Thus the authors concluded that shear stress may arise when inflating the aorta, confirming their earlier finding [86]. To investigate this, shear tests were performed on bovine rectangular aortic wall blocks in longitudinal and circumferential directions. No difference in the shear stress response was found between the two directions but a redistribution of the interstitial fluid due to shear deformation was observed. More interestingly regarding vascular damage, the histology performed in this work revealed growth of local voids within medial tissue along the collagen fibres (Figure I.9), indicating inter-fibre crosslink rupture. The increasing number of such voids was hypothesized to favor crack propagation in the arterial wall by connecting them. Furthermore, some bridge-crossing fibres can be seen in Figure I.9. The nature of these bridging fibres (collagen, elastin, or both) remains to be clearly identified, as they were designated as elastin fibres in Pasta et al. [168] while they are clearly collagen in Haslach et al. [84] who used collagen staining. Focusing on more relevant and advanced tests for understanding dissection micro-mechanisms, Haslach et al. [84] performed the ring inflation experiment by making an additional radial cut on the intimal side, with the aim of simulating an intimal tear initiating a dissection. Their results showed that the crack first grew in circumferential direction, and eventually this circumferential crack propagation stopped when a radial crack formed and completely broke the sample. Since circumferential crack propagation cannot be induced by circumferential stress or radial compressive stress, this observation suggested that a non-zero shear stress was present during inflation. It was concluded that rupture of the aortic ring in this test involved mode II fracture propagation, probably caused by shearing of inter-fibre crosslinks, and a final rupture due to a mode I radial crack by pull-out or rupture of the collagen fibres. Though this study was performed in the absence of blood, it questions the influence of shear-driven, hence mode II, effects in dissection. A hypothesis that can be formulated is that the early stages of crack opening would be controlled by mode II properties, while the following propagation would be driven by mode I properties when the blood rushes into the crack. The authors concluded that mode II should be considered with more interest in future research. Haslach et al. [85] inflated healthy bovine aortic rings with an intimal-medial longitudinal tear. The crack propagated in the circumferential direction suggesting that mode II fracture is predominant compared to mode I opening, confirming the precedent results. In order to quantify these shear rupture phenomena, Sommer et al. [204] performed tri-axial shear tests on 16 human thoracic aortas. The tri-axial shear tests were done following the different orientations of the orthotropic microstructure of the aorta. The aortic medial shear strength was found to be higher in the rz-plane and $r\theta$-plane ('out of plane') than in the $z\theta$-plane ('in plane'). Furthermore, higher ultimate 'in-plane' shear stresses and

amounts of shear were found in the longitudinal direction compared to the circumferential direction which denotes an anisotropy of the tissue concerning failure under shear loading. Ultimate 'in plane' shear stresses in the circumferential and longitudinal direction were not significantly different for aneurysmatic tissues, but significantly different for dissected tissues. In addition, uni-axial tensile tests were performed in circumferential, longitudinal and radial directions in the same study. They revealed much lower failure strength under 'in plane' shear loading compared to longitudinal and circumferential tensile strength, suggesting that aortic tissues are weaker against shear stress compared to tensile stress. In a comprehensive study, Witzenburg et al. [246] investigated and quantified the failure behaviour of aortic tissue by performing uni-axial, equi-biaxial, peel and shear lap tests on porcine ascending aortas. Uni-axial testing revealed higher strength in the lamellar plane (circumferential and longitudinal direction), while peel and shear lap tests showed a low strength for interlamellar connections (radial direction). Unlike Sommer et al. [204], shear lap tests showed a significantly higher peak stress in circumferential direction (185.4 ± 28.4 kPa) than in longitudinal direction (143.7 ± 16.0 kPa). Note, however, that this difference may be explained by the differences between tests or tissues. The authors noticed that the shear lap failure stress was remarkably lower than the uni-axial failure stress in both longitudinal (753 ± 228 kPa, n=11) and circumferential (2510 ± 979 kPa, n=11) directions, confirming the previous observations in [204].

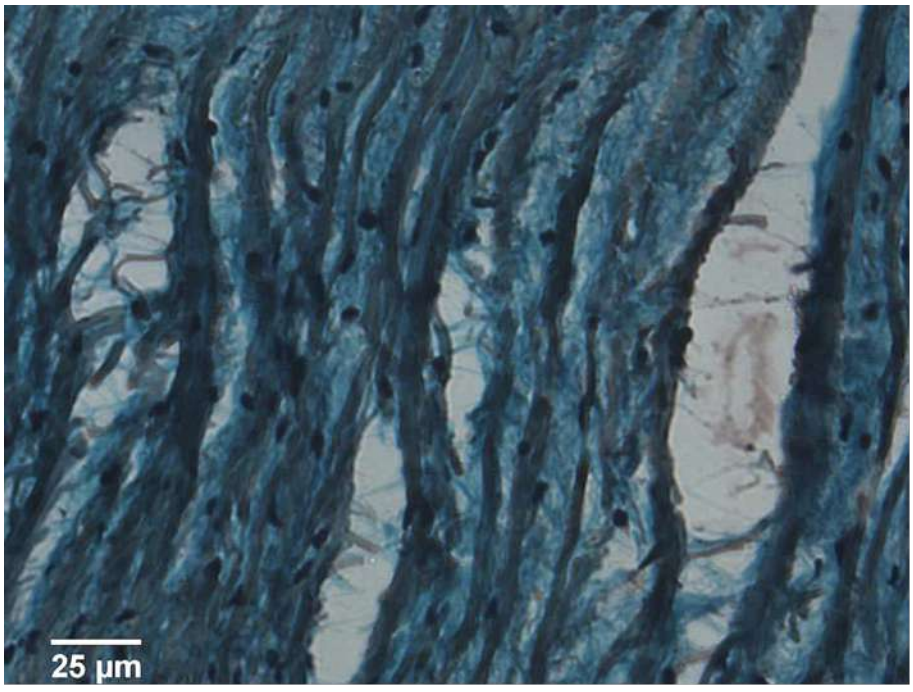

Figure I.9 – Slice of bovine descending aorta after translational shear test, loaded in the circumferential direction, with ×400 magnification. Voids can be seen between collagen fibres in the medial circumferential-radial plane. Bridges crossing these voids are also visible. The vertical direction is circumferential. The stains used were Fast Green FCF, which stains the collagen green, Safranin O, which stains the proteoglycans and other tissue polyanions reddish, and Hematoxylin, which stains cell nuclei. Reproduced from Haslach et al. [84].

Tension-inflation test

In many *ex vivo* models, a tear was created in an excised sample of aorta, a pulsatile pump

mimicked the blood flow, and pressure and flow rate were recorded [35, 228, 53, 57]. In particular, the recent study by Peelukhana et al. [169] investigated the effect of geometric and hemodynamic parameters on the propagation of dissection in descending thoracic porcine aortas. A single entry tear was made inside the samples and a pulsatile pressure setup was used to propagate the dissection. A significant effect of the initial intimal-medial tear geometry (circumference, longitudinal length, and depth) on the dissection propagation was observed. Furthermore, unlike the mean pressure, pulse pressure was found to be the major contributor to flap movement and hence to dissection propagation. Using a similar setup, Prokop et al. [175] and Van Baardwijk et al. [11] both found that $(\frac{dP}{dt})_{\max}$ had a significant influence on the dissection propagation in contrast to mean pressure. Based on mathematical reasoning, Rajagopal et al. [179] questioned this conclusion and hypothesized that both pulse pressure and cycle frequency, which are related to $(\frac{dP}{dt})_{\max}$, are the main contributors to dissection propagation.

In *ex vivo* models, the procedure to create the initial tear is obviously less complex than in *in vivo* models. Furthermore, the different parameters like location and geometry of the initial tear or pressure and flow rate of the blood flow can be controlled, making this method useful to investigate the influence of these parameters on the propagation of dissection. Another advantage, compared to *in vivo* models, is that human aorta can be studied. However, this type of model was only useful to study propagation of dissection and not the initiation. In addition, the underlying micro-mechanisms could not be described based on the cited work of this subsection, suggesting the need to develop experiments at lower scales.

***In situ* testing**

In situ imaging combined with mechanical testing is a promising approach to observe microstructural deformation, and possibly rupture. This allows the identification of underlying phenomena occurring under mechanical loading. Ideally, the sample should be imaged by a 3D non-invasive imaging technique, under physiological conditions [46], thus preventing the use of histology as it alters the mechanical integrity of the sample. With such approaches, all previous tests presented in section I.3.2.1 could be performed to investigate the respective mechanisms involved and quantify structural descriptors at the relevant scale depending on the imaging technique. Therefore, *in situ* imaging is extremely interesting in the investigation of aortic dissection because it theoretically allows the observation of the initiation sequence and the propagation. The main limitation is the temporal resolution, as aortic dissection is a sudden rupture event. Due to this obstacle, the literature is limited on the application of such method on aortic dissection.

Among possible techniques, X-ray computed tomography is a non-destructive technique widely used in both industrial and medical fields. The principle is based on the attenuation of X-rays by matter and their detection by an X-ray sensor after penetration throughout the opaque sample. Several views are taken at different angles and mathematical methods allow the 3D geometry and the internal structure to be reconstructed. To image soft tissues, a contrast agent is needed to obtain enough contrast with conventional absorption-based equipment [158]. The resolution with this technique can be close to 1 µm and the field of view is around 1 mm^3. However, µ-CT can damage the sample due to radiation induced by the photon beam [42] and this should be kept in consideration and carefully checked. X-ray phase-contrast imaging, derived from the same technique, is also suitable for low contrast tissue and was already used by Walton et al. [235] to achieve sub-µm spatial resolutions. Using absorption-based X-ray tomography, Helfenstein-Didier et al. [89] did *in situ* tensile

tests on medial layers of porcine thoracic aorta (Figure I.10), with sodium polytungstate as contrast agent, to assess the microstructural deformation and rupture of the samples under tension. The contrast agent allowed to observe lamellar units of the media. The images showed that the medial rupture always starts on the intimal side. Furthermore, the process of damage initiation, delamination and rupture of the media was described. The authors highlighted the importance of intra-lamellar delamination (mode II) and the need for further investigation.

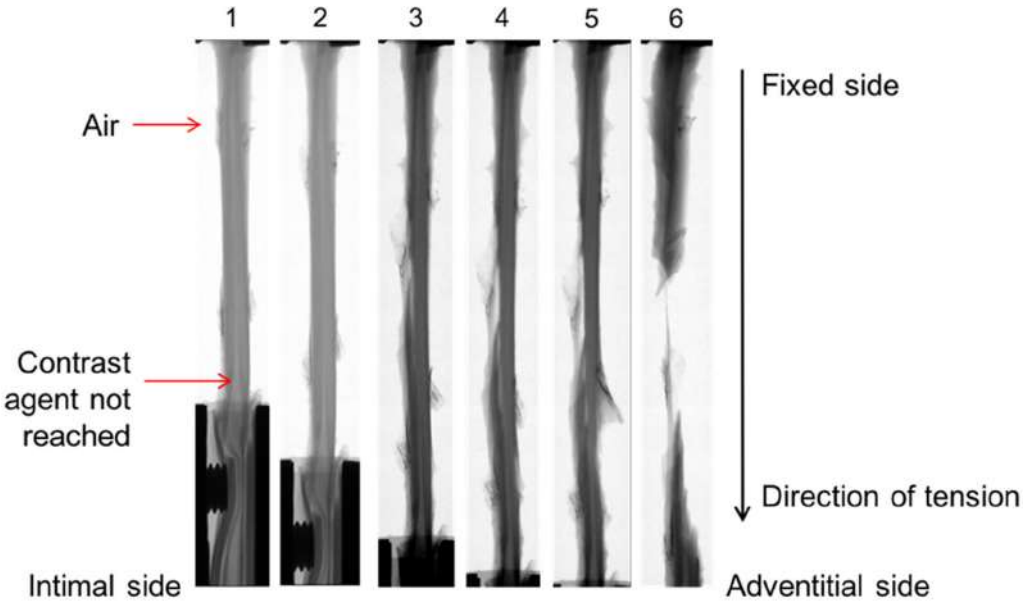

Figure I.10 – X-ray computed tomography images of a tensile test on a porcine medial sample at different time steps obtained by Helfenstein-Didier et al. [89].

Another *in situ* imaging technique is optical coherence tomography (OCT), it is particularly used in ophthalmology to image transparent media such as retinal tissue and detect the presence of diseases [88]. This technique provides good axial and lateral resolution ($\sim$ 10 µm), and better imaging depth ($<$ 5 mm) than most other optical techniques [78]. Thanks to its high speed acquisition, some studies combined OCT and digital volume correlation during mechanical test to measure the three dimensional deformation fields [66, 1]. Advances in laser field led to µ-OCT, this technique allows the observation of cellular and sub-cellular structure with an axial resolution of $<$ 1 µm, a lateral resolution of $<$ 2 µm [23, 49, 125], and a maximum imaging depth of 500 µm [1, 5], making this technique a potential candidate for microstructural investigations in arterial tissue. However, practical implementation for thick non-transparent tissues is not straightforward. A limitation to this technique is that deeper tissue may benefit from less contrast and luminosity due to shadowing effect. Ferruzzi et al. [62] used OCT to observe the passive and active behaviour, under biaxial loading, of vulnerable thoracic aortas of mouse models predisposed to aortic dissection, with and without treatment with rapamycin (a macrolide antibiotic and immunosuppressive compound used to coat coronary stent and prevent organ transplant rejection). The authors observed that daily in vivo treatment with rapamycin preserved or restored biaxial contractile properties, but not passive properties. The OCT images showed spontaneous in vitro delaminations, under physiological loading, in the specimens. In addition, samples from rapamycin-treated mice, tested with induced smooth muscle cell contractility, were all protected against intramural delamination whereas delamination occurred in 55% of the samples after inactivation of smooth

muscle cells. In addition, calculations showed that contraction reduced circumferential and longitudinal stresses, suggesting that smooth muscle cell tonus may act as a stress shield for a vulnerable extracellular matrix.

In recent literature, multiphoton microscopy has been a popular imaging modality to observe the aortic wall structure, however, to the author's knowledge, this technique was never used in conjunction with a mechanical test, in the case of aortic dissection or arterial rupture. The main advantage of multiphoton microscopy is the possibility to use two-photon fluorescence (generated by both elastin and collagen) and second harmonic generation (generated by collagen only) and collect their signals which are easily separable due to their distinctive wavelengths. Hence, it allows imaging collagen and elastin components without any alteration of the sample. Another advantage of this technique is that 3D observation is possible; however maximum depth is around 300 - 600 µm in very best cases, unless optical clearing techniques are used, as was done in Schriefl et al. [198]. Some studies used multiphoton microscopy to observed fibres and characterize tissue morphology (fibre orientation [120, 167], waviness [127, 34], ...) and developed models based on these observations. Several studies also used this image modality to perform *in situ* testing on arterial samples, yet without addressing dissection so far [197, 240, 29, 120]. The main drawback with multiphoton microscopy is that the volume of observation is limited (current limit is approximately 750x750x300 μm^3, depending on the setup) or that the merging of multiple scans is needed. This limitation may be too restrictive to observe an entire dissection. Also, using a clearing agent to overcome the depth limitation alters the mechanical properties of the tissues due to the dehydration of the sample [41].

In situ imaging methodologies are really promising in the understanding of aortic dissection, especially for the initiation sequence. The choice of the imaging technique is determined as a trade-off between their advantages and drawbacks. X-ray computed tomography has a large field of view but its resolution is not as good as OCT, furthermore, despite its small field of view, multiphoton microscopy can image collagen and elastin fibres without any manipulation of the sample. Hence, future investigations may benefit from methods based on such techniques which seem promising in the understanding of aortic dissection, especially for the initiation sequence.

I.3.2.2 *In vivo* characterizations on animal models

In vivo studies are extremely valuable to understand the evolution of a disease in a physiological environment. Because *in vivo* investigations on human subjects are not possible for obvious ethical reasons, animal models were developed to further our knowledge of the mechanisms behind the initiation and propagation of aortic dissection. Three main types of animal models were commonly used in aortic dissection studies: drugs- or chemicals-induced, genetically modified, and surgery-induced models. The first and second are used with mice and are of extreme importance to the understanding of aortic dissection underlying phenomena, while the latter can be used with bigger animals and provides a good insight on the effectiveness of aortic dissection treatments over time.

Angiotensin II-infused ApoE -/- mouse is a popular, though not unique, mouse model for aortic aneurysm research [43] but Trachet et al. [224] demonstrated that this model is also suitable for studying aortic dissection. This model induces several microstructural changes like elastin degradation, macrophage infiltration or thrombus formation. Trachet et al. [227] used *in vivo* monitoring and *ex vivo* observation on n=6 controls and n=47

angiotensin II-infused mice. The *in vivo* monitoring was done with high-frequency ultrasound and contrast-enhanced microcomputed tomography after 0, 3, 10, 18 and 28 days of angiotensin II infusion. *Ex vivo* investigation used phase-contrast X-ray tomographic microscopy. These *in vivo* and *ex vivo* observations allowed monitoring the progress of the disease and provided quantitative information about interlamellar hematoma and medial layer ruptures. In particular, the results showed that aortic regurgitation and luminal volume of the ascending aorta significantly increased over time in angiotensin II-infused mice. Furthermore, a significant increase in single laminar ruptures and several focal dissections were observed in the animals. Another classical model used to study aortic dissection is mice infused with β-aminopropionitrile monofumarate (BAPN); it can be combined with angiotensin II to induce the formation of aortic dissections in 100% of the mice [107, 181]. In the same group than Trachet et al. [227], Logghe et al. [126] used propagation-based phase-contrast synchrotron imaging to observe n=3 controls and n=10 BAPN/AngII-infused mice after 3, 7 and 14 days of infusion. They were able to reconstruct the complete geometry of murine aortas in 3D with an isotropic voxel size of 1.625 micron, thus quantifying the number of ruptures in medial layers. They also observed that several micro-ruptures developed over time in BAPN/AngII-infused mice and, at a certain moment, connect and create larger tears. This observation suggests a new multi-focal propagation mechanism which would deserve further investigations.

Another type of model, used to investigate the pathogenesis of thoracic aortic disease, is genetically engineered mouse models. For instance, $\text{Fbn1}^{mgR/mgR}$ and $\text{Fbn1}^{C1039G/+}$, two mouse models of marfan syndrome, are widely used. They are obtained by mutation in fibrillin-1 (FBN1) gene and provided advances into the knowledge of molecular pathophysiology mechanisms associated with the onset and the development of the disease as described in the review of Milewicz et al. [142]. Several other genetically engineered mouse models exist and are used to investigate aortic dissection [141]. Although these models are critical to the understanding of the pathogenesis of this disease, they are not within the scope of this state of the art.

One of the limitations of mouse models is the difference in the number of elastic lamellae in the media, $\sim$7 for mice and $\sim$50 for humans, which may significantly affect the mechanical relevance of the model. Indeed, a medial layer rupture will have a much greater impact on mouse media than human media. However, these models can provide valuable data on the initiation stage of the aortic dissection that can be helpful in the understanding of human aortic dissection.

Another way to create *in vivo* aortic dissection models is surgery, either open surgery or minimally invasive surgery [180, 215, 163]. The principle of these approaches is to create the initial tear in the aorta and propagate the dissection with surgical instruments (Figure I.11). Though initiation can obviously not be studied, this procedure has proven to be useful to study the effectiveness over time of several treatments on aortic dissection like stent graft placement or aortic fenestration [135, 146]. However, with this technique, only traumatic dissection due to surgery can be investigated. Other limitations of this procedure are the invasiveness of the method and the difficulty to control the propagation of the dissection, compromising the possibility to extract quantitative data.

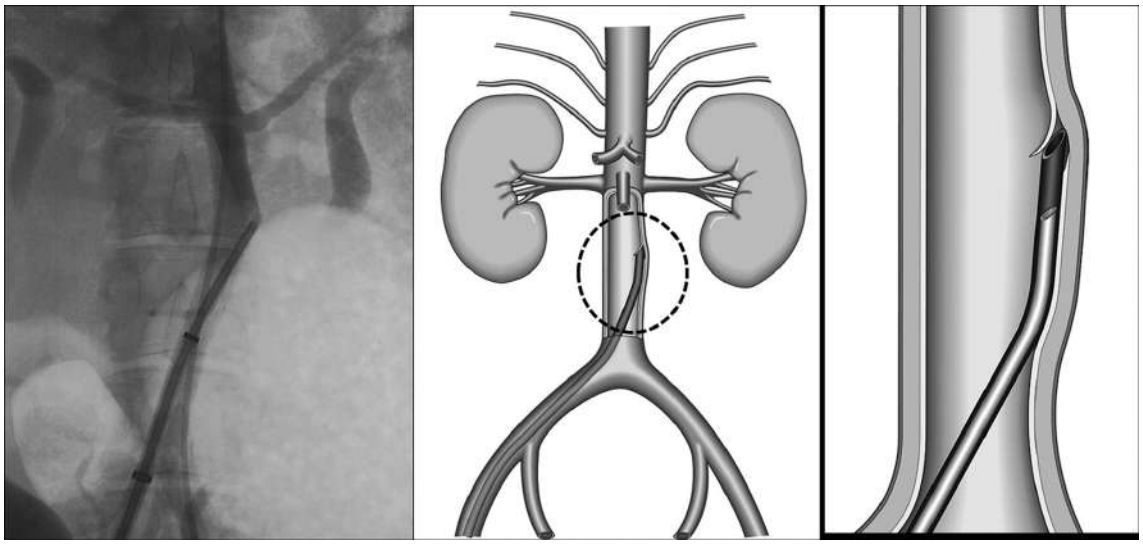

FIGURE I.11 – (a) Intraoperative fluoroscopic image showing the tip of a catheter rupturing the abdominal aortic wall. (b) and (c) schematics representing the creation of a surgically induced dissection. Reproduced from Okuno et al. [163].

Highlights

The current state of experimental findings about initiation and propagation of arterial dissection was reviewed in section I.3.2. In summary, it should be highlighted that the aortic wall presents an anisotropy in term of tensile strength with a higher ultimate tensile stress in circumferential direction compared to longitudinal direction [204] which may explain why the majority of intimal tears are observed to lie in a radial-circumferential plane, transverse to the longitudinal direction [217]. The aorta also presents an anisotropic behaviour concerning the failure under shear loading [204]. Another observation is that the aortic wall presents a lack of resistance against shear loading compared to tension loading [246]. This may be of uttermost importance considering that Haslach et al. [84] showed that shear stress may be present in the wall during inflation. Fracture mode I and II were investigated in several directions; however, the ratio of each mode in the initiation and propagation of aortic dissection and the mechanisms driving the transition from an initial radial tear, or local medial defect to the crack propagation in the tangential plane of the artery remain unclear. This highlights the lack of experimental studies investigating the relationship between microstructure and mechanical response. *In situ* imaging combined with mechanical testing seems promising to observe the early stage of aortic dissection and shed light on the underlying phenomena driving aortic dissection.

I.3.3 Models

Although arterial dissection is a challenging phenomenon with many open scientific questions, models trying to investigate dissection are rather scarce in the literature. This is likely due to the fact that aortic dissection is a complex process involving several phenomena at different scales, requiring several assumptions to be made and thus affecting their relevance and potential use.

I.3.3.1 Macro-scale models

The initiation of aortic dissection occurs when the wall stress locally exceeds the tissue's strength. Accordingly, some studies computed the wall stress using finite element analysis and investigated the influence of different parameters on the value and location of peak wall stresses [20, 154], as was often done to assess the rupture risk of aneurysms. The strong assumption behind these studies was that the initiation of dissection is more likely to occur at the peak wall stress location. However, the calculation of this stress was subject to several limitations: the material was considered homogeneous, isotropic, linear elastic and uniform throughout the aorta, with constant thickness. Furthermore, the microstructure of the aortic wall was not taken into account during the construction of the models while it seems to be of high importance in the understanding of aortic wall rupture as peak wall stress was shown to be a poor predictor of the location of rupture [30]. Last, it should be recalled that the relevant measure of stress to be computed in rupture risk assessment remains an open question.

Gasser et al. [72] developed a non-linear continuum framework based on a continuous and a cohesive materials. The continuous material was modeled as a fibre-reinforced composite with collagen fibres embedded in a non-collageneous isotropic ground matrix, while the cohesive material was represented by a cohesive constitutive law implemented at pre-defined interfaces between adjacent regions of the model. The two materials were independent from each other. The framework was then implemented in a finite element model to reproduce a peeling test and investigate the propagation of arterial dissection. Ferrara et al. [60] presented a numerical model of dissection based on cohesive fracture theory as an evolution of an earlier model applied on the fracture of atherosclerotic plaques [61]. The model was implemented in a numerical finite element simulation of a peeling test (Figure I.12 (a)). A sensitivity analysis was then performed to evaluate the influence of the cohesive parameters leading the interlamellar propagation of the dissection in the media and the influence of the reinforcing collagen fibres on the separation of the layers. These simulations suggested that normal and shear strengths played an important role in the separation process, unlike the critical energy release rate. This study highlighted the importance of shear stress in dissection and the need for a failure criterion including the contribution of shear stress. However, the authors underlined that the influence of fibre orientation on shear strength of biological tissues needs further investigation. In addition, this model needs experimental validation. Based on the experimental tests performed by Helfenstein-Didier et al. [89], Brunet et al. [25] confirmed that shear delamination strength between medial layers may contribute to the initiation of aortic dissection by simulating a uni-axial tensile test using a finite element model with cohesive interfaces.

Using finite element method, Wang et al. [238] proposed a computational model to study the propagation of a tear in a fibre-reinforced tissue. An energy-based approach was used by calculating the energy release rate, allowing the identification of the values of pre-existing tear length and internal pressure needed to propagate the tear. The effect of fibre orientation and surrounding connective tissues was also investigated. The model was verified for simple cases, using analytical solutions. The results demonstrated that the presence of fibres reduced the risk of tear propagation, especially when the fibres are parallel to the tear. Nevertheless, decreasing the stiffness of surrounding tissues increased the tear growth. This suggested that connective tissue degeneration leading to softening may facilitate the dissection propagation. Later, in the continuation of their previous works, Wang et al. [239] developed a residually-stressed two-layer arterial model. As previously,

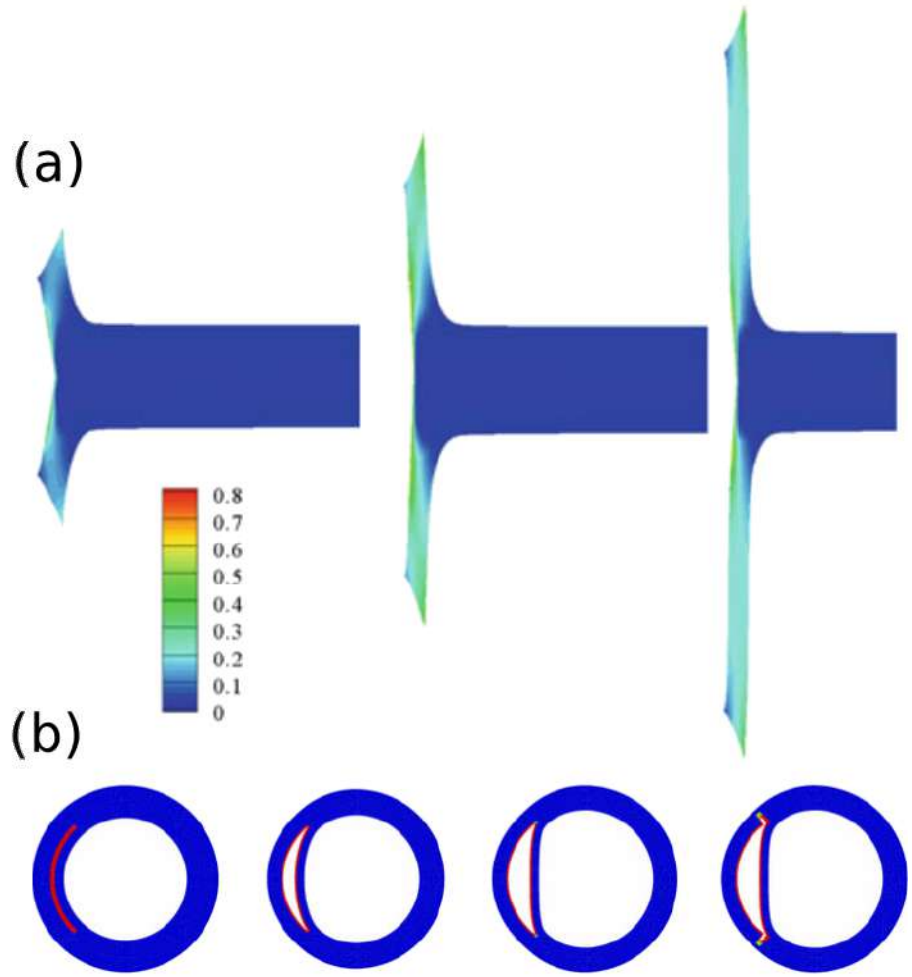

FIGURE I.12 – (a) Three different steps of the peeling simulation with the contour level referring to the first principal Cauchy stress in MPa. Reproduced from Ferrara et al. [60]. (b) Evolution of the tear propagation during the inflation of the residually-stressed artery at four different stages. Reproduced from Wang et al. [239].

the material properties were modelled with Gasser-Holzapfel-Ogden model. The initiation and propagation of the tear were modelled using the extended finite element method, with the behaviour of the propagation being described with a linear traction-separation law. The study determined the critical pressure at which the dissection started to propagate (Figure I.12 (b)). The critical pressure investigated was dimensionless (normalized against the neo-Hookean parameter) and, thus, independent of material properties. Both very short and very long circumferential tears were more stable, meaning that the critical pressure was higher in these cases. Another finding was that longer tears lead to inner wall buckling, as seen on clinical CT scans. Concerning the effect of residual stress, the opening angle increased with the critical pressure, demonstrating that residual stress reduces the risk of propagation. Thus, this model suggests that tear length and residual stress play a key role in the tear propagation. This model was also used in Wang et al. [237] to investigate the influence of several parameters on the dissection propagation by simulating peeling and pressure-loading tests. The main findings were that the tear preferentially propagates along the stiffest direction, which is ruled by the fibre orientation. Furthermore, the model could reproduce various buckling configurations seen on clinical CT images and suggested

that a deeper tear is more likely to propagate, confirming that aortic dissection propagates preferentially in the outer third media [165]. This result was also observed experimentally, with different tests, by Tam et al. [213] and Peelukhana et al. [169].

Humphrey and colleagues developed several computational models to examine the influence of medial pooling of glycosaminoglycans on aortic dissection. They demonstrated, using semi-analytical and finite-element-based continuum models, that accumulated glycosaminoglycans may lead to significant intramural stress concentrations and intra-lamellar Donnan swelling pressures [190, 189]. However, damage was not included in these models. Later, Ahmadzadeh et al. [3] developed a particle-based computational model using an extended smoothed particle hydrodynamics (SPH) method. The SPH model was composed of a bi-layered murine aorta. It was verified with a continuum model and validated against experimental data. The purpose of the study was to investigate the role of pooling of glycosaminoglycans in the initiation and propagation of intra-lamellar delamination. The results showed that smooth muscle cell activation can partially prevent damage in the aortic wall, as demonstrated in the literature [62]. The simulations also suggested that close pools of glycosaminoglycans may initiate and propagate a delamination by extending and coalescing.

The models presented in this subsection proved successful to accurately describe aortic dissection behaviour at organ or wall-scale. However, nearly no information about microstructure and associated mechanisms can be obtained with these models apart from the fibre orientation. For a better understanding of the mechanisms behind dissection initiation and propagation, lamellar-scale and micro-scale models are needed (i.e. models where each lamella, or each micro-scale constituent like collagen or elastin fibres is modeled with its own properties). These are presented in the following section.

I.3.3.2 Multi-scale models

Shah et al. [199] presented a computational model combining micro-scale and macro-scale components. The microstructure was modelled as an interconnected fibre network in parallel with a neo-Hookean component that represents the non-fibrous contribution of the extracellular matrix and the smooth muscle cells (Figure I.13 (a)). Damage was introduced at the fibre level, with fibres failing when their stretch exceeds a critical threshold. This value was identified, along with elastic parameters, by fitting uni-axial and biaxial extension tests on porcine aortic media. The model was able to reproduce the uni-axial and biaxial responses with good agreement in both pre-failure and failure range. In addition, the model was able to replicate radial tension response from the literature [130] that were not used during the fitting process. The fitted values of the parameters governing the fibre behaviour corresponded to elastin fibre rather than collagen fibre, suggesting that elastin is leading the tissue response. Though it may prove highly valuable for understanding dissection, the lamellar structure of the media is not considered in this model, which is a major limitation. Witzenburg et al. [246] proposed an extension of the previous model, based on histological observations. This time, the microstructure was modelled as a fibre network composed of a 2D sheet of elastin and collagen fibres attached radially by interlamellar connections representing smooth muscle cells and fibrillins. The failure process at the fibre level was maintained from the previous model. This model was able to match the multiple experimental tests (uni-axial, equi-biaxial, peel, and shear lap tests) performed on porcine ascending aorta and agreed well with experiments in the literature. This model constitutes one of the most relevant microstructure-based models currently available. With

a similar approach, Thunes et al. [218, 219] used a structural finite element model of the medial lamellar unit including elastic lamellae and collagen fibre network (Figure I.13 (b)). The influence of these two load-bearing components on the in-plane tissue strength was investigated, allowing a better understanding of aortic dissection initiation. The model parameters were calibrated using multiphoton microscopy imaging and uni-axial tensile tests in circumferential direction on non-aneurysmal aorta from patient with a normal tricuspid aortic valve, aneurysmal aorta from patients with a tricuspid aortic valve, and aneurysmal aorta from patient with a bicuspid aortic valve. The model was, then, validated against experimental tensile tests in longitudinal direction. According to the results, one of the leading parameter governing tissue strength was the orientation distribution of collagen fibres which controls the fraction of collagen fibres engaged at a given stretch.

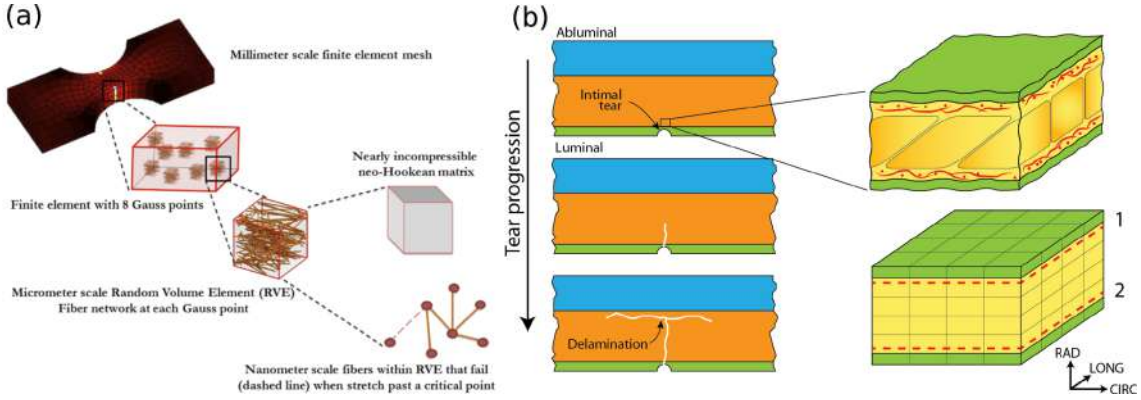

FIGURE I.13 – Two examples of multiscale models. (a) Each element of the uni-axial or biaxial finite element geometry is composed of eight Gauss points. These Gauss points consist of representative volume elements (RVE) composed of a fibre network in parallel with a nearly incompressible neo-Hookean matrix. Reproduced from Shah et al. [199]. (b) The model is composed of three layers: the intima (green), media (orange), and adventitia (blue). An intimal tear is present and initiates the aortic dissection (top panel), the tear propagates in the media (middle panel), and delaminates the medial layers (bottom panel). The media consists of several lamellar units, each of them composed of elastic lamellae (green region) and interlamellar space (yellow region). A collagen fibre network (red) is present near the lamellae. Reproduced from Thunes et al. [219].

Pal et al. [166] based their model on the observations of Pasta et al. [168], and more specifically the increase in peeling force up to a certain value, followed by an oscillation around a plateau value. This demonstrated that delamination does not propagate continuously. An explanation for this phenomenon might be that fibres, present between the layers, create "bridges" between them and support the load induced by delamination. As a portion of fibres breaks, the measured force drops, until new fibres are recruited, allowing the force to increase again. This hypothesis was supported by SEM observations where the authors mentioned a large number of broken elastin fibres in the delamination plane (Figure I.14 (a)). In Pal et al. [166], the authors requalified these fibres as collagen and elastin, eventually proposing a predictive mechanistic model that investigated the effect of radially running collagen fibres on the delamination strength (Figure I.14 (b)). Using a finite element code, the peel tension response was validated against the results of the tests conducted by Pasta et al. [168]. The model was used to show that the density and failure energy of the radially-running collagen fibres were the main contributors to the delamination strength; however, the failure strength of these fibres only affected the initiation of

delamination. These findings remain to be confirmed experimentally.

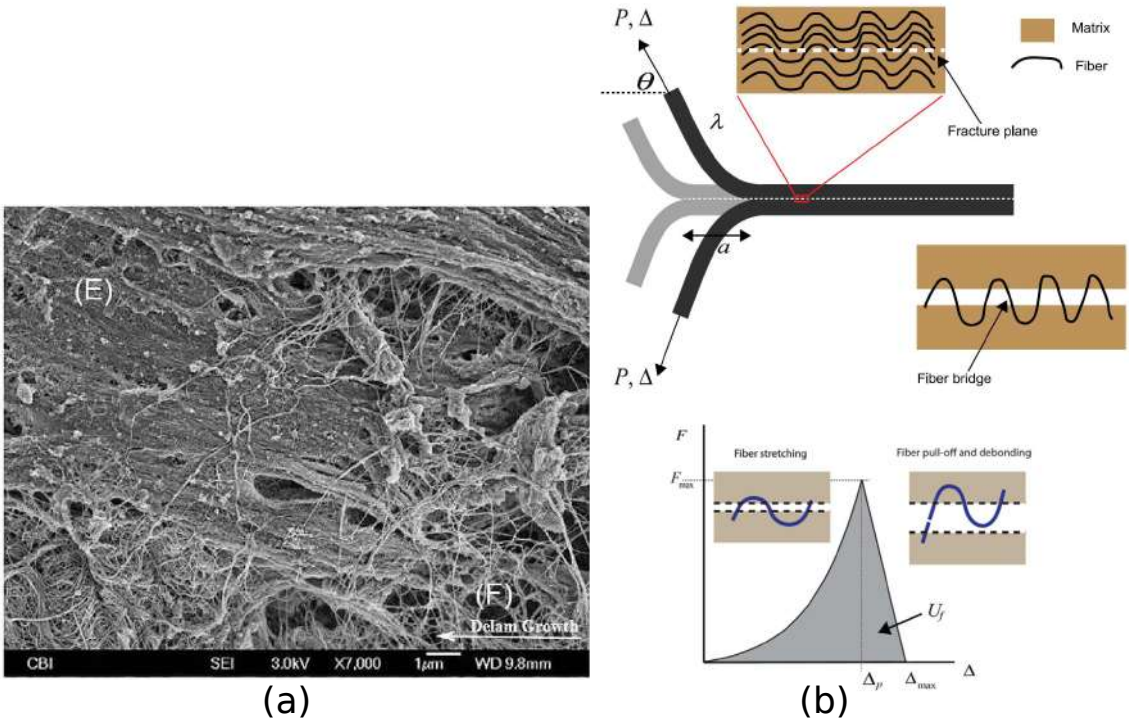

Figure I.14 – (a) High magnification SEM image of the delamination plane after a peeling test on an ascending thoracic aortic aneurysm with tricuspid aortic valve showing bundles of broken elastic fibres (F) existing between elastic sheets (E). Reproduced from Pasta et al. [168]. (b) Schematic of (1) an artificial dissection, (2) the arrangement of collagen fibres in the fracture plane, (3) a fibre bridge in the delamination plane, and (4) the force-displacement behaviour of a collagen fibre. Reproduced from Pal et al. [166].

Highlights

Different models trying to understand the mechanisms of initiation and propagation of aortic dissection were reviewed in this section. Macro-scale models led to several important results for the comprehension of this disease. The importance of shear stress and the need to investigate its influence was highlighted [60], confirming experimental results [84, 246]. Pools of glycosaminoglycans may create significant intramural stress concentrations [190, 190] and play a role in the initiation and propagation of aortic tears [3]. Residual stress and smooth muscle cell activation tend to increase the load bearing capacity of the aortic wall [239, 3]. Furthermore, as demonstrated by experiments [213, 169], a deeper tear is more likely to propagate [237]. These models provided valuable information on aortic dissection mechanisms; however the aortic wall is a complex heterogeneous structure and models at a lower scale are needed to investigate and quantify the influence of the different components. Multi-scale models reproduced different mechanical tests with great accuracy and highlighted the importance of elastin fibres [199] and collagen fibres orientation distribution [219]. The radially-running fibres were investigated by Pal et al. [166] and seem to be of major importance in the propagation of aortic dissection. Unless explicitly mentioned above, the absence of experimental validation remains a limitation and highlights the lack of experimental data on aortic dissection.

I.3.4 Discussion and conclusions of the state of the art

A number of experimental methods and their results were discussed. These different tests provided qualitative information and quantitative values on the phenomena occurring during aortic dissection. Several questions regarding the pathogenesis and the initiation sequence of the disease remain unanswered. Concerning the initiation sequence, two mechanisms leading to aortic dissection were suggested, originating either from an intimal or intramural tear [161, 156].

The first mechanism is believed to concern the majority of cases: when an intimal tear is present in the aortic wall, this tear will propagate in the outer third of the media, involving about one half of the circumference and creating an aortic dissection [217]. In 85% to 95% of cases, the intimal defect is in the transverse direction, and in a few occurrences in the longitudinal direction [217]. The most common location of intimal tear is a few centimeters above the aortic valve, along the right lateral wall where the shear forces caused by the blood flow are the strongest. The second location of intimal tear is below the ligamentum arteriosum, in the descending thoracic aorta, where the anchoring of the aortic arch with the thoracic cage causes a large increase in stiffness of the arterial wall [187, 161]. As a consequence of the resulting stress or strain state, these areas may be more prone to develop aortic dissections. The origin of intimal tears, or defects that may initiate the dissection, is not well understood, except in the case of injury due to endovascular interventions. This important aspect would also deserve specific research. Nevertheless, it is commonly accepted that a medial degeneration, either from an inherited connective tissue disorder or from an acquired condition compromising the aortic integrity, is fundamental to allow aortic dissection [220, 155, 54]. This degeneration manifests itself by inflammation and extracellular matrix degradation [156, 14, 129]. Hence, mechanical phenomena inducing

intimal tears should be investigated in conjunction with biological events that may favor the occurrence of these intimal injuries. For instance, disrupted smooth muscle cell contractility or mechanosensing seems to be the primary driver of aortic dissection [140, 62, 141].

Another essential question concerns the failure modes involved in aortic dissection at the early stage of propagation. Some authors proposed that propagation of an intimal tear is the consequence of a peeling mechanism induced by blood flowing into the defect and pushing the medial layers apart, hence creating a dissection. This scenario involves mode I separation. Another hypothesis is that the intimal tear is propagated by circumferential shear stress, hence involving mode II separation. Haslach et al. [84] hypothesized that shear forces may be present in the arterial wall during the systolic phase suggesting that crack growth is, at an early stage, driven by internal wall mechanical forces. Supporting this hypothesis, Khanafer et al. [113] demonstrated, thanks to a fluid-structure interaction model, that the peak wall stress and the maximum shear stress are highest in the medial layer. Furthermore, Witzenburg et al. [246] demonstrated the lack of resistance of the aortic media against shear stress compared to uni-axial tensile stress. Thus mode I and II fracture may be the consequence of the intramural mechanical stress induced by the blood flow. More details and evidence are still necessary to clarify these scenarii.

The second mechanism believed to initiate aortic dissection involves an intramural tear, clinically observed in the form of an hematoma due to a rupture of the vasa vasorum [161, 116, 90]. This scenario is supported by the fact that no intimal tear is found in 4% to 12% of aortic dissections [77, 92, 56, 145, 157, 201]. These non-communicating dissections indicate that an intimal tear is not crucial to initiate aortic dissection. Instead, a weak cohesion of the medial layer would be critical. Khanafer et al. [113] demonstrated that the presence of an intramural hematoma in the aortic wall has a significant effect on the peak wall stress acting on the inner layer, supporting that such a defect can lead to aortic dissection. Furthermore, it was suggested that intramural hematoma may eventually reach the lumen and create an intimal entry [92]. In this scenario, the intimal tear is secondary to the intramural hemorrhage, as reported in several clinical cases [250, 145, 157, 70]. Thus, intramural hematoma may be the cause of some aortic dissections with intimal flap observed in previous studies. It was also noted in several studies that the vasa vasorum plays a key role in the aortic integrity and that its impairment is followed by mechanical changes resulting in a weakened medial layer [208, 7, 165].

Recent developments in imaging techniques foresee new advances in the understanding of cardiovascular pathologies and especially aortic dissection. The microstructural phenomena are certainly the key to a complete understanding of the initiation and propagation of dissection [221]. Thus, modalities allowing the observation of the microstructure without damaging the sample are crucial. Several techniques seem promising, for instance synchrotron-based X-ray phase-contrast imaging [126] allowing to investigate the microstructure of a sample with a high resolution, on a large field of view while preserving the integrity of the tissue. However, the main challenge to be addressed is to observe a sudden microscopic phenomenon propagating in one or a few seconds [187].

Similar trends were observed with the evolution of modeling approaches, where microstructure is more and more taken into account. Studies combining both experiments and numerical simulation would deeply improve current knowledge. In this context, modeling the medial structure with multiple lamellar units seems unavoidable to determine and quantify the mode of failure involved in aortic dissection. However, a lack of experimental data, in

particular on the initiation sequence of aortic dissection, prevents further advances. Such data would be necessary to feed models, and more importantly to validate them.

On this aspect, promising techniques which could be used to investigate dissection are emerging. Zitnay et al. [249] presented a novel method using a collagen hybridizing peptide to optically detect, using fluorescence properties of the peptide, the failure of collagen fibres at the molecular level. With this technique, they were able to track the collagen fibre failure in a rat tail tendon fascicle during a tensile test. In a combined experimental-modelling approach, the same method was used during a tension-inflation test on sheep middle cerebral arteries to investigate the relationship between collagen fibre damage and its impact on the mechanical properties of the tissue [40, 131]. The results showed that the collagen fibres aligned with the direction of loading were the first to damage. More importantly, the authors observed that the tissue-level yielding may be associated with the onset of collagen damage. This promising technique could be used to detect and follow the initiation sequence of aortic dissection or to quantify the implication of collagen fibres in the different rupture mechanisms.

The understanding of aortic dissection has improved this past decade due to advances in imaging techniques and in computational modeling. Nevertheless, some unknowns remain, especially on the initiation process leading to the propagation of the dissection. Short-term efforts should focus on describing and quantifying the mechanisms involved in the initiation sequence, as well as the relative contribution of each failure mode. The next step will have to involve mechano-biology and remodeling, central issues to later address clinically-relevant matters like the identification of patients at risk, together with the development of clinical decision support tools to adress their follow-up and treatments.

Highlights

- The aortic mechanical behaviour was extensively characterized at the macro-scale. However, few studies investigated the evolution of the aortic wall at lamellar- and micro-scale, especially during the initiation of aortic dissection.
- Computational models showed that the microstructure may be the answer to multiple mechanisms of aortic dissection. Nevertheless, lack of experimental data prevents the validation of these models.
- *In situ* techniques combining mechanical testing and imaging modalities seem promising in the investigation of aortic dissection.

I.4 Scientific questions, hypotheses and objectives of the study

The state of the art highlighted the lack of experimental data concerning the initiation sequence of aortic dissection at a local scale, preventing the validation of models. This absence can be explained by the difficulty to create and observe an *in vitro* dissection, mainly because aortic dissection is a swift and intramural process. This lack in the literature also concerns the deformation of the macro- and micro-structure during the aortic dissection.

In previous experiments [89], our team performed *in situ* observations on porcine aortic tissue rupture by combining a uniaxial test with micro-CT. A contrast agent was used to

allow the observation of the tissue under X-ray. This work served as proof of experiment and starting point for this doctoral study.

Thereby, the main objective of this doctoral work is to provide a better understanding of the mechanisms triggering aortic dissection and the parameters influencing its propagation by investigating its initiation sequence.

To reach this goal, an approach divided into three parts will be developed. Firstly, *in situ* mechanical tests will be combined with finite element simulations to investigate the mode of rupture of the aortic wall. Secondly, a simulation of the aortic dissection involving rupture of the aortic wall will be developed. Finally, an *in situ* mechanical tests closer to the *in vivo* conditions will be developped to observe and quantify the evolution of a dissection inside an aorta.

In order to design the *in situ* mechanical test, the first step was to define the requirements that the test had to complete, which were:

- to be as close as possible to *in vivo* conditions,
- to be observable continuously during the test as the deformation of the lamellar structure will be imaged at different times of the test,
- to allow us to reproduce an *in vitro* aortic dissection propagation.

The mechanical test chosen was a tension-inflation test as it complies with all the requirements. The *in vitro* dissection was initiated by creating a notch inside the artery to mimic an intimal tear. The pressure during the test was chosen to be quasi-static. Most likely, the tear formation is a fatigue process triggered by the heart pulse waves; however, the propagation along the length of the aorta is a sudden process that takes only one or few seconds [187]. It can be triggered by a supraphysiological blood pressure (during weighlifting for instance [202]). In the present experiment, the tear formation is not studied, only the propagation of this tear is investigated, supporting the choice of a static pressurisation. This reflects the sudden *in vivo* process. The influence of different parameters on the propagation of the notch were investigated. The medial degeneration often associated with inflammation and extracellular matrix degradation, though fundamental to understand aortic dissection, were not studied in this work.

Concerning the imaging technique to couple with the mechanical test, the requirements for the imaging modality are:

- non-invasive, allowing the observation of the 3D structure without affecting the mechanical properties of the tissue,
- good spatial resolution, to investigate the dissection at the lamellar-scale,
- large field of view, allowing the observation of a volume large enough to contain the whole dissection.

Micro-CT was chosen based on the characteristics presented in Table I.1. This imaging technique presents the best compromise between spatial resolution, time resolution, and field of view in the case of this study (Table I.1). In this doctoral work, porcine carotid artery tissue and rabbit aorta were chosen as the size of this vessel ensures a good compromise between resolution and field of view.

At the same time, numerical simulations of the mechanisms observed were developed. The phenomena occurring during an aortic dissection are complex and models can shed light

on these events by allowing a deeper investigation and study of the influence of various morphological and mechanical parameters. In this work, we chose a traction-separation approach to model the rupture of the tissue. With this approach, the material damage starts once it locally reaches a fracture criterion, and the rupture occurs when all the fracture energy is dissipated according to the cohesive behaviour defined for the material.

The description and quantification of the mechanisms occurring during aortic dissection provided by this doctoral thesis could lead to the development and validation of complex models dedicated to the diagnosis of patients at risk or could serve as a basis for the improvement of aortic dissection treatments.

Chapter II

Modélisation de la rupture aortique en traction - *Modelling of aortic rupture in traction*

This chapter describes a preliminary numerical study. It consists in the analysis of the experimental work of Helfenstein-Didier et al. [89]. This study proposes an analytical and a numerical model that reproduces a uniaxial test on medial arterial samples observed under X-ray tomography in Helfenstein-Didier et al. [89]. The aim is to quantify rupture-related parameters and to evaluate the influence of the shear delamination strength. This study was published in the Journal of the Mechanical Behavior of Biomedical Materials (vol. 95, pp. 116-123, July 2019).

Contents of the chapter

Résumé du chapitre

Dans ce chapitre, la propagation de fissure dans des échantillon aortiques est étudiée afin de mieux comprendre quelles sont les conditions nécessaires au déclenchement de la dissection aortique.

Cette étude se base sur le travail expérimental de Helfenstein-Didier et al. [89]. Des tests uniaxiaux sur des échantillons de media d'aortes porcines ont été réalisés. Grâce à des observations *in situ* sous tomographie aux rayons X, un mécanisme de rupture à été identifié: (i) un groupe de couches médiales rompt suivant le mode I de rupture, (ii) ce groupe se délamine le long de l'échantillon en suivant le mode II de rupture, (iii) un nouveau groupe de couches médiales rompt en suivant le mode I et ainsi de suite jusqu'à rupture totale de l'échantillon.

Dans cette étude un modèle analytique reproduisant les tests uniaxiaux réalisé dans Helfenstein-Didier et al. [89] est développé afin de quantifier les paramètres liés à la rupture en mode I. Le modèle est composé de plusieurs couches représentant des groupes de couches médiales, chacun ayant des propriétés élastiques et de rupture. Des modèles éléments finis ont été créés pour valider le modèle analytique en utilisant des paramètres définis arbitrairement. Une fois le modèle validé, une analyse inverse a été utilisée pour ajuster les paramètres du modèle aux courbes expérimentales obtenues grâce aux tests uniaxiaux de Helfenstein-Didier et al. [89]. Les paramètres hyperélastiques sont d'abord identifiés, puis les paramètres de rupture.

La résistance à la délamination entre les couches n'étant pas prise en compte, un modèle d'éléments finis incluant ce phénomène a également été développé pour en étudier l'influence sur la courbe contrainte-déformation par le biais d'une analyse de sensibilité. Il a été démontré qu'une faible résistance à la délamination par cisaillement entre les couches, c'est-à-dire la séparation de mode II, est essentielle dans le processus de rupture observé expérimentalement.

II.1 A combined experimental-numerical lamellar-scale approach of tensile rupture in arterial medial tissue using X-ray tomography

Extracted from the paper "A combined experimental-numerical lamellar-scale approach of tensile rupture in arterial medial tissue using X-ray tomography." published in Journal of the Mechanical Behavior of Biomedical Materials (vol. 95, pp. 116-123, July 2019) [25]. The text is shortened and modified herein to avoid repetitions.

Abstract

Aortic dissection represents a serious cardio-vascular disease and life-threatening event. Dissection is a sudden delamination event of the wall, possibly leading to rupture within a few hours. Current knowledge and practical criteria to understand and predict this phenomenon lack reliable models and experimental observations of rupture at the lamellar scale. In an attempt to quantify rupture-related parameters, the present study proposes an analytical model that reproduces a uniaxial test on medial arterial samples observed under X-ray tomography. This model is composed of several layers that represent the media of the aortic wall, each having proper elastic and damage properties. Finite element models were created to validate the analytical model using user-defined parameters. Once the model was validated, an inverse analysis was used to fit the model parameters to experimental curves of uniaxial tests from a published study. Because this analytical model did not consider delamination strength between layers, a finite element model that included this phenomenon was also developed to investigate the influence of the delamination on the stress-strain curve through a sensitivity analysis. It was shown that shear delamination strength between layers, i.e. mode II separation, is essential in the rupture process observed experimentally.

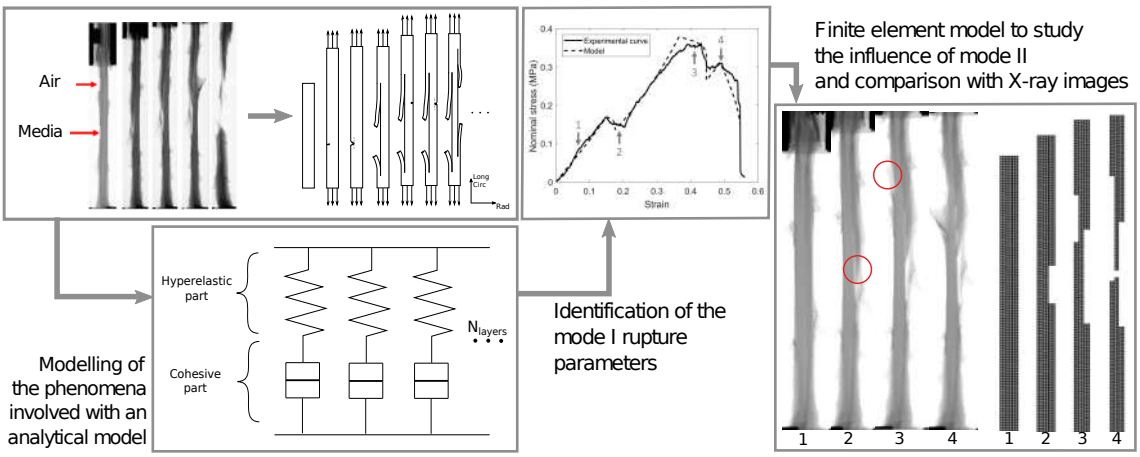

II.1.1 Introduction

In a previous study, an X-ray tomography experiment taking advantage of the versatility of the technique to perform *in situ* tensile testing was developed. Using a specific staining technique and a specific tensile machine, this study provided unprecedented observations of medial tissue under tension, and a meso-scale description of medial rupture, possibly constituting a model for *in vitro* dissection [89].

The present study aimed at characterizing and quantifying the mechanisms triggering and propagating a dissection in medial tissue. To this aim, an analysis of the previously published experimental work [89] is proposed based on analytical and numerical approaches using linear cohesive models, first introduced by Dugdale and Barrenblatt [50, 16], and as often used in commercial codes to model crack opening and rupture. The approach was used to identify the cohesive model's parameters, which were later used in a finite element (FE) model to assess the relative influence of different crack propagation modes in the tissue.

II.1.2 Methods

II.1.2.1 Experimental data

In a previously published experimental study [89], uniaxial rupture tests were performed *in situ* on medial layers of porcine aortic samples under X-ray micro-tomography. Briefly, the technique required the use of sodium polytungstate as a contrast agent, applied by immersing the samples in such a solution. This made it possible to image the lamellar units in the tissue when performing 3D scans of the samples. X-ray micro-tomography provided a mean to monitor damage initiation, delamination and rupture of medial tissue under tensile loading. The process was described as an elementary process repeating several times until complete failure. This elementary process initiated with a sudden mode I fracture (in the loading direction) of a group of lamellar units, followed by an elastic recoil of these units, causing mode II separation creating a delamination plane as shown in Figure II.1.

To build dissection models and identify their parameters, the qualitative observations made during the tensile tests performed up to rupture were used, along with the force-displacement curves obtained at the same time. Ten samples and their corresponding data were used in the present study.

II.1.2.2 Analytical multi-layer cohesive model

A 1D analytical model was created to numerically reproduce the uniaxial test responses of medial tissue. The dimensions taken into account (length, thickness and width of the rectangular samples) were obtained from the X-ray tomography images [89]. The model was composed of several layers in parallel, all layers were assumed to have the same dimensions. Each layer represented a group of several lamellar units, the number of groups was determined based on the traction curve, as detailed in section 2.3 below. The behavior of each layer was governed by an incompressible hyperelastic contribution and a cohesive contribution, both assumed to work in series (see Figure II.2). Note that this 1D model, can only include mode I fracture; mode II will be addressed later in the proposed FE model.
Because the model primarily aims at studying the response at rupture, the medial tissue was assumed to have an isotropic mechanical behavior for the hyperelastic contribution

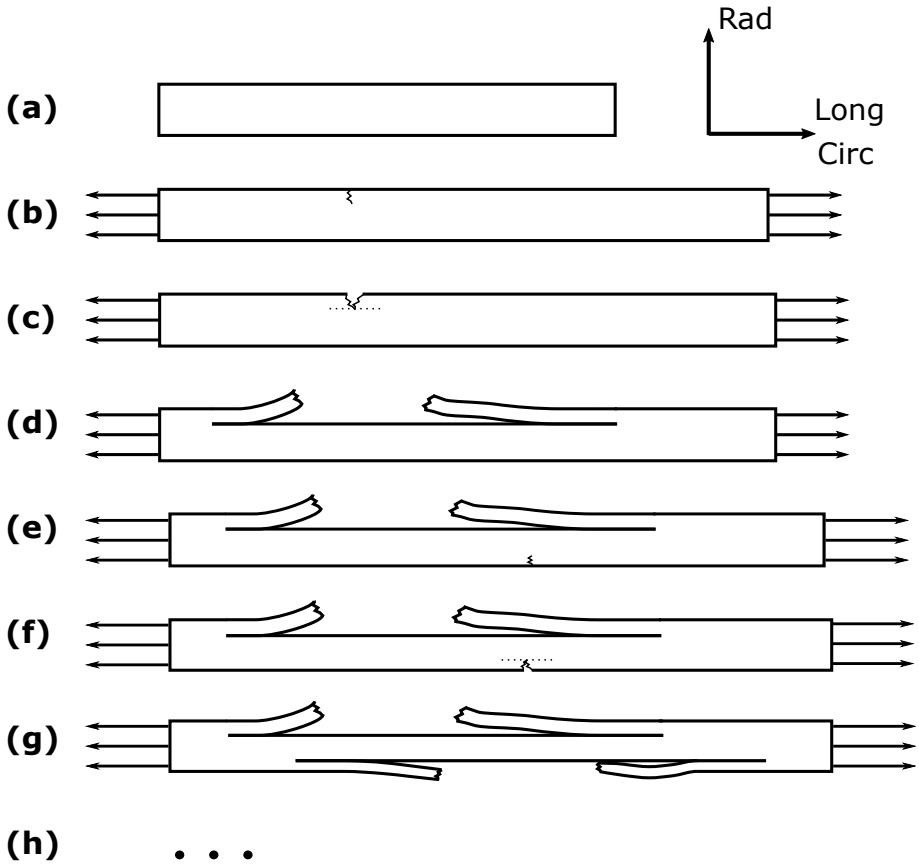

Figure II.1 – Schematic representation of the damage initiation and propagation mechanism observed *in situ*. (a) intact sample, (b and c) initial radial crack, opening in mode I, (d) elastic recoil of the ruptured layers, causing a mode II longitudinal crack to form and propagate, (f, g, h. . .) the process repeats until complete failure of the sample. Modified from Helfenstein-Didier et al. [89].

which was modeled with an incompressible second order reduced polynomial constitutive equation [184]. The strain energy function of this model was defined as:

$$\Psi = C_{10}(\bar{I}_1 - 3) + C_{20}(\bar{I}_1 - 3)^2, \tag{II.1}$$

with C_{10} and C_{20} the material parameters and $\bar{I}_1$ the first deviatoric strain invariant defined as $\bar{I}_1 = tr\,\bar{C}$. $\bar{C} = \bar{F}^t\bar{F}$ is the deviatoric right Cauchy-Green tensor and $\bar{F}$ is the deviatoric part of the deformation gradient tensor.

The specificity of this analytical model of the media was to also include a cohesive part in each layer. The objective was to reproduce the damage initiation and evolution until total rupture observed during the uniaxial tests. The motivation to use independent cohesive interfaces in each layer was that layers, comprising several lamellar units, were observed not to break at the same time in our previous uniaxial tests [89]. It was assumed that the cause of this phenomenon was the presence of defects in the layers. Thus, to reproduce different defects with different possible rupture thresholds, cohesive interfaces were introduced, in series with the hyper-elastic material. In this model, the global strain is equal to the strain in each layer, and the global force is the sum of the contributions from all layers. The response of a cohesive interface is illustrated in Figure II.3. Only traction (related to mode I of rupture) was taken into account in this 1D model.

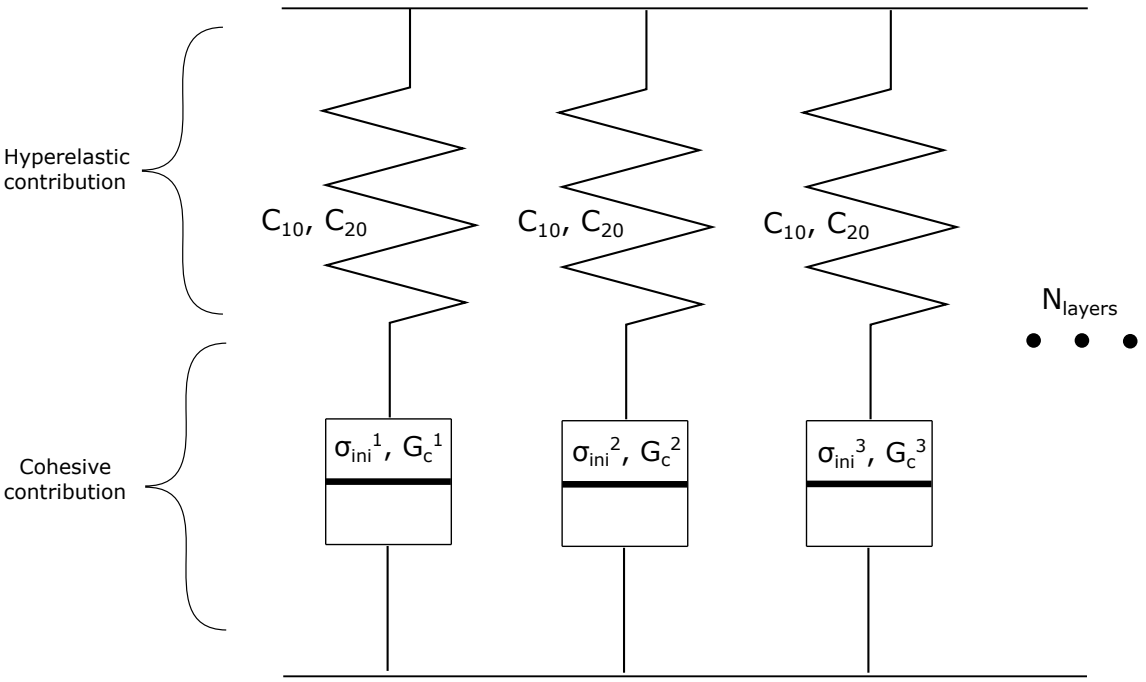

FIGURE II.2 – Schematic representing the analytical model and its material parameters.

The response of the cohesive zone is defined based on the normal stress as:

$$max\left[\frac{\sigma}{\sigma_{ini}}\right] = 1 \tag{II.2}$$

where σ(MPa) is the normal stress in the normal direction (ie. the loading direction here) and σ_{ini} is the damage initiation criterion which represents the peak value of the normal stress. This criterion indicates the beginning of damage in the cohesive zone. Damage evolution was then defined by a decreasing linear law which describes the rate of degradation of the cohesive zone stiffness. This law was defined based on the fracture energy G_c which is the amount of energy dissipated during the complete rupture of the cohesive zone. The choice of this cohesive zone model was motivated by the study of Miao et al. [139], which compared the effects of four types of cohesive zone model shapes: triangular, trapezoidal, linear-exponential and exponential-linear, on the predictability of arterial wall failure. The results indicated that triangular and exponential-linear cohesive zone models were able to reproduce the aortic tissue failure behavior well, justifying the choice of the simplest model in this study. In summary, the constitutive response of the model under uniaxial tension was governed by the following parameters:

- C_{10} and C_{20}, the material parameters defining the hyperelastic behaviour. They were identified by an inverse curve-fitting method (see next section).
- σ_{ini}, the damage initiation criterion. In the present model, there were as many damage initiation criteria as layers. They were set manually based on the uniaxial tension curves.
- G_c, the critical fracture energy and is defined as the area under the damage part of the cohesive response curve (Figure II.3). There were as many critical fracture energies as layers. They were identified using an inverse method (see section 2.3).
- N_{layer}, the number of layers present in the analytical model (typically 1 to 5).

Using a Matlab® code, nominal stress and nominal strain were calculated in each layer and the stress-strain curve of the whole model was obtained. The next steps were (i) to

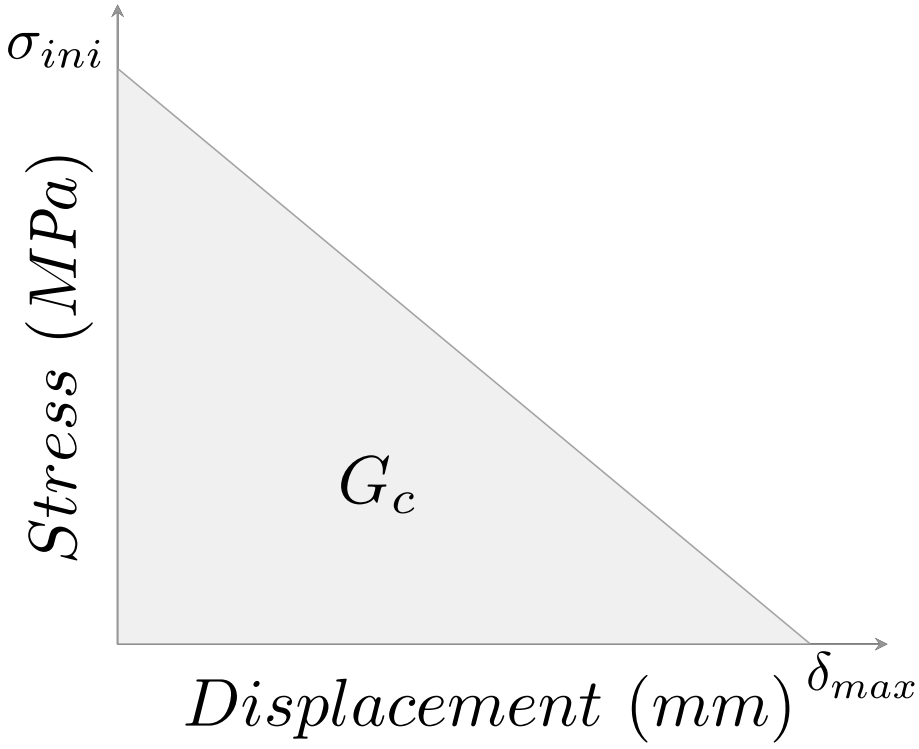

Figure II.3 – Cohesive behaviour with the stress as a function of the opening of the crack.

validate the implementation of the model (see next paragraph), and (ii) propose a strategy to identify the parameters of the model based on experimental tensile curves (see next section).

II.1.2.3 Model implementation validation

To validate the implementation of the analytical model, two finite element models were built in Abaqus®. The first model consisted of a single layer and the second model of two layers. The same dimensions were used in the analytical model and the finite element models. Cohesive zones were placed at the center of each layer to allow rupture in traction. The hyperelastic and cohesive parameters were set at the same values for the finite element and analytical models. Arbitrary, but realistic, fixed parameters were used. The stress-strain curves of both models were compared and the coefficients of determination, r^2, were calculated.

II.1.2.4 Inverse parameter identification

The following step of this study was an inverse analysis to obtain the set of parameters fitted to the experimental curves. The method was based on an cost function which quantifies the difference between the result of the simulation and the experimental data, and on an optimization algorithm which finds the parameters minimizing this function. The algorithm used here was described in Lagarias et al. [122], and was programmed within an in-house Matlab® code. Because the developed model involved many parameters to be identified for each curve, a global optimization on the whole curve would have given non-unique solutions. Instead, a three-step strategy based on separating the elastic response and the post-damage initiation response was used, and the damage initiation stresses were directly identified.

The first step aimed at identifying hyperelastic parameters C_{10} and C_{20}. The cost function used in the optimization algorithm was defined as follows:

$$Cost\ Function = \sum_{n=1}^{N} \frac{(\sigma_{num} - \sigma_{exp})^2}{N}, \tag{II.3}$$

where σ_{num} and σ_{exp} were the model and experimental stress values at the n^{th} point, respectively. N was the total number of points in the range of strain observed experimentally on the stress-strain curves. Only the undamaged part of the experimental curve (i.e. before any discontinuity in the slope) was used for this identification.

The second step of the method consisted in a direct identification of the different damage initiation criteria. This was performed by the manual selection of break points in the slope of the experimental curves (an example is shown Figure II.4), considering that break points correspond to the rupture of one or multiple layers.

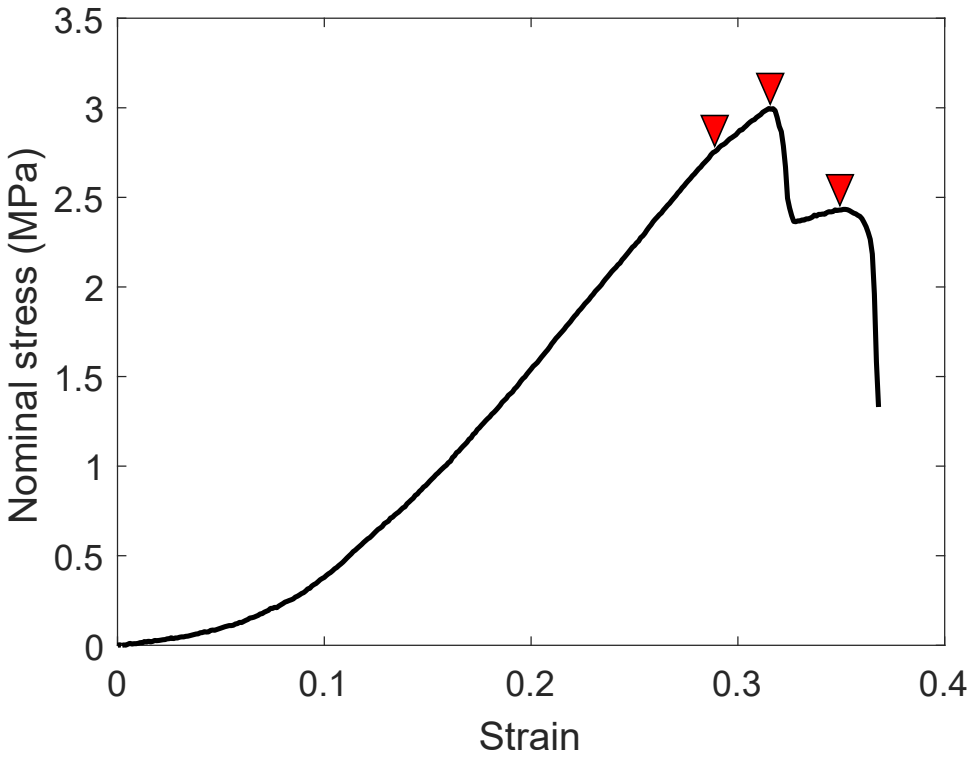

FIGURE II.4 – Example of experimental stress-strain curve, with manually selected damage initiation points (red arrow).

Last, the third step consisted in an inverse identification of the critical fracture energies of each cohesive zone (there was one cohesive zone per layer). To this aim, the same cost function as defined in Eq. 3 was used, with n varying in the range of strain beyond elastic strain.This identification provided the last set of parameters needed to completely define the model.

II.1.2.5 FE model to study the influence of mode II separation

During *in vitro* tensile tests, it was observed that layers initially break in mode I and then separate from each other, in mode II [89]. The analytical model presented above was suit-

able to identify the rupture parameters in mode I but did not allow for the identification of the parameters related to mode II. Thus, a 2D FE model that included delamination between layers was created using Abaqus®. Its dimensions were kept the same as those of the analytical model. Cohesive zones were defined (i) in the middle of each layer, in the transverse direction, to account for mode I separation, and (ii) between layers, parallel to the loading direction, to account for mode II separation which was not included in the analytical model. Mode I cohesive properties of each layer were taken from the previous analysis, but the weakest one was always chosen on the intimal side as observed experimentally [89]. Regarding mode II, a sensitivity analysis was performed to assess the influence of mode II initiation criterion and fracture energy. Uniaxial tension boundary conditions were applied. The mesh was comprised 600 CPS4 elements (four-node plane stress element) and the quasi-static problem was solved using the implicit solver of Abaqus®.

II.1.3 Results

II.1.3.1 Verification

The results of the verification of the analytical model against a finite element implementation are presented in Figure II.5 for the one-layer model (Fig II.5a) and the two-layer model (Fig II.5b). The comparison was focused on the nominal stress as a function of the total strain of the specimen. In this work, only the nominal strain was considered.

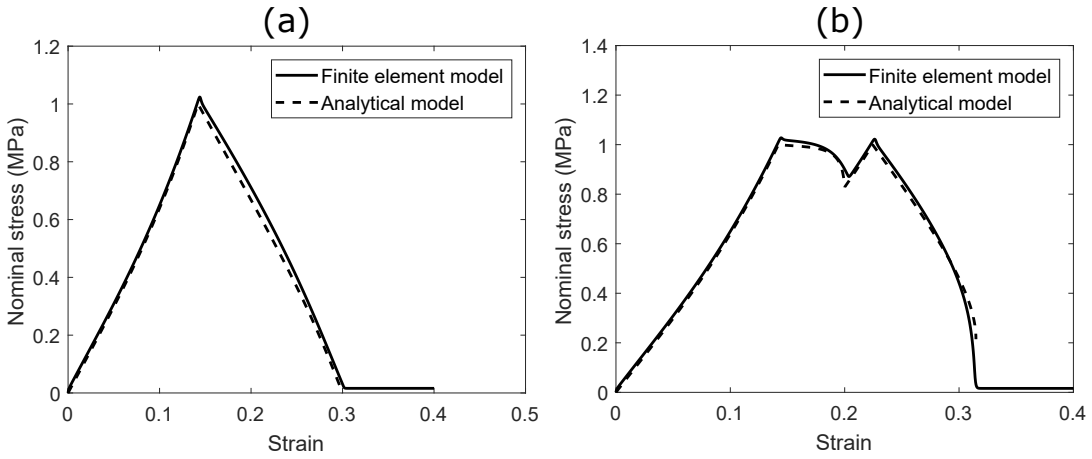

Figure II.5 – Responses of analytical model (dashed curve) and finite element model (solid curve) with (a) one layer and (b) two layers, with the two peaks corresponding to each layers damaging successively.

The different parameters used in the verification are presented in Table II.1. For the one-layer model, the coefficient of determination r^2 was 0.997 and for the two-layer model, 0.994, confirming proper implementation of the analytical model.

II.1.3.2 Inverse identification of hyperelastic and cohesive parameters

Table II.2 provides the values of all the parameters obtained following the three-step identification procedure detailed in Section 2.3, for 10 experimental specimens tested in Helfenstein-Didier et al. [89]. The comparisons between the analytical model and experimental tensile test stress-strain curves exhibited a good quantitative agreement considering that the r^2 values were in a range of 0.97 to 0.99 (Figure II.6). It can be observed that

TABLE II.1 – Parameters used during the verification with the one-layer model and the two-layer model.

	C_{10} (MPa)	C_{20} (MPa)	C_{20} (MPa)	C_{20} (MPa)
Model with one layer				
Layer 1	1	3	1	3
Model with two layers				
Layer 1	1	3	1	2
Layer 2	1	3	2	6

the global shape of the curves was well reproduced by the model although the smallest slope-breaks were neglected.
A comparison between the experimental images from one test and the model is presented in Figure II.7. The parameters of the model were identified from the corresponding stress-strain curve. In the first step, one can observe the undamaged media, then a first rupture on the intimal side corresponding to a change in slope on the stress-strain curve, followed, in the third step, by a second rupture on the adventitial side of the media and finally, in the fourth step, the remaining part of the media damaging before complete rupture. Note that, in the last step, the middle layer is in a partial damage state where δ_{max} has not been reached yet (Figure II.3). The finite element model shows a good qualitative agreement with the X-ray images.

Table II.2 – Parameters obtained for all experimental curves.

Test number	$\mathbf{C_{10}}$ (MPa)	$\mathbf{C_{20}}$ (MPa)	$\boldsymbol{\sigma_{ini}}$ **1** (MPa)	$\boldsymbol{\sigma_{ini}}$ **2** (MPa)	$\boldsymbol{\sigma_{ini}}$ **3** (MPa)	$\boldsymbol{\sigma_{ini}}$ **4** (MPa)	$\boldsymbol{\sigma_{ini}}$ **5** (MPa)	$\mathbf{G_c}$ **1** (MPa.mm)	$\mathbf{G_c}$ **2** (MPa.mm)	$\mathbf{G_c}$ **3** (MPa.mm)	$\mathbf{G_c}$ **4** (MPa.mm)	$\mathbf{G_c}$ **5** (MPa.mm)
1	0.00103	0.181	0.815	0.815	0.871	1.045	–	2.40	2.40	3.48	3.41	–
2	0.758	3.06	2.81	3.44	4.30	–	–	6.61	9.24	9.08	–	–
3	1.64	1.03	2.75	3.00	3.32	–	–	9.98	1.7	11.0	–	–
4	0.125	0.0705	0.543	0.750	0.750	0.800	0.800	2.70	3.57	3.57	1.84	1.84
5	0.210	0.0474	0.299	0.319	0.774	0.848	–	0.574	2.32	4.87	4.57	–
6	0.175	0.0331	0.686	0.742	0.759	0.759	–	4.52	4.19	1.93	1.93	–
7	0.184	0.0943	0.484	0.522	0.845	0.990	0.990	1.68	3.65	4.75	4.56	4.56
8	0.196	0.00170	0.567	–	–	–	–	3.76	–	–	–	–
9	0.140	0.0574	0.484	0.524	0.549	–	–	2.37	2.09	1.029	–	–
10	0.0744	0.0988	0.434	0.747	0.820	–	–	1.62	3.25	3.025	–	–

II.1.3.3 FE model to study the influence of mode II

The stress-strain curves obtained from the finite element simulations including mode II separation in longitudinal cohesive zones are shown in Figure II.8. The parameters of mode II used for the simulation are displayed on the graphs.

The simulation showed that, if the mode II damage initiation stress was increased in the longitudinal cohesive zone, the two adjacent layers of this zone would not separate. Instead, they formed a single unit where the strongest layer (not broken in mode I) supported the weakest one (already broken in mode I) and prevented its elastic recoil. Both layers would recoil later, at the same time, when the strongest one failed in mode I. This phenomenon can be seen from the dashed curve in Figure II.8a where the global resistance of the model was increased but the rupture was sudden. The latter observation would contradict the experimental observations, which suggests that the resistance to mode II separation in the longitudinal direction is probably one of the most influential factors in dissection-like propagation. Note however, that the mode II critical fracture energy was found to have a relatively low influence on the model response (Figure II.8b).

II.1.4 Discussion

This paper follows up on a series of experimental uniaxial tests made on porcine medial aorta samples under X-ray tomography [89]. These tests observed the media at the lamellar-scale during damage progression and rupture and showed that layers (i.e. a group of lamellar units) successively break in tension (mode I) followed by a sudden delamination due to their elastic recoil (mode II separation). These findings motivated this study aiming at further understanding and quantifying these phenomena. An analytical model was developed with the objective of reproducing the uniaxial tests and identifying the different parameters in each layer relative to rupture.

The implementation of the model was numerically verified against a finite element model based on the same assumptions and parameters. Subsequently, all parameters of the model were successfully identified for each available experimental curve with the method described herein. It is worth noting that these results did not differ when repeating the procedure several times on the same experimental curves, showing the robustness of the method, even if part of this method remains operator-dependent since the damage initiation stresses are set manually. For all experimental samples, the damage initiation stress and the critical fracture energy were obtained for a finite number of layers (structurally, these layers include several lamellar units). The values of damage initiation stresses are in the range of maximum stresses found in literature (750 kPa – 2500 kPa [246]). Regarding the critical fracture energy, it can be noted that a marked variability between the different samples was obtained, which is mainly attributable to the variability of the curves themselves as reported by Helfenstein-Didier et al. [89]. Nevertheless, our study is, to the best of our knowledge, the first to report experimentally-supported values of mode I critical fracture energy at the lamellar-scale of aortic medial tissue. They can serve as a basis to the development of numerical models of arterial damage.

Because the analytical model did not take into account mode II strength and separation of different layers, a finite element model was built which included this phenomenon between layers. The same values of hyper-elasticity and mode I rupture were used as in the analytical model, while for mode II, a sensitivity analysis on the associated values was performed to assess the influence of mode II separation in this mechanical rupture test. The analysis

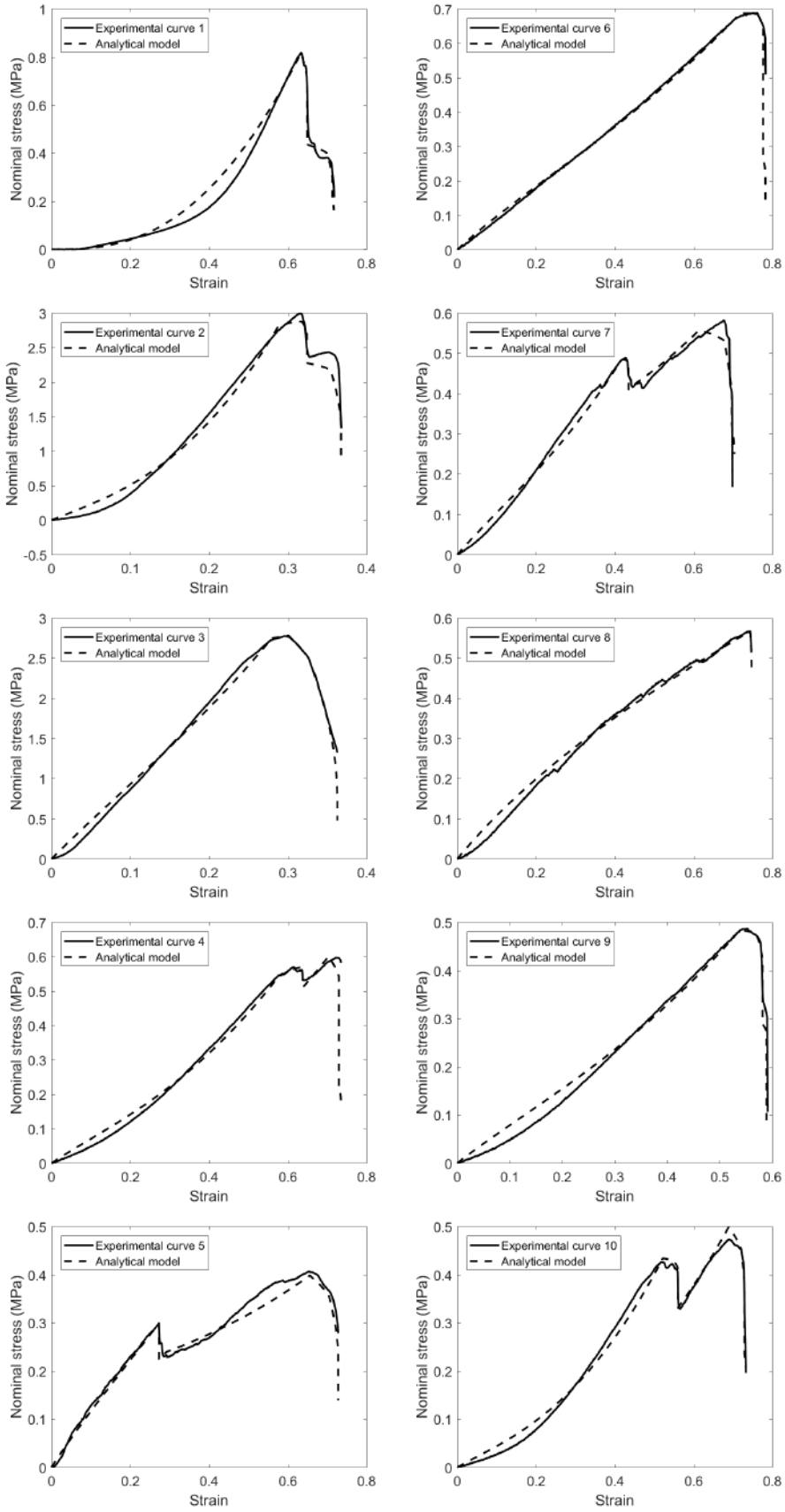

Figure II.6 – Comparison between the analytical model (dashed curve) and the experimental tensile test (solid curve). The r^2 are in a range of 0.97 to 0.99

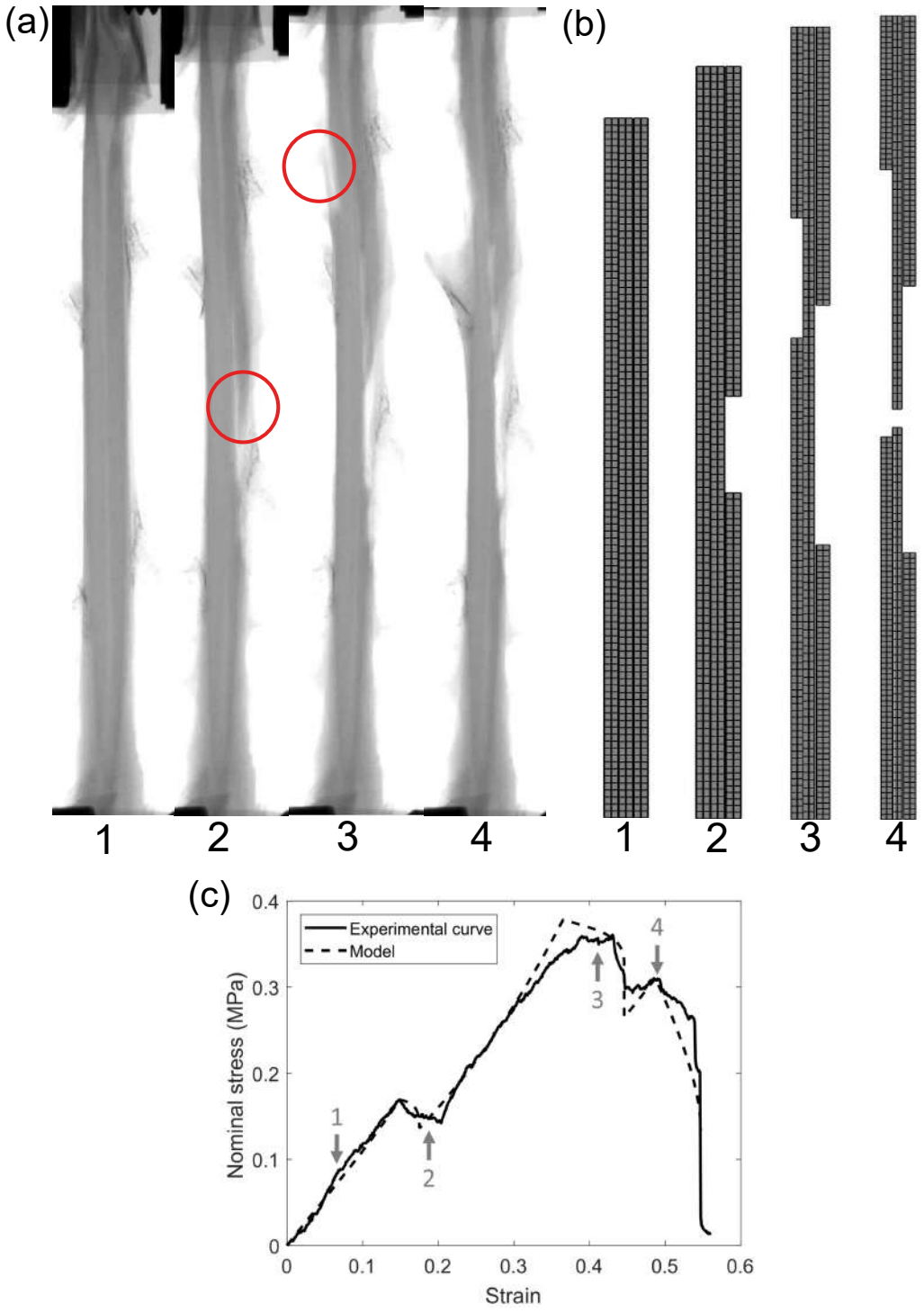

FIGURE II.7 – Analyses of an experimental case. The parameters were identified thanks to the stress-strain curve of the test and the cohesive interfaces were placed in the same configuration as in the X-ray images. (a) Images of the uniaxial tensile test under X-ray tomography at different time steps. The red circles highlight the visible sites of ruptures of layers. (b) Images of the finite element model at the same time steps with the parameters corresponding to the case (a). (c) Stress-strain curves of the test (a) and of the model response with the fitted parameters.

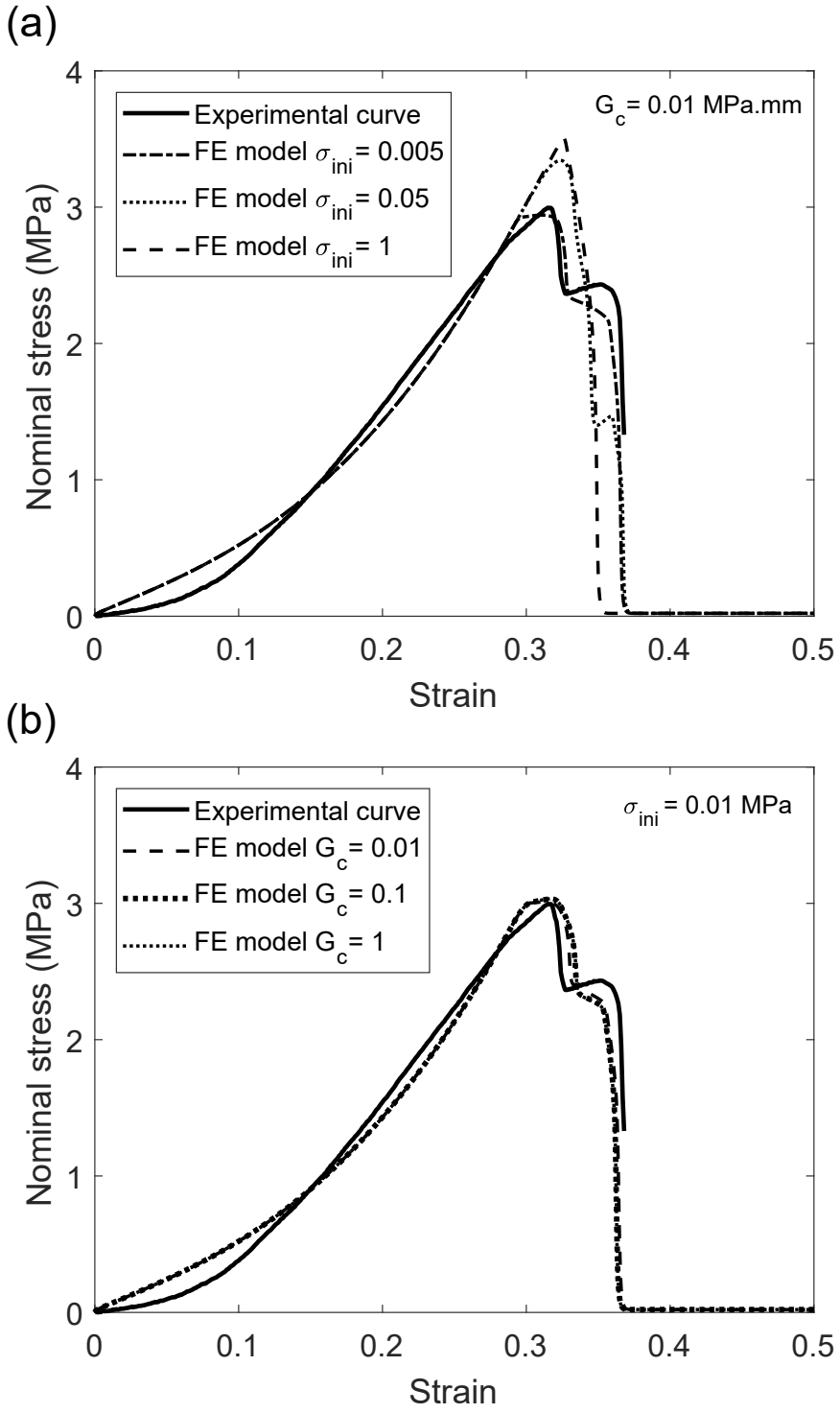

Figure II.8 – Comparison of the experiment and the finite element simulations to investigate the influence of the delamination parameters σ_{ini} and G_c. (a) G_c is fixed to 0.01 MPa.mm while σ_{ini} varies. When $\sigma_{ini} = 0.005$ MPa the three layers of the finite element model broke successively like the experiment, when $\sigma_{ini} = 0.05$ MPa the two first layers of the finite element model broke at the same time and the third layer broke later, and when $\sigma_{ini} = 1$ MPa the three layers broke at the same time. (b) σ_{ini} is fixed at 0.01 MPa while G_c varies. The three curves are relatively similar, this demonstrates the limited influence of G_c.

showed that the role of mode II is essential in maintaining layers together. If mode II strength is too high, two adjacent layers would not separate and they would recoil at the same time when the strongest one fails in mode I. Our experiments showed, however, that after breaking in mode I, a layer suddenly recoils and separates from its neighbouring layer in a mode II separation. The combination of these observations suggests that mode II separation may play a major role in crack propagation, as occurring in dissection. More specifically, our model confirmed that a first crack forms due to mode I failure, which then propagates in mode I in the transverse direction until the elastic recoil stress exceeds the mode II strength of a longitudinal plane. The crack will then propagate in the direction of less energy, hence following this plane and forming a delamination plane, as observed clinically and experimentally. Several studies investigated the mechanisms of dissection using different experiments. Tam et al. [213], created blebs in the media by injecting saline solution. Sommer et al. [203] and Wang et al. [240], used peeling test (hence mode I longitudinal separation), which are probably more suitable for the analysis of dissection propagation when a relatively long flap is already formed, or for plaque delamination. The present work is believed to be more appropriate for the onset of dissection.

Pasta et al. [168] demonstrated the presence of radially-running fibers of collagen and elastin that create "bridges" between lamellae and support the load induced by delamination. Pal et al. [166] proposed a predictive mechanistic model that investigated the effect of these fibers and reproduced the response of the peeling tests. The results showed that the density and failure energy of the radially-running collagen fibers to be the main contributors to the delamination strength. However, the mode of rupture in this study and in the present work are not the same. In the delamination model of Pal et al. [166], the fibers between the two strips of the peeling test rupture in mode I, whereas in the present model, the different layers separate from each other in mode II. From the present work, it is hypothesized that the separation in mode I between layers would not be activated until a channel is formed and blood rushes into that channel, thus pushing the layers apart. Mode II separation would be the precursor to this channel formation.

As previously shown, delamination is triggered when the recoil of ruptured lamellar units induces shear stress which exceeds mode II strength of the adjacent lamellar unit. Thus, the present study suggests that wall defects may be directly involved in determining the initiation location of the delamination process. Indeed, they could locally weaken this mode II strength. In other words, it is likely that a disease or an intra-mural hematoma already present at the beginning of the rupture of the intima would promote dissection. It is even possible that the delamination between lamellae has already been propagating when the intimal tear appears.

Limitations of this work are detailed herein. First, it was based on uniaxial tests, while the *in vivo* loading corresponds to a biaxial or even triaxial stress state. In a study closer to *in vivo* conditions of dissection, this aspect should be considered by implementing a 3D model. Another limitation of the present model based on cohesive zone modeling is that the path of the crack is pre-defined. Here, all experimental observations were consistent regarding the rupture pattern and our cohesive zones were positioned accordingly (transverse and longitudinal). However, in another loading configuration, a different configuration should be considered.

This work provided valuable data toward the characterization of arterial rupture at the lamellar-scale, which could be used in further modeling endeavors. Also, it yielded useful insights into the determinants and conditions that promote dissection *in vivo*. While

additional experimental validation is warranted to precisely address *in vivo* dissection conditions, this work opens a way to potentially important clinical applications in monitoring patient-specific vascular risk factors, and management of patients with dissection.

Highlights

- An analytical model, reproducing uniaxial tensile testing in medial arterial samples, was used to identify rupture-related parameters at the lamellar scale.
- A finite element model that includes cohesion between layers showed that a low shear delamination strength between layers, i.e. mode II separation, is essential to explain the rupture process observed experimentally.

Chapter III

Caractérisation de la rupture en mode II - *Characterisation of mode II fracture*

The Chapter II demonstrated the low resistance to mode II delamination in the rupture of aortic samples. In the present study, this mechanism is investigated by performing tensile test on notched specimens under X-ray imaging. The mode II is then identified in the circumferential and longitudinal directions by calibrating a finite element model with cohesive interface. This study was inspired by the work of Brooks Lane in the laboratory Sainbiose who performed the same experiment under optical coherence tomographie.

Contents of the chapter

Résumé du chapitre

L'étude de Helfenstein-Didier et al. [89] a montré que la rupture de l'échantillon aortique résulte d'une rupture en mode I suivi d'une délamination en mode II. Le chapitre II a modélisé les essais de traction réalisés par Helfenstein-Didier et al. [89] et a démontré l'importance de la faible résistance à la delamination en mode II dans la rupture de l'échantillon aortique. En conséquence, ce mécanisme a été étudié dans la présente étude en effectuant des essais de traction *in situ* sur des échantillons entaillés dans les directions circonférentielle et longitudinale. Ce test mécanique a été observé par radiographie afin d'étudier la propagation de fissure dans l'échantillon. Par la suite, les essais mécaniques ont été modélisés et les propriétés de rupture de l'aorte ont été quantifiées par des méthodes inverses. Les propriétés du matériau ont été identifiées à partir d'essais de traction dans les directions circonférentielle et longitudinale en ajustant un modèle hyperélastique. Le mode I a été défini grâce à des essais de pelage réalisés précédemment par le laboratoire Sainbiose. Les paramètres du mode II ont été quantifiés en calibrant un modèle éléments finis combiné à des interfaces cohésives pour simuler la rupture de l'échantillon. Le modèle éléments finis 2D est composé d'une géométrie idéalisée avec des propriétés matériaux anisotropes. Un critère d'endommagement quadratique a été assigné au modèle combinant mode I et II. Une étude de l'impact du maillage sur les résultats a montré que la taille de maillage choisie n'influait que de façon négligeable la rupture. Les résultats expérimentaux ont montré que l'échantillon circonférentiel a subi une délamination sur une grande surface avant la rupture totale, contrairement à l'échantillon longitudinal qui a subi une petite délamination avant de rompre en mode I. Ainsi, la tension *in vivo* n'est pas un facteur prédominant dans la propagation longitudinale de la dissection aortique. La résistance au cisaillement (mode II) a été identifiée comme étant plus élevée dans la direction longitudinale que dans la direction circonférentielle, conformément à la littérature. L'énergie de fracture en mode II a révélé une influence limitée sur la réponse du modèle, ce qui correspond aux résultats du Chapitre II. Les observations cliniques montrent que la dissection se propage dans la direction longitudinale, pourtant les valeurs de résistance à la rupture en mode I et II ont été trouvées plus élevées dans la direction longitudinale. Ainsi, d'autres mécanismes semblent jouer un rôle dans l'initiation et la propagation de la dissection aortique. Un modèle plus proche des conditions *in vivo* est nécessaire afin de mieux comprendre les phénomènes derrière cette maladie.

III.1 Investigation and identification of interlamellar failure properties using X-ray tomography

Abstract

After apparition of an intimal tear in the aortic wall, the crack direction changes and propagate between the medial lamellae as observed in Chapter II. Shear stress is considered to be responsible for this interlamellar failure. To study this process tensile tests on notched samples, observed on X-ray images, were performed in the circumferential and longitudinal directions. The purpose of the present study was to model these mechanical tests and quantify the failure properties of the aorta. Inverse methods were used to identify the elastic and mode II properties successively. The material properties were identified in the circumferential and longitudinal directions from the undammaged part of the tensile test curves by fitting an hyperelastic model. The mode II parameters were quantified by calibrating a finite element model combined with cohesive interfaces to simulate the failure of the samples. The results showed that the circumferential sample delaminated on a large area before total failure conversely to the longitudinal sample which underwent a small delamination before total rupture. Thus, the *in vivo* tension of the aorta is not a primary factor in the longitudinal propagation of the aortic dissection. The shear strength (mode II) was identified to be higher in the longitudinal direction than in the circumferential direction in accordance with the literature. As in Chapter II, the mode II critical fracture energy was found to have a limited influence on the result.

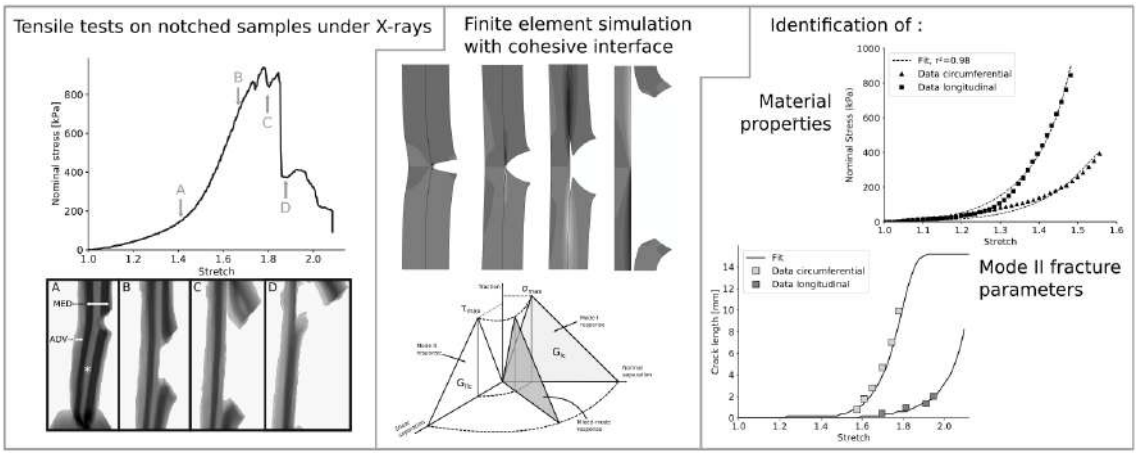

III.1.1 Introduction

The study of Helfenstein-Didier et al. [89] showed that the rupture of aortic sample result from a distinct pattern of mode I followed by mode II delamination. The Chapter II modelled the tensile tests performed in Helfenstein-Didier et al. [89] and demonstrated the importance of mode II fracture in the rupture of aortic sample. As a consequence, the delamination in mode II was investigated in the present study by performing tensile tests on notched samples.

Although, in physiological condition the aortic wall withstands a biaxial loading, the tensile test on notched sample were used to investigate the response of the aorta once an initial tear is present. The presence of the crack creates a disruption in the tensile behaviour of the aorta by adding shear stress leading to the delamination of the medial layers. The same phenomenon was observed in Helfenstein-Didier et al. [89]; however, the strain energy stored prior to crack propagation causes an unstable and dynamic failure, which is poorly suited for quantification. With the notch tensile test the propagation of the crack is quasi-static which makes it possible to quantify the delamination failure properties of the aorta.

The methodology of the present work is similar to the study of Brian FitzGibbon et al. [65] in which they investigated mode II fracture in notched bovine aortic tissue using a shear fracture ring test. The mode II shear strength and fracture energy were identified by calibrating a finite element model combined with cohesive interface. Although this method allows a complete characterisation of the mode II failure of the tissue in the circumferential direction, the shear properties in the longitudinal direction couldn't be identified in their work. This is a major limitation as in clinics 80 to 95% of the intimal tear are in the circumferential direction and propagate in the longitudinal direction [217].

The purpose of the present study was to characterise the interlamellar mode II fracture properties of porcine aortic specimens. Firstly, a tensile test on notched samples was performed in the circumferential and longitudinal directions. Secondly, a cohesive zone model was calibrated on the mechanical test using the crack length curve in order to identify mode II interlamellar fracture properties. The investigation and quantification of the mode II delamination properties in both directions could lead to a better understanding of the mechanisms occurring during aortic dissection.

III.1.2 Materials and methods

III.1.2.1 *In situ* mechanical test on notched samples

Sample preparation

A porcine descending aorta was obtained in a local slaughterhouse few hours after death. Two rectangular specimens were cut with a stainless blade, one in the circumferential direction and the other in the longitudinal direction. A notch about half the thickness was cut on the intimal side of each specimen through all their width. The dimensions of the samples were reported in Table III.1. The specimens were then immersed in a diluted solution of sodium polytungstate (15 g/L) to ensure a good contrast on the X-ray images and were kept at 4 °C for 24 hours. The optimal immersion time has been determined in a previous study [89]. Only two samples are presented here in order to illustrate the methodology to quantify mode II, other experiments have been carried out by our laboratory on the *in situ* tensile test but they will not be described here.

Tensile testing

A custom tensile testing machine equipped with a 250 N load cell was placed in an X-ray microtomography (XRCT) setup. For more information on the XRCT equipment see Helfenstein-Didier et al. [89]. The sample was then mounted on the clamps of the custom tensile testing machine. Special attention has been given to ensure that no slippage appeared at the clamps. The mechanical test was performed at 0.625 mm/s until complete rupture of the sample while recording the displacement and load. The *in situ* tensile test was observed with a continuous 2D radiographic acquisition at 5 images per second. The voxel size was 10 x 10 x 10 µm. The width of the specimen was oriented perpendicular to the X-ray beam. The mechanical test and the dimensions of the sample are presented in Figure III.1. The stretch was obtained by dividing the current length of the sample by its initial length. The First Piola-Kirchhoff stress P was calculated by dividing the load F by the initial remaining section of the sample A

$$P = \frac{F}{A}, \quad A = W(T - D_c) \tag{III.1}$$

with W, T, and D_c the width of the sample, the thickness of the sample, and the notch depth, respectively.

Specimen	Length (mm)	Width (mm)	Thickness (mm)	Notch depth (mm)
Circumferential	15	6	2.45	1.24
Longitudinal	14	7.5	2.46	1.21

Table III.1 – The 2 specimens dimensions.

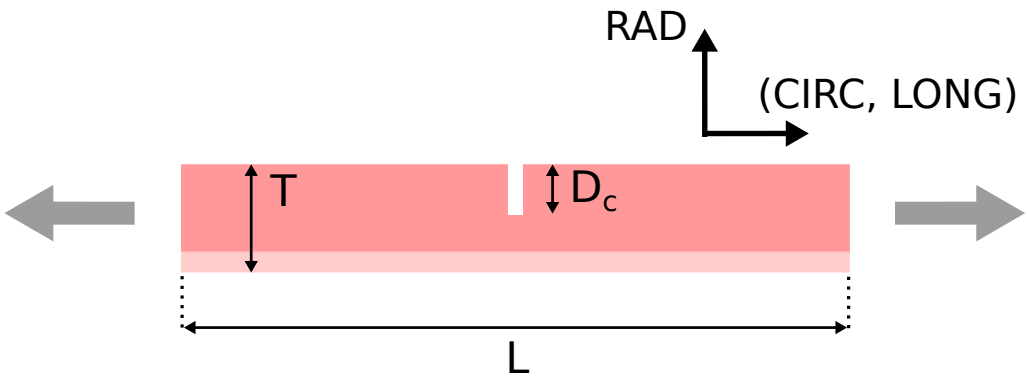

Figure III.1 – Sketch of the tensile test on notched sample. The dimensions of the aortic specimen are represented. T: thickness, L: length, D_c: depth of the crack. The brighter layer is the adventitia. The X-ray beam is oriented normal to the figure.

III.1.2.2 Numerical model

In this section we present a FE model of the tensile test on notched sample developed to identify the failure properties of the porcine aortic specimens. A 2D model with an idealised geometry and anisotropic hyperelastic properties was defined. Cohesive interfaces were introduced to model the delamination of the medial layer. Both ends of the sample were controlled in displacement to perform the tension. The elastic properties were identified by fitting the stress-strain curves from uniaxial tensile tests performed in circumferential and

longitudinal directions. The delamination properties of 2 specimens, one in the circumferential direction and the other in the longitudinal direction, were identified by calibrating a finite element model using the length of the crack as a function of the stretch of the sample. The FE simulation were run in Abaqus/Standard (Dassault Systemes, 2018).

Geometry and mesh

A 2D idealised geometry composed of a notched rectangle was implemented as presented in Figure III.1). The dimensions of the 2 specimens were reported in Table III.1. The corresponding dimensions were used in the FE simulation to identify the delamination properties. The media and the adventitia were considered the same material. In the simulation, the tension was performed by controlling both ends of the sample in displacement. Sample delamination was modelled by introducing a cohesive interface in the mesh along the sample at the tip of the notch to model interlamellar mode II delamination as observed in the experimental tests. The FE model was meshed with 3700 CPS4H elements. A convergence study, presented in Appendix A.1, was conducted to ensure that the mesh does not affect the simulation result.

Constitutive model

In the present study, we used the Holzapfel-Gasser-Ogden model (HGO) proposed by Gasser et al. [71], based on Holzapfel et al. [95]. This model is represented as a collagen-fibre-renforced material with two families of collagen fibres symmetrically arranged embedded in an isotropic groundmatrix. The deviatoric strain energy function $\bar{\psi}$ is divided between an isotropic part $\bar{\psi}_m$ and an anisotropic part $\bar{\psi}_{f,i}$ as given by

$$\bar{\psi} = \bar{\psi}_m + \sum_{i=4,6} \bar{\psi}_{f,i}\,. \tag{III.2}$$

The elastin fibres and the ground substance are modelled as a neo-Hookean material and is defined as

$$\bar{\psi}_m = \frac{\mu}{2}(\bar{I}_1 - 3), \tag{III.3}$$

where $\mu > 0$ is the neo-Hookean parameter and $\bar{I}_1 = tr\bar{C}$ is the first invariant of the Cauchy-Green tensor $\bar{C}$ (with $\bar{C} = \bar{F}^T\bar{F}$ and $F = J^{\frac{1}{3}}\bar{F}$). The strain energy function related to the two families of collagen fibres is defined as

$$\bar{\psi}_{f,i} = \frac{k_1}{2k_2}(e^{k_2(\kappa\bar{I}_1+(1-3\kappa)\bar{I}_i-1)^2} - 1), \quad i = 4, 6, \tag{III.4}$$

where $i = 4$ and $i = 6$ correspond to the two families of fibre. The modified pseudo-invariants $\bar{I}_4 = \bar{C} : a_{01} \otimes a_{01}$ and $\bar{I}_6 = \bar{C} : a_{02} \otimes a_{02}$ are equal to the square of the stretch of the fibres in the fibre directions. The vectors a_{01} and a_{02} represent the two symmetrically arranged fibre directions with respect to the circumferential direction, defined by their angle α. The parameter $\kappa \in [0, \frac{1}{3}]$ correspond to the dispersion of the collagen fibres. Finally, $k_1 > 0$ is a stress-like parameter and $k_2 > 0$ is a dimensionless parameter.

Cohesive interface model

Cohesive interfaces were used to model the damage and failure observed in the experimental tests. The reason of choosing this method rather than a more complex approach such as extended FE method or phase-field method is that the crack path is already known from

the XRCT observations made during the uniaxial tests. According to these observations, a cohesive interface was placed along the sample.

The model governing the cohesive interface was defined as a linear traction-separation law composed of an elastic part followed by the initiation and evolution of damage. In the absence of damage, the elastic response of the cohesive interface in tension and shear was defined as

$$\begin{pmatrix} \sigma_I \\ \sigma_{II} \end{pmatrix} = \begin{pmatrix} K_I \\ K_{II} \end{pmatrix} \begin{pmatrix} \delta_I \\ \delta_{II} \end{pmatrix} \tag{III.5}$$

where the indices I and II represent the normal (mode I) and tangential (mode II) components, respectively. σ is the contact stress, δ is the separation displacement, and K is a stiffness parameter assumed mode-independent. To avoid an influence of the elastic part of the cohesive interface on the model behaviour, the cohesive stiffness was assumed much higher than the stiffness of the model, thus $K_{I,II} = 10^3$ MPa/mm.

The initial behaviour of the cohesive interface was assumed to be linear. Once the damage initiation criterion is met, the degradation of the interface begins. The criterion was defined as

$$\left(\frac{\sigma_I}{\sigma_I^0}\right)^2 + \left(\frac{\sigma_{II}}{\sigma_{II}^0}\right)^2 = 1, \tag{III.6}$$

where σ_I^0 and σ_{II}^0 are the maximum contact stresses in the normal and tangential directions, respectively. The advantage of this criterion is to take into account the contribution of both stresses.

Following the initiation of damage, a linear law defined the evolution of the cohesive interface degradation. A scalar damage variable D was defined, representing the state of material stiffness degradation. D evolves monotonically from 0 initially to 1 upon complete separation. The damage evolution of the cohesive interface was defined as

$$\begin{aligned} \sigma_I &= \begin{cases} (1-D)\sigma_I & if\, \sigma_I > 0 \\ \sigma_I & if\, \sigma_I < 0 \end{cases} \\ \sigma_{II} &= (1-D)\sigma_{II} \end{aligned} \tag{III.7}$$

The cohesive interface remains undamaged in pure compression. The behaviour of the cohesive interface is reported in Figure III.2 and the mixed-mode behaviour is presented in Figure III.3. G_c is the fracture energy dissipated during the failure process. It is equal to the area under the traction-separation curve as shown in Figure III.2.

Identification of material properties

The constitutive parameters of the model (μ, k_1, k_2, α, and κ) were fitted to the undammaged part of the experimental data. Curves from the circumferential and longitudinal directions were fitted simultaneously by minimizing a cost function $J(\vec{\chi})$ with the Sequential Least Squares Programming (SLSQP) algorithm. The cost function was defined as

$$J(\vec{\chi}) = \frac{1}{n}\sum_{i=1}^{n}\left[\left(\sigma_{\theta\theta}^{exp}(\lambda_\theta^i) - \sigma_{\theta\theta}^{mod}(\lambda_\theta^i)\right)^2 + \left(\sigma_{zz}^{exp}(\lambda_z^i) - \sigma_{zz}^{mod}(\lambda_z^i)\right)^2\right], \tag{III.8}$$

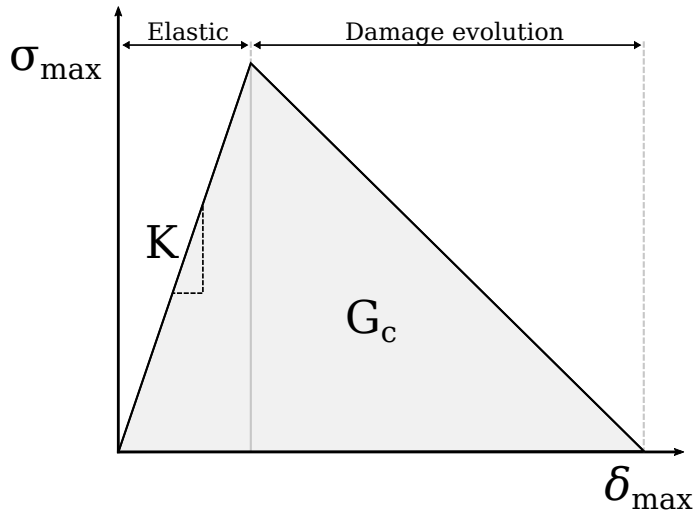

FIGURE III.2 – A graph representing the cohesive response. In a first time, the behaviour of the cohesive interface is linear elastic. Once the damage initiation criterion is met the damage start to accumulate. The evolution of cohesive zone degradation was defined by a linear law. The parameter K defines the stiffness of the elastic part.

where $\vec{\chi}$ is the vector containing the constitutive parameters to be identified and n is the number of data points. The abbreviations *exp* and *mod* mean experiment and model, respectively. The Cauchy stresses, predicted by the constitutive model (presented in section III.1.2.2), in the circumferential and longitudinal directions at the i^{th} data point were defined as

$$\sigma_{\theta\theta,i}^{mod} = \left(\lambda_\theta \frac{\partial \psi}{\partial \lambda_\theta}\right)_i \tag{III.9}$$

and

$$\sigma_{zz,i}^{mod} = \left(\lambda_z \frac{\partial \psi}{\partial \lambda_z}\right)_i \tag{III.10}$$

where λ_θ and λ_z are the principal stretches in the circumferential and longitudinal directions. The coefficient of determination r^2 was calculated to assess the quality of the fit.

Identification of mode II fracture

Once the material properties were identified, a finite element model of the tensile test on notched samples was calibrated with experimental data to identify the mode II parameters. The geometry and the mesh of the simulation were defined in Section III.1.2.2. The mode I critical fracture energies were quantified with "T"-shaped peeling test previously performed by the laboratory on porcine samples (in the process of being published). According to Leng et al. [123] only mode I is involved in "T"-shaped peeling test, allowing a separate quantification of the two modes. The maximum contact stress in the normal direction was assigned according to FitzGibbon and McGarry [65]. The mode I failure parameters in circumferential and longitudinal direction are presented in Table III.2. The fracture properties of the aorta related to mode II were identified by fitting the mean experimental curves of the length of crack $a_{\theta,z}$ as a function of the displacement of the clamps $d_{\theta,z}$. The two cost functions to minimise were defined as

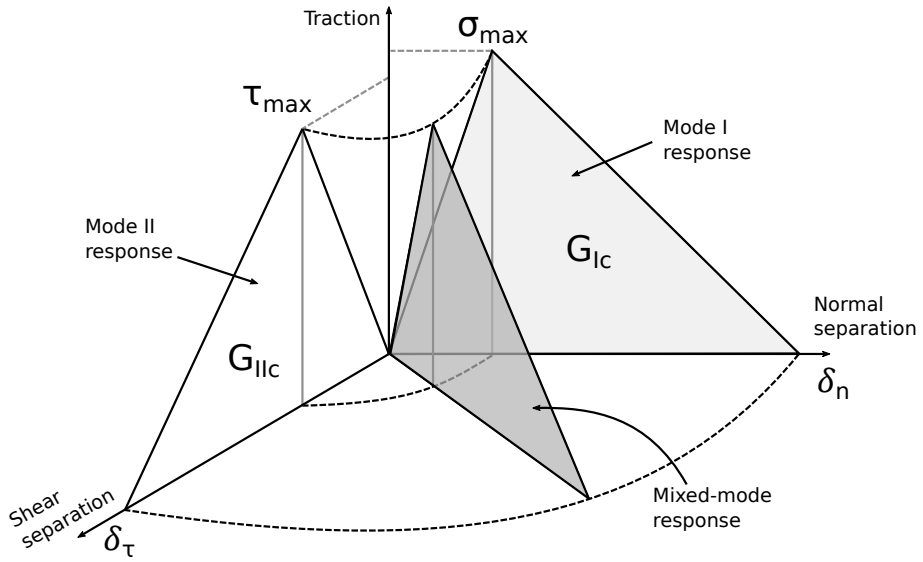

Figure III.3 – A graph defining the mixed-mode behaviour when mode I and II fracture are involved.

$$J_k(\vec{\chi_{II}}) = \frac{1}{n}\sum_{i=1}^{n}\left(a_k^{exp}(d_k^i) - a_k^{mod}(d_k^i)\right)^2, \quad k = \theta, z \tag{III.11}$$

where $\vec{\chi_{II}}$ is the vector composed of the failure parameters σ_{II}^0 and G_c^{II} to identify, in the circumferential and longitudinal directions. $a_{k,i}$ and d_k^i are the length of crack and the displacement at the clamps, respectively, at the i^{th} data point, in the $k = \theta, z$ direction.

	σ_I^0 (kPa)	G_c^I (N/mm)
Circumferential	220	0.12
Longitudinal	220	0.13

Table III.2 – The mode I failure parameters.

III.1.3 Results

III.1.3.1 Tensile test on notched samples

The stress-strain curves and key images of the tensile tests on notched samples are presented in Figure III.4 and III.5 for the circumferential and longitudinal directions. The results showed that the crack propagated perpendicular to the notch and a delamination of the specimen occurred before total failure in mode I. The circumferential specimen delaminated on a much larger area before complete failure than the longitudinal sample. The delamination area of the circumferential specimen was about five times larger than that of the longitudinal specimen.

III.1.3.2 Identification of material properties

The results of the material behaviour identification are presented in Figure III.6. The identified hyperelastic parameters are reported in Table III.3. The coefficient of correlation r^2 was equal to 0.98 showing that the elastic model captured well the nonlinear behaviour of the aortic wall in circumferential and longitudinal directions.

	μ (kPa)	k_1 (kPa)	k_2	α (°)	κ
Aortic wall	8.6	411.7	7.1	48.3	0.09

TABLE III.3 – Hyperelastic parameters of the HGO model identified by the fitting.

III.1.3.3 Identification of mode II fracture

The experimental and numerical curves from the tensile tests on notched samples used for the calibration are given in Figure III.7. The results are showing a good agreement, ensuring a correct calibration of the models. The identified mode II failure stress σ_{II}^0 was 130 kPa and 249 kPa for the circumferential and longitudinal directions, respectively. Decreasing the maximum contact stress in mode II shifts the crack length curve on the left, conversely increasing the value shifts the curve on the right. The critical fracture energy was found to not have significant influence on the crack length response. The value was varied between 0.05 and 1 N/mm. After a certain stretch, the crack length reached a plateau in both direction (Figure III.7) corresponding to the total failure of the cohesive interface. Numerical simulation images with the shear stress contour are presented in Figure III.8. High shear stress can be observed around the cohesive interface during the delamination process.

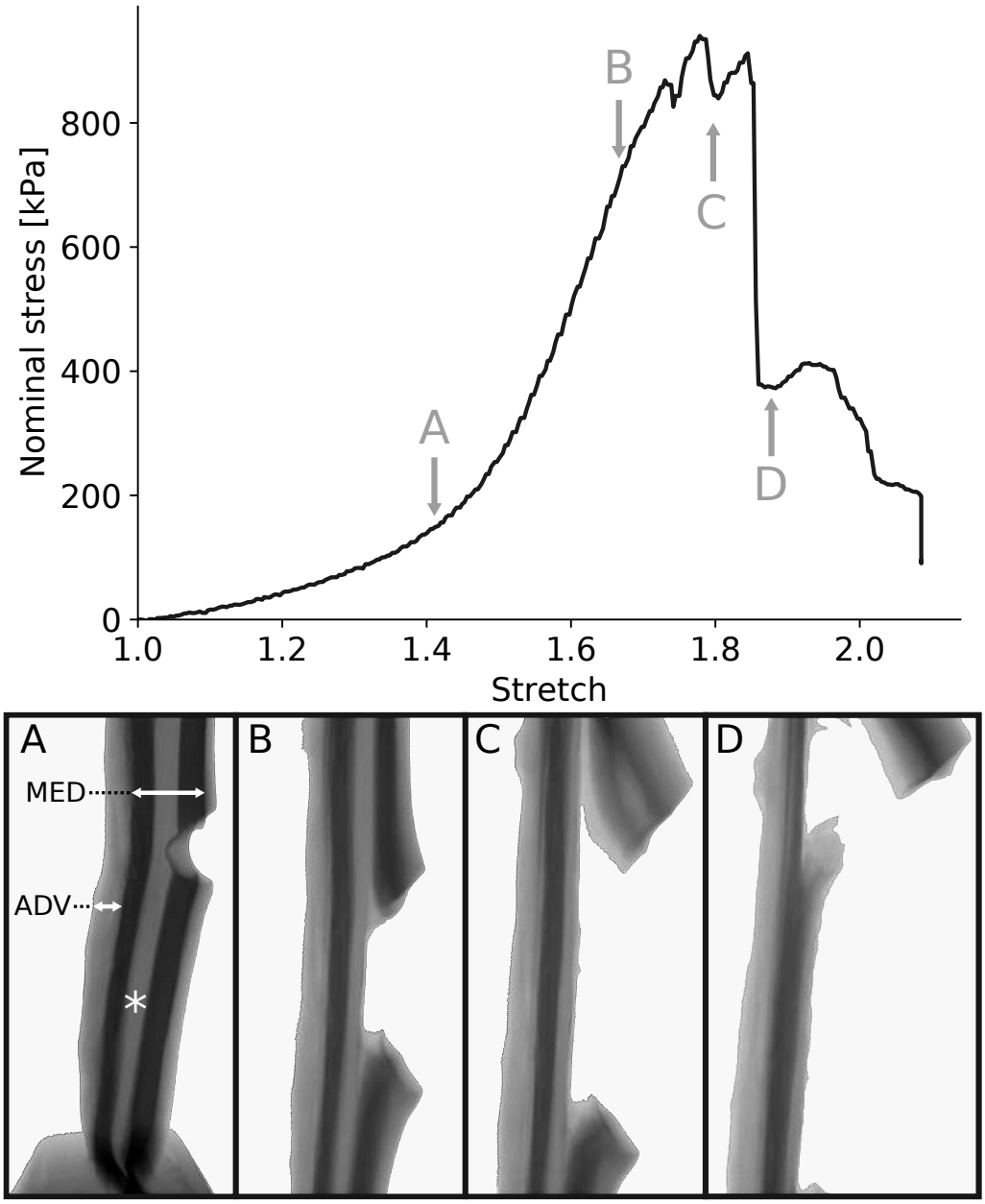

Figure III.4 – Stress-strain curve of the uniaxial tensile test on a notched porcine aortic specimen oriented in the circumferential direction is presented with four radiographic images corresponding to different stretches of the sample. MED: media, ADV: adventitia. The contrast agent did not reach the centre of the specimen, shown by the white $*$.

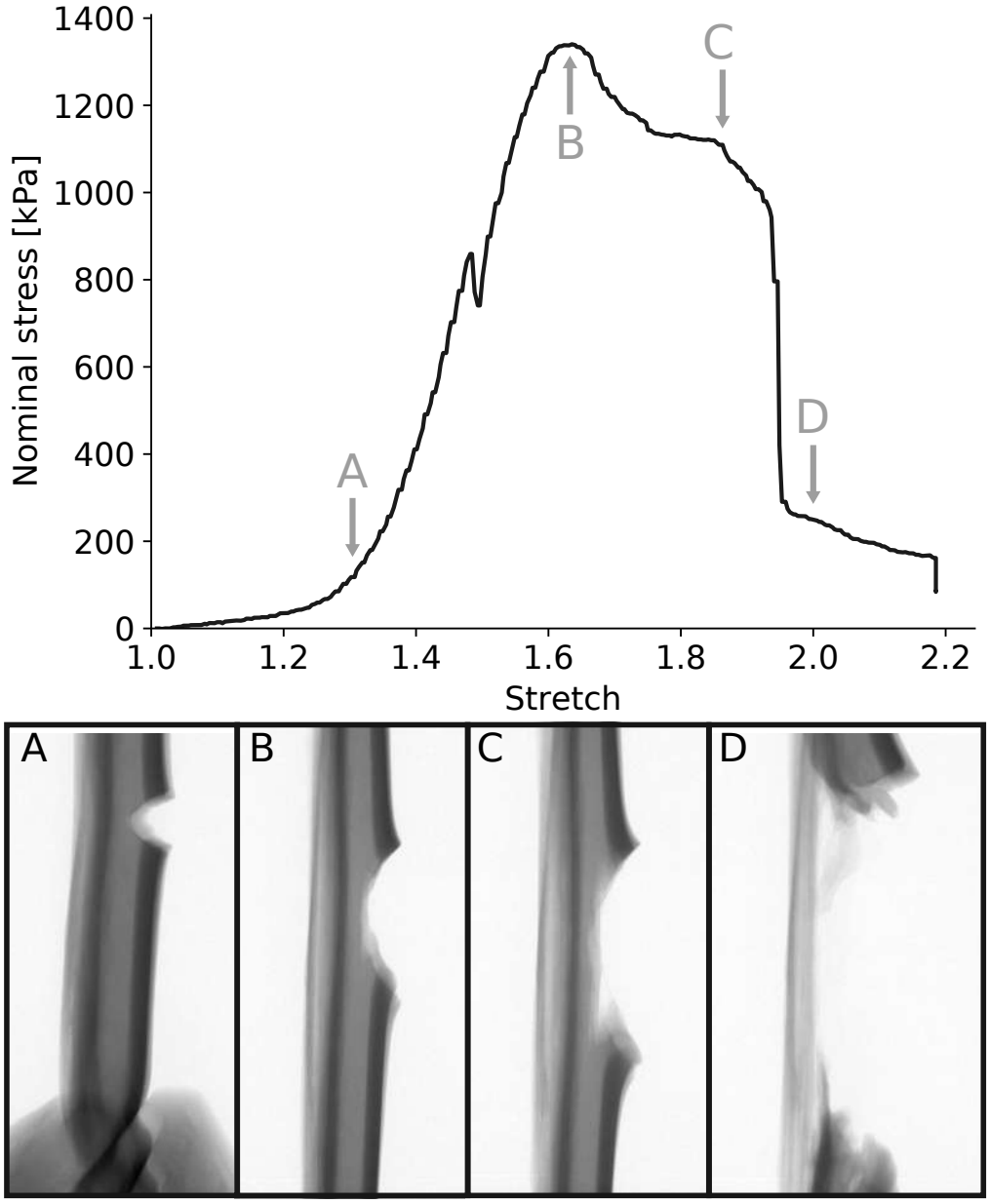

FIGURE III.5 – Stress-strain curve of a representative uniaxial tensile test in the longitudinal direction on a notched porcine aortic specimen is presented with four radiographic images corresponding to different stretches of the sample.

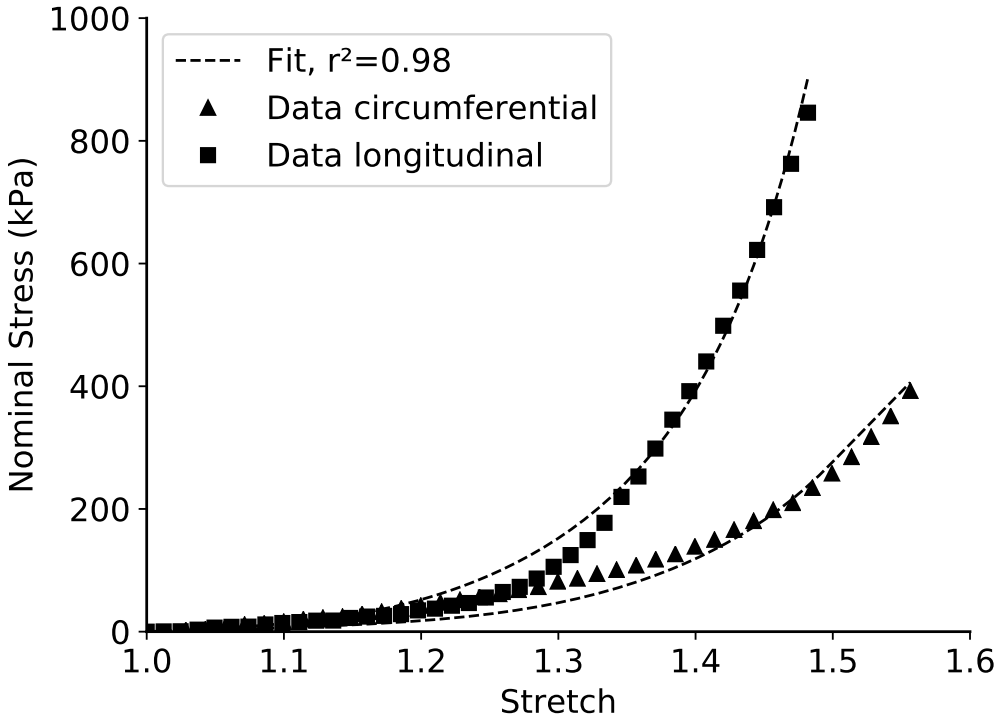

Figure III.6 – Comparison of the experimental data and the fitted constitutive model with the Cauchy stress versus the stretch

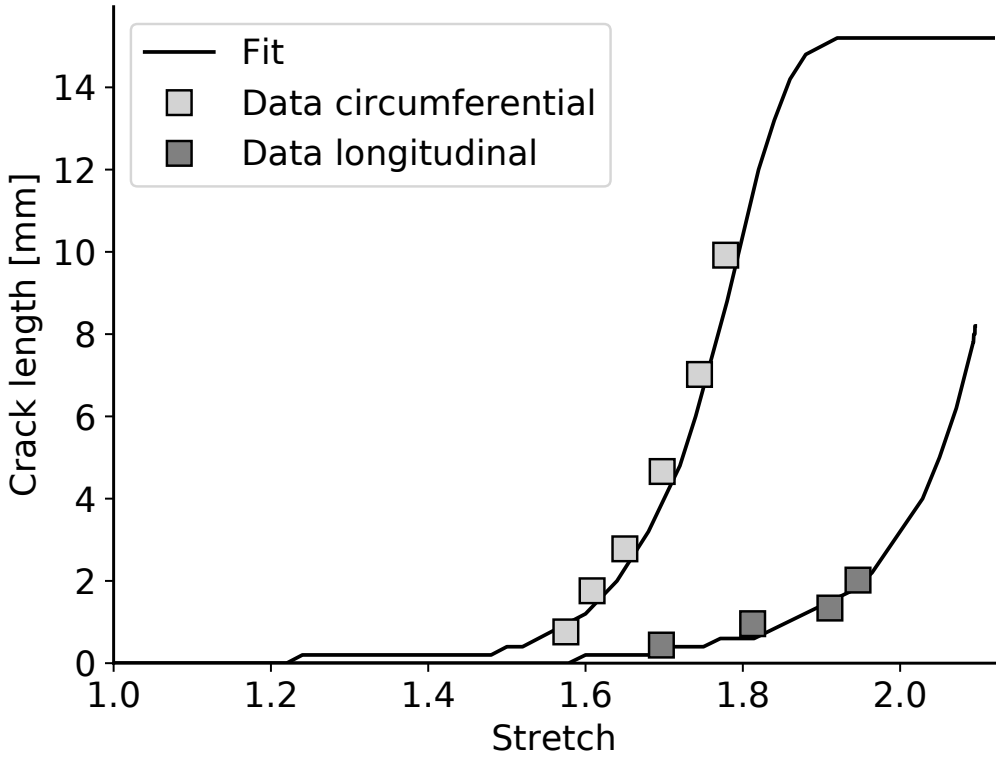

Figure III.7 – Length of crack versus displacement resulting from the tensile tests on notched samples in the circumferential and longitudinal directions.

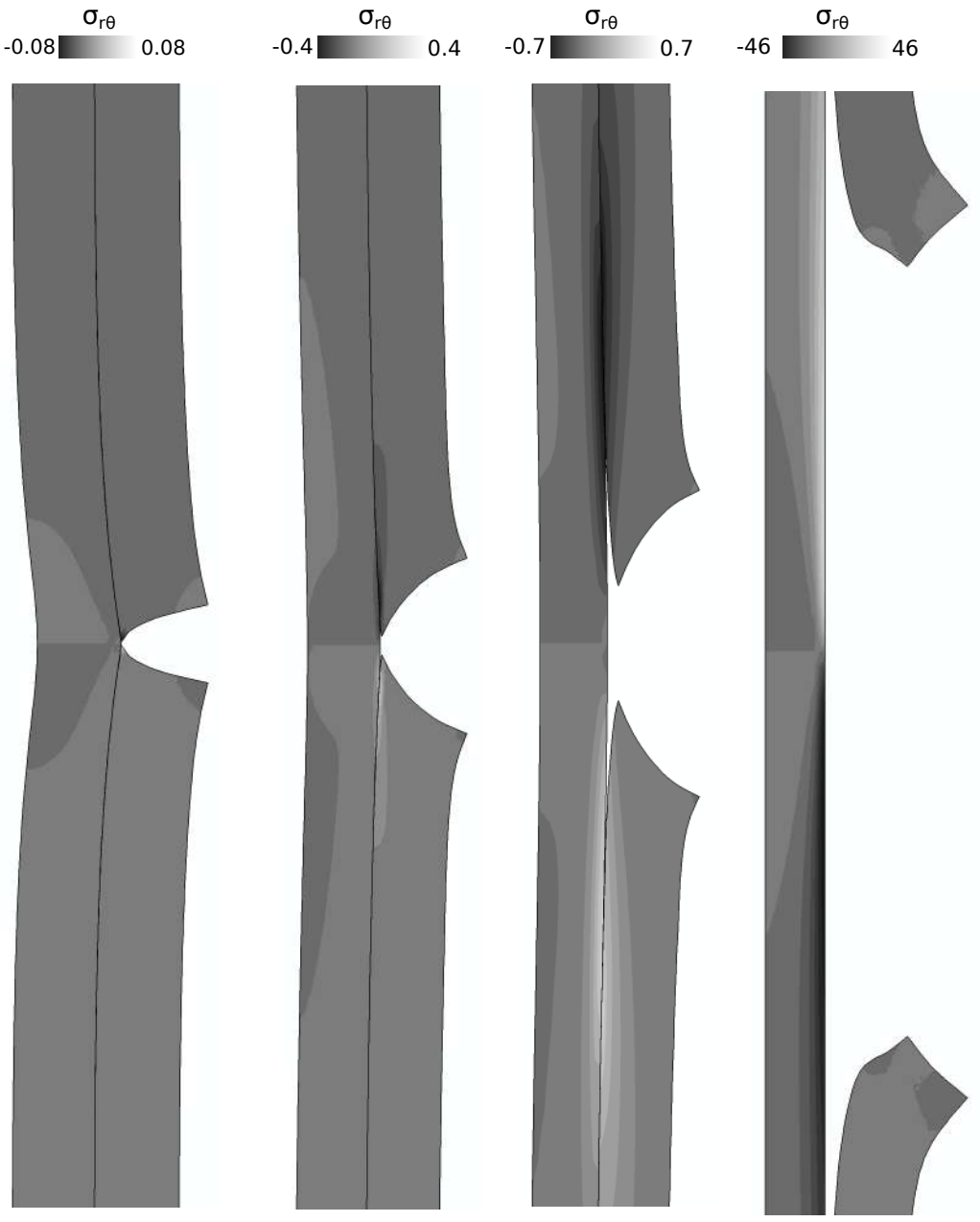

FIGURE III.8 – Maximum shear stress contour is plotted at four different steps of the simulation of the tensile test on a notched sample in the circumferential direction.

III.1.4 Discussion

In this study, the material and mode II failure properties of porcine aorta were quantified to investigate the mode II fracture and its effect on aortic dissection. An *in situ* tensile test on notched samples was performed. The anisotropic elastic properties of the HGO model were identified on the undammaged part of the experimental tests. The mode II was quantified in the circumferential and longitudinal directions by calibrating a numerical model on the experiment.

This study investigates the propagation of a dissection along the aorta. Once an intimal and possibly medial tear appears in the aortic wall, a high shear stress is present at the tip of the notch. The interlamellar strength being the weak point of the aorta due to its structure [246], the crack direction changes to propagate between the lamellae. The delamination phenomenon is due to the laminated structure of the aortic medial layer as the notch tensile test on other type of tissue does not give the same result, e.g. with skin or bone tissues [248]. The experiments and the models showed a lower shear strength in the circumferential direction than in the longitudinal direction. This is in accordance with Sommer et al. [204] which performed shear test on human diseased aortic samples. However, the values identified in the present study were higher in the longitudinal direction than the failure values found in Sommer et al. [204]. A marked reduction of the interlamellar elastin fibres was observed in patients with aortic dissection [153] which could explain this difference in values as Sommer et al. [204] performed their experiment on diseased tissues.
The limited influence of the mode II critical fracture energy is similar to the findings concerning mode I fracture energy in Chapter II and Ferrara et al. [60] who found no influence of the mode I fracture energy on the response of the finite element model.

In clinic, most of the time the intimal tear involves half the aortic circumference and propagates in the longitudinal direction, along the aorta [187]. This is intriguing because the pressurisation favours the circumferential stress. Thus the dissection should propagate in the circumferential direction and not in the longitudinal direction. In addition the mode I and II fracture properties are higher in the longitudinal direction than in the circumferential direction [203, 204]. These differences between the experimental tests and the *in vivo* condition may be due to the difference of morphology between the tensile test specimen and a complete aorta.

Haslach et al. [85] performed an inflation test on bovine aortic rings with a longitudinal notch. The crack propagated in the circumferential direction, between the lamellae, independently of the orientation of the notch. This result is similar to our experiment and model where the notched aortic wall delaminated easily in the circumferential direction when submitted to tension. Nevertheless, this is not representative of the majority of aortic dissection cases, in clinic 80% to 95% of the intimal tear are in the circumferential direction and delaminate in the longitudinal direction. This tear configuration was not tested by Haslach et al. [85]. In the present work, the notched longitudinal sample rupture entirely after a small delamination at the tip of the notch, contrarily to the notched circumferential sample which delaminated on a much larger area before rupture, as observed in Figure III.4 and Figure III.5. This phenomena is explained by the higher tensile strength of the aortic wall in the circumferential direction compare to the longitudinal direction [232, 246] and the lower resistance against shear stress of the interlamellar bonds in the circumferential direction. It demonstrates that the tensile and shear stresses induced by tension are not sufficient to propagate a tear in the longitudinal direction, which means that another mechanisms are involved during aortic dissection and propagate the tear along

the aorta as observed in clinic. These mechanisms may be the fluid pressure or the biaxial stress state which are present in physiological condition.

Some limitations to this study should be noted. The samples were immersed during 24 hours, which can affects the mechanical properties [209, 44, 162]. Moreover the media and adventitia were not separated to quantify the material properties and in the finite element model which can affect the values obtained though the identification.

Another limitation is the lack of consideration of the microstructure in the numerical modelling. The material was considered homogeneous which is not the case in reality. Bridging fibres could be observed around the crack site during the tensile tests on notched samples as evidenced in Pasta et al. [168]. In addition, the tensile test does not reproduce the biaxial in vivo stress state. Biaxial tests on notched samples could give interesting results as this test would be closer to physiological conditions.

III.1.5 Conclusion

In this study, *in situ* tensile tests on notched specimens were performed. The material and delamination failure properties of porcine aortic samples were quantified. The hyperelastic parameters were identified by fitting the analytical HGO model on the undammaged part of the experimental tensile curves in the circumferential and longitudinal directions. The mode II fracture properties were identified in the circumferential and longitudinal directions by calibrating a numerical model on the experimental data. The method used in this study provides a complete characterisation of the elastic and mode II delamination strength of the aorta. The small dissected area for the longitudinal sample compare to the circumferential specimen demonstrates that the tension of the aortic wall is not a predominant factor during the longitudinal propagation of an aortic dissection but could be during the circumferential propagation of radial-longitudinal tear. These data allow a better understanding of aortic dissection mechanisms and could be used in complex models of this disease.

Highlights

- Tensile test on notched samples were performed under X-ray images to investigate the interlamellar failure properties.
- The circumferential sample delaminated on much larger area before total failure than the longitudinal sample.
- A numerical model with cohesive interface was developped to simulate the experiment.
- The material properties and the mode II were identified by inverse methods.
- The shear strength was higher in the longitudinal direction than in the circumferential direction in accordance to the literature.

Chapter IV

Simulation numérique de la dissection aortique - *Numerical simulation of aortic dissection*

This chapter describes a numerical investigation of the initiation and propagation of a dissection inside an aorta with the extended finite element method. In this study, a finite element model is developped as close as possible to the in vivo state. The aim is to investigate the influence of the primary factors contributing to aortic dissection by quantifying their impact on the critical pressure and the direction of propagation with a design of experiment. This study was accepted in the IEEE Transactions on Biomedical Engineering (January 2021).

Contents of the chapter

Résumé du chapitre

Les Chapitres II et III ont étudié la rupture en mode I et II de la paroi aortique. Malgré l'intérêt de ces études, elles ont montré leurs limites en raison de leur éloignement des conditions physiologiques. Ainsi, un modèle plus proche des conditions *in vivo* est nécessaire pour comprendre les mécanismes derrière la dissection aortique.

Cette maladie est initiée par une fissure qui se propage le long de la paroi aortique. La taille de telles fissures peut varier de quelques dizaines de millimètres à plusieurs centimètres. Dans la littérature, plusieurs articles ont étudié la propagation de fissures dans la paroi artérielle grâce à des essais mécaniques comme les tests de traction radiale, de peeling, de perfusion de liquide, ou encore de gonflement. La majorité des ces études analyse la résistance de l'aorte face à la propagation de fissure mais peu de ces travaux ont questionné l'influence de l'orientation de la fissure initiale ainsi que les éléments favorisant l'initiation de sa propagation et de son évolution en dissection aortique. Ainsi, dans ce chapitre, un modèle est créé afin de comparer différentes orientations de fissure et de quantifier l'influence de plusieurs paramètres géométriques et mécaniques sur leur propagation et leur évolution en dissection aortique.

Le modèle est composé d'un cylindre parfait divisé entre : la media, qui représente 80% de l'épaisseur de la paroi aortique, et l'adventice, qui en représente 20%. La géométrie a été modélisée avec un angle d'ouverture afin de tenir compte du stress résiduel présent physiologiquement dans la paroi aortique. La fissure initiale a été modélisée par une surface (les éléments adjacents sont déconnectés) afin d'initier la dissection. Trois configurations de fissures différentes ont été créées. Le comportement de l'aorte est défini par le modèle hyperélastique de Gasser-Holzapfel-Ogden divisé entre une partie isotrope représentant la matrice extra-cellulaire et les fibres d'élastine, et une partie anisotrope représentant deux familles de fibres de collagène. Le comportement en rupture de l'aorte est anisotrope. Ainsi, quatre critères de rupture basés sur la théorie de Hashin ont été développés afin de faire varier la résistance du matériau selon la direction. Ces critères de rupture ont été implantés dans Abaqus grâce à une subroutine FORTRAN (UDMGINI) et à la méthode des éléments finis étendues (XFEM). Les valeurs de résistance à la traction et au cisaillement de la paroi ont été définies à partir de la littérature afin d'être au plus proche de la réalité clinique.

Les différentes étapes de la simulation numérique étaient :

- fermer l'angle d'ouverture afin de prendre en compte la contrainte résiduelle présente dans l'aorte.
- appliquer un allongement axial à l'aorte afin de prendre en compte le pré-allongement de l'aorte.
- appliquer la pression à l'intérieur de l'aorte jusqu'à propagation de la fissure.

Un plan d'expériences numériques pour chaque cas de fissure a été mis au point afin d'analyser l'influence de 7 paramètres sur la pression critique et la direction de propagation de la fissure initiale. Les paramètres étaient :

- les facteurs géométriques de la fissure,
- la position de la fissure dans la direction radiale,
- la résistance à la traction de la paroi,
- la résistance au cisaillement de la paroi,

- l'angle d'ouverture,
- l'allongement axial initial de l'aorte.

Les résultats ont montré que les pressions critiques (moyennes entre 206 et 251 mmHg) obtenues sont conformes aux mesures de la littérature. La résistance à la traction uniaxiale s'est avérée être le facteur le plus influent, ce qui suggère qu'une dégénérescence médiale est nécessaire pour atteindre une pression critique physiologique et pour propager une déchirure lors d'une dissection aortique. La géométrie de la fissure et sa localisation à l'intérieur de la paroi aortique jouent également un rôle important non seulement dans la pression nécessaire pour déclencher la propagation de la déchirure, mais aussi dans l'évolution de la déchirure vers une rupture aortique ou une dissection aortique. Une fissure initiale plus large et plus profonde augmente le risque de dissection aortique. Bien que ces résultats doivent être validés expérimentalement, ils permettent de mieux comprendre les phénomènes à l'origine de la dissection aortique et peuvent aider au diagnostic et au traitement de cette maladie.

IV.1 A parametric study on factors influencing the onset and propagation of aortic dissection using the extended finite element method

Extracted from the paper "A parametric study on factors influencing the onset and propagation of aortic dissection using the extended finite element method." accepted in IEEE Transactions on Biomedical Engineering (January 2021). The text is shortened herein to avoid repetitions.

Abstract

Aortic dissection is a life-threatening event which starts most of the time with an intimal tear propagating along the aortic wall, while blood enters the medial layer and delaminates the medial lamellar units. Studies investigating the mechanisms underlying the initiation sequence of aortic dissection are rare in the literature, the majority of studies being focused on the propagation event. Numerical models can provide a deeper understanding of the phenomena involved during the initiation and the propagation of the initial tear, and how geometrical and mechanical parameters affect this event. In the present paper, we investigated the primary factors contributing to aortic dissection. A two-layer arterial model with an initial tear was developed, representing three different possible configurations depending on the initial direction of the tear. Anisotropic damage initiation criteria were developed based on uniaxial and shear experiments from the literature to predict the onset and the direction of crack propagation. We used the XFEM-based cohesive segment method to model the initiation and the early propagation of the tear along the aorta. A design of experiment was used to quantify the influence of 7 parameters reflecting crack geometry and mechanics of the wall on the critical pressure triggering the dissection and the directions of propagation of the tear. The results showed that the obtained critical pressures (mean range from 206 to 251 mmHg) are in line with measurement from the literature. The medial tensile strength was found to be the most influential factor, suggesting that a medial degeneration is needed to reach a physiological critical pressure and to propagate a tear in an aortic dissection. The geometry of the tear and its location inside the aortic wall were also found to have an important role not only in the triggering of tear propagation, but also in the evolution of the tear into either aortic rupture or aortic dissection. A larger and deeper initial tear increases the risk of aortic dissection. The numerical model was able to reproduce the behaviour of the aorta during the initiation and propagation of an aortic dissection. In addition to confirm multiple results from the literature, different types of tears were compared and the influence of several geometrical and mechanical parameters on the critical pressure and direction of propagation was evaluated with a parametric study for each tear configuration. Although these results should be experimentally validated, they allow a better understanding of the phenomena behind aortic dissection and can help in improving the diagnosis and treatment of this disease.

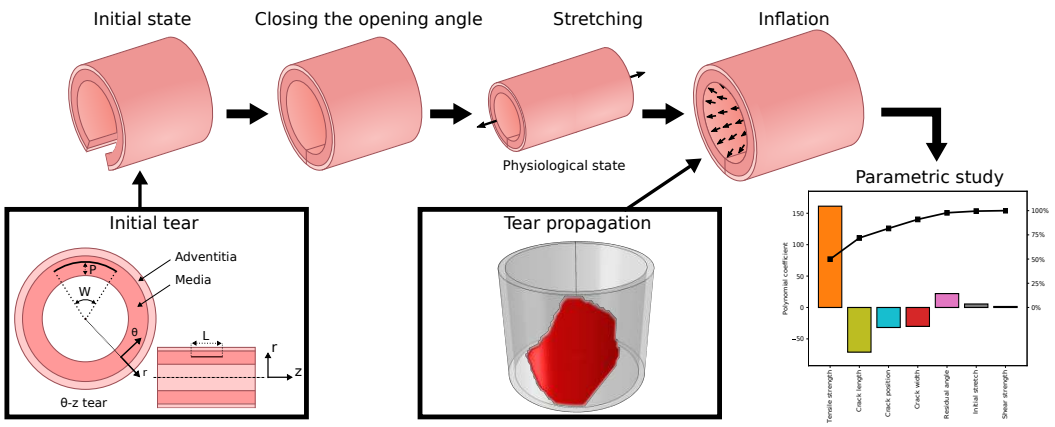

IV.1.1 Introduction

Chapters II and III investigated the mode I and II fracture in the aortic wall. Despite the interest of these studies, a limitation of these studies is their distance from physiological conditions. A model closer to the *in vivo* conditions would be a step forward in understanding the mechanisms behind aortic dissection.

A tear occurs when the biomechanical stress exceeds the local resistance of the wall [188]. The pressure and wall shear stress of the fluid contribute to the internal stresses in the wall. Using comtational fluid dynamics, Chi et al. [32] have shown that the location of intimal tear corresponds to the area of maximum wall shear stress. Therefore, the formation of the tear appears to be a fatigue process. However, according to Carson et al. [28], the peak pressure to initiate the propagation of the dissection is a non-physiological blood pressure suggesting that abnormal blood pressure or medial degeneration compromising aortic integrity is necessary to create an aortic dissection [220, 155, 54]. The tear size can vary from less than 1 cm [178, 152] to several centimeters [211]. In some cases, the intimal tear does not propagate or propagates to a limited extend, this phenomenon is called subtle-discrete aortic dissection [55]. However, it should be noted that such reports of tear size and geometry refer to already extended tears (hence advanced dissection) that can be observed during surgery or imaging examinations.

The propagation of the initial tear was investigated in multiple experimental studies. For instance, liquid infusion test was used to investigate the influence of different parameters on tear propagation [220]. Tam et al. [213] showed that the pressure required to propagate dissection is negatively correlated with the depth of the tear. Using tension-inflation in an *ex-vivo* model of aortic dissection associated with a pulsatile pump mimicking blood flow, [169] found that geometrical factors of the entrance tear have a significant effect on the propagation of aortic dissection. Recently, shear stress has been identified as a possible determining factor in the initiation of aortic dissection [85, 85].

The propagation of aortic dissection was modelled by multiple studies in real or idealized geometry using different approaches, for instance crack phase-field modelling [81], constrained mixture theory [149], or extended finite element method (XFEM) [239, 237]. The XFEM has been used in the present work because it allows the simulation of crack initiation and propagation along an arbitrary path without the requirement of remeshing. For more information on mechanical testing and modelling literature on aortic dissection, see Brunet et al. [26].

In the absence of external load, the aortic wall is not stress-free. If an unloaded aorta is cut

radially and transected longitudinally, an opening angle and retraction, respectively, can be observed [27]. Under physiological conditions, the residual stress present in the aorta reduces the transmural stress gradient and contributes to the homeostatic state [96, 121]. In a numerical study [239], it was shown that residual stress protects the aorta from tear propagation; however, only the circumferential residual stress, not the axial pre-stretch, was considered in this study.

In most of the studies presented above, the orientation of the initial tear was assumed to be either in the tangential plane [239], longitudinal-radial plane [85], or transverse plane [81]. Nevertheless, to the authors' knowledge, there was no investigation in the literature comparing the different orientations of the tears and quantifying their effect on initiation and propagation. For this purpose, a numerical study is proposed involving a computational model of a tension-inflation test on an aortic segment with idealized geometry. Three different cases of tear orientation present in the medial layer and their propagation were simulated using XFEM. A numerical design of experiment (DoE) was used to perform a sensitivity analysis on the influence of different key parameters on the pressure required to propagate the tear and the direction of tear propagation. The objective was to determine the most influential factors in the propagation of an aortic dissection in order to better assess the patient at risk.

IV.1.2 Materials and methods

This section presents the finite element model of the aortic segment with an initial tear, and the DoE approach used in this study.

IV.1.2.1 Geometry

The geometry was composed of a two-layer cylinder with a length of 20 mm and a luminal radius of $r_i = 10$ mm in the *in vivo* state (Figure IV.2) [121]. The initial diameter and initial layer thicknesses of the model were calculated in each simulation to obtain the same diameter ($r_i = 10$) and thicknesses ($T_m = 1.44$ and $T_a = 0.36$) in the zero-pressure, initially stressed state. The intima was not considered in this model because it was assumed that it does not contribute significantly to the aortic wall mechanics. The medial layer and the adventitial layer were defined as 80% and 20% of the total aortic wall thickness, respectively [103]. The medial and adventitial thicknesses are listed in Table IV.1.

As demonstrated by Holzapfel et al. [96], the aorta is subjected to a complex three-dimensional residual stress state under *in vivo* conditions. To account for the physiologically present residual stress in the aortic wall, the geometry was modelled with an opening angle α. Although the opening angles of the intima, media, and adventitia are different, a unique opening angle was taken for the entire model for the sake of simplicity. An axial pre-stretch was also applied to the model during the simulation to account for the residual longitudinal stretch present under physiological conditions (see Section IV.1.2.4).

The aorta was meshed with 58500 C3D8H elements in Abaqus based on a mesh sensitivity analysis previously performed on the critical pressure to ensure that the influence of the mesh size on the results was negligible (Appendix B.1). Hybrid elements were used to ensure incompressibility and avoid volumetric locking. A tear was modelled as a surface in the aortic media - disconnecting adjacent elements - to initiate aortic dissection. Three different types of tear, presented in Figure IV.1, were modelled. The tears were named

according to the plane in which they were located: a θ-z tear is a tear in the circumferential-longitudinal plane, a r-z tear is a tear in the radial-longitudinal plane, and a r-θ tear is a tear in the radial-circumferential plane. These different cases correspond to the different initial tear geometries seen in the literature [217, 213].

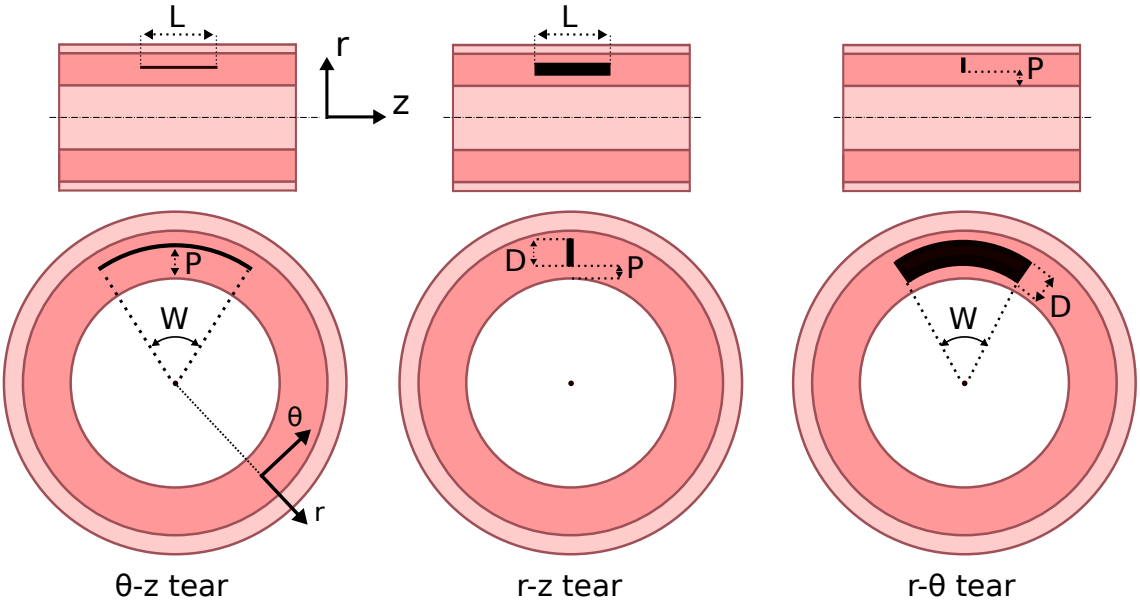

Figure IV.1 – The three tear configurations with the parameters defining each tear: P is the position of the tear in the radial direction, W is the width of the tear, L is the length of the tear, and D is the depth of the tear. The tears are named according to the plane in which they were located.

	Thickness (mm)	μ (MPa)	k_1 (MPa)	k_2 (-)	γ (°)	κ (-)
Media	1.44	0.032	0.09	19.0	41.6	0.12
Adventitia	0.36	0.027	0.37	15.2	54.8	0.25

Table IV.1 – Thickness and elastic constitutive parameters of the numerical model of the aortic wall layers, obtained from the literature [103, 241]

IV.1.2.2 Elastic constitutive model

The aortic wall was modelled with the Gasser-Holzapfel-Ogden (GHO) hyperelastic model. The material was assumed fully incompressible. A multiplicative split of the strain–energy function into a volumetric and a deviatoric part was performed to ensure incompressibility. For further information on the theory behind this model see Holzapfel [93]. The isochoric strain energy function is composed of an isotropic neo-Hookean term $\bar{\psi}_m$, representing the ground matrix and the elastin fibres, and anisotropic terms $\bar{\psi}_f$, accounting for two families of collagen fibres symmetrically arranged [95]. The model was extended to account for the dispersion of collagen fibres [71]. The isochoric strain energy function is defined as :

$$\bar{\psi} = \bar{\psi}_m + \bar{\psi}_f, \tag{IV.1}$$

with the isotropic term defined as

$$\bar{\psi}_m = \frac{\mu}{2}(\bar{I}_1 - 3), \tag{IV.2}$$

where μ denotes the neo-Hookean parameter and $\bar{I}_1 = tr(\bar{C})$ is the first invariant of the deviatoric right Cauchy-Green tensor $\bar{C}$ (with $\bar{C} = \bar{F}^T\bar{F}$ and $F = J^{\frac{1}{3}}\bar{F}$). The anisotropic terms are defined as

$$\bar{\psi}_{f,i} = \frac{k_1}{2k_2}[e^{(k_2(\bar{I}_i^* - 1)^2)} - 1], \tag{IV.3}$$

with

$$\bar{I}_i^* = \kappa\bar{I}_1 + (1 - 3\kappa)\bar{I}_i, \quad i = 4, 6, \tag{IV.4}$$

where $i = 4$ and $i = 6$ correspond to the two families of fibres. $\bar{I}_4 = \bar{C} : M \otimes M$ and $\bar{I}_6 = \bar{C} : M' \otimes M'$ are the two modified pseudo-invariants and are equal to the square of the stretch of the fibres initially oriented along M and M'. These vectors are symmetric with respect to the longitudinal direction of the aorta, their direction is defined with respect to the circumferential direction with an angle γ (Figure IV.2). γ and κ are, respectively, the mean orientation of the fibres and the parameter accounting for their dispersion. k_1, k_2 are material parameters determined by mechanical testing. The constitutive parameters were taken from [241]. They are reported in Table IV.1.

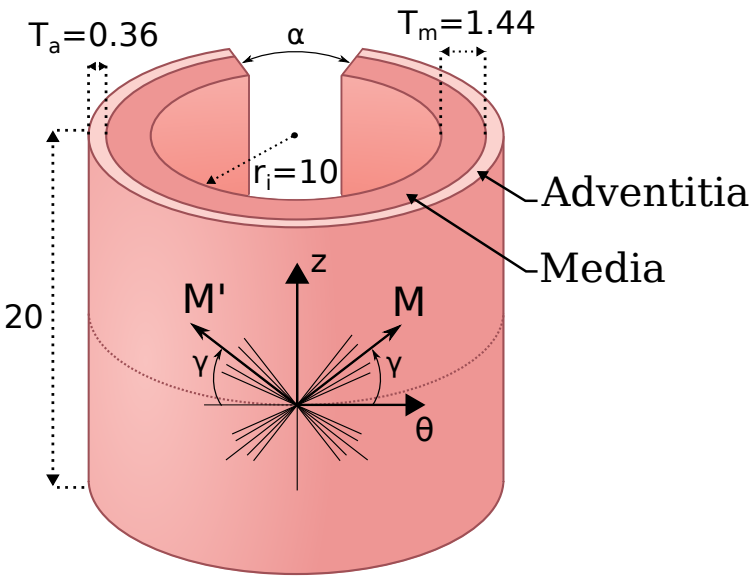

FIGURE IV.2 – Geometry of the aortic segment used in the numerical model. All dimensions are in millimeters.

IV.1.2.3 Failure criteria

The mechanical behaviour of the aorta is anisotropic: this is the case not only with the elastic constitutive behaviour but also with the tensile and shear strengths, which vary according to the direction. Hence, four failure criteria were created with an associated direction of crack propagation (Eq IV.6, IV.7, IV.8, IV.9).
The Cauchy stress tensor was defined by

$$\sigma = \begin{bmatrix} \sigma_{rr} & \sigma_{r\theta} & \sigma_{rz} \\ \sigma_{r\theta} & \sigma_{\theta\theta} & \sigma_{\theta z} \\ \sigma_{rz} & \sigma_{\theta z} & \sigma_{zz} \end{bmatrix}, \tag{IV.5}$$

and the failure criteria were

$$\text{Radial failure criterion : } \sqrt{(\frac{\sigma_{rr}}{T_r})^2 + (\frac{\sigma_{r\theta}}{S_{r\theta}})^2 + (\frac{\sigma_{rz}}{S_{rz}})^2} = 1, \tag{IV.6}$$

$$\text{Circumferential failure criterion : } \sqrt{(\frac{\sigma_{\theta\theta}}{T_\theta})^2 + (\frac{\sigma_{r\theta}}{S_{r\theta}})^2 + (\frac{\sigma_{\theta z}}{S_{\theta z}})^2} = 1, \tag{IV.7}$$

$$\text{Longitudinal failure criterion : } \sqrt{(\frac{\sigma_{zz}}{T_z})^2 + (\frac{\sigma_{rz}}{S_{rz}})^2 + (\frac{\sigma_{\theta z}}{S_{\theta z}})^2} = 1, \tag{IV.8}$$

$$\text{Off-axis failure criterion : } \frac{\sigma_p}{\sqrt{(T_r.\overrightarrow{e_1}.\overrightarrow{r})^2 + (T_\theta.\overrightarrow{e_\theta}.\overrightarrow{n})^2 + (T_z.\overrightarrow{e_z}.\overrightarrow{n})^2}} = 1. \tag{IV.9}$$

The use of these criteria, based upon Hashin failure theory [83], was inspired from a previous use in Feerick et al. [59]. Damage initiates when one of the criteria reaches a value of one. Failure in the cylindrical directions was defined by: the radial failure criterion (Eq. IV.6), the circumferential failure criterion (Eq. IV.7), and the longitudinal failure criterion (Eq. IV.8). The parameters T_i and S_{ij} $(i, j \in r, \theta, z)$ define the tensile and shear strengths, respectively. The last failure criterion (Eq. IV.9) defines the off-axis directions. In this criterion, the principal stress σ_p is divided by a relative contribution of the different tensile strengths. $\overrightarrow{n}$ is the normal vector to the crack surface and $\overrightarrow{e_i}$ $(i, j \in r, \theta, z)$ are the local cylindrical directions at the point. In all criteria, the crack propagates in the plane normal to the direction assigned to the criterion.

The failure criteria were implemented in Abaqus using the FORTRAN user subroutine UDMGINI in conjunction with XFEM to model crack propagation. With this method, the propagation of the tear is computed by incorporating additional enrichment functions to the continuous displacement field to capture the singularity around the crack tip (asymptotic crack tip functions) and the jump in displacement across the crack surfaces (Heaviside jump functions) [21]. The XFEM method was chosen in preference to the cohesive zone method to simulate crack propagation because the location of the crack path is not known *a priori*. A hard contact was defined between the new crack surfaces to avoid intersection of the elements after crack opening. The propagation of the crack was governed by a linear traction-separation law. A scalar damage variable, d, was defined for each failure criterion. This damage parameter is initially set to zero ($d = 0$). Once one of the failure criteria was reached and damage was initiated, the cohesive stiffness was degraded upon further loading until complete freedom of the nodes ($d = 1$). The total energy dissipated during the separation of the surfaces is G_c.

The tensile strengths of the media in the longitudinal and circumferential directions were defined according to Angouras et al. [6]. In this study, they performed tensile tests in different areas of ascending thoracic aortas. The tensile strengths of the right lateral region were used in our study because this is the most common location of aortic dissection [187]. The radial tensile strength and the shear strength of the media in the different directions were taken from Sommer et al. [204] who performed uniaxial tests and triaxial shear tests on aneurysmatic and dissected human thoracic aortas. The standard deviations were used to define the domains of the strength variables in the designs of experiment (Section IV.1.2.5). These values are reported in Table IV.2. The tensile and shear strengths of the adventitia were considered infinite because aortic dissection propagates only in the medial layer. The fracture energy per reference area G_c was assumed to be 5.0 mJ/cm^2 [203].

Type	Parameters	Medial failure stress (kPa)	Reference
Tensile	T_r	131 ± 56	[204]
	T_θ	1061 ± 128	[6]
	T_z	551 ± 98	[6]
Shear	$S_{r\theta}$	97 ± 6	[204]
	S_{rz}	120 ± 6	[204]
	$S_{\theta z}$	918 ± 313	[204]

TABLE IV.2 – Failure parameters of the numerical model (mean ± SD).

IV.1.2.4 Finite element simulation

The first step of the simulation consisted in closing the opening angle to obtain a residually stressed model (Figure IV.3b). Then, the aortic model was stretched axially to account for the axial stretch present *in vivo* in the aorta (Figure IV.3c) [104, 10]. At this point in the simulation, the unloaded *in vivo* configuration was reached. The initial aortic diameter was recalculated for each simulation to obtain a similar diameter of 20 mm in the *in vivo* configuration. Finally, the aorta was inflated until the crack propagated (Figure IV.3d). Pressure was also applied to the crack surfaces during inflation. The wall shear stress was neglected in the loading conditions of the model due to its relatively low magnitude compared to the pressure [17]. Concerning the boundary conditions, once the opening angle was closed and the model pre-stretched, the proximal and the distal faces were axially blocked to prevent the aorta from returning to its original position. Radial displacement remained free.

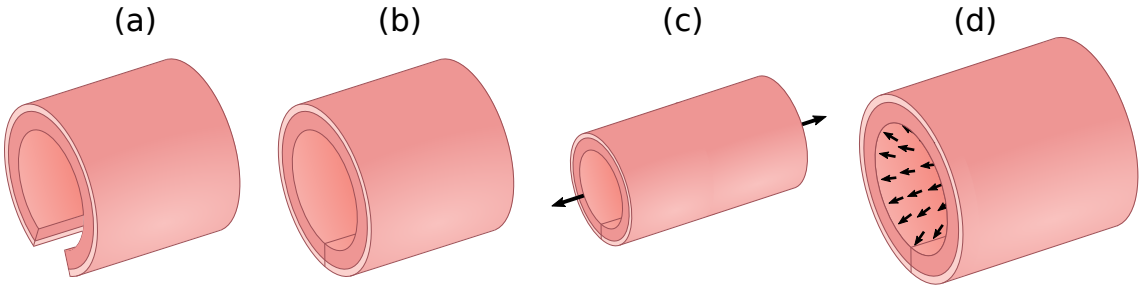

FIGURE IV.3 – Sketch of the different steps of the simulation. (a) The two-layer model in the initial state. (b) The residual angle is closed. (c) The axial stretch is applied; the physiological state is reached. (d) The pressure is applied inside the aorta until propagation of the crack.

IV.1.2.5 Design of experiment

The influence of different factors on the onset and propagation of aortic dissection was investigated for all three tear configurations. The hyperelastic parameters were kept constant. Three full factorial experimental designs with interactions were performed. The parameters studied were as follows:

- Crack geometrical factors (D the crack depth, L the crack length, W the crack width). Two of the three parameters are studied for each tear configuration according to the plane in which the initial tear is located. They are presented in Figure IV.1.
- Crack position in the radial direction, defined as P (Figure IV.1).

	θ-z tear		r-z tear		r-θ tear	
Parameters	Min	Max	Min	Max	Min	Max
Crack depth (mm)	-		0.2	0.72	0.2	0.72
Crack length (mm)	0.5	2.5	0.5	2.5	-	
Crack width (°)	10	60	-		10	60
Crack position (mm)	0.36	1.1	0	0.7	0	0.7
Tensile strength (kPa)	$T - 2$ SD	$T + 2$ SD	$T - 2$ SD	$T + 2$ SD	$T - 2$ SD	$T + 2$ SD
Shear strength (kPa)	$S - 2$ SD	$S + 2$ SD	$S - 2$ SD	$S + 2$ SD	$S - 2$ SD	$S + 2$ SD
Opening angle (°)	0	140	0	140	0	140
Initial stretch (-)	1.0	1.2	1.0	1.2	1.0	1.2

Table IV.3 – Ranges of the parameters of the numerical model used in the sensitivity study

- Tensile strength. The parameter range was defined by varying the tensile strengths T_i by ± 2 SD$_i$ with $i = r, \theta, z$ and SD$_i$ the standard deviation of the stress strength value associated in the i direction. The values of the tensile strengths and the associated deviations were chosen according to the literature (Table IV.2).
- Shear strength. The parameter range was defined by varying the shear strengths S_i by ± 2 SD$_i$ with $i = r, \theta, z$ and SD$_i$ the standard deviation of the stress strength value associated in the i direction. The values of the shear strengths and the associated deviations were chosen according to the literature (Table IV.2).
- The opening angle α. The maximum value was chosen according to Saini et al. [194].
- λ, the initial stretch applied to the aorta to account for the physiological stretch. The maximum value was chosen according to Humphrey et al. [103].

Their domains are presented in Table IV.3. The value of two standard deviations was chosen as it includes 95% of the strength values. The tensile and shear strengths were varied as a whole and not per directions to keep the computational time reasonable as a simulation took around one hour to complete on a computer cluster.

The influence of 7 factors were assessed, thus, $2^7 = 128$ simulations were run for each tear orientation. One simulation was added to account for the middle points for each experimental design. The outputs of the simulation were:

- The critical pressure at which the tear started to propagate.
- The plane of propagation of the crack, defined by its normalized normal vector with r, θ and z components (e.g. a $[0, 1, 0]$ vector means a propagation in the plane normal to the θ direction). Each component of the vector was taken as an output.

The 4 outputs were computed as a linear combination of the different parameters by fitting a polynomial with the ordinary least squares method for each output. The polynomials were defined by

$$Y = \beta_0 + \sum_{k=1}^{N} \beta_k x_k + \sum_{i,j=1,j>i}^{N} \beta_{ij} x_i x_j \ + \epsilon \qquad i \neq j, \tag{IV.10}$$

where Y is the output, N = 7 is the number of parameters, x is the parameter value in its coded space (between -1 and 1), β reflects its influence (except for β_0), and ϵ is the estimated error.

Statistical analysis

A statistical analysis was used to assessed the quality of the fitted response. After ensuring that the residuals followed a normal distribution, an analysis of variance (ANOVA) was performed. The coefficients of determination r^2 were calculated and an F-test was used to evaluate the overall validity of each design of experiment. Finally, the significance of each parameter on the response was assessed using a Student's t-test.

In the DoE, one of the main assumptions is that the response is linear, which may not be the case with a complex model like the one presented herein. The curvature of the response was tested in each tear configuration using centre points by adding a $\beta_c x_c$ term to the Equation IV.10 with $x_c = 0$ if a center point is tested and $x_c = 1$ otherwise. Finally, the hypothesis $\beta_c \neq 0$ was tested to investigate the presence of curvature.

IV.1.3 Results

The simulations of tear propagation were performed and three illustrative results of crack propagation are presented, along with a graph representing the crack surface as a function of the pressure in Figure IV.4. The crack initiation was caused by stress concentration at the tear site. In the θ-z tear configuration in Figure IV.4, the crack appears to propagate in the same direction as one of the fibre family as seen in Gültekin et al. [81]. In the r-z tear configuration example, the propagation mainly follows the circumferential direction whereas in the r-θ tear configuration the propagation principally follows the longitudinal direction. The graphs in Figure IV.4c show that the crack does not propagate linearly but by jumps, before diverging. This is explained by the fact that the model is pressure-controlled, which leads to an instability. As observed experimentally by Roach et al. [185] in a volume-driven study, once the critical pressure is reached, the crack begins to propagate, however, the pressure decreases or remains constant during the propagation.

IV.1.3.1 Design of experiment

Critical pressure

The mean critical pressures were 206 ± 203 mmHg, 251 ± 152 mmHg, and 239 ± 153 mmHg for the θ-z, r-z, and r-θ tear configurations, respectively. The first-order polynomial coefficients were fitted and are reported in Figure IV.5 along with the corresponding Pareto curves. The factor interactions are presented in Appendix B.2. The higher the absolute value of the coefficient, the greater the influence of the corresponding parameter on the critical pressure. The F-test probability was inferior to 0.001 for all tear configurations. The r^2 is a measure of how well a model reproduces the observed results. The r^2 were 0.90 for the θ-z tear configuration, 0.95 for the r-z tear configuration, and 0.93 for the r-θ tear configuration. Tensile strength is by far the most influential parameter as it accounts for about 50% of the impact of the parameters on the model response in all tear configurations. Depending on the plane where the initial tear is located, the influential factors differ. The initial stretch is mostly influential in the r-z and r-θ tear cases. The effect of residual stress and shear strength appear to be limited in all three cases as they accounts for less than 10% of the total response.

The curvatures (non-linearities) of the responses were evaluated using centre points and stands in a low range ($p > 0.1$), not compromising the validity of the model. Furthermore, it should be emphasized that the main objective of the study was not to build a response

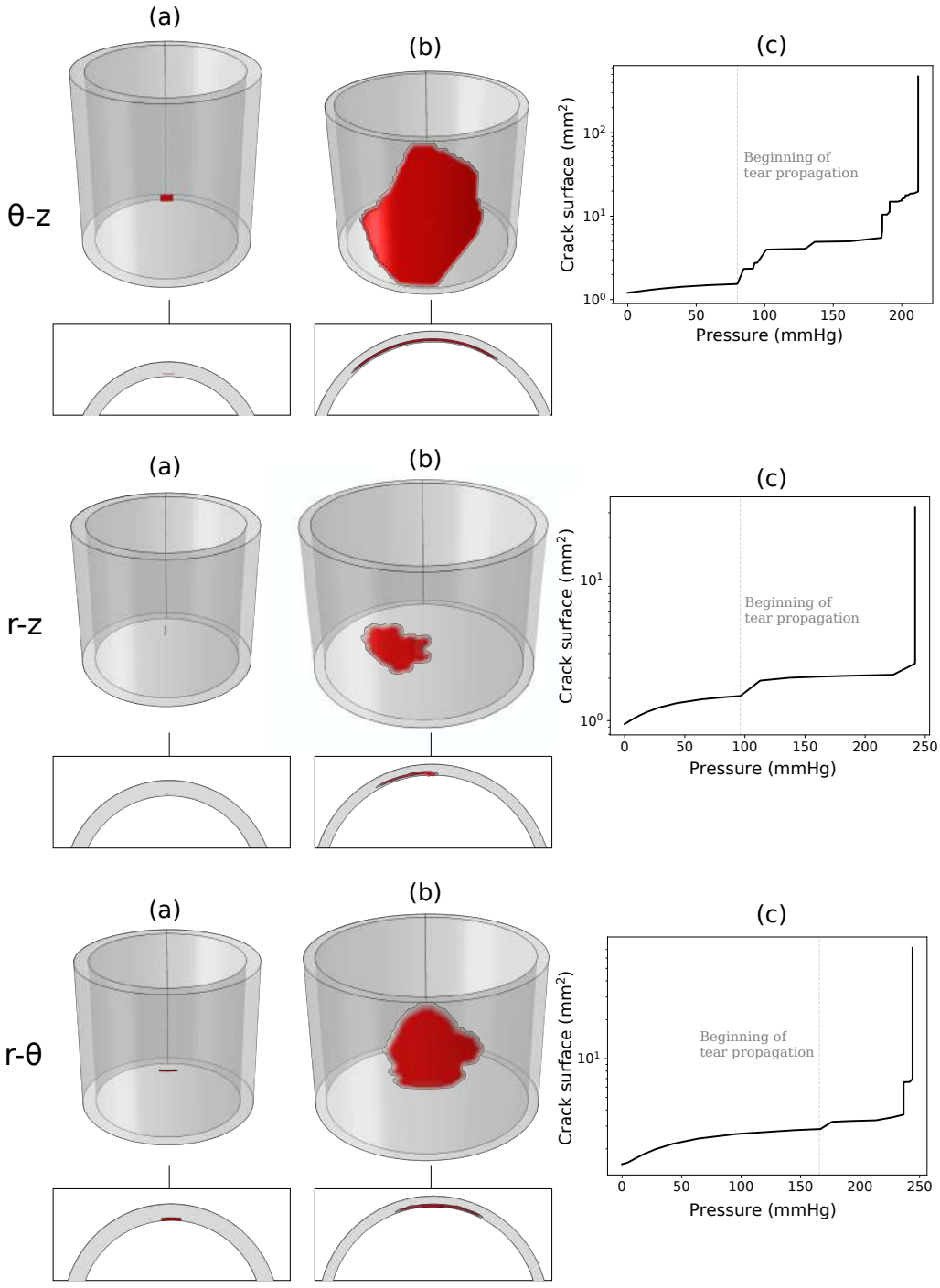

Figure IV.4 – The evolution of a tear propagation was presented for each tear configuration. A 3-D view and a cross-section view of the aortic wall are presented: (a) in the residually stressed state and (b) after crack propagation. Isosurfaces are used to visualize the crack propagation with $d > 0.5$. (c) A graph representing the crack surface as a function of the pressure is also presented. The y axis is in logarithmic scale.

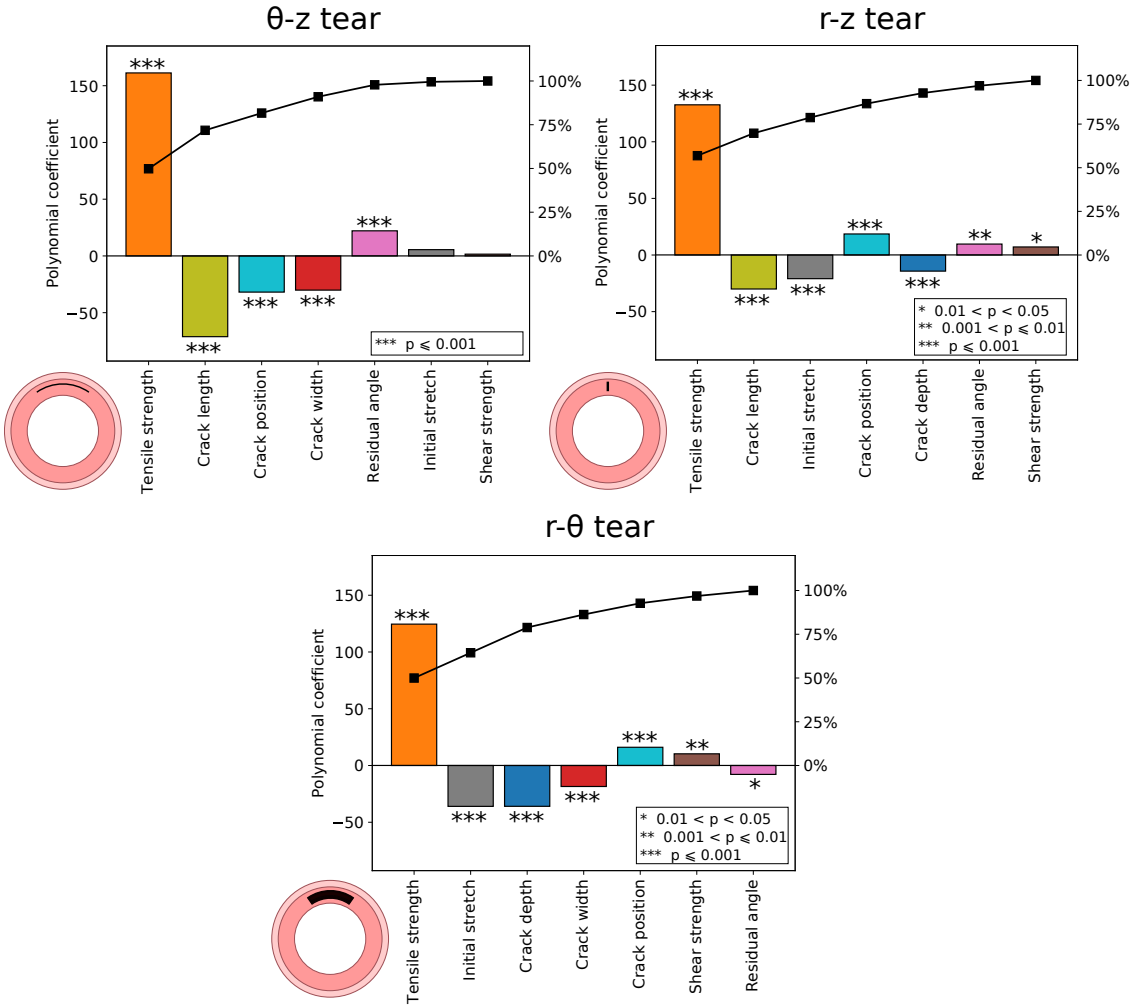

FIGURE IV.5 – First-order polynomial coefficients in each tear configuration with the critical pressure as output. The factors are presented in decreasing order in terms of absolute values. For each graph, the Pareto curve is shown in black with the scale on right axis, it represents the cumulative percentage of the parameter influences. The letter p stands for significance.

surface of the FE model, but to assess the overall influence and to find the most significant factors in the propagation of a tear.

Direction of propagation

Only height simulations propagated normal to an off-axis direction, and in all cases the failure directions were close to one of the cylindrical directions. Thus, the off-axis directions were set to the nearest cylindrical direction. The distributions of the propagation planes are reported in Figure IV.6 for each tear configuration. In the θ-z tear configuration, 80% of the simulations propagated in the θ-z plane, 6% in the r-z plane, and 14% in the r-θ plane. In the r-z tear configuration, 50% of the simulations propagated in the θ-z plane, 38% in the r-z plane, and 12% in the r-θ plane. In the r-θ tear configuration 45% of the simulations propagated in the θ-z plane, 16% in the r-z plane, and 39% in the r-θ plane. The first-order polynomial coefficients for each direction of propagation are reported in Figure IV.7 along with the corresponding Pareto curves, for all three tear cases. The factor interactions are presented in Appendix B.3. For a defined tear configuration, the higher the absolute value of the coefficient, the higher the influence of the corresponding

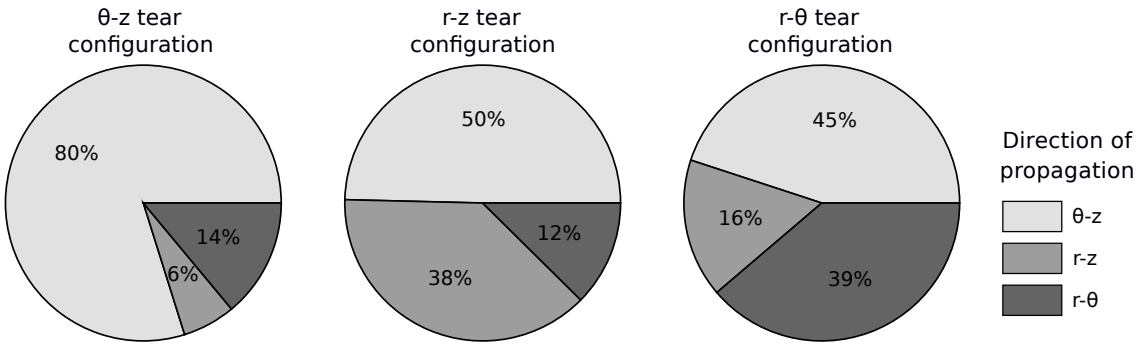

Figure IV.6 – Distribution of the planes of tear propagation for each tear configuration.

parameter on crack propagation in the plane presented. The F-test probability was inferior to 0.001 for all tear configurations. The increase in tensile strength decreases the risk of crack propagation in the θ-z plane in all three tear configurations. The position of the tear has an influence of about 30% on the probability of propagation of the tear in the θ-z plane only in the θ-z tear configuration. The initial stretch increases the probability of a tear propagating in the r-θ plane from 30% to 40%, for every tear configuration.

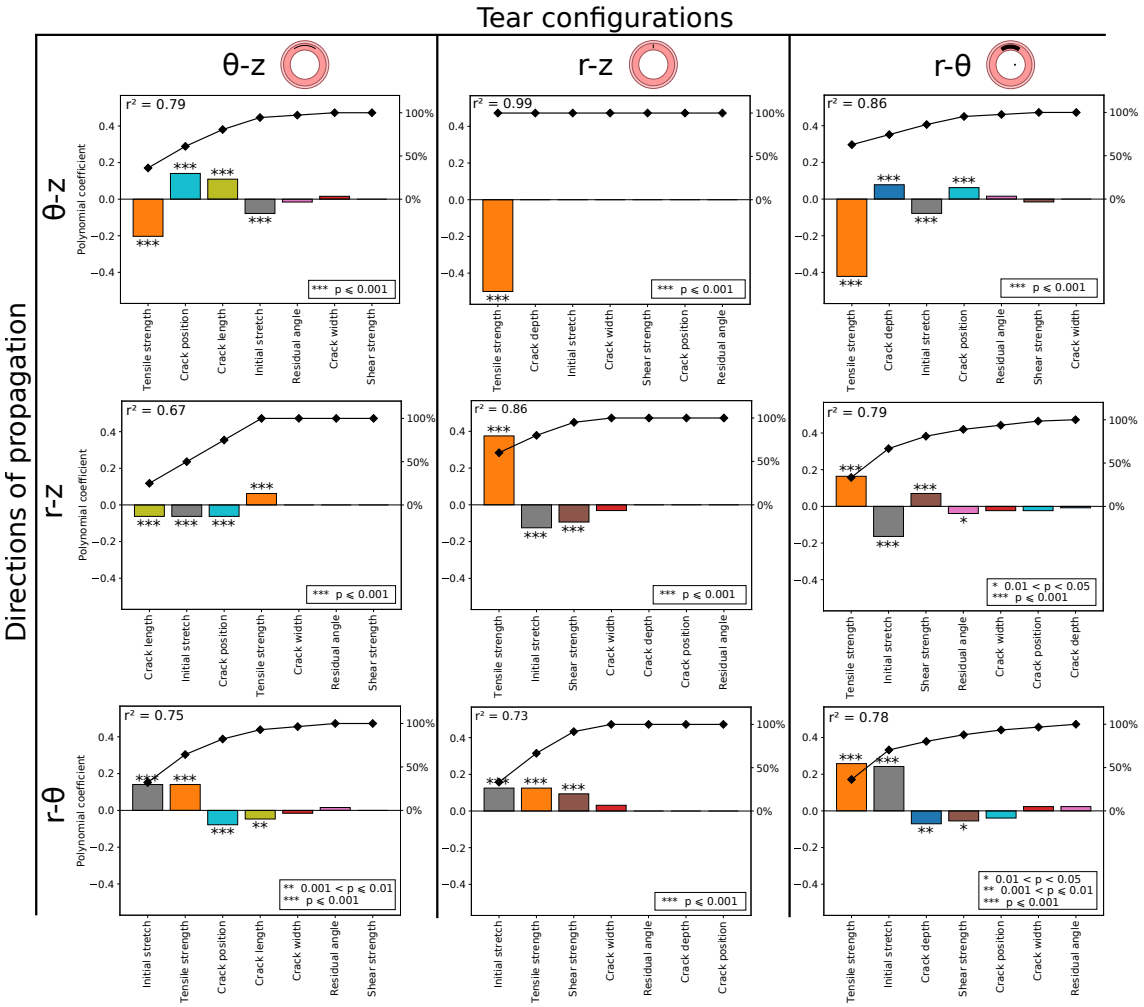

FIGURE IV.7 – First-order polynomial coefficients in each tear configuration with the different plane of propagation as outputs. The factors are presented in decreasing order in term of absolute value. For each graph, the Pareto curve is shown in black with the scale on right axis, it represents the cumulative percentage of the parameter influences. The r^2 are shown on the top left corner of each graph. F-test probability <0.001 for all tear configurations. The letter p stands for significance. An example of how to interpret these results: for an initial tear in the θ-z plane, increasing initial stretch increases the likelihood of a propagation in the r-θ (bottom left plot).

IV.1.4 Discussion

In the present work, a model for the initiation and propagation of aortic dissection was developed in three tear configurations based on the extended finite element method. The influence of multiple parameters of the model on the critical pressure and plane of propagation was assessed using designs of experiment.

Post-initiation numerical convergence was difficult to achieve due to the unstable nature of crack propagation in soft tissue, along with the nonlinearity of the material. The use of a commercial finite element code (Abaqus/Standard) limits the possibilities to address the convergence issue, e.g. XFEM cannot be used with explicit methods. Therefore, the investigation was limited to the early stages of aortic dissection: the initiation and beginning of tear propagation.

The creation of an intimal tear may be initiated by a fatigue process activated by blood pressure. Hypertension, one of the main risk factors for aortic dissection [156], amplifies this phenomenon. The fatigue process locally decreases the strength of the aortic wall, resulting in the creation of a tear and its propagation along the aorta. The propagation can be triggered by a sudden high blood pressure, e.g. when playing sports [87]. A summary of experimental and numerical data related to critical pressure is given in Table IV.4. It is generally accepted that pulsatile flow reduces the critical pressure compared to static pressure due to the dependence of critical pressure on $\frac{dP}{dt}_{max}$ [175, 12]. It should be noted that comparison of the studies presented in Table IV.4 is complex due to the differences in techniques and tissues. The mean critical pressures found in the present study are in the experimental range; however, they are lower than the literature values obtained with static pressure. This is certainly due to the fact that the strength values used for the fracture criteria were derived from mechanical tests on diseased aortic tissue. Hence, the results suggest that the critical pressures in a diseased aorta with a tear can be reached under physiological conditions, such as during weight lifting, for example [87, 136]. The most influential factor in reducing the critical pressure is the medial tensile strength, indicating that a medial degeneration is a possible cause for an aortic dissection to occur. The tensile strength also greatly influences the plane of propagation, an impaired media has a higher probability of propagating a tear along the aorta (in the θ-z plane) in all tear configurations (Figure IV.7). On the other hand, medial shear strength does not significantly affect critical pressure or plane of propagation. This result may be caused by structural effects at the scale of the medial lamellae, which were not taken into account due to the continuous nature of the FE model, as shear fracture (mode II) was identified as a key process in delamination [85, 25]. Haslach et al. [85] suggested that shear stress is strongly related to the lamellar structure of the media due to the relative slip between medial layers. In the present study, the media was modelled by a continuous material without taking into account the medial structure, which may also explain why our model failed to capture the influence of shear strength on tear initiation and propagation.

Experimental studies				
Tissue	Flow state	Experimental method	Critical pressure (mmHg)	Reference
Canine descending thoracic aorta	Static	Intramural liquid infusion	472 ± 76	Hirst and Johns [91]
Canine descending thoracic aorta	Pulsatile	Slit intramural bleb followed by inflation	185 (pulse pressure 160)	Prokop et al. [175]
Canine thoracic aorta	Pulsatile (no flow)	Intramural liquid infusion	370 ± 89	Baardwijk et al. [12]
Pig upper descending thoracic aorta	Static	Intramural liquid infusion	579 ± 11	Carson et al. [28]
Human aorta	Static	Intramural liquid infusion	596 ± 214	Tiessen et al. [220]
Canine thoracic aorta	Pulsatile	Aortic pocket followed by inflation	125 (pulse pressure 50)	Mitsui et al. [143]
Porcine lower thoracic aorta	Static	Intramural liquid infusion	854 ± 134	Roach et al. [185]
Porcine lower abdominal aorta	Static	Intramural liquid infusion	634 ± 204	Roach et al. [185]
Porcine thoracic aorta	Static	Slit intramural bleb followed by inflation	306 ± 72	Tam et al. [213]
Porcine thoracic aorta	Pulsatile	Contralateral incisions followed by inflation	152 ± 43	Dziodzio et al. [53]
Descending thoracic porcine aorta	Pulsatile	Creation of dissection on inverted aorta followed by inflation	180 (pulse pressure 200)	Peelukhana et al. [169]
Numerical studies				
Tissue	Flow state	Numerical method	Critical pressure (mmHg)	Reference
Human ascending thoracic aortic aneurysm	Static	Constrained mixture model	263	Mousavi et al. [149]
Human thoracic aorta	Static	Phase-field model	Between 120 and 600 mmHg	Gultekin et al. [81]
Human ascending aorta	**Static**	**XFEM - θ-z tear configuration**	**206 ± 203**	**Present study**
		XFEM - r-z tear configuration	**251 ± 152**	
		XFEM - r-θ tear configuration	**239 ± 153**	

TABLE IV.4 – Critical pressure of aortic tissue in experimental and numerical studies. The critical pressures are presented as mean ± SD.

In their experimental study, Tam et al. [213] observed that a lower pressure was required to propagate a dissection close to the adventitia, confirming that aortic dissection propagates preferentially in the outer third media [164]. The same result was found in our study for the θ-z tear configuration as a result of the stress concentration created by the discontinuity, confirming that non-communicating dissections preferentially occur closer to the adventitia. Furthermore, Figure IV.7 showed that the closer the θ-z tear is to the adventitia, the higher the probability of propagating along the aorta (in the θ-z plane). Concerning the r-z and r-θ tear configurations, the position parameter is not relevant as it seems unlikely that a tear appears in either plane without being connected to the lumen.

Geometrical factors are shown to significantly affect critical pressure as demonstrated in Peelukhana et al. [169]. This result was expected as a larger and deeper tear results in higher stress concentrations at the edge of the crack, diminishing the pressure required to initiate a dissection. The length of the crack appears to be the most influential factor among the geometrical factors in the θ-z and r-z tear configurations, whereas in the r-θ tear configuration, it is the depth of the crack. It was also shown that the initial axial stretch decreases the critical pressure in the r-z and r-θ tear configurations. This parameter increases the longitudinal stress in the wall and reduces the amount of stress required to reach the longitudinal tensile strength of the tissue. Increasing the axial stretch also increases the probability of tear propagation in the r-θ plane and, consequently, aortic rupture. On the other hand, the residual stress protects the aorta from tear propagation in the θ-z configuration as the critical pressure increases significantly with the residual stress. The same result was found numerically in Wang et al. [239]. The distribution of directions of propagation (Figure IV.6) shows that the θ-z plane is predominant in all tear configurations. This means that interlamellar propagation of the tear is the most likely scenario, especially in the θ-z configuration. This result, in agreement with most of clinical observations of extended dissections, can be explained by the low cohesion between the medial lamellae, represented in our model by the low radial cohesive strength [246].

Some limitations to this study should be noted. A stress-based fracture criterion such as the one used in this work is straightforward because it can be determined directly with values from the literature; nevertheless, other formulations might be better suited to heterogeneous anisotropic material such as energy-based criterion [80]. A numerical limitation of this study is the dependence of the results on the domain used for each parameter in the designs of experiments. Soft tissues exhibit a large variability in their mechanical behaviour depending on multiple factors such as, for instance, location, individual, disease. The domains were selected on the basis of experimental investigations from the literature, taking into account the variability of each parameter; however, some limitations should be noted. The domains of the geometrical factors were chosen to investigate the effect of a small tear on the propagation of dissection, although much larger tears were observed in the literature [211]. We assumed that aortic dissection originates from a small tear and that the tear becomes larger with the propagation of the aortic dissection. Another limitation to this work is the assumption that the media is homogeneous when in reality it is not. The medial inner layers differ from the medial outer layers in term of mechanical properties [6]. The location around the aorta also has an influence on the mechanical behaviour [6]. The reason behind these changes is related to local differences in the microstructure. The microstructure plays a key role in the stress distribution along the aorta [30]. In our work, each layer of the aortic wall was assumed to be homogeneous for simplicity; however, taking into account these local differences seems fundamental in the modelling of a

complete dissection along the aorta, especially since the crack path would be influenced by heterogeneities. Other numerical studies investigated the effect of different microstructural components on the mechanical behaviour and fracture of the aortic wall [166, 190, 246]; nevertheless, they did not study the effect of a tear on aortic dissection propagation. Furthermore, surrounding tissues around the aorta were neglected for simplicity in this study, although they may induce pressure on the adventitial side of the aortic wall. Therefore, the internal pressure can be interpreted as a relative pressure equal to the blood pressure applied to the intimal side of the aortic wall minus the pressure induced by the surrounding tissues.

Finally, the main limitation of this study is the lack of validation. The lack of experimental data concerning the investigation of the early stage of aortic dissection is an issue. It can be explained by the difficulties to observe such an event. Nevertheless, the recent developments in imaging techniques may be used to overcome these difficulties and shed light on the early steps of aortic dissection. In addition, this model was used to assess the relative contribution of each factor rather than providing predictive values. In this context, it definitively helps to understand the governing mechanisms of this event. For example, knowing that tensile strength is the main factor contributing to the initiation of dissection (and even more so for θ-z tears) may help with better screening at-risk individuals.

IV.1.5 Conclusion

Aortic dissection is a complex process involving multiple mechanical factors. The fact that only the final state of the disease is clinically observed hides this complexity. Numerical models can help to understand and quantify the mechanisms involved. The model presented in this study was able to replicate the behaviour of the aorta during the initiation and propagation of an aortic dissection. In addition, different types of tears were compared and the influence of several parameters on the critical pressure and direction of propagation was evaluated with a parametric study for each tear configuration. Although this study remains to be validated with experimental data, it provides a better understanding of the mechanisms of aortic dissection propagation. Further studies could investigate and quantify the most influential parameters found in this work in patients suffering from aortic dissection. This could lead to improvements in the detection and treatment of this disease.

Highlights

- A two-layer aortic model with an initial tear was developed in three different configurations depending on the initial direction of the tear.
- Anisotropic damage initiation criteria were developed based on mechanical tests from the litterature.
- A design of experiment was used to quantify the influence of 7 parameters on the critical pressure triggering the dissection and the directions of propagation of the tear.
- The numerical model was able to reproduce the behaviour of the aorta during the initiation and propagation of an aortic dissection.
- The medial tensile strength was found to be the most influential factor, suggesting that a medial degeneration is needed to propagate a tear in an aortic dissection.
- The geometry of the tear and its location inside the aortic wall were also found to have an important role on the critical pressure and direction of propagation.

Chapter V

Étude expérimentale de la dissection dans l'artère carotide - *Experimental investigation of dissection in the carotide artery*

The preliminary study [89] done by our laboratory showed the feasibility of the coupling of X-ray microtomography and mechanical testing. This led to the design of a new experimental method for the investigation of aortic dissection which is described in this chapter. In this study, an in vitro aortic dissection in porcine carotide artery is performed under X-ray microtomography. The objective is to observe the dissection of the segments and quantify the morphology of the notch and the aorta. This paper was published in Experimental Mechanics (Sp Iss: Experimental Advances in Cardiovascular Biomechanics, 2020) [24]. In a second part, the failure properties of the porcine carotide artery are assessed using tensile and peeling tests. The objective of this study is to understand why the carotid artery is less prone to dissection than the aorta. Yasmine Guendouz contributed to the experiments of this study through a research project during her last year at École des Mines de Saint-Etienne.

Contents of the chapter

Résumé du chapitre

Ce chapitre regroupe deux études sur le comportement mécanique des artères carotides porcines à la rupture.

Le Chapitre IV a quantifié l'influence de nombreux paramètres géométriques et mécaniques sur l'initiation et la propagation de la dissection aortique, cependant, une validation de ces résultats est nécessaire. Ainsi, dans la première étude de ce chapitre une dissection *in vitro* est réalisée grâce à un test de traction-gonflement.

La compréhension des phénomènes à l'origine de la dissection aortique est limitée par la difficulté d'observation de ce processus. Non seulement la dissection aortique est interne à la paroi mais elle est aussi extrêmement soudaine (quelques secondes). Les progrès des techniques d'imagerie permettent de surmonter en partie ces difficultés, notamment grâce à la micro-tomographie aux rayons X. Cette technique, couplée à un test mécanique, permet d'observer la structure interne de la paroi artérielle à différents états de contrainte et de rupture. Une machine a été créée afin de réaliser un test de traction-gonflement à l'intérieur d'un tomographe à rayons X.

Un tube de PMMA contenant l'échantillon relie les deux extrémités de la machine afin de laisser traverser les rayons X et de permettre la rotation de la machine. Une roue et vis sans fin opèrent la translation de la partie basse de l'échantillon afin d'appliquer un déplacement. Une pompe péristaltique permet d'augmenter la pression à l'intérieur de l'artère. La force et la pression appliquée sur l'échantillon sont mesurées au cours du test par deux capteurs. Dans cette étude, le test mécanique a été contrôlé en déplacement et en pression. Pour éviter la déshydratation durant l'expérience, le tube était rempli de vapeur grâce à un humidificateur.

Des artères carotides porcines ont été utilisées dans cette étude car elles garantissent un rapport optimal entre la résolution et le champ de vision. Les carotides de porc ont été récupérées à la boucherie locale quelques heures après la mort des cochons et des échantillons de 50 mm ont été coupés. Les échantillons ont ensuite été trempés durant 24h dans un agent de contraste (sodium polytungstate) avec une concentration de 15 g/L afin de pouvoir observer les feuillets d'élastine composant la couche médiale sans dégrader les

propriétés mécaniques de la paroi. L'intérêt de cet agent de contraste réside dans le fait qu'il n'est pas nécessaire de déshydrater l'échantillon afin d'obtenir une pénétration et un contraste suffisant. Une fissure est ensuite créée à l'intérieur de la paroi artérielle avec une machine conçue au laboratoire Sainbiose dans le cadre de cette thèse. Cette machine est composée d'une lame de scalpel attachée à un tube métallique qui s'insère dans l'artère, lui-même guidé verticalement à l'aide de douilles linéaires à bille. L'échantillon est ensuite ligaturé au système de traction-gonflement. Un allongement de 150% est appliqué et une série de scans à différentes pressions est effectuée.

Dans cette étude, les résultats de deux échantillons sont présentés. Concernant le premier échantillon, le diamètre initial était de 4,4 mm et l'épaisseur de la media était de 1,1 mm. La reconstruction 3D de l'artère montre clairement la media et la fissure. Des scans ont été pris à différentes pressions jusqu'à un maximum de 730 mmHg. Une segmentation de la fissure a été réalisée grâce à une méthode semi-automatique et différentes informations ont été extraites (longueur, largeur, profondeur). La force exercée aux extrémités de l'échantillon diminue avec la pression. Le diamètre intérieur de l'artère ainsi que le volume de la fissure sont proportionnels à la pression, contrairement à l'épaisseur de la media qui elle est inversement proportionnelle à la pression. Une micro-propagation de la fissure a été détéctée à partir de 300 mmHg. Le deuxième échantillon, d'un diamètre intérieur initial de 4,2 mm et d'une épaisseur initiale de 1,1 mm, a subi une propagation prématurée sur plus de la moitié de la circonférence de l'artère. La présence de plans de délaminage aux sites de rupture a pu être observée.

Le principale avantage de cette expérience est de permettre à la fois une observation globale de la fissure mais aussi locale des plans de dissection à l'intérieur de la paroi. Pendant le gonflement, une forte concentration de contrainte est présente en bout de fissure induisant un fort cisaillement entre les lamelles intactes et les lamelles endommagées. Ce phénomène a été observé dans la littérature par différentes études expérimentales [89, 85]. Cependant, il a été montré que les carotides porcines disséquaient à des pressions très supérieures à la pression physiologique et parfois ne disséquaient pas du tout, même à très haute pression malgré des entailles profondes et larges.

Pour expliquer la grande résistance à la dissection des carotides porcines, une campagne de tests mécaniques, divisée entre essai de traction uniaxial et essai de délamination, a été réalisée. L'objectif était de mesurer le comportement mécanique élastique des artères carotides porcines d'une part, et les valeurs de rupture d'autre part car ces valeurs ne sont pas présentes dans la littérature. Pour cela, des artères carotides communes ont été obtenues par un abattoir local. Les échantillons pour le test de traction uniaxial ($n = 21$) ont été coupés en forme d'éprouvette, tandis que ceux de l'essai de pelage ($n = 14$) ont été coupés de façon rectangulaire et ouverts à une extrémité afin de pouvoir les monter sur le banc d'essai. Les tests ont été effectués dans les directions circonférentielle et longitudinale afin de prendre en compte l'anisotropie du tissu. Une machine de traction 5960 (Instron; Norwood, MA) équipée d'une cellule de force de 500 N a permis de réaliser les essais. Du papier de verre a été utilisé afin d'éviter le glissement des échantillons. Les résultats ont montré une anisotropie des propriétés mécaniques ainsi qu'une plus grande rigidité dans la direction circonférentielle comparée à la direction longitudinale. De plus, l'énergie nécessaire à la décohésion des échantillons est supérieure dans la direction longitudinale comparée à la direction circonférentielle. Ces résultats sont similaires à d'autres tissus artériels comme les tissus aortiques. Cependant, les énergies de dissection nécessaire pour délaminer l'artère carotide sont beaucoup plus importantes que celles pour délaminer l'aorte

humaine ou porcine. Ces propriétés peuvent expliquer pourquoi l'artère carotide est moins soumise à la dissection que l'aorte.

V.1 A novel method for in vitro 3D imaging of dissecting pressurized arterial segments using X-ray microtomography

Extracted from the paper "A novel method for in vitro 3D imaging of dissecting pressurized arterial segments using X-ray microtomography." published in Experimental Mechanics (Sp Iss: Experimental Advances in Cardiovascular Biomechanics, 2020) [24]. The text was shortened and modified herein to avoid repetitions.

Abstract

Background: It is commonly admitted that a dissection initiates with an intimal tear or at least a defect inside the arterial wall. Nevertheless, few studies investigated the initiation sequence due to the difficulty to monitor this process.

Objective: The objective of this work was to observe and investigate the mechanisms leading an intimal tear to propagate into a dissection.

Methods: A custom-made tension-inflation device fitting inside an X-ray microtomography setup was designed. A notch was created inside a porcine carotid artery before performing the tension-inflation test. The X-ray tomography setup allowed observing the wall-structure and the notch behavior during the inflation of the carotid artery.

Results: A quantitative description of the notch morphology was performed, suggesting the prevalence of high shear stress in the region of the crack tip as a possible trigger for propagation of a dissection.

Conclusions: The present experimental approach allowed understanding better the mechanisms leading to dissection and constitutes a first step toward the improvement of failure modeling and risk assessment of this disease.

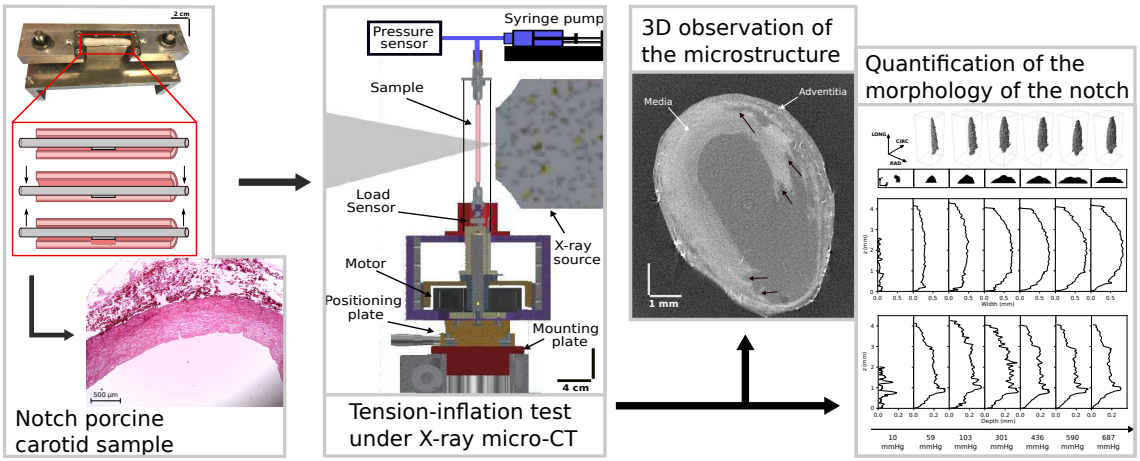

V.1.1 Introduction

In Chapters IV, a numerical model was used to investigate and quantify the influence of multiple parameters on the initiation and propagation of an intimal tear inside the aortic wall. Nevertheless, there are no experimental data available in the literature to validate the model and the results obtained. The reason behind this lack is that the morphology of the aorta during the dissection process is difficult to capture. The aortic dissection is intramural and occurs in few seconds. To observe this dynamic process, an *in situ* method combining a mechanical test and an imaging technique seems the best approach.

A major challenge in the vascular biomechanical field is the understanding of damage and rupture properties in arteries. This understanding is limited by the complexity of arterial microstructure. Several approaches were used to investigate the mechanisms behind these complex and non-linear events. Most of these studies measured properties at the macro-scale in order to develop continuum constitutive models [203, 214, 168]. Nevertheless, the understanding of the microstructure influence seems to be the key to evidence the phenomena leading to rupture and to propose appropriate modeling approaches. In that purpose, studies combining mechanical loading and microstructural observations are crucial to investigate damage propagation in arteries.

Several experimental studies investigated the behavior of arterial wall related to dissection: liquid infusion test [28, 220, 185, 213], radial tensile test [130, 203], peeling test [203, 223, 168], shear test [85, 204, 246]. Although these mechanical tests allowed characterizing the rupture properties of arterial tissue, there is a lack of understanding on the early stages of aortic dissection, especially at the microstructural scale. The tension-inflation test is closer to *in vivo* conditions and was performed in multiple experimental studies to create an *in vitro* dissection [35, 228, 53, 57, 169]. Nevertheless, one of the difficulties with the investigation of dissection is that it is an intramural process which complicates observation. Combining the tension-inflation test with an appropriate imaging technique would overcome that issue and allow observing and quantifying the different steps of aortic dissection, especially in the early stages.

Different imaging techniques were used to observe arterial tissue. However, few were used in combination with mechanical tests. Recently multiphoton microscopy was often used to image arterial tissue as it allows observing collagen and elastin fibers. These studies investigated the organisation of collagen fibers structure inside the arterial wall during uniaxial and biaxial loading tests [240, 29, 120]. Although this approach provides many insights into the behavior of arterial wall at a micro-scale, the limited volume of observation ($<$1 mm^3) is a major limitation in the observation of aortic dissection. X-ray microtomography (micro-CT) is an alternative non-destructive imaging method with a larger field of view (1-10 mm^3). This technique allows observing the 3D microstructure of soft tissue with high resolution [144, 235]. However, *in situ* tests on soft tissues like arteries are still scarce in the literature. In a previous study, Helfenstein-Didier et al. [89] performed *in situ* uniaxial tensile tests on medial layer strips of porcine thoracic aorta inside a micro-CT setup with a resolution of 4 µm to investigate the damage initiation and propagation mechanisms. Sodium polytungstate was used as a contrast agent to observe the musculo-elastic units of the media. The results highlighted the importance of the shear delamination of the medial layers in the failure process. This conclusion was supported by histological observations on the ruptured samples. Similar observations were also presented in the study of Sherifova et al. [200] which concluded that the microstructure and especially the collagen fiber architecture but also the different types of cross-links are of first importance in the

uniaxial failure of soft tissues. In another *in situ* study using micro-CT, Trachet et al [225] performed tension-inflation test on mice left common carotid arteries, using synchrotron-based phase-contrast imaging. High resolution images of the carotid artery were obtained with a resolution of 1.625 µm, allowing the elastic lamellae to be segmented. The results showed that the lamellae stretch simultaneously as luminal pressure increases.

In the present work, an *in vitro* dissection was created and observed by combining a tension-inflation test with micro-CT. A notch was created inside the porcine common carotid artery to initiate the dissection. The structure of the artery was observed while performing the mechanical test by designing a custom-made device fitting inside a micro-CT setup. The objective was to follow-up the notch evolution during the inflation and investigate the damage propagation in the medial layer.

V.1.2 Material and method

V.1.2.1 Sample preparation

Porcine hearts with aorta and carotid arteries from 6-month-old pigs were purchased from a local butchery few hours after death. Common carotid arteries were carefully excised and 50 mm long samples were cut. Pig was chosen as the arterial diameter and medial lamellae number are close to human [38] and suitable for a good compromise resolution/field of view with the micro-CT equipment used here. The present study aims at demonstrating the capacity of the experiment and its relevance in analysing early dissection progress, the results of two samples are presented. The first sample (sample 1) reached complete dissection prematurely, and could only be observed in the dissected state. The second sample (sample 2), analyzed in this paper, was followed up to a pressure that was not sufficient to fully propagate dissection.

Contrast agent

A major issue with arterial tissues and soft tissues in general is that the images obtained by micro-CT do not exhibit sufficient absorption contrast [158]. One solution to overcome this problem is to use synchrotron-based phase-contrast imaging as demonstrated by Logghe et al. [126]; however, access to this type of equipment is rare. In this work, a conventional micro-CT equipment was used in combination with a contrast agent binding with some components of the tissue to increase their absorption. Immediately after collection, the samples were immersed in a diluted solution of sodium polytungstate (15 g/L) and placed in the fridge during 24 hours at 4 °C. The immersion time of the sample ensuring a full penetration of the contrast agent in the tissue was adjusted in a previous study [89]. According to the same study, this contrast agent allowed observing the elastin sheets of the medial layer without significantly affecting the characterized mechanical properties of the tissue. The interest in using sodium polytungstate relies on the fact that there is no need of dehydration of the sample during the staining process to obtain sufficient contrast. Dehydration would affect the structure of the sample and deteriorate the mechanical properties.

Notch creation

In order to cause and observe a dissection propagating within the field of view, a custom device was designed to create a longitudinal notch inside the carotid artery without opening it (Fig. V.1). The system was composed of a surgical scalpel blade of 8 mm length and 2 mm depth, attached to a rod to be inserted in the artery, itself guided vertically by

linear ball bearings. To create the notch, the controlled device was used to cut through the intima and part of the media. The defect was created in the radial-longitudinal plane and not in the radial-circumferential plane due to technical difficulties. Although, intimal tears in the transverse direction are reported to be more common in the literature, the crack is seldom entirely in the radial-circumferential plane and often has a longitudinal component [47]. An optical coherence tomography (OCT) image of the notched carotid artery is shown in Fig. V.2. This optical technique was used to adjust and assess the notch depth in a preliminary study. To this aim, four carotid arteries were harvested on pigs from the local butchery, 3 specimens with a length of 17.5 mm were cut from each carotid artery. A longitudinal notch was made in each specimen with the machine. Finally, the samples were opened and the 12 notches were observed and measured using OCT. It showed that the notch depth had a value of 263 ± 83 µm (n = 12). Though these results present a large variability, it must be noted that the exact notch depth will be measured in the micro-CT images of the subsequent tension-inflation test.

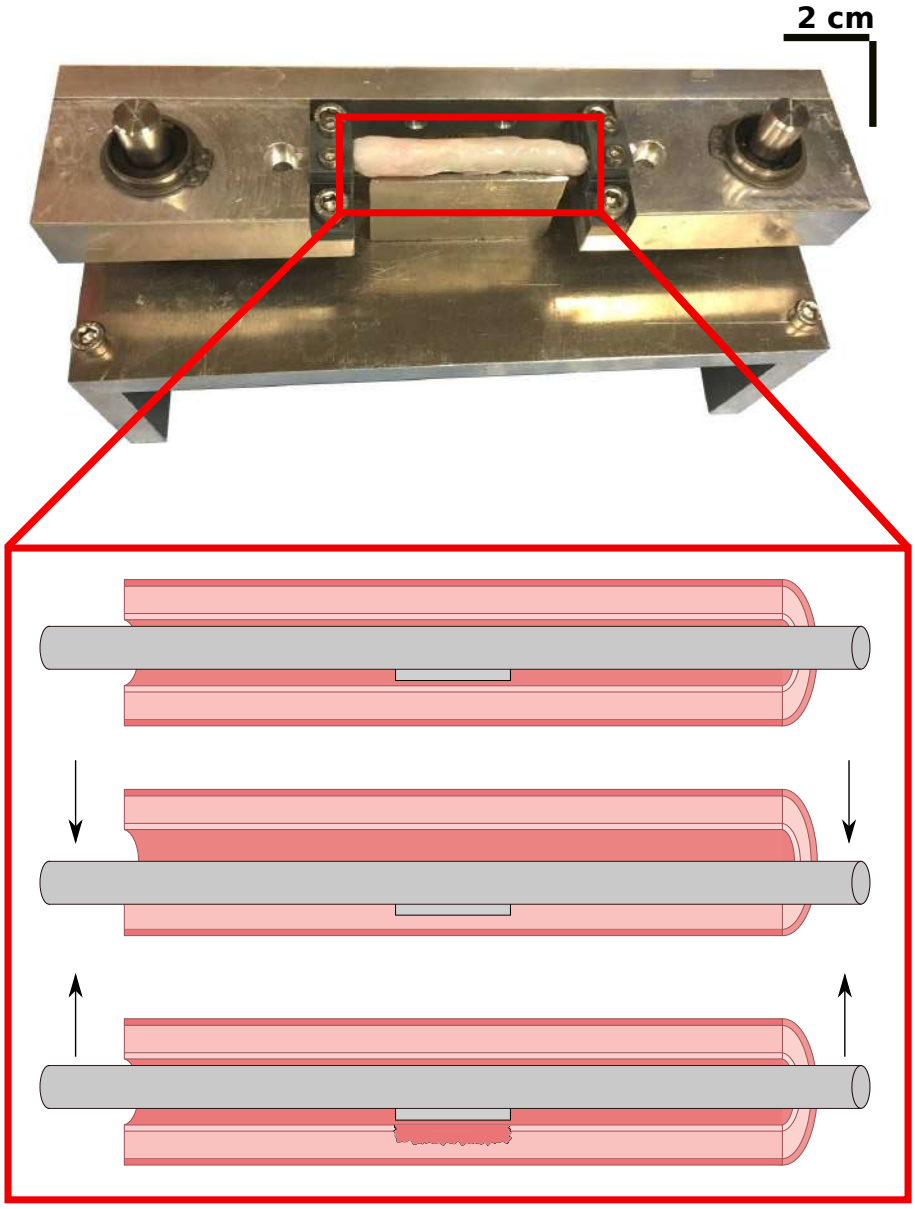

FIGURE V.1 – The custom-made device to create the notch inside the carotid artery with a schematic of the cutting process.

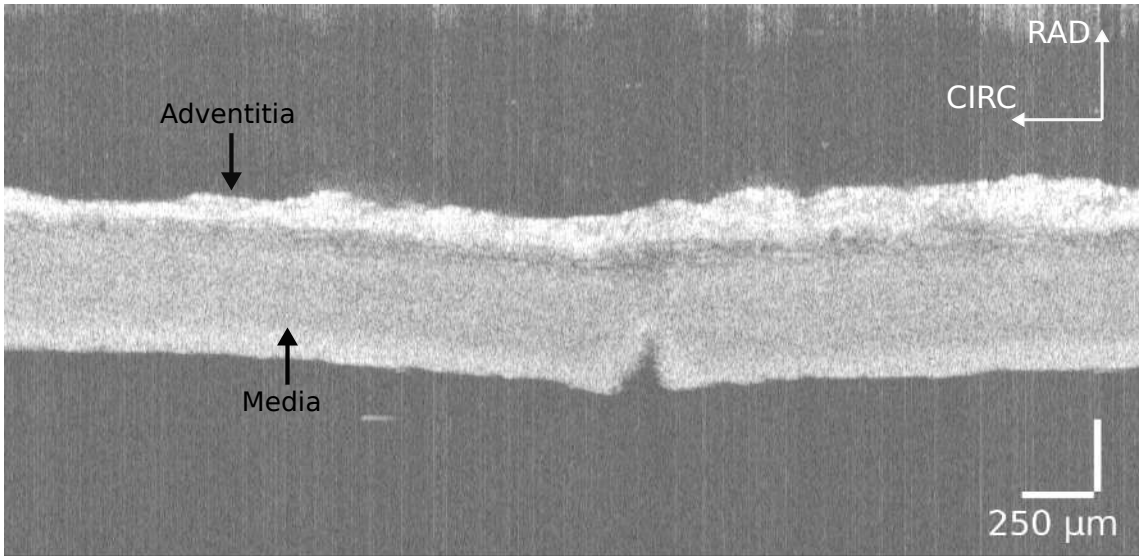

Figure V.2 – OCT image of a flat-opened carotid wall with a notch created by the cutting device.

V.1.2.2 Tension-inflation device

Mechanical setup

A custom-made tension-inflation machine was designed to fulfil the constraints of the experiments planned in the study (Fig. V.3). The main constraint was to fit the machine inside the micro CT equipment. To this aim the test was performed in a 50 mm diameter cylindrical PMMA tube, constituting the machine structure between both ends of the sample, to not interfere with the X-rays passing through and allow rotation of the whole machine. A motorized worm gear was used to apply displacement to the lower end of the sample with a maximum displacement of 50 mm and a maximum displacement rate of 1.25 mm/s. Through the upper end, a syringe pump quasi-statically infused a saline solution to increase the pressure inside the sample. A load sensor (LCM201, Omega^{TM}, $\pm$300 N) and a pressure sensor (PXM319, Omega^{TM} 0 - 3.5 bar) recorded the load and pressure all along the test. The device was fixed on the micro-CT rotating platform by screws. A custom-made program was developed to control the machine. Displacement- or load-controled and pressure- or volume-controled test could be performed in order to test a wide range of biaxial states. In the present study, the experiments were driven in displacement and pressure. To prevent dehydration of the sample during the test the tube was filled with steam by a humidifier. Previous tests with a humidity sensor (DHT22) showed that the atmosphere inside the tube was saturated.

X-ray tomography setup

X-ray computed tomography is a non-destructive technique that allows the 3D reconstruction of a sample. It is widely used in both industrial and medical fields. The principle is based on the attenuation of X-rays by matter and their recording by an X-ray detector after going through the sample. Several views are taken at different angles and mathematical methods allow the 3D geometry and the internal structure to be reconstructed. For more information on X-ray tomography principle see Baruchel et al. [18].

In this study a Phoenix^{TM} VtomeX tomograph equipped with a Varian^{TM} Paxscan X-Ray detector was used, featuring a resolution of 1920 x 1536 pixels. The X-ray source was

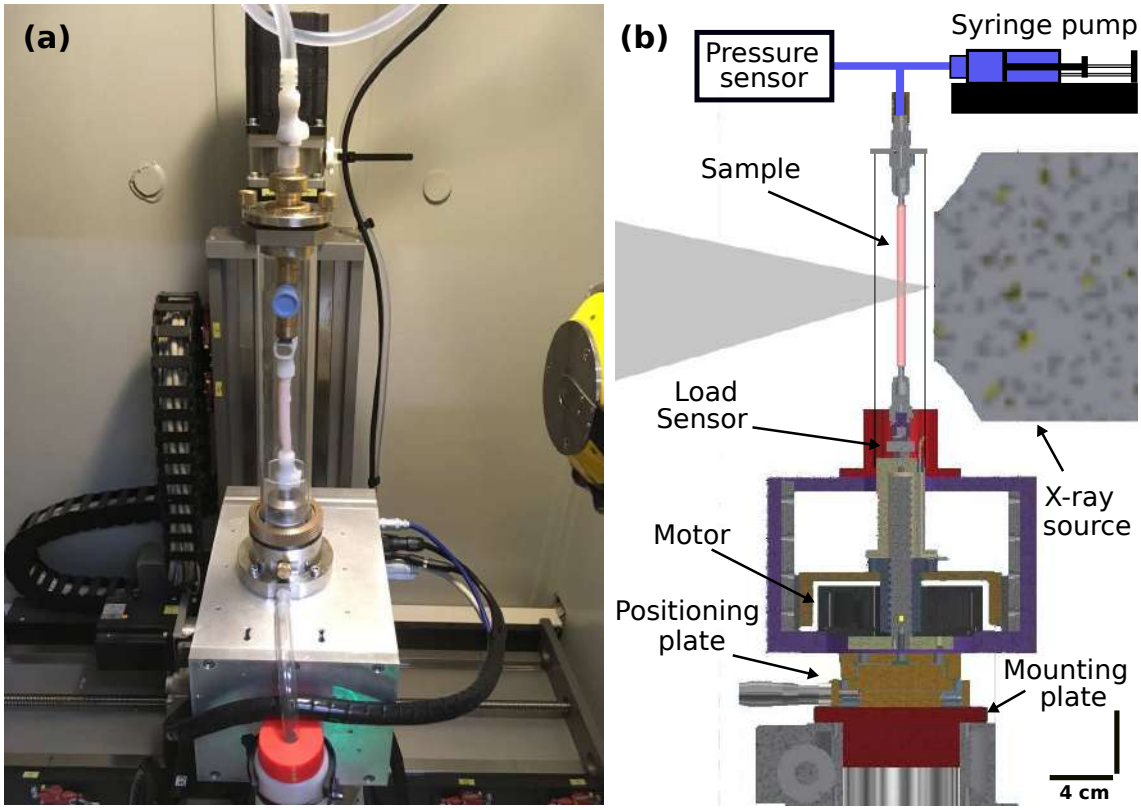

FIGURE V.3 – (a) Photo and (b) schematic of the custom-made tension-inflation device inside the micro-CT equipment.

supplied with a voltage of 80 kV and a current of 280 µA. The voxel size was 7 x 7 x 7 μm^3. No physical filters were used during the acquisition. Soft tissues are not as stable as hard tissues during the mechanical test with possible motion of the sample due to creep and stress relaxation resulting in a blurry image. To avoid these effects, a fast acquisition was needed and a compromise between resolution and scan time was made. The projection number was 800 and the total acquisition time was 266 seconds.

Protocol

After staining, the notched sample was ligatured to the tension-inflation device. An initial high resolution scan was performed in the unloaded configuration. Then, a physiological stretch of $\lambda_z = 1.5$ was applied [172]. Once the stretch was applied, another scan was performed, followed by infusion at a rate of 0.026 mL/s. Pre-conditionning was not performed as it could trigger the propagation. 3D scans were acquired after reaching given pressure steps and allowing a relaxation time (5 to 10 minutes to stabilize the sample before imaging). The steps were set at 15, 80, 130, 315, 485, 620, 730 mmHg. At each pressure step a relaxation of the carotid artery was observed. After 10 minutes, when the pressure was considered stable, the scan was performed. The mean pressures present in the sample during the scans are reported in Table V.1.

V.1.2.3 Post-processing

Measure of diameter and thickness

To measure the diameter of the vessel at the different pressure steps, the inner contour of the arterial wall was segmented, and an ellipse was fitted on it. The mean between the

Pressure target (mmHg)	Scan pressure (mmHg)
15	10
80	59
130	103
320	301
485	436
620	590
730	687

Table V.1 – Pressure targeted during the inflation and the actual mean pressure obtained after relaxation during the scan.

major and the minor axes was taken as the diameter of the lumen.

The medial thickness was measured manually at 10 random locations along the vessel. The adventitial thickness could not be measured as the delimitation between the adventitial layer and the connective tissue could not be determined clearly with the current resolution.

Crack follow-up
A semi-automatic method was developed to segment the notch on the X-ray images and, thus, follow its evolution with the pressure increase. A median filter was applied to reduce noise followed by a threshold applied to differentiate the wall from the solution inside the carotid artery. Different morphological operations were performed to remove spurious islands and holes, and the separation between the lumen and the notch was drawn manually. Finally, the notch could be segmented and several parameters were calculated like its width, depth, and volume.

Wall integrity follow-up
To follow the possible propagation into a dissection, which could be detected in the images, the histogram of the gray values along the radial direction was plotted at different locations in the cross-section corresponding to the maximum notch depth (Fig. V.4): one next to the notch and ten far from it (in a region assumed to be perfectly non-damaged). To diminish the noise and avoid wall heterogeneities, at each point on the radial profile the value taken was the mean of the gray values of a square of 20 x 20 pixels. A decrease of the gray level at a given radial location means that the notch propagated in the form of a crack in the circumferential direction. This technique was complementary with the segmentation presented above as the algorithm had difficulty to segment micro-cracks.

V.1.3 Results

The reconstructed 3D images of the carotid artery showed clearly the media and the notch. Nevertheless, the medial lamellae could not be distinguished in all scans with the current resolution. As stated in the subsection V.1.2.1, only sample 2 was quantitatively analyzed in the present study. The results of the prematurely-dissected sample 1 are displayed at the end of this section. Concerning sample 2, the scan in the unloaded configuration showed that the initial inner diameter and medial thickness of the specimen were 4.4 mm and 1.1 mm respectively. Cross-sectional views at the middle of the axially stretched sample are shown in Fig. V.5 at different pressures. The evolution of the notch geometry is visible.

The notch was segmented at the different pressure steps and different information were extracted and displayed in Fig. V.6. Fig. V.6a shows a 3D view of the segmented notch.

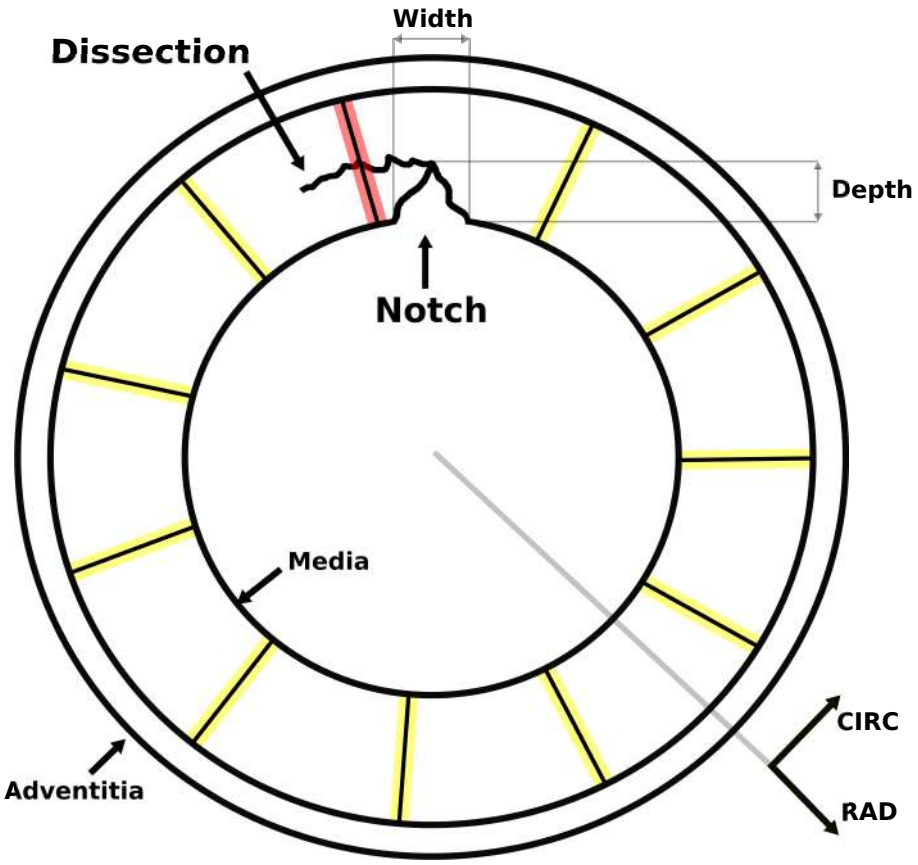

FIGURE V.4 – Schematic representing a cross-section of the vessel with a dissection at the tip of the notch. The different locations where the histograms were plotted are shown with radial lines. The profiles are represented in red for the one measured close to the notch and in yellow for the ones measured far from it.

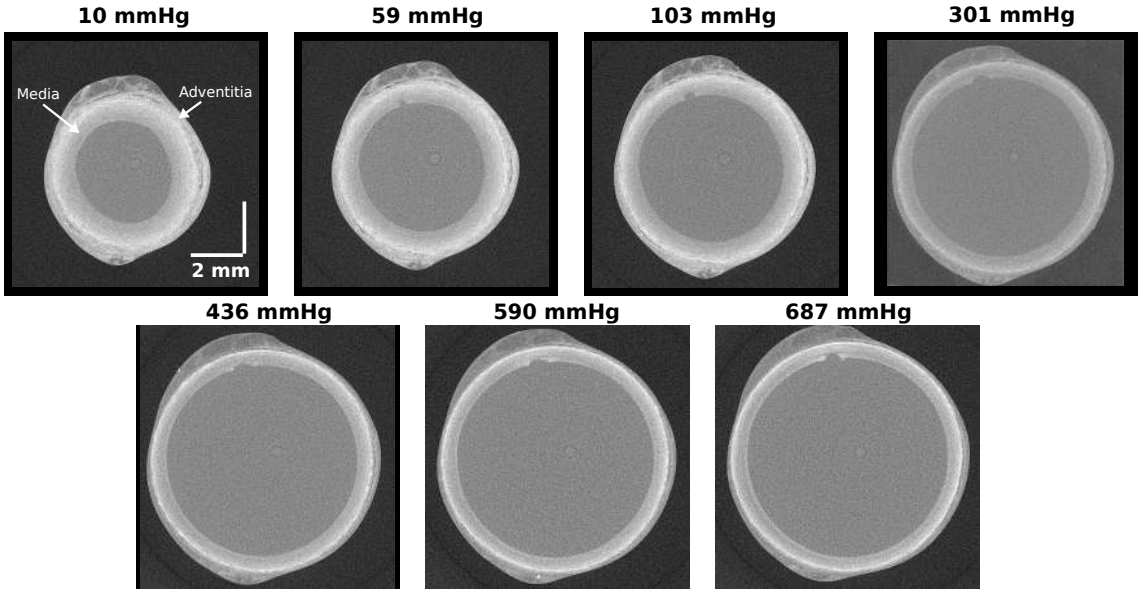

FIGURE V.5 – Cross sectional views of the carotid speciment (sample 2) at a stretch of 1.5 and at the different pressure steps.

Fig. V.6b shows a view in the transverse plane at 30% of the height of the notch. The crack follows the stretch of the wall; however, no propagation could be observed on the segmented images. The width and the depth of the notch were plotted in Fig. V.6c and in Fig. V.6d respectively. The decrease of notch height between 103 and 301 mmHg is explained by the imprecision of the segmentation method on the edges of the notch, especially at high pressures. The segmentation was also challenging for the lowest pressure as the notch was almost not visible because of the absence of pressure. The blade is curved on its edges to avoid stress concentration, explaining that the length of the notch was smaller than the blade length. This sample had an initial maximal notch depth of 182 µm, in the very low range of usual notch depth created with our setup, likely explaining why complete dissection was not reached with our pressurization setup.

Fig. V.7a presents the mean axial loading at each pressure steps. Fig. V.7b, V.7c, and V.7d show the inner diameter, the medial thickness, and the notch volume respectively. The latter markedly increased for low pressures and became relatively constant after, similarly to the inner diameter, and inversely to the medial thickness. It is interesting to note that the maximum variation of the lumen diameter along the vessel for all pressure steps was equal to 50 µm.

On the graph Fig. V.8, the arrow shows the presence of a micro-crack in the circumferential direction near the notch. This crack appeared on the images at 301 mmHg and continued to be visible for higher pressures.

In the Fig. V.9, an histological cross-section of the second sample is presented. The notch and the micro crack at the tip of the cut are visible.

A cross section view of the prematurely-dissected sample 1 is shown in Fig. V.10. The initial inner diameter and the medial thickness of the specimen were 4.2 mm and 1.1 mm respectively. During the test, the media ruptured entirely; however, the adventitia was unruptured. The notch propagated on more than half the circumference of the artery and a considerable circumferential elastic recoil of the media was observed. The arrows highlight the presence of delamination planes at the rupture site.

V.1.4 Discussion

This paper presented a novel experimental approach to study the mechanical events involved in the propagation of arterial dissection. *In situ* testing combining tension-inflation test with micro-CT allowed observing the internal structure of notched carotid arteries as an *in vitro* model of dissection.

In the present context, the main advantage of this imaging technique is to offer a suitable resolution/field of view compromise to enable both a global observation of the damage site (here, the notch) and lamellar-scale details such as intramural dissection planes which were evidence here around the notch. The deformation of the notch volume with the pressure followed the deformation of the wall. This is shown by the similar shape of the pressure-diameter curve (Fig. V.7b) and the pressure-notch volume curve (Fig. V.7d). This can also be seen by the evolution of the notch shape Fig. V.6b where the notch flattened and became relatively stable after 301 mmHg. The absence of propagation of the notch is rather clear in one of our experiment. According to Chapter IV, a pressure of 730 mmHg should have been sufficient to propagate the tear; however, the type of tissue is not the same. The absence of propagation could also be explained by the lack of medial degeneration in the sample, which is usually considered as one of the main causes of aortic

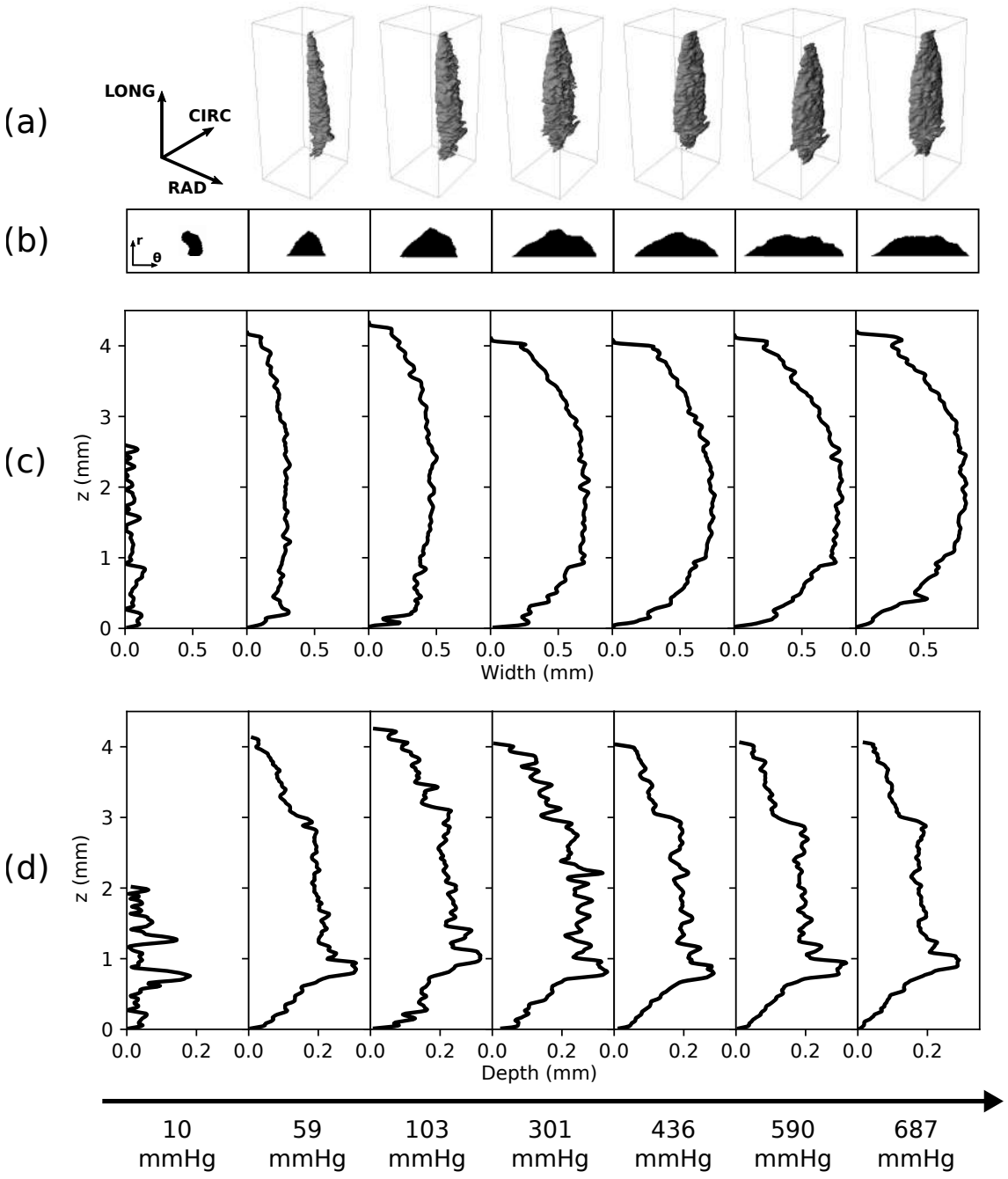

FIGURE V.6 – Evolution of the notch morphology (sample 2). (a) A 3D view of the notch at the different pressure steps. (b) Cross-section of the notch at 30% of the height of the sample. (c) The width of the notch. (d) The depth of the notch.

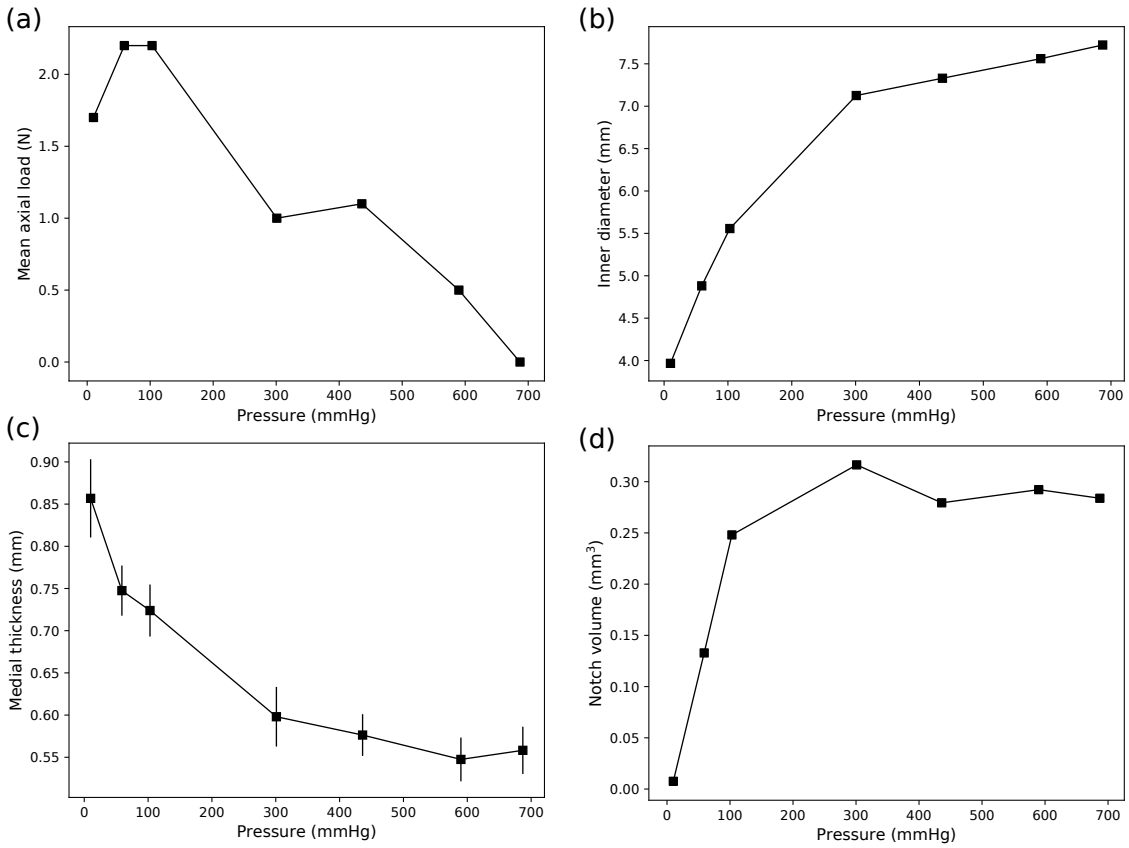

Figure V.7 – (a) Axial load, (b) inner diameter, (c) medial thickness, (d) notch volume as a function of pressure (sample 2).

dissection. Nevertheless, aortic dissection can be triggered by a supra-physiological blood pressure (during weighlifting for instance [202]), meaning that maximum pressure may play a role in aortic dissection. Concerning the axial load, multiple factors could explain the decrease observed in Fig. V.7a, for instance the axial pre-stretch being slightly lower than the actual in vivo stretch [104, 10]. The inner diameter measured during the experiment is consistent with the results found in the literature from tension-inflation test on healthy carotid arteries [22, 234]. In our experiment, the notch did not seem to affect the diameter as there were almost no variations in the inner diameter along the vessel; however, the depth of the notch was limited, which could explain this result.

During the inflation of the carotid artery, at the tip of the notch, a high tension stress is present in the remaining intact medial lamellae, and hence a high shear stress between intact and ruptured lamellae. The propagation of the notch in the circumferential direction, observed in Fig. V.8, can be hypothesized to be a consequence of this local stress state, indicating the importance of shear delamination in dissection propagation. The same observation was made by Haslach et al. [85], where bovine aortic rings with a longitudinal notch on the intimal side were inflated until failure. The propagation of the crack occurred nearly in the tangential plane and the authors concluded that it was a consequence of the shear deformation present inside the wall during inflation. This conclusion is supported by the study of Witzenburg et al. [246] which demonstrated the very low interlamellar strength of arterial tissue, especially against shear stress. Other studies used uni-axial test to highlight the importance of shear delamination stress in the failure process [89, 200]. Using histology, these studies observed delamination planes at the rupture zone, similarly

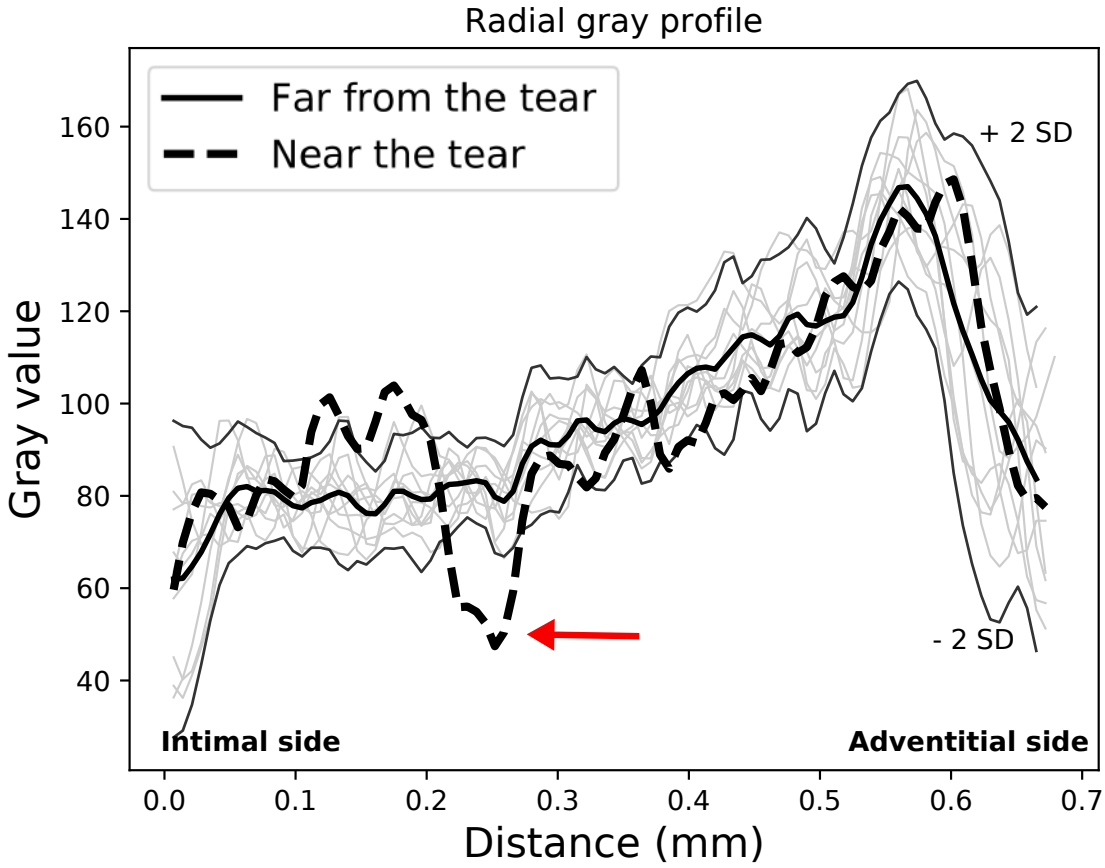

FIGURE V.8 – Radial gray values profile at 301 mmHg in the cross-section corresponding to the maximum notch depth at different locations of the arterial wall (sample 2). The thick dash curve corresponds to the measure close to the notch. The thick solid curve characterizes the mean of the profiles measured far from the notch. The curves representing the mean ± 2 standard deviations (SD) were also plotted. The arrow shows a decrease in gray values close to the notch compared to the normal profile in the healthy part of the sample, demonstrating the presence of early crack propagation.

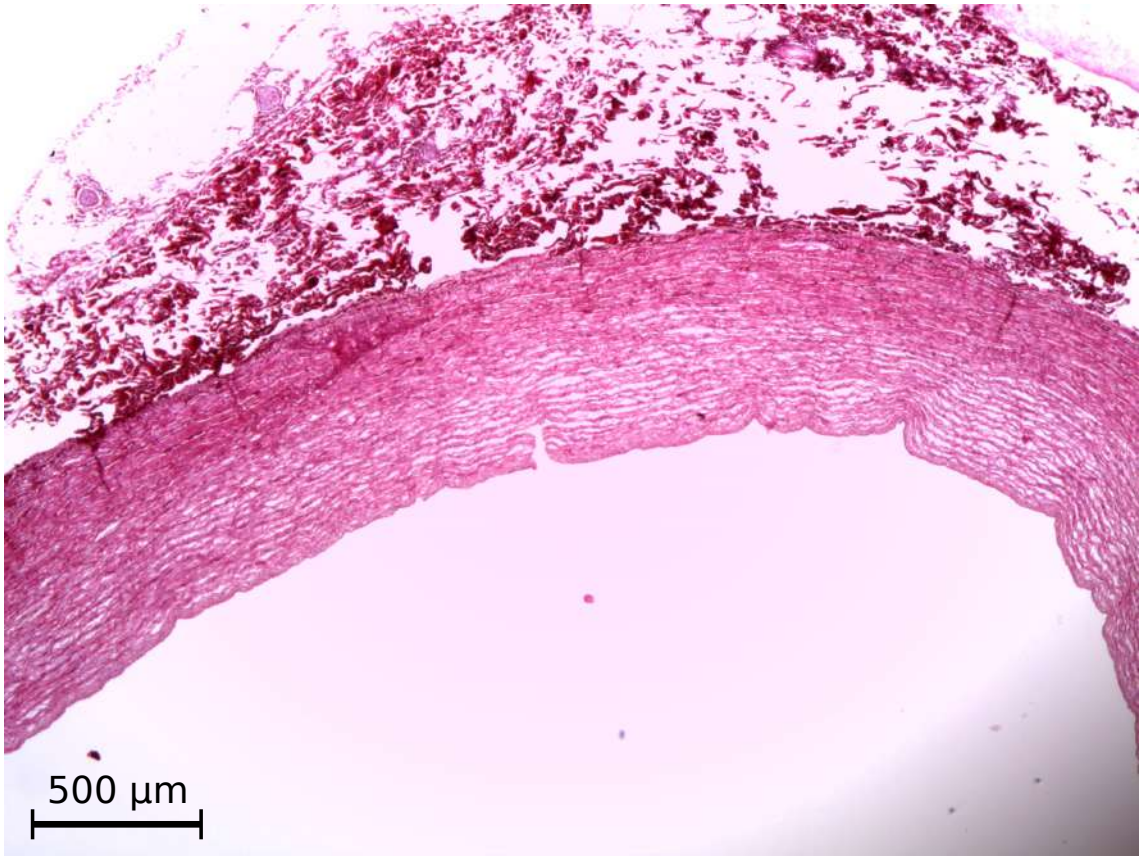

Figure V.9 – Representative histological images illustrating the notched aortic wall after the tension-inflation test. Sirius red staining. Original magnification 4×.

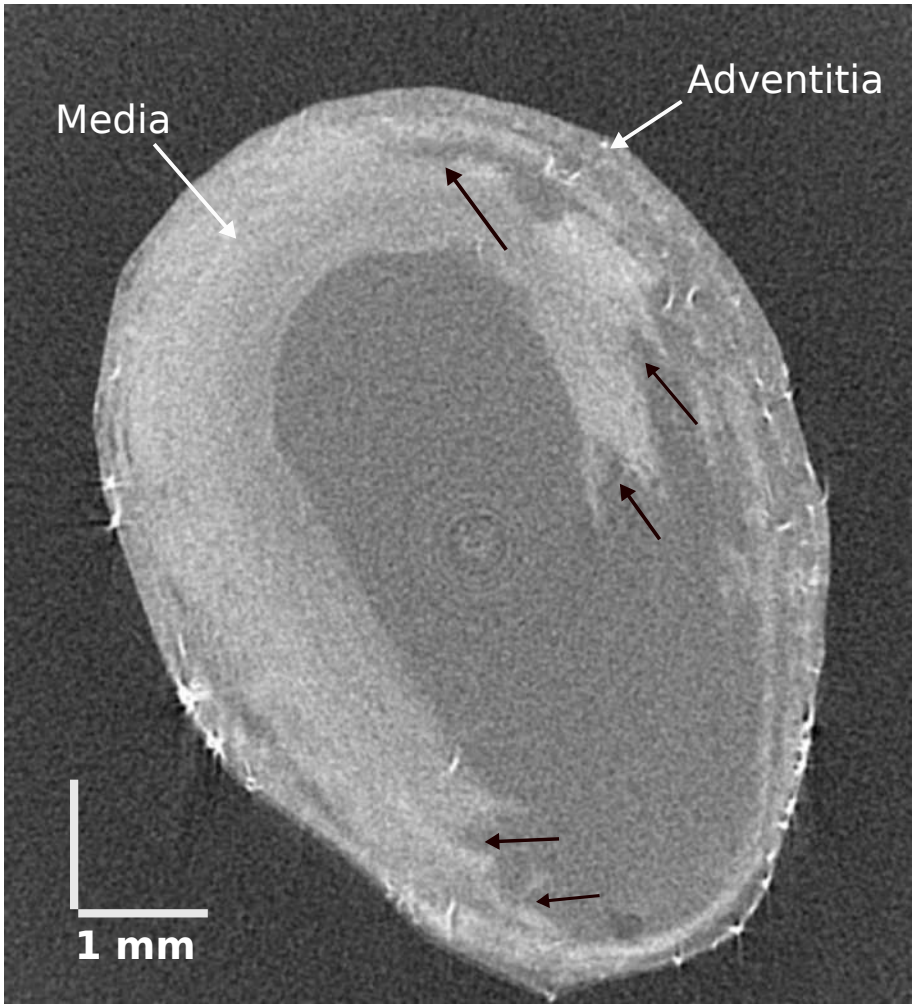

FIGURE V.10 – Cross-section of the dissected specimen (sample 1). The arrows indicate delamination planes.

to the observation made in Fig. V.10. This confirms the presence of shearing mechanisms during the propagation of the dissection in the tension-inflation test. Helfenstein-Didier et al. [89] also identified a pattern of rupture during uniaxial tension tests on medial samples. The results showed that an elementary rupture sequence repeated until complete failure: a bunch of musculo-elastic units breaks in tension (mode I), followed by a delamination (mode II) of this layer from the wall. Based on these observations, [25] showed that shear delamination strength is most likely the predominant factor in the initiation of dissection. The Fig. V.10 seems to exhibit a similar failure sequence, the presence of multiple delamination planes indicates that several bunches of musculo-elastic units broke and started to delaminate from the arterial wall. At one point, the delamination shear stress between lamellae created by this mechanical state overcame the interlamellar strength and the crack propagated in the tangential plane in mode II delamination. Nevertheless, the second test did not reach failure due to low notch depth and could not confirm these observations; thus, further tests are needed.

The majority of aortic dissections involve more than half of the circumference of the aorta [217]. The same phenomenon was observed on the X-ray images of the present study (Fig. V.10), confirming that the *in vitro* dissection obtained during the experiment is similar to those seen in clinic. Furthermore, the dissection propagated up to the boundary between media and adventitia, as described in experimental studies where the dissection is shown to propagate in the outer media [165, 6]. The fact that the adventitia was unruptured illustrates its protective role for the artery. Holzapfel et al [96] showed that the residual stress present in the arterial wall is layer-dependent and that the media, once separated from the other layers, shortens significantly. Thus, the elastic recoil of the medial layer observed in this sample is explained by the release of its tension stress initially present when the carotid artery was intact.

This work demonstrated the feasibility and relevance of the proposed experimental approach; however, the following limitations should be mentioned. First, in clinics most of the intimal tears encounter are in the transverse plane. In future work, we could perform this test with a transverse intimal notch to compare the influence of the notch direction on the propagation, or absence of propagation, of the defect. Another limitation is that the separation between the adventitia and the connective tissue during the preparation of the sample is complicated as there is a continuity between the two in this type of tissue. Further analysis could address the question of preferred propagation direction or fracture modes involved. Other interesting perspective might be to apply volume correlation analysis to quantify the strain of the arterial wall at different steps of the dissection; thus, these data could be used to validate complex model involving damage and rupture.

V.1.5 Conclusion

In conclusion, an experimental approach was presented to create an *in vitro* dissection model and observe it with micro-CT. This experimental approach allowed following the deformation of a notch and investigating the early stages of dissection propagation. The micro-CT images highlight the importance of shear delamination strengh during the propagation of the dissection. *In situ* testing associated with X-ray microtomography is a promising way to assess the mechanisms leading to rupture in biological tissue. In addition, the resistance of carotid tissue to dissection was evidenced. Further studies are needed to exposed the reason behind this phenomena.

Highlights

- A new method for observing the propagation of a 3D *in vitro* dissection in porcine carotids with an X-ray tomograph has been developed.
- A quantitative description of the morphology of the notch during its evolution with pressure was presented. In addition, the presence of numerous delamination planes in a dissected sample was demonstrated.
- These results suggest the prevalence of high shear stress in the region of the crack tip as a possible trigger for the propagation of a dissection.

V.2 Why is the carotid artery less prone to dissection than the aorta ?

Abstract

Porcine carotid arteries exhibit a strong resistance against dissection, unlike aortic tissue. No failure data on porcine carotid artery are present in the literature to explain this phenomenon. Therefore, the objective of this study was to perform uniaxial tensile and peeling tests on porcine carotid artery to understand why this tissue is less prone to dissection compared to other arterial tissues like aorta. The results showed an anisotropy of the tissue, with a stiffer behaviour in the circumferential direction. The tensile strength was higher in the circumferential direction, in contrast to the dissection energy per reference area, which was higher in the longitudinal direction. These results are in accordance with the literature. Furthermore, the porcine carotid artery exhibited higher dissection energies in both directions compared to aortic tissue. These properties may explain why carotid artery is more resistant to dissection than the aortic tissue.

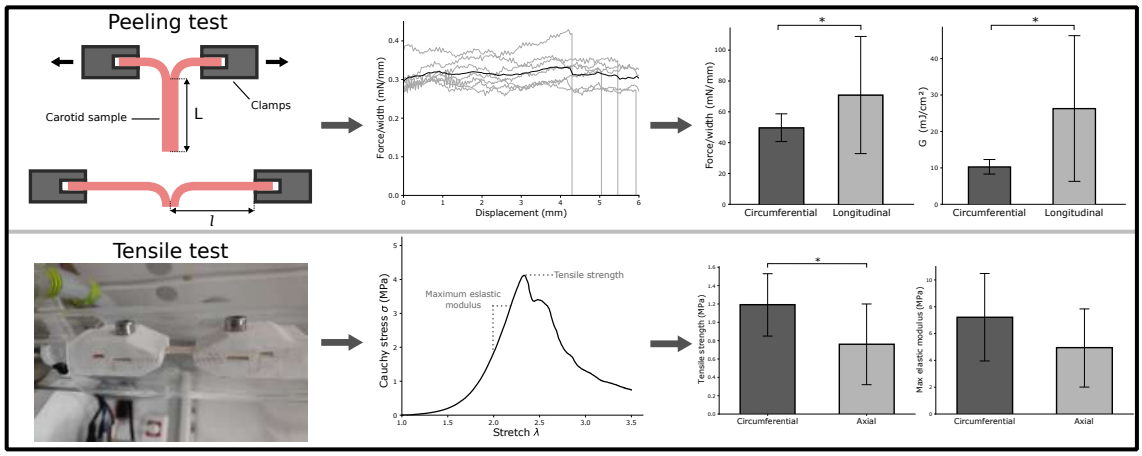

V.2.1 Introduction

In Section V.1 we presented an experimental study where tension-inflation tests were performed on two notched porcine carotid arteries, the first sample did not propagate whereas the second sample did. It was assumed that the lack of total propagation was caused by the shallow initial tear in the specimen. However, after numerous tension-inflation tests it appears that dissection in carotid artery sample is difficult to achieve, even at high pressure ($>$ 1500 mmHg), with a deep initial notch, or with different notch orientations. A low proportion of samples dissected and no difference was found between the dissected specimens and the non-dissected ones. Thus, this difference was assumed to be a lower cohesion of the medial lamellae in the dissected samples.

On the other hand, aortic tissue is more prone to dissection as demonstrated in multiple experimental studies of the literature [11, 28, 220, 185, 213]. The critical pressures varied from 152 $\pm$ 43 mmHg to 854 $\pm$ 134 mmHg, which is much lower than the pressures we used on carotid artery to make them dissect. The difference in methods between these studies and the work performed in Section V.1 cannot explain this outcome. Therefore, to better understand why carotid arterial tissue is less prone to dissection than aortic tissue, a characterisation of its mechanical behaviour is necessary.

Unlike data on aortic tissue, data concerning failure properties of carotid arteries are scarce in the literature. A summary of multiple studies that performed tensile and peeling tests on aortas and carotid arteries in human and pig is presented in Table V.2. Rupture properties of the aorta and carotid arteries depend on several factors, for instance age [112, 69, 222], location [193, 151], possible disease [232]. In both tissues the tensile strength in the circumferential direction is higher than in longitudinal direction. Conversely, the fracture dissection energy resulting from peeling tests is superior in the longitudinal direction compared to the circumferential direction. This difference can be explained by the collagen fibre arrangement. The collagen fibres in the media are divided in two fibre families, predominantly aligned along the circumferential direction [193, 97], reinforcing the material in that direction. Furthermore, the peeling tests in the longitudinal direction generate a highly "rougher" surface compared to the surfaces created by peeling in the circumferential direction [203, 223], demonstrating the anisotropy of the tissue and the importance of the microstructure in the understanding of the arterial failure behaviour.

In Saez et al. [193], the collagen fibres orientation and mechanical behaviour of the porcine carotid arteries were characterised by performing tension-inflation and uniaxial tests. The results confirmed the anisotropic behaviour of the tissue which is stiffer in the circumferential direction compared to the longitudinal direction. However, only the elastic behaviour is assessed and no data on the failure of the tissue are reported. Uniaxial tensile strength of human atherosclerotic carotid arteries was assessed in Teng et al. [214]. The failure properties against uniaxial tension was investigated for the three layers of the tissue. The results showed that adventitia is the strongest of the three layers. Furthermore, the intact specimens showed similar failure properties as medial samples, except for longitudinal ultimate strength which is twice as high in the intact samples than in the medial specimens. In Tong et al. [223], uniaxial tensile test in the radial direction and peeling test were performed in order to quantify the dissection properties of human carotid bifurcations. The results showed that the ultimate strength in radial direction and the dissection energy per reference area vary significantly with the location along the carotid bifurcation but also along the thickness of the sample. The highest radial failure strength (132 $\pm$ 20 kPa, n = 25) occurs at the interface between the media and the adventitia, whereas the lowest (104

$\pm$ 24 kPa, n = 18) was between the diseased media and intima. The strength of the tissue in the radial direction was higher at the bifurcation.

Another method to characterise the energy necessary to propagate a dissection is by the liquid infusion test. In Roach et al. [185], the results showed that the energy per reference area to split porcine samples were 2.84 $\pm$ 1.19 mJ/cm^2 for the upper thoracic aorta, 2.90 $\pm$ 1.21 mJ/cm^2 for the lower thoracic aorta, 1.88 $\pm$ 0.89 mJ/cm^2 for the upper abdominal aorta, and 11.34 $\pm$ 4.05 mJ/cm^2 for the lower abdominal aorta. These values are lower than the energies obtained with peeling tests for the same tissue. This may be explained by the difference between the tests.

Tensile tests					
Study	Tissue	Healthy / Diseased	Additional information	Circ. failure stress (MPa)	Axial failure stress (MPa)
Shah et al. [199]	Porcine ascending aorta	Healthy		2.510 ± 0.439 (n=11)	0.750 ± 0.103 (n=11)
Peña et al. [170]	Porcine descending aorta	Healthy	Whole	0.83 ± 0.57 (n=7)	0.45 ± 0.16 (n=7)
			Intima	1.42 ± 0.32 (n=7)	1.06 ± 0.53 (n=7)
			Media	1.70 ± 0.64 (n=7)	0.55 ± 0.14 (n=7)
			Adventitia	1.43 ± 0.40 (n=7)	1.34 ± 1.09 (n=7)
Vorp et al. [232]	Human ascending aorta	Healthy		1.800 ± 0.240 (n=7)	1.710 ± 0.140 (n=7)
		Aneurysm		1.180 ± 0.120 (n=23)	1.210 ± 0.090 (n=17)
García-Herrera et al. [69]	Human ascending aorta	Healthy	Age < 35	2.180 ± 0.240	1.140 ± 0.100
			Age > 35	1.200 ± 0.200	0.660 ± 0.070
Khamin et al. [112]	Human carotid artery	Healthy	Age 11-20	5.185 ± 0.215	3.885 ± 0.150
			Age 21-30	3.921 ± 0.308	2.695 ± 0.256
			Age 31-40	2.559 ± 0.243	1.862 ± 0.232
			Age 41-50	1.937 ± 0.154	1.261 ± 0.144
			Age 51-60	1.414 ± 0.071	1.077 ± 0.098
			Age 61-70	1.275 ± 0.099	0.855 ± 0.065
			Age < 71	0.906 ± 0.142	0.853 ± 0.107
Teng et al. [214]	Human carotid artery	Atherosclerosis	Media	0.519 ± 0.270 (n=11)	1.230 ± 0.533 (n=13)
			Adventitia	1.996 ± 0.867 (n=12)	1.802 ± 0.703 (n=12)
			Whole	1.047 ± 0.536 (n=13)	1.022 ± 0.427 (n=12)
This study	Porcine carotid artery	Healthy		3.089 ± 0.917 (n=10)	2.088 ± 0.865 (n=11)

Peeling tests					
Study	Tissue	Healthy / Diseased	Additional information	Circ. dissection energy (mJ/cm^2)	Axial dissection energy (mJ/cm^2)
Sommer et al. [203]	Human abdominal aorta	Healthy	Media	5.1 ± 0.6 (n=5)	7.6 ± 2.7 (n=7)
Kozuń et al. [118]	Human thoracic aorta	Atherosclerosis	A + MI	5.6 ± 0.9 (n=26)	7.6 ± 1.7 (n=7)
			AM + I	4.1 ± 1.0 (n=22)	4.7 ± 0.9 (n=8)
Noble et al. [159]	Porcine thoracic aorta	Healthy	Control	15.18 ± 2.70 (n=16)	18.33 ± 6.42 (n=16)
			Collagenase	10.81 ± 2.80 (n=17)	13.58 ± 3.12 (n=14)
			Elastase	13.24 ± 4.0 (n=16)	17.18 ± 7.12 (n=14)
			Glutaraldehyde	19.01 ± 6.05 (n=13)	18.63 ± 3.35 (n=14)
Myneni et al. [151]	Porcine ascending aorta	Healthy		20.55 ± 2.68 (n=11)	25.64 ± 9.56 (n=11)
	Porcine upper descending aorta			12.96 ± 3.72 (n=11)	16.42 ± 4.64 (n=11)
	Porcine lower descending aorta			11.27 ± 3.46 (n=11)	18.05 ± 9.58 (n=11)
Tong et al. [223]	Human carotid bifurcations	Healthy	A + M	6.5 ± 2.7 (n=19)	5.0 ± 1.0 (n=18)
			I + M	5.2 ± 3.1 (n=18)	3.6 ± 0.7 (n=17)
			Media	6.0 ± 1.6 (n=16)	4.8 ± 1.0 (n=14)
This study	Porcine carotid artery	Healthy		10.3 ± 2 (n=7)	26.3 ± 20 (n=7)

TABLE V.2 – Failure properties from aortic and carotid arterial tissue resulting from tensile and peeling tests. The values are presented as mean ± standard deviation. I: Intima, M: Media, A: Adventitia.

The purpose of this work is to understand the causes of the higher resistance of carotid artery against dissection compared to aortic tissue. In the present study, uniaxial and peeling tests were performed on porcine carotid artery in longitudinal and circumferential directions to characterise the anisotropic behaviour of this tissue. The rupture properties were also measured: the tensile strength and the critical fracture energy were reported in both principal directions.

V.2.2 Materials and methods

V.2.2.1 Specimen Preparation

Fresh porcine carotid arteries specimens were obtained from a local slaughterhouse. All tests were performed on the day of the animals' death. Loose connective tissues were carefully removed with a surgical scalpel before opening of the carotid arteries. The specimens were put in phosphate buffer saline (PBS) to avoid dehydration until use. Uniaxial tension samples were cut into dog-bone shapes either in longitudinal or circumferential direction (Figure V.11), while the samples for peeling test were cut into rectangular strips. For the peeling tests, the rectangular strips were cut and slit open at one end in order to obtain two "tongues" mounted on the tensile testing machine. The dimensions of the samples were measured using a Vernier caliper. During the tests, the samples were kept hydrated using a humidifier.

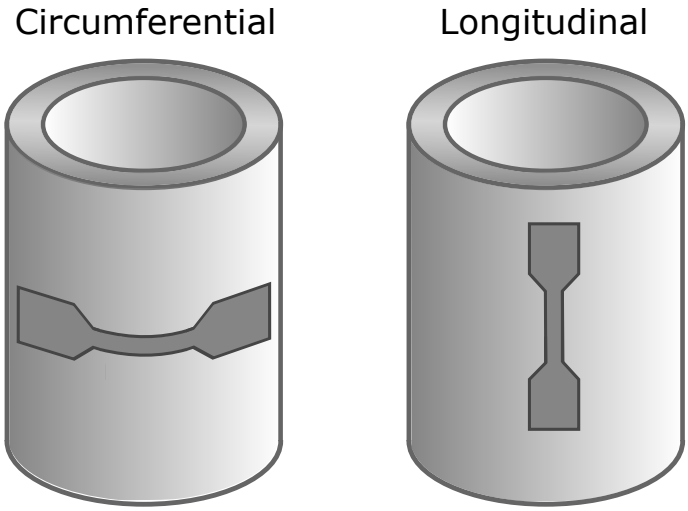

Figure V.11 – Schematic of the orientation of the carotid specimens.

V.2.2.2 Mechanical testing

Tensile test

Uniaxial tensile tests were performed using an Instron 5960 (Instron; Norwood, MA) testing system equipped with a 500 N load cell (Figure V.12). The samples were fixed using clamping jaws and sandpaper to avoid slipping. The extension rate was equal to 15 mm/min throughout the tests. Force and displacement were obtained using the testing interface software Bluehill. The tensile tests were performed in both directions until complete failure of the samples. Assuming incompressibility, the Cauchy stress σ was calculated as the force F divided by the deformed cross-sectional area A, and the stretch in the tension

direction λ was calculated as total length of the deformed sample normalised by the initial specimen length.

$$\sigma = \frac{F}{A}\,, \quad \text{with } A = \frac{WT}{\lambda}, \tag{V.1}$$

where W and T are the initial width and thickness of the sample respectively. From the stress-strain curve obtained for each sample, the maximum elastic modulus was calculated as the maximum slope, while the tensile strength was taken as the ultimate stress before failure of the specimen (Figure V.13).

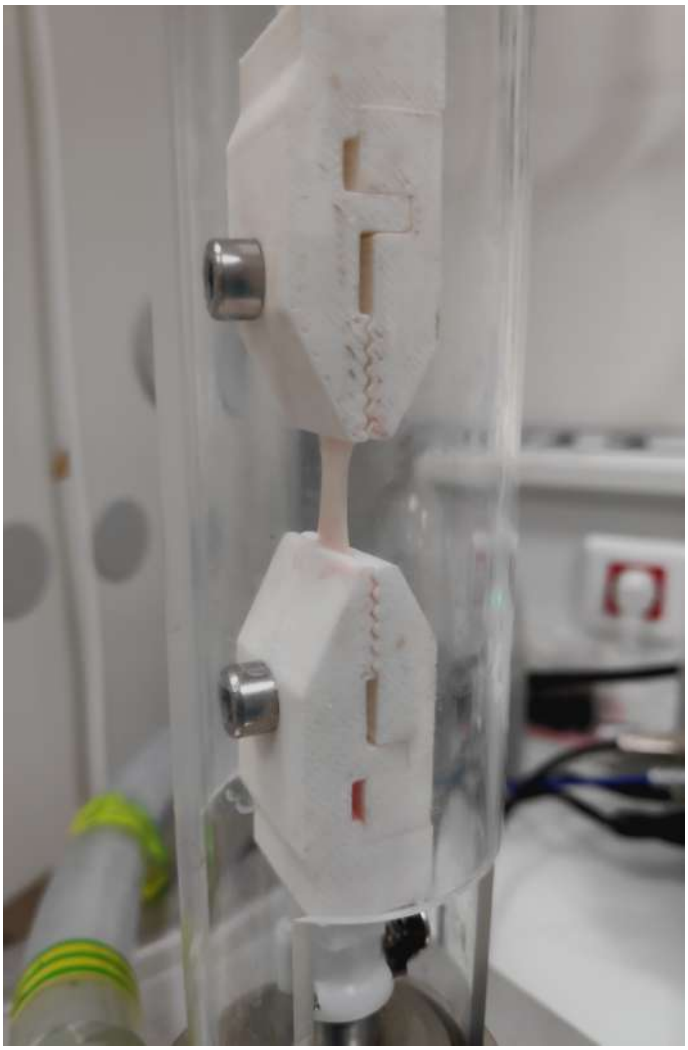

FIGURE V.12 – Photo of the uniaxial tensile system with a carotid specimen clamped in the jaws.

Peeling test

Both tongues of the samples were mounted on the machine clamps with sandpaper. As tensile test, the strain rate was 15 mm/min and the force and displacement were recorded throughout the test. India ink was used prior and after testing in order to measure the delamination length. Following the study of Sommer et al. [203] and Noble et al. [159], the critical energy release rate G_c was quantified as:

$$G_c = \frac{(W_{ext} - W_{elastic})}{L}, \tag{V.2}$$

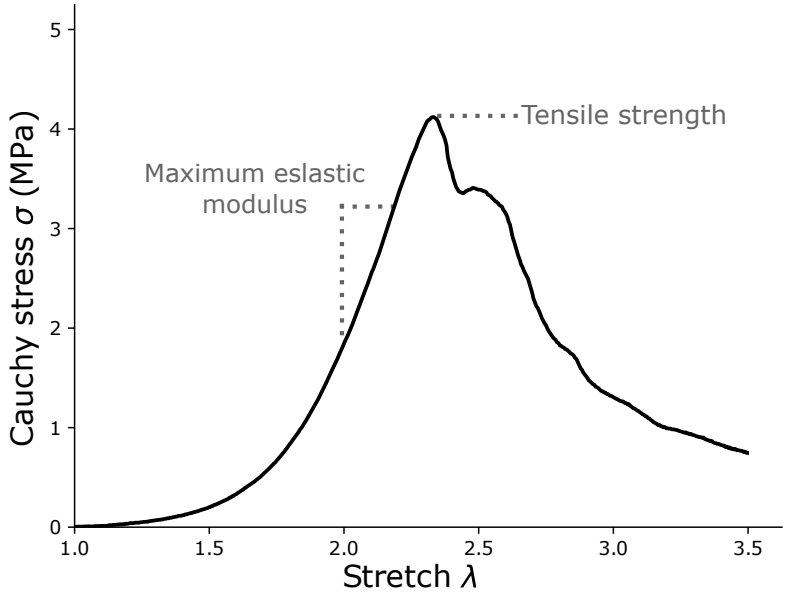

Figure V.13 – Representative stress-strain curve demonstrating the definitions of the maximum elastic modulus and the tensile strength used in this study.

where W_{ext} and $W_{elastic}$ are the externally applied work and stored energy per unit width, and L is the length of tissue before peeling. W_{ext} is defined as:

$$W_{ext} = 2Fl, \tag{V.3}$$

where F is the mean peeling force per unit width, and l is the length of tissue dissected in the stretch state. Finally, $W_{elastic}$ is calculated as:

$$W_{elastic} = F(l - L). \tag{V.4}$$

A schematic of the peeling test is presented in the Figure V.14.

V.2.2.3 Statistical Analysis

Mann–Whitney U tests were performed to compare tensile strengths and dissection energies in both directions resulting from the tensile and peel tests. The significance was assumed for a p-value less than 0.05.

V.2.3 Results

The mean thickness of the samples was 1.08 ± 0.19 mm.

V.2.3.1 Tensile test

Seven pigs provided 10 specimens oriented in the circumferential direction and 11 samples oriented in the longitudinal direction. The measured tensile strength of carotid arterial tissue in the circumferential direction (3.089 ± 0.917 MPa) was found to be significantly ($p < 0.05$) different than in the longitudinal direction (2.088 ± 0.865 MPa) (Figure V.15). A similar finding was observed for the maximum elastic modulus in the circumferential direction (7.22 ± 3.26 MPa) compared to the longitudinal direction (4.92 ± 2.91 MPa) (Figure V.15), however, no significant difference was noted (p=0.1).

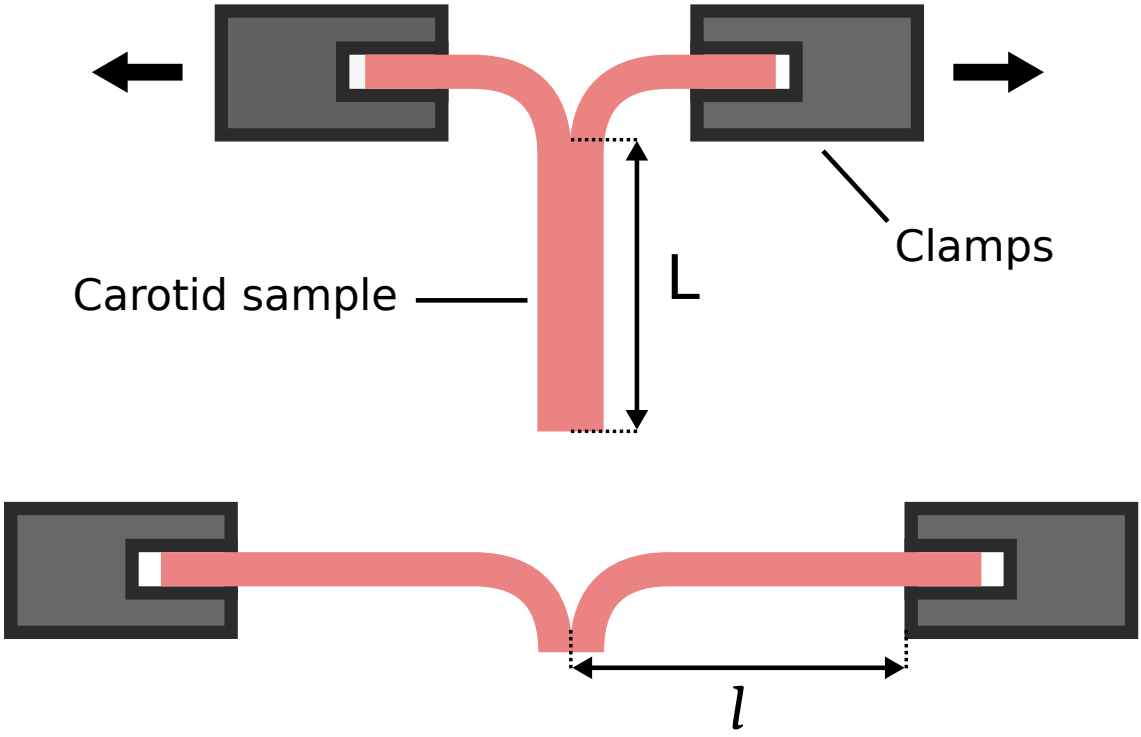

FIGURE V.14 – Schematic of the peeling test before and after the delamination of the tissue. The top image shows the setup before the experiment with the both tongues being held by the clamps, L is the length of tissue before peeling. In the bottom image l is the length of tissue in the stretch configuration.

The initial failure always occurred at the intimal side, with a rupture of the intima and the media while the adventitia hold the remaining load. In few cases, the stress in the adventitia alone became higher than the first peak stress until complete failure (Figure V.16).

V.2.3.2 Peeling test

Four pigs provided 7 specimens oriented in the circumferential direction and 7 samples oriented in the longitudinal direction. The results of the peeling tests are presented in Figure V.17. The force per width was found to be significantly greater ($p < 0.05$) in the circumferential direction (49.7 ± 9 mN/mm) than in the longitudinal direction (70.9 ± 38 mN/mm) (Figure V.18). Similarly, the dissection energy was significantly higher ($p < 0.05$) in the circumferential direction (10.3 ± 2 mJ/cm^2) compared to the longitudinal direction (26.3 ± 20 mJ/cm^2) (Figure V.18).

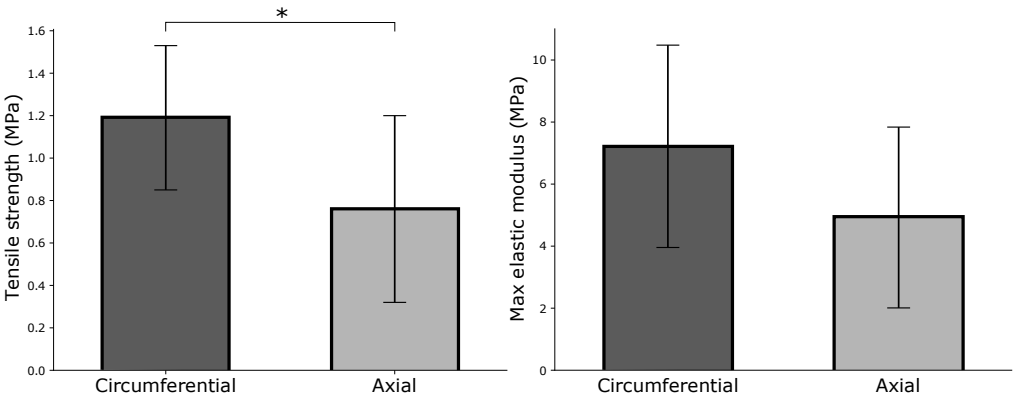

Figure V.15 – Tensile strengths and maximum elastic modulus of the carotid arterial tissue in the circumferential and longitudinal directions. Values are presented as mean ± standard deviation.

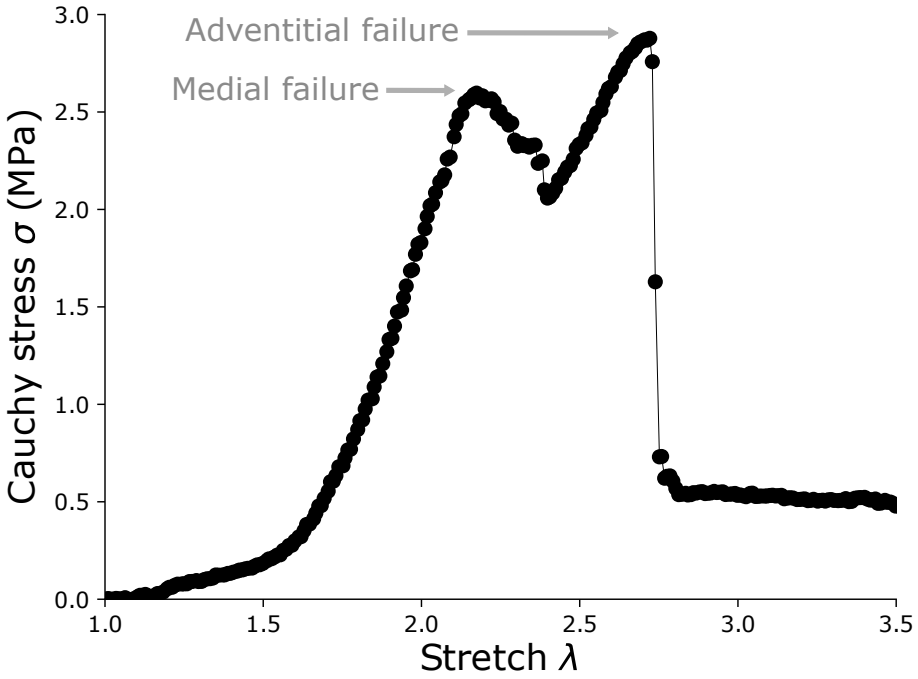

Figure V.16 – Characteristic stress-strain curve where the first peak correspond to medial failure while the second peak is adventitial failure.

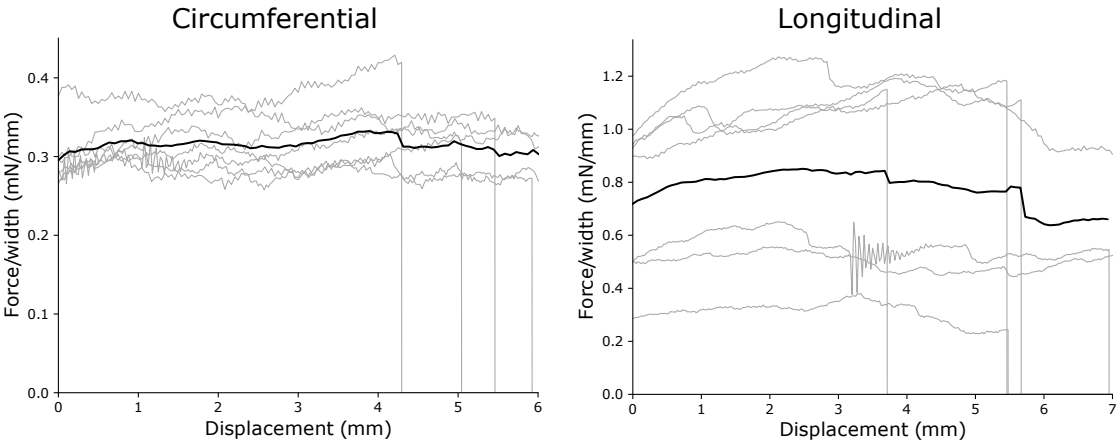

FIGURE V.17 – Force per width as a function of the displacement for circumferential and longitudinal directions generated from peeling tests. The thick curve is the mean curve of all the experimental tests.

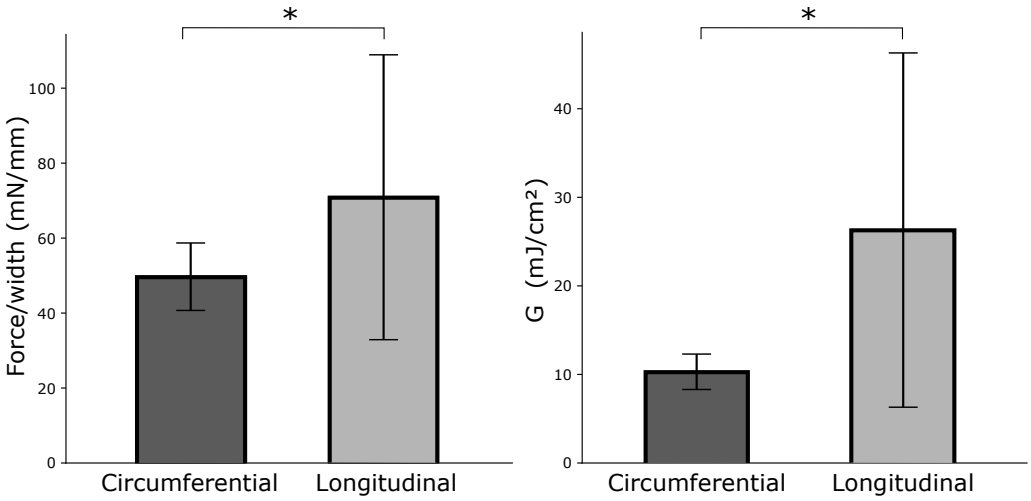

FIGURE V.18 – Forces per width and critical fracture energies of the carotid arterial tissue generated from peeling test in the circumferential and longitudinal directions. Values are presented as mean ± standard deviation.

V.2.4 Discussion

The purpose of this study was to investigate the reasons behind the greater resistance of porcine carotid arteries against dissection compared to porcine or human aorta. Therefore, we performed uniaxial tensile and peeling tests in circumferential and longitudinal directions on porcine carotid arteries in order to assess the mechanical behaviour of this tissue. To the author's knowledge, no failure values on porcine carotid arteries were previously reported in the literature.

As in other arterial tissues, the uniaxial tensile tests showed an anisotropy of the tissue with a stiffer behaviour in the circumferential direction than in the longitudinal direction (Figure V.15). The ultimate tensile strength was also higher in the circumferential direction compared to the longitudinal direction (Figure V.15). The tensile failure values in the circumferential (3.089 ± 0.917) and longitudinal (2.088 ± 0.865) direction are higher than the failure values found in the literature from other arterial tissues (Table V.2). Only the tensile strengths of the human carotid arterial tissue of young patients exceeded these values [112]. These results demonstrate the strong resistance of the tissue against failure. Furthermore, the larger the vessel radius the higher the wall tension withstood by the arterial wall. The diameter of the aorta is about 3 time that of the carotid artery while the thickness is only about 1.5 times [108, 2], therefore, the ratio radius divided by thickness is higher in the carotid artery. As a consequence, for the same pressure, the circumferential stress supported by the aorta is considerably larger than for the carotid artery, making it more prone to aortic dissection.

The force per width and the dissection energy per reference area generated by the peeling tests also showed a strong resistance of porcine carotid arteries in both directions compared to human carotid arterial and aortic tissues [223, 118, 222], and compared to porcine aortic tissue in longitudinal direction or both directions depending on the location along the aorta [151, 159]. This results may explain the difficulty to create an *in vitro* dissection in carotid artery samples with the tension-inflation test. A higher dissection energy means that the pressure necessary to propagate the notch would be higher than in aortic tissue.

The initial rupture of the media before the adventitia observed in this study (Figure V.16) was also noted in Teng et al. [214]. This phenomena is caused by the lower strength of the media against tensile loading compared to the adventitia, but also by the low strength of the tissue in the radial direction as shown in the literature [203, 223] and demonstrated in I. Therefore, when the media breaks, the cohesion strength between the media and the adventitia is not enough to hold the two layers together. It could be interesting to perform a shear test or a tensile test in the radial direction to measure these properties in the case of the porcine carotid artery.

Different limitations need to be pointed out to evaluate the relevance of this study. Preconditioning was not applied for uniaxial tensile specimens before mechanical testing. This could affect the mechanical behaviour of the tissue, however, the principal objective of this study was to assess the failure properties and not the elastic behaviour. Another limit is the lack of precision in the creation of the initial cut in the samples for the peeling test due to the small dimensions of the specimens, this may affect the result as it was demonstrated that the result of the peeling test varies depending on the location of the rupture along the thickness of the sample [223].

V.2.5 Conclusion

The present study quantified the failure properties of the porcine carotid artery in the circumferential and longitudinal directions by performing uniaxial tensile test and peeling test. The tensile failure values and the fracture energy required to peel the porcine carotid artery samples was much higher than to peel human carotid artery or aorta for both directions. This result may explain the difference in resistance against dissection of porcine carotid artery compared to other tissues. These new failure data may contribute to the the understanding of the underlying phenomena leading to aortic dissection.

Highlights

- Carotid artery is less prone to dissection than aorta
- Tensile and peeling tests were performed on carotid artery in circumferential and longitudinal directions
- The porcine carotid artery exhibited higher dissection energies in both directions compared to aortic tissue explaining why this tissue is more resistant to dissection than aorta

Chapter VI

Étude des mécanismes de la dissection aortique grâce aux rayons X - *Investigation of aortic dissection mechanisms using X-ray tomography*

The previous chapter demonstrated the high resistance of carotide artery to dissection compared to aorta. Therefore, in this study, a tension-inflation test is performed on notched rabbit aortas and the dissection of the segments is observed with X-ray microtomography. The objective is to assess the influence of the notch on the critical pressure and to describe the mechanisms underlying aortic dissection.

Contents of the chapter

Résumé du Chapitre

Dans le chapitre précédent, l'étude des propriétés de rupture de l'artère carotide porcine a révélé une résistance à la dissection supérieure à l'aorte, expliquant pourquoi la dissection de ce tissu grâce à un test de traction-gonflement était aléatoire, même à haute pression. Ainsi, afin d'obtenir une dissection répétable, le test *in situ* de traction-gonflement a été réalisé cette fois-ci sur des segments aortiques de lapin avec une fissure initiant la délamination. La séquence d'initiation de ce processus est mal décrite dans la littérature en raison de la difficulté d'observation de cette maladie intramurale et dynamique. L'objectif de cette étude était de mieux comprendre les mécanismes conduisant à l'initiation et à la propagation de la dissection aortique. Deux types de fissures ont été réalisées, dans la direction circonférentielle ($n = 4$) et dans la direction longitudinale ($n = 2$). Au cours de l'essai mécanique, la tomographie à rayons X a été utilisée pour observer la méso-structure de la paroi aortique à différentes étapes de pression avant la dissection complète de l'échantillon. Il a été démontré que la morphologie de l'entaille suivait la géométrie de la paroi aortique pendant le gonflement comme démontré dans le Chapitre V, et restait donc relativement constante. L'aorte a également été imagée pendant le début de la dissection, ce qui a permis de décrire les phénomènes avant la propagation de la déchirure et de démontrer la présence d'un renflement de la paroi aortique à l'extrémité de l'entaille déformant la paroi restante et créant une forte concentration de contraintes. Des corrélations ont été observées entre la pression critique et la profondeur de la fissure, l'ouverture de la fissure et sa largeur. Aucune différence nette entre les fissures initiales circonférentielles et longitudinales n'a été observée, bien que le petit nombre d'échantillons empêche toute conclusion. Il n'existe pas d'étude expérimentale dans la littérature présentant des informations sur la géométrie de l'aorte avant et après dissection. Les images 3D de la structure de l'aorte à différentes étapes de la dissection présentées dans cette étude répondent à ce manque et pourraient permettre la validation de modèles numériques, comme le modèle du Chapitre IV. De plus, ces résultats permettent de mieux comprendre les mécanismes impliqués dans la dissection aortique et pourraient conduire à un meilleur diagnostic et à de meilleurs traitements des patients souffrant de cette maladie.

VI.1 *In situ* X-ray microtomography visualization and investigation of aortic dissection initiation and propagation in rabbit aorta by tension-inflation test

Abstract

Aortic dissection is a complex disease involving multiple mechanisms. The initiation sequence of this process is poorly described in the literature due to the difficulty of observation of this intramural and dynamic disease. The purpose of this study was to better understand the mechanisms leading to the initiation and propagation of aortic dissection by performing *in situ* tension-inflation test on notched rabbit aortic segments. Two types of notches were performed, in the circumferential direction (n = 4) and in the longitudinal direction (n = 2). During the mechanical test, X-ray tomography was used to observed the meso-structure of the aortic wall at different pressure steps before complete dissection of the specimen. The morphology of the notch was shown to follow the geometry of the aortic wall during inflation, and thus remained relatively constant. The aorta was also imaged during the initiation of the dissection allowing a description of the phenomena prior to propagation of the tear and demonstrating the presence of a bulge of the aortic wall at the tip of the notch deforming the remaining wall and creating a high stress concentration. Correlations were observed between the critical pressure and the tear depth, tear opening, and the tear width. No clear difference between circumferential and longitudinal initial notches was observed, although the small number of specimens prevents any conclusion. These findings provide a better understanding of the mechanisms involved in aortic dissection and could lead to better diagnosis and treatments of patient suffering from this disease.

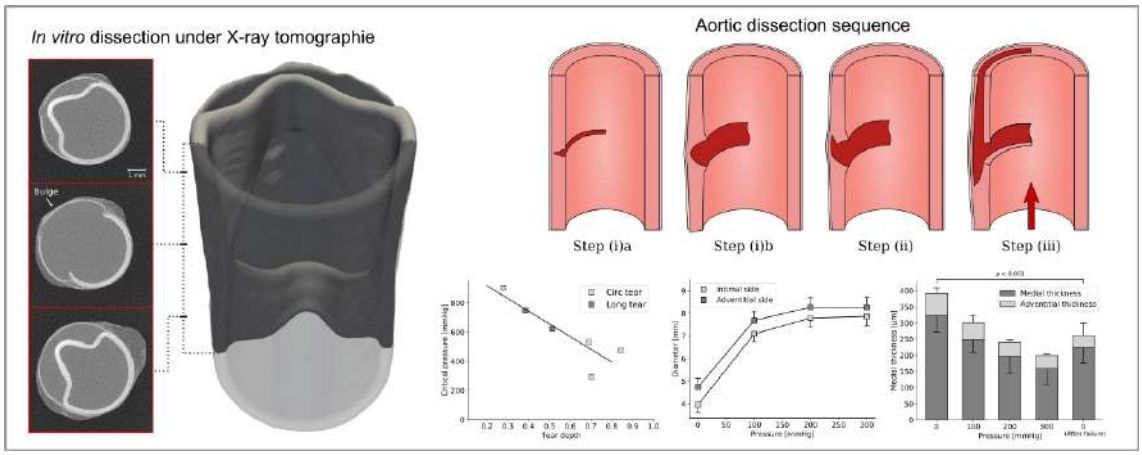

VI.1.1 Introduction

In Chapter V, the results showed that the porcine carotid artery was resistant to dissection due to its high tensile failure values and fracture energy in both circumferential and longitudinal directions. As a consequence, a new tissue was necessary to achieve an *in vitro* dissection. The tissue should be prone to dissection in a repeatable way. Furthermore, the pressurized sample should fit in a box of 10 x 10 x 10 mm^3. After an investigation of different tissues, we chose to use rabbit aortas. Previous mechanical tests on rabbit tissue showed that a dissection consistently occurs in the tissue for a pressure inferior to 800 mmHg. Moreover, the rabbit aorta fit in the field of view of the X-ray tomography setup [247].

The loading state leading to the initiation and propagation of a tear in the aorta is poorly understood. The creation of a tear seems to involve mechanobiology and medial degradation combined with mechanical fatigue [190, 156]. On the other hand, the propagation of a tear is a purely dynamic process that can be modeled experimentally by reproducing the dissection event in a controlled manner. This makes it possible to study different questions concerning aortic dissection. One of them is the reason why, in clinics, 80% of intimal tears happen in the transverse direction. According to the author's knowledge, only one experimental study in the literature investigated the impact of the orientation of the initial tear on its propagation [85]. This study inflated bovine aortic rings with a notch on the intimal side. The tear was either in the radial or 45°-from-radial direction. The results showed that, regardless of the direction, the crack propagated in the circumferential direction in a similar manner. However, this study did not investigate the pressure required to propagate the notch.

Numerical models investigating aortic dissection have become increasingly complex. Starting from simple 2D isotropic models [217], recent studies have used 3D anisotropic models involving failure as seen in Chapter IV and in the literature [81, 64]. Nevertheless, a major issue encountered by these studies is the lack of experimental data concerning aortic dissection. A complete set of 3D imaging data from the same aorta before and after an aortic dissection would be an important contribution to the scientific community. This data would allow a complete modeling of the pathology and lead to a better understanding of the phenomena involved. The creation of such a database is one of the objectives of this study.

In the present study, a tension-inflation test was performed on notched rabbit aorta inside an X-ray microtomography setup. During the mechanical test, the microstructure was observed at different pressure steps until dissection occurred. The objective was to evaluate the impact of the initial tear geometry and orientation on its propagation into an aortic dissection. Furthermore, these data would be valuable in the modelling of aortic dissection.

VI.1.2 Materials and methods

VI.1.2.1 Tension-inflation device

The tension-inflation custom-device used in the present work is the same as the one presented in Chapter V. Nevertheless, a change should be noted: a proportional–integral–derivative controller (PID controller) was integrated into the control software in order to maintain a constant pressure during the X-ray scan, thus avoiding viscoelastic effects or compensating possible leaks.

VI.1.2.2 Sample preparation

The descending aorta from the left subclavian artery to the diaphragm was carefully excised from 6 rabbits just after death. The branches were sutured with silk wire with the help of a dissecting scope. During this process, the aortas were immersed in phosphate-buffered saline (PBS) to avoid dehydration of the tissue. The samples were subsequently frozen at -20°C for future use. After defrosting at room temperature, each sample was immersed for 12 hours in a diluted solution of sodium polytungstate (15 g/L) at 4 °C to ensure a good contrast on the X-ray tomography images. The immersion time has been determined in a previous study and guarantees full penetration of the contrast agent in the tissue. This time was half the immersion time found in Helfenstein-Didier et al. [89] due to the lower sample thickness.

The day of the test, the aorta was turned inside out and a notch was created on the intimal side of the specimen with a micro dissecting knife. The notch was cut on the opposite side of the intercostal branches. The notches were cut in two orientations: circumferential (n = 4) and longitudinal (n = 2). The sample was then mounted on the tension-inflation device. Attachment of the sample to the machine connectors was done with silk wire.

VI.1.2.3 X ray

As described in Chapter V, we used a Phoenix^{TM} VtomeX tomograph equipped with a Varian^{TM} Paxscan X-Ray detecton of size 1920 x 1536 pixels. The X-ray tomography setup was powered at a voltage of 80 kV and a current of 370 µA. The current was increased compared to Chapter V in order to reduce the acquisition time to 180 seconds. The number of projections was 900. The voxel size was 7 x 7 x 7 µm^3 and the field of view was 10.5 x 10.5 x 8.75 mm.

VI.1.2.4 Protocol

Once the sample was attached to the device, two radios were taken at 0 and 90 degrees to calculate the initial diameter of the sample. Then, an axial pre-stretch of 1.27 was applied to the specimen to reproduce the physiological state. A syringe pump infused PBS into the aorta to increase the pressure at a quasi-static rate (5 ml/min). Scan were taken at 0 mmHg and every 100 mmHg until failure. Each scan lasted 180 seconds, during that time the PID controller maintained the pressure constant. Whenever possible, radiographic images were taken at a rate of 5 image per second during the propagation of the dissection.

VI.1.2.5 Data analysis

Measurement

The morphology of the notch was quantified with three metrics:

- the tear depth,
- the width, measured by the angle of the notch in the circumferential direction,
- the length, measured by the size of the notch in the longitudinal direction,
- the tear opening length in order to compare specimens with a circumferential and a longitudinal notch.

The tear depth was normalized with the medial thickness to allow a comparison between specimens and to take into account the decreasing of the aortic diameter during inflation: the value ranges between 0 (intimal side) and 1 (adventitial side). The different measurements were taken manually with the software imageJ [196, 192]. The mean of at least three measures was taken as the final value to avoid local effects. The measures of diameters were taken far from the notch for the same reason. The segmentation of the aorta and the 3D representation were performed with 3D Slicer [58]. The software ParaView [206] was used for the 3D display.

Stretch-stress calculations

The circumferential stretch of the aortic wall λ_θ was calculated by

$$\lambda_\theta = \frac{r_m}{r_m^0}\,, \tag{VI.1}$$

where r_m is the midwall radius of the aorta and r_m^0 is the initial midwall radius at 0 mmHg of pressure. The aortic wall was assumed thin (diameter/thickness > 20). As a consequence, the circumferential Cauchy stress σ_θ was calculated by

$$\sigma_\theta = \frac{P\,(D+h)}{2h}\,, \tag{VI.2}$$

where P is the internal pressure, D is the inner diameter of the aorta, and h is the wall thickness. A paired Student's t-test was performed to assess the difference between the aortic thickness before and after propagation of the dissection.

VI.1.3 Results

The notch propagated in all the specimens for critical pressures ranging from 291 to 902 mmHg. Local propagation of the crack was observed at different stages of inflation; however, the critical pressure was taken as the pressure at which the tear propagates throughout the segment. The mean critical pressure was 551 ± 256 mmHg (Mean ± SD, n = 4) and 685.5 ± 88.4 mmHg (n = 2) for the tear in the circumferential and longitudinal direction, respectively. In most of the samples the dissection propagated in the antegrade and retrograde directions, this could be explained by the absence of flow in our experiment. No re-entry tear was identified; however, the entire aorta could not be assessed due to the limited field of view in the axial direction (8.75 mm). A front view with a focus on the notch area at different pressures and after the propagation of the tear is presented in Figure VI.1. The notch is clearly visible, the delamination started between 100 and 200 mmHg. Figure VI.2 shows a 3D view with three cross-sections of a representative dissected specimen. Higher than 300 mmHg of pressure, the scan could not always be performed due to movement of the tissue during the acquisition and difficulty of reconstruction. Nevertheless, at high pressure the geometry of the aorta remained largely unchanged until dissection. In most of the specimens a rupture occurred in the false lumen after the dissection in order to reduce the pressure imposed by the pressure-controlled pump. The same phenomenon is observed in clinic as the rupture appears most of the time in the false channel due to the small thickness of the outer wall [186, 217]. A succession of radiographic images taken during the dissection is presented in Appendix C.1. According to these images, the dissection propagated in the specimen in less than a second; however, some local changes can be seen before the propagation around the notch.

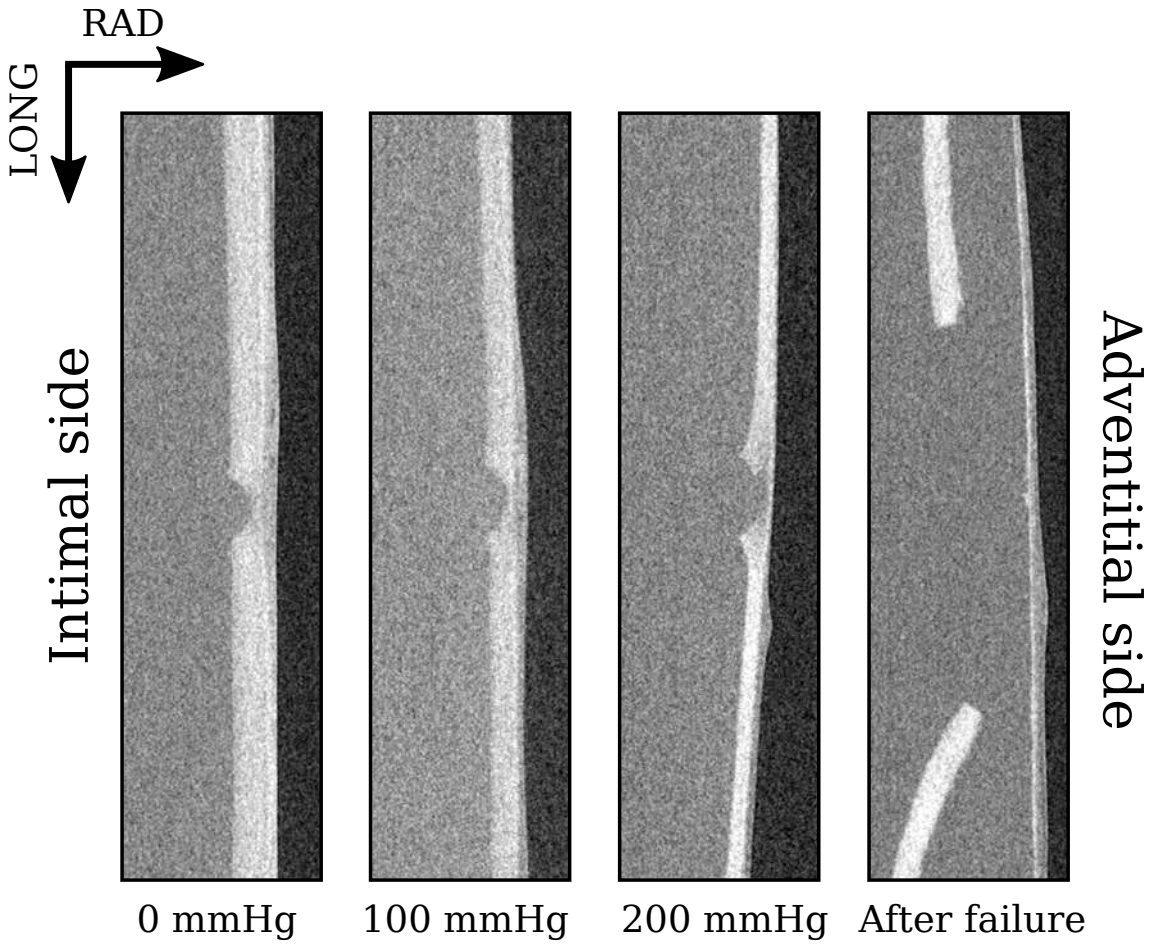

Figure VI.1 – Front view of the aortic wall with a focus on the notch at different pressures and after propagation of the dissection along the aorta. The intimal side is on the left whereas the adventitial side is on the right.

In the Figure VI.3, a specimen is presented before and after propagation of the dissection for different types of initial notches. The circumferentially notched sample with a deep tear (I) delaminated over more than half its circumference at close to the interface between media and adventitia. The specimen with a shallow circumferential notch (II) delaminated over most of its circumference; moreover, the intimal tear also propagated in the radial-longitudinal plane creating the pattern observed in Figure VI.3 all along the sample. The medial thickness decreased between the two states for all the samples. In addition, a bulge could be observed at the tear site in sample I, the same phenomenon was shown in Figure VI.2 in the middle cross-section. This mechanism is associated with a reduced radius of curvature of the undissected wall around the tear site which can be observed in the middle cross-section in Figure VI.2. Thus the aortic wall morphology was deformed by reducing the true lumen diameter to produced this bulge shape. Furthermore, the circumference was equal between the aortic segment in the initial state and after dissection, indicating that the outer wall, composed of the adventitia and few medial lamellae, did not underwent a plastic effect. This phenomenon was observed only on samples with a deep circumferential tear. Specimens with a shallow circumferential tear propagated in the radial-longitudinal plane in addition to the circumferential-longitudinal plane and either delaminated on a large part of the circumference or rupture close to the notch.

As observed and quantified by Holzapfel et al. [96] a complex 3D residual stress is present

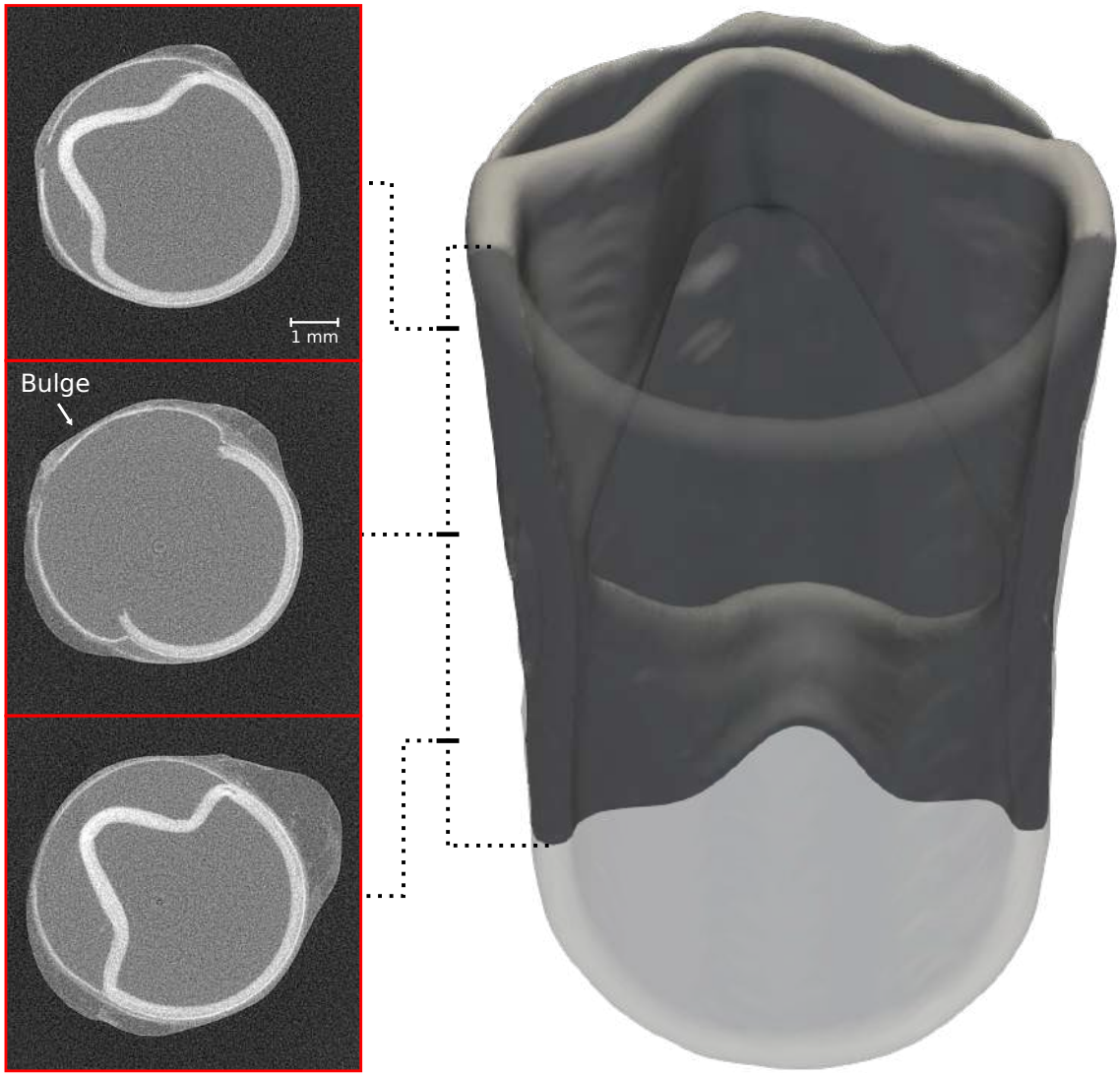

FIGURE VI.2 – Three-dimensional segmentation of a representative specimen with a circumferential notch after aortic dissection. Three cross-sections were displayed at different locations along the longitudinal axis. The total length of the specimen is 8.75 mm. The outer wall presents a bulge in the middle cross-section.

in the arterial tissue. As a consequence, the intimal flap shortens once separated from the outer wall due to the release of residual stresses [245]. This phenomenon hinders the investigation of an eventual permanent deformation due to the high stress experienced by the aortic segments before dissection. The elastic recoil of the intimal flap in the circumferential direction was measured between 5.3% and 12.3% in this study and can be observed in Figure VI.2. This caused a partial collapse of the flap and in some cases a complete obstruction of the true lumen.

The evolution of the morphology of the notches is presented in Figure VI.4. These dimensions are, in most cases, constant during the inflation of aortic samples. These observations confirmed that the morphology of the notch follows the geometry of the aortic wall as showed in Chapter V. The critical pressure as a function of the tear depth, the tear opening, and the tear width are presented in Figure VI.5. The critical pressure (P_c) was correlated with the tear depth (d)

$$P_c = -873\ d + 1092, \tag{VI.3}$$

the tear opening (c_o)

$$P_c = -514\ c_o + 1203, \tag{VI.4}$$

and the tear width (w)

$$P_c = -2,6\ w + 799, \tag{VI.5}$$

with r^2 of 0.76, 0.67 and 0.42, respectively. These linear relations should be taken with caution as they were calculated with only six points (four points for the circumferential tear and two points for the longitudinal tear). For the same reason, the correlations were calculated one variable at a time and not with a multiple linear regression.

The inner diameter of the specimen before applying the pre-stretch was 4.51 ± 0.41 mm. Manual measurements of diameters and thicknesses revealed a marked increase of the inner and outer diameter before reaching a plateau around 100 mmH, while medial and adventitial thicknesses decreased with the pressure (Figure VI.6) as observed in Figure VI.3. Furthermore, the thickness before and after propagation of the tear were compared and it appears that they are significantly different ($p < 0.001$) with the lower being the thickness after failure. The thickness was measured far from the failed part of the aorta to avoid local effect induced by the dissection. The same effect was observed on specimens that underwent a first inflation to 300 mmHg without propagation of the notch. The mean circumferential Cauchy stress in the aortic specimens is plotted as a function of the pressure and stretch in Figure VI.7.

Since the pressure steps were large, a sample was followed with radiographic images during the inflation between 0 and 300 mmHg to investigate the exact shape of the observed curves. The result of this test is presented in Appendix C.2.

During the preparation of the sample, the notch was made between the intercostal arteries in order to avoid any interferences with the dissection. Due to the field of view, it was rarely possible to see the aortic dissection interact with a branch. However, in one of the samples, the dissection was stopped in the circumferential direction by an intercostal artery, leading to the rupture of the aortic wall near the branch ostium, as shown in Figure VI.8.

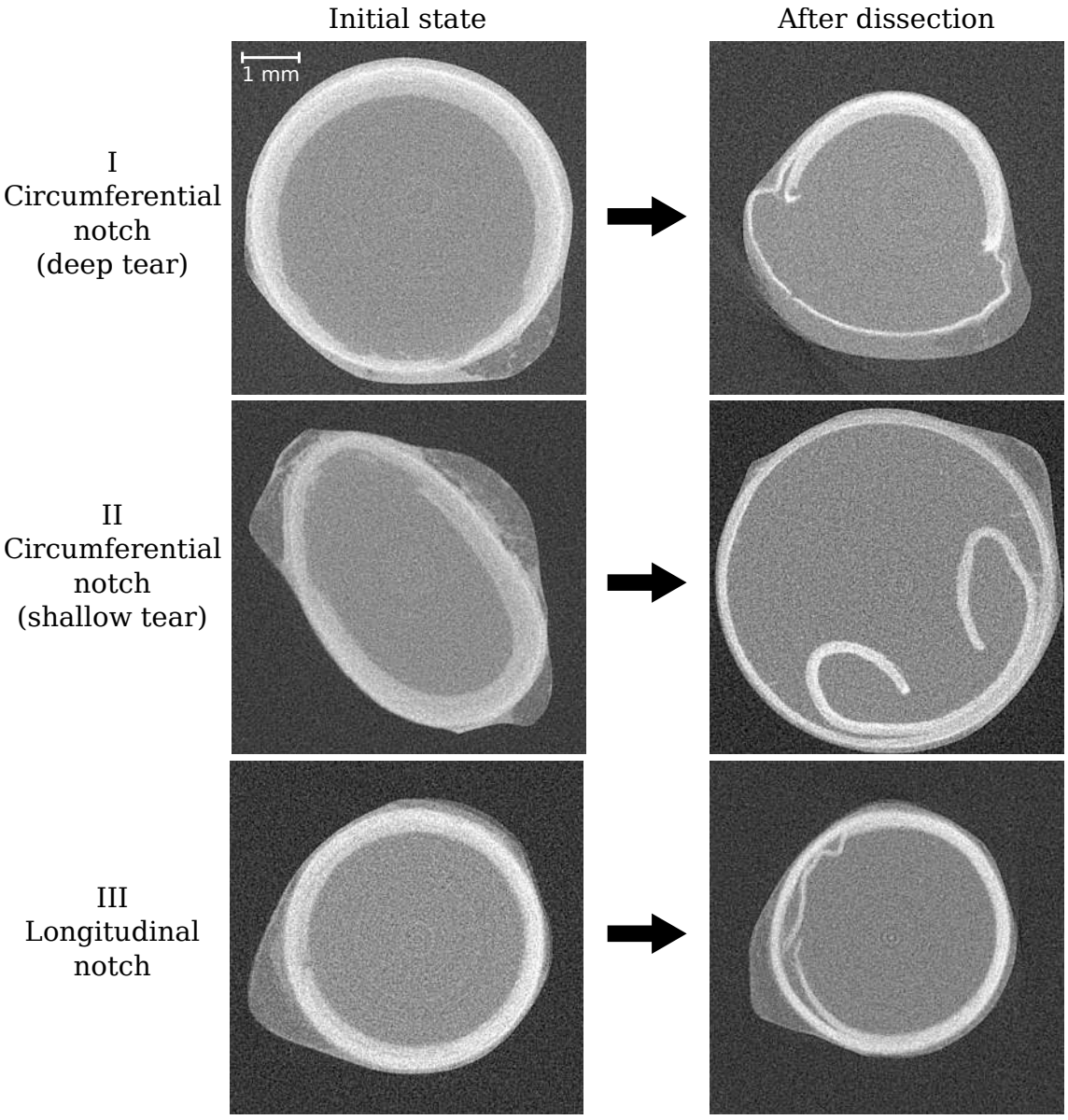

FIGURE VI.3 – Cross-sections of three specimens at the beginning of the inflation test and after propagation of the dissection. Three different types of initial notches are presented. The initial and final scans were taken at 0 mmHg of pressure. The images show the middle of the sample, where the depth of the intimal tear is the highest. The specimens were named I, II, and III for simplicity. The positions of the notches are bottom in sample I, top-left in sample II, left in sample III. In specimen I, the propagation followed a similar path to the one presented in Figure VI.2. In sample II the notch propagated on a large part of the circumference but also in the radial-longitudinal plane along the segment. In sample III the notch propagated also in the circumferential direction and in the radial-longitudinal plane.

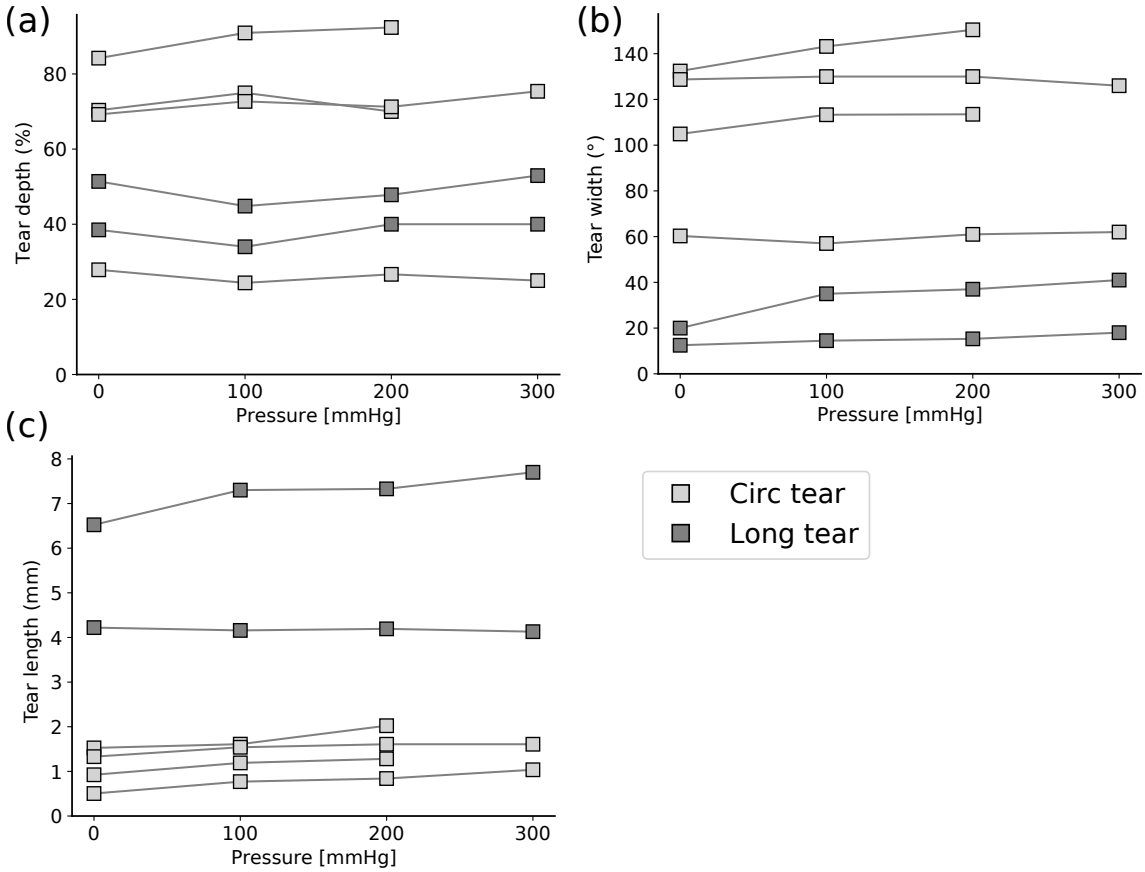

Figure VI.4 – (a) the tear depth, (b) the tear width, and (c) the tear length were plotted as a function of the pressure for each sample. Samples with a circumferential and longitudinal notch were differentiated.

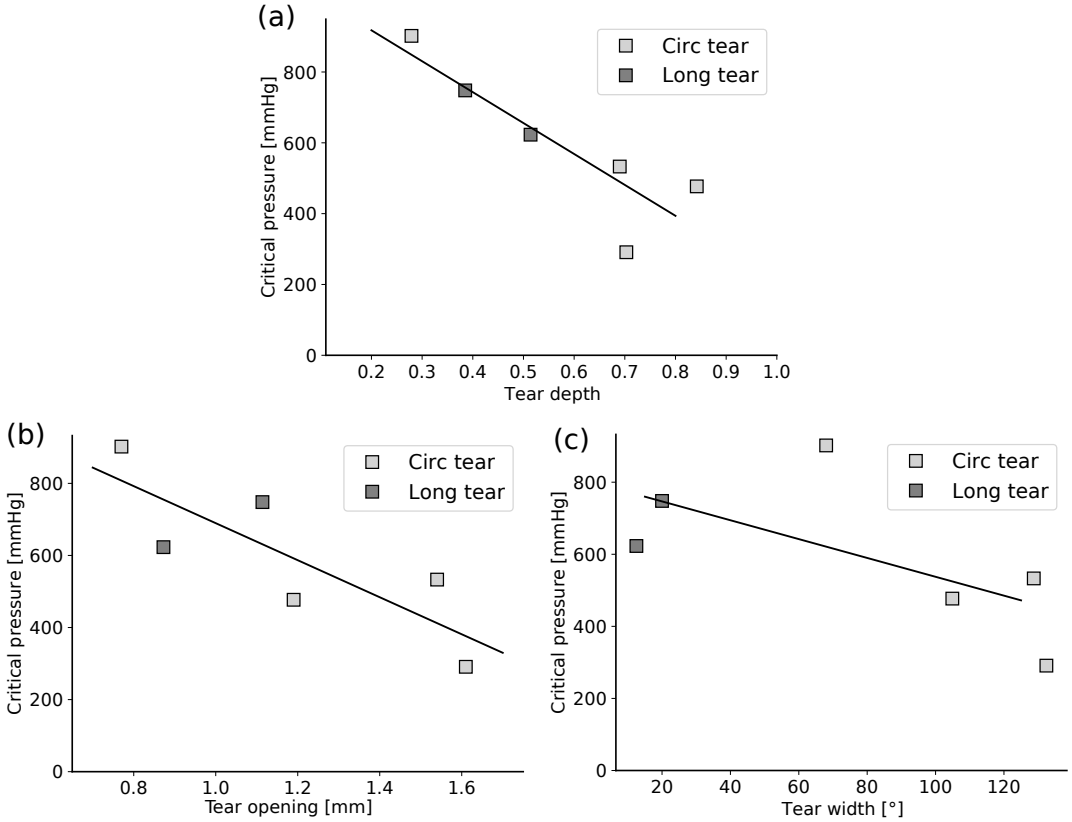

FIGURE VI.5 – The critical pressures required to propagate the circumferential and longitudinal notches were plotted as a function of (a) the tear depth measured at 0 mmHg, and (b) the tear opening measured at 100 mmHg, and (c) the tear width measured at 0 mmHg. The tear opening was measured at 100 mmHg and not at 0 mmHg because a measure in the initial state would not have been representative of the real tear opening length. The tear depth was normalized with the medial thickness, a value of 0 corresponds to the medial side while a value of 1 indicates the adventitial side. The lines represents the correlation found between the two variables. The r^2 of (a), (b), and (c) were 0.76, 0.67 and 0.42 respectively.

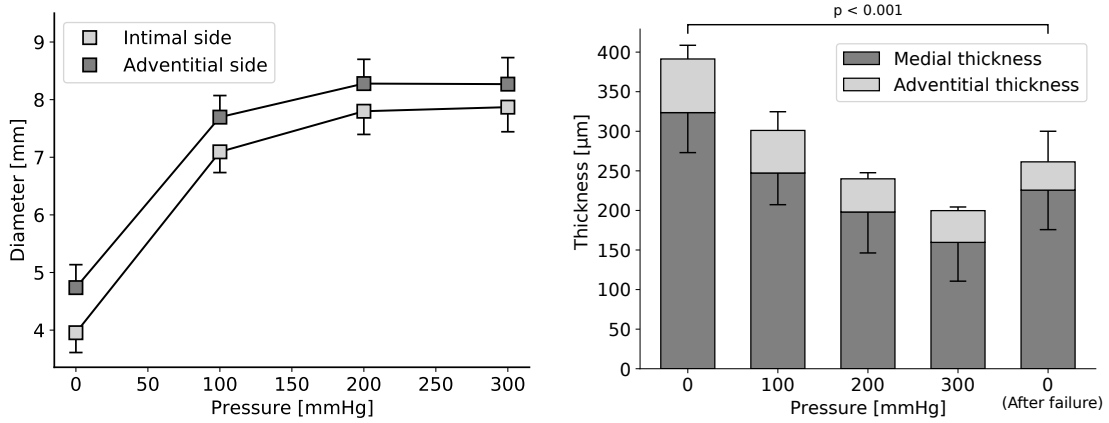

FIGURE VI.6 – (a) Inner and outer diameter of the aortic wall (mean values and standard deviations) as a function of the pressure. (b) Evolution of the medial and adventitial thicknesses (mean values and standard deviations) at each pressure steps and after propagation of the tear.

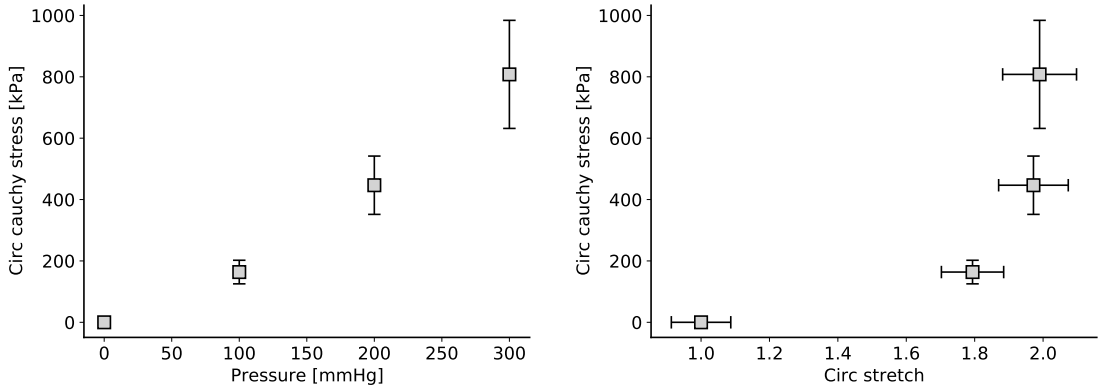

Figure VI.7 – (a) The circumferential Cauchy stress as a function of the pressure. (b) The circumferential Cauchy stress as a function of the circumferential stretch of the aortic wall.

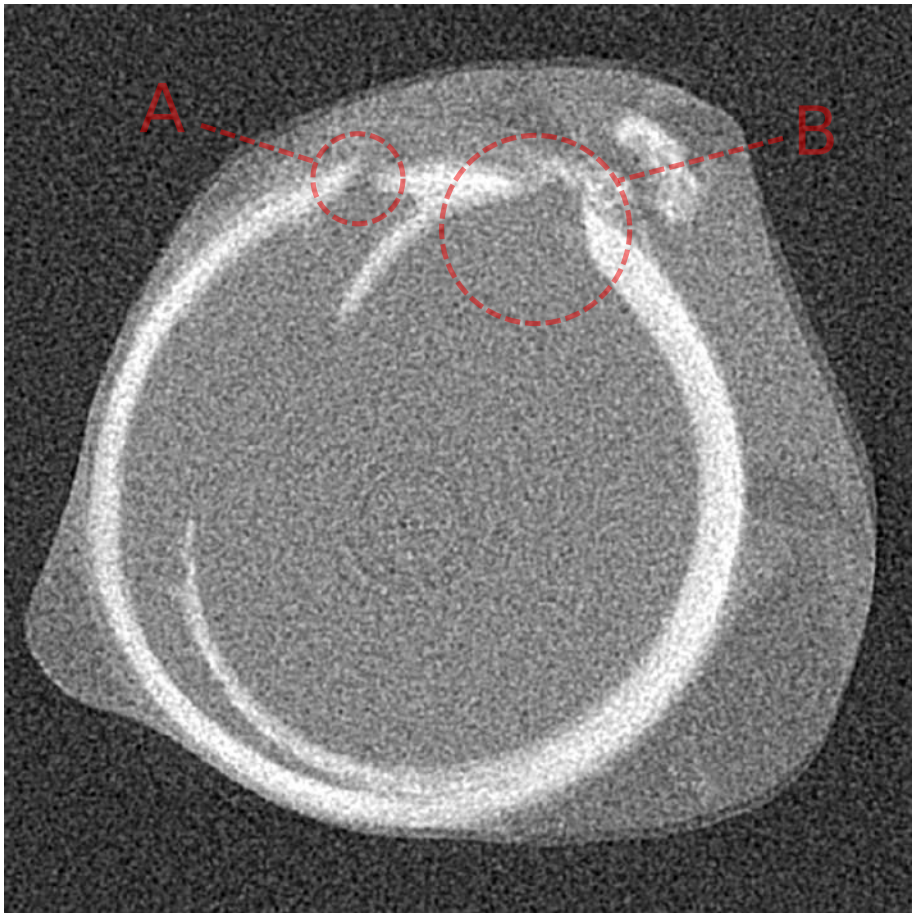

Figure VI.8 – Cross-section of a dissected sample. The circumferential propagation of the notch was stopped by an intercostal branch (B). As a consequence, the wall ruptured near the small branch (A). Conversely, the propagation of the tear in the longitudinal direction was not affected

VI.1.4 Discussion

In this study, an *in situ* tension-inflation test was performed on notched rabbit aortic tissues until dissection of the sample. The mechanical test was imaged by X-ray tomography at different steps of pressure to observe the evolution of the notch morphology, the aortic geometry, and their influence on the critical pressure and propagation of the dissection.

VI.1.4.1 Global behaviour of the aorta

The observations on the global behaviour of the aorta are consistent with the results from Chapter V on the porcine carotid arteries. The curves of diameter and circumferential stress as a function of the pressure can be divided in two parts: (i) before 100 mmHg, the collagen fibres are crimped and the mechanical behaviour of the aorta is led by the elastin fibres, (ii) after 100 mmHg, the collagen fibres begin to unfold and align themselves along the circumferential direction, thus stiffening the material as seen in Figure VI.7b. This mechanism also explains the evolution of the aortic diameter observed in Figure VI.6. A plateau is reached because the collagen fibres unfold and stiffen the aortic specimen. This reorientation of the fibres in the circumferential direction is of major importance as it may affect the failure properties of the aorta in the different directions. Finally, the decrease in thickness after pressurization could be due to the rearrangement of the fibres or to a permanent deformation in the radial direction during the tension-inflation test. An histological analysis will be carried out as part of a more in-depth study in order to shed light on the phenomenon behing this observation.

VI.1.4.2 Comparison with other experimental dissection models

The peak pressures required to propagate a notch were mostly non-physiological, and a deep and wide tear was necessary to reach a physiological blood pressure. This confirms the presence of a medial degeneration prior to the development of an aortic dissection as observed in the literature [220, 153]. The values of critical pressure found in this study are coherent with the literature according to the Table IV.4. However, a further comparison seems difficult as the tissues and the methods are different. The first type of mechanical test presented in the Table IV.4, the intramural liquid infusion test, investigates the interlamellar failure in mode I due to the peeling exerted by the fluid, or the blood in patient experiencing an aortic dissection, present in the aortic wall. Nevertheless, the mechanisms studied by this test are far from those at play during the initiation of an aortic dissection. For instance, with the intramural liquid infusion test it was found that a higher pressure was required to propagate the dissection in the outer layers (closer to the adventitia) compared to the inner layers [28, 195]. This result is contrary to the findings of studies which performed mechanical tests closer to the physiological condition like inflation test [11, 213, 169] and to the finding of the present work. This is also in accordance with the results of Chapter IV. The second type of mechanical test investigating the propagation of aortic dissection is the inflation test. In these studies an intimal tear was created inside the aorta with different methods, the segment was then inflated until propagation of the tear [11, 213, 169]. The main limitation of these studies in the investigation of the early stages of aortic dissection is that the crack was already partially propagated (several centimeters) between the medial layers before the inflation test which may explain the lower critical pressures obtained compared to the present work. In addition, this limitation prevents the study of the shift in the direction of the crack from radial to interlamellar propagation.

VI.1.4.3 Aortic dissection sequence

The aortic dissection can be divided into three stages: (i) an intimal tear is created in mode I and propagates in the radial direction of the aortic wall up to the outer half of the media [187] while the blood pressure deforms the notch and the aortic wall, (ii) the crack shifts in direction towards an interlamellar propagation in the media (circumferential-longitudinal plane) due to the high shear stress at the tip of the tear and to the low failure properties between the lamellae compared to other directions [246] as observed in Chapter I, and finally (iii) the blood penetrates through the intimal tear between the lamellae and delaminate the aorta. These different steps are presented in Figure VI.9. In this study, we examined steps (ii) and (iii).

Creation of the intimal tear

Step (i) is considered to be the consequence of a medial degeneration, due to aging or an inherited connective tissue disorder [155], thus it would be difficult to model this phenomenon experimentally, hence the creation of a notch to initiate the dissection. Genetically-modified mouse models can be used to investigate the pathogenesis of aortic dissection; however, the dissection process cannot be controlled like in the present work [126]. In some patients, only the step (i) and eventually step (ii) is achieved, with the tear never propagating, thus forming an abortive, discrete dissection, also called incomplete dissection [150, 211, 55, 205].

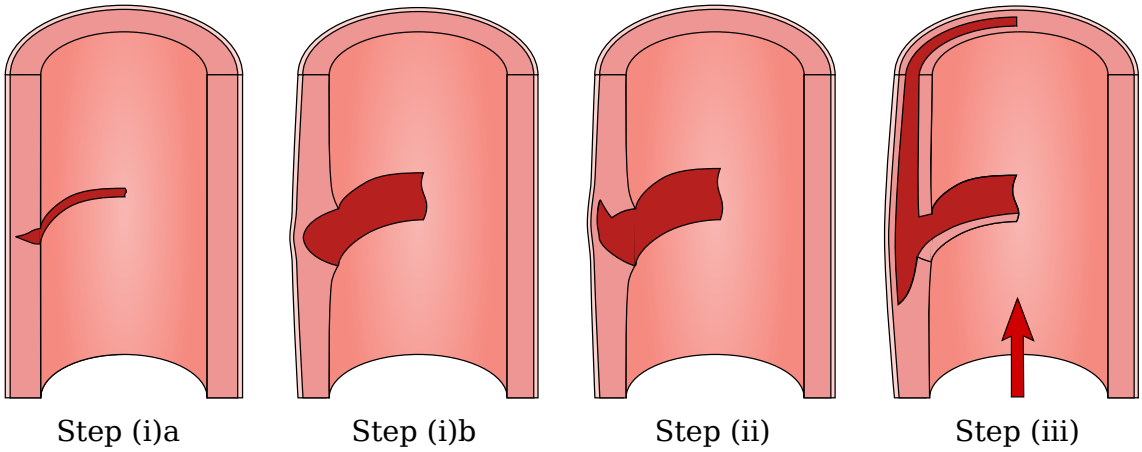

Figure VI.9 – Schematic describing the steps of aortic dissection. (i)a a tear appears in the intima and propagates to the outer media in mode I fracture, while (i)b the blood pressure deforms the tear and the aortic wall increasing the stress concentration at the tip of the notch where a bulge can be observed, (ii) the crack changes of direction in mode II fracture due to the laminated structure of the medial layer and the high shear stress at the tip of the notch, and (iii) the blood enters between the lamellae and pushes them apart in mode I. The arrow shows the direction of the blood flow.

Shift of the crack towards interlamellar propagation

In the research community, it is increasingly believed that step (ii) is a consequence of the shear stress imposed on the aortic wall [84, 204, 85, 65]. Haslach et al. [85] explained the shift of the crack direction from a radial plane to a circumferential-longitudinal plane as a consequence of the circumferential shear deformation between the medial lamellae, especially around the notch, during the inflation. The same mechanism could be observed

in the present study for specimen with a radial-longitudinal notch, the pressure increased the shear stress at the notch tip until propagation occurs. Nevertheless, Haslach et al. [85] only investigated the propagation of a notch in the radial-longitudinal plane, whereas 80 % to 95 % of the intimal tears observed in clinic are in the radial-circumferential plane [217]. The same limitation applies to the study of FitzGibbon and McGarry [65] where they performed shear fracture ring test to assess the mode II fracture in ovine aortic ring. The justification for a radial-longitudinal notch advanced by Haslach et al. [85] is that a tear is never perfectly in the radial circumferential plane and always possesses a longitudinal component; however, it seems uncertain whether similar experiments could propagate a radial-circumferential tear along an aortic specimen. Indeed, the mechanisms leading to aortic dissection in the case of a radial-circumferential tear appear to be different from those of a radial-longitudinal notch as shown in Figure VI.3. This difference was also observed in Chapter III in the uniaxial tension tests, the circumferentially notched specimen delaminated over a large area prior to failure, whereas the longitudinal notched specimen delaminated only on a limited area prior to failure. This suggests that the axial tension in the aortic wall, due to axial pre-stretch for example, is not the only mechanism involved in the aortic dissection. The factors present in the tension-inflation test and not in the uniaxial test are the biaxial stress state, which rigidified the aortic wall, and the fluid pressure. An hypothesis explaining these phenomena could be that the pressure exerted on the surfaces of the notch contributes to the delamination of the medial layers by increasing the shear stress at the tip of the notch initiating the interlamellar propagation in mode II fracture as shown in Figure VI.1 and VI.9. It is interesting to note that the images at 0, 100, and 200 mmHg are extremely similar to the images of the uniaxial test on notched specimens in Chapter III. Although the shear stress triggers the change of direction of the crack into a propagation between the lamellae, it is not sufficient to achieve a complete propagation along the aorta. The second consequence of the fluid pressure is a deformation of the adventitia and remaining media, forming a bulge at the tip of the notch as shown in Figure C.1, which increases the stress concentration at the notch tip. This remodelling of the aortic morphology is due to the loss of elasticity of the outer wall, therefore the remaining layers deforms for compensating the decreased tension and maintaining the equilibrium in pressure. The argument that this bulge may only be present at supra-physiological pressure is not valid since an eccentric bulge is often observed in clinics on patient with discrete aortic dissection [211, 33]. These two effects may explain the reason behind the negative correlation of the depth of a tear with the critical pressure as shown in Figure VI.5. A deeper tear means a higher load pulling the tear apart, which increases the shear stress at the tip of the notch. Furthermore, the deeper the tear, the smaller the remaining thickness of the aortic wall, the bulge can therefore easily occur due to the reduced bending stiffness of the remaining wall. This is corroborated by an absence of a bulge in samples with a shallow radial-circumferential notch as seen with sample II in Figure VI.3. This is also confirmed by clinical observations where most dissections propagate into the outer half of the aortic wall [187, 165, 216]. During this step (ii), although the change of direction of the tear occurs in mode II, the following stress state appears to be a mix between tensile and shear stress, thus mode I and II failure.

Delamination of the aorta

Finally, in the step (iii), once the critical pressure was reached and the propagation of the tear began, the blood enters between the lamellae adding opening stress in addition to the shear stress (Figure VI.9). According to Roach and Song [185] the pressure required to

continue separating the lamellae decreases. In the present study, the inflation was pressure-driven, as a consequence the dissection occurred rapidly and the X-ray video at 5 frames per second could not capture the different stages of the propagation process (Figure C.1). This is consistent with the clinical observations that only a few seconds are needed to dissect the entire aorta [187, 216]. It is likely that the mechanisms involved in this step are similar to those observed in a liquid infusion or peeling test, i.e. predominantly mode I fracture. Nevertheless, most of the studies which performed peeling or shear tests on aortic tissue showed that peel strength (Table V.2) and shear strength [204] are higher in the longitudinal direction compared to the circumferential direction. This is in contradiction with clinical observations in patients with aortic dissection, where the dissection propagates along the aorta in the longitudinal direction involving about half the circumference of the aorta [150, 216]. The same observation could be made for all the specimens in the present study (Figure VI.2), except for the specimen II in which the dissection involved almost its entire circumference (Figure VI.3). The involvement of only half the circumference of the aorta despite lower resistance to mode I and II in the circumferential direction may be explained by the change of morphology of the aorta in order to maintain the hydrostatic pressure. It seems that this complex geometry favours the axial propagation despite the higher resistance of the tissue against mode I and II fracture in this direction. This change of aortic morphology was quantified by Williams et al. [245], in this study, true lumen, false lumen, and flap deformation was investigated in a dissected aorta by inflating human and porcine dissected aortic specimens with a dissection that involved different fractions of the wall circumference. The results showed that the false lumen underwent a significant dilatation with the increase in pressure compared to the true lumen and flap, which underwent moderate stretching. Furthermore, aging may amplify this mechanism as axial pre-stretching decreases with age [98], thus decreasing wall stiffness and facilitating the change in aortic geometry. In addition to this remodelling phenomenon, the release of residual stress and the elastic recoil of the detached flap leads to a collapse of the flap and increase the stress concentration at the crack front. These mechanisms creates a chain reaction that propagates the dissection along the aorta until this process is interrupted, for instance by an atherosclerosis plaque [187, 138] or by a second tear, either in the inner or outer wall (Figure VI.8). Another factor playing an important and unstudied role in this study is the difference in material properties depending on the location along the aorta but also around the circumference and through the thickness [6].

VI.1.4.4 The particular case of longitudinal tear

The phenomena previously described (i.e. change of aortic morphology, bulge effect, elastic recoil of the flap) were not observed on samples with a longitudinal tear. The fact that the notch depths of the two longitudinally notched specimens were small compared to the well-dissected samples could be an explanation. Furthermore, the notch propagated in the radial-longitudinal plane in addition to the circumferential-longitudinal plane, thus no false channel was created, or at least not in the field of view given by the X-ray tomography. The pressure required to dissect a segment with a circumferential notch was lower than for a specimen with a longitudinal notch; however, the difference in geometry of the notches and the small number of samples prevent a definitive conclusion from being reached. In addition, both longitudinally notched specimens seem to follow the same trends observed on circumferentially notched specimens in terms of correlation with various factors, such as depth of tear. Thus, the prevalence of circumferential tear in clinics may be due mainly

to the lower resistance of aortic tissue to longitudinal versus circumferential tension which activates the step (i) of aortic dissection as shown in Table V.2.

VI.1.4.5 Limitations and future work

Some limitations to this work should be noted. Multiple studies have shown that freezing samples prior to testing does not change the mechanical properties [209, 44, 162]. However, an alteration of the mechanical properties of the tissue was reported when stored at +4°C during 24 hours. To limit this change, the immersion time in the contrast agent was reduced to 12 hours in this study compared to Chapter V. The small number of samples is also a limitation of this study, as it prevents definitive conclusions from being drawn, for instance on the differences between circumferential and longitudinal notches. The tension-inflation test was performed at static pressure, which may be the reason for the non-physiological pressure necessary to propagate the notch, as in the literature $(\frac{dP}{dt})_{\max}$ was shown to have a significant influence on the critical pressure compared to the mean pressure [175, 11]. Nevertheless, to generate the tear in these experiments a bleb was created by injecting few millilitres of fluid inside the media before making a circumferential cut to simulate an intimal tear. As a consequence, the initial tear was already propagated before the inflation in the interlamellar plane on at least 1 cm. Further investigations are necessary to quantify the influence of this parameter on the initiation of aortic dissection.

In this work, the mechanical behaviour of the tissue during aortic dissection was investigated at a meso-scale; however, multiple micro-scale mechanisms contribute to this complex disease, e.g. the clustering of glycosaminoglycans/proteoglycans [102, 190] or bridging fibers [168, 166]. In order to investigate these effects, a higher resolution is necessary to identify the micro-components. A solution to this problem could be the synchrotron-based phase-contrast imaging [225]. With this technique it should be possible to observe the microstructure without compromising too much on the field of view or the time resolution.

The 3D images of the meso-structure of the aortic wall at different steps of pressure and after the dissection could be combined with a numerical model in order to investigate and quantified the mode of rupture involved during the initiation and the propagation of the tear. The extended finite element method and the model used in Chapter IV could be use to reproduce the phenomena observed in the present study; however, high convergence issues were observed during the propagation of the crack. An explicit method to solve the simulation could resolve this problem. A phase-field model could also be used to simulate the aortic dissection as performed in Gültekin et al. [81]. With these two methods it is not required to define the crack path beforehand, thus the observations of the present study could be used to validate these models. Finally, a finite element model using cohesive interface, as in Chapter II and III, could also be used to model the initiation and propagation of the dissection. The crack path is already defined by the observations of the present study. This method may be used to quantified the fracture modes at the tip of the notch and the proportion of mode I and II during the different steps of the delamination. Furthermore, the mechanisms observed, like the bulge, could also be investigated.

VI.1.5 Conclusion

In this study, an *in situ* tension-inflation test was performed on notched rabbit aortic segments in order to observe the dissection of the sample with X-ray microtomography. To the authors' knowledge, this is the first study to observe the complete aortic dissection

process with the entire 3D geometry and a resolution allowing quantification. This experiment allowed the investigation of aortic dissection at different pressure steps, after the dissection, and even during the delamination process using X-ray images. The morphology of the tear was shown to influence the critical pressure as demonstrated in Chapter IV. This study also highlighted the deformation undergone by the aortic geometry during the dissection with a bulge at the tip of the notch, increasing the interlamellar stress. The observation reported in this work could be of great use in computational modelling by filling the lack of experimental data and enabling the aortic dissection models to be validated. Finally, further analysis on this animal model with more powerful imaging techniques like synchrotron-based imaging may lead to a complete description of the mechanisms occurring during aortic dissection and help in the diagnosis of patients at risk or in the development of better treatments of aortic dissection.

Highlights

- *In situ* tension-inflation test on notched rabbit aortic segments were performed with two types of notches.
- The morphology of the tear was shown to influence the critical pressure as demonstrated in Chapter IV.
- The aortic wall created a bulge shape at the tip of the notch deforming the remaining wall and creating a high stress concentration
- The observation reported in this work could be of great use in computational modelling by filling the lack of experimental data and enabling the aortic dissection models to be validated.

Conclusion Générale - *General Conclusion*

Synthèse

La dissection aortique est un évènement résultant d'une combinaison de phénomènes mécaniques et biologiques complexes encore mal compris. Ce travail, mêlant études expérimentales et approches éléments finis, s'est focalisé sur l'aspect mécanique afin de mieux comprendre l'initiation et la propagation d'une dissection aortique.

Dans un premier temps, une étude préliminaire a été menée afin d'identifier les propriétés de rupture d'échantillons de média d'aortes porcines grâce à une analyse inverse. Ce modèle analytique a permis de reproduire le comportement élastique et le comportement en rupture de 10 échantillons en identifiant les propriétés de rupture des différentes couches lamellaires. Par la suite, un modèle éléments finis a permis de montrer la faible résistance au cisaillement entre les lamelles de la couche médiale. La rupture lors du test de traction étant dynamique, la délamination des couches en mode II est difficilement quantifiable, en particulier en raison des effets viscoélastiques. Cette étude a permis d'obtenir des informations quantitatives sur le mode I, qualitatives sur le mode II, et de poser les hypothèses pour la suite de ce travail, notamment le mécanisme d'endommagement reposant sur une rupture préliminaire en mode I puis une propagation en mode II.

Afin de mieux comprendre l'influence du mode II et de le quantifier, nous avons réalisé des test de traction *in situ* sur des échantillons encochés dans les directions circonférentielle et longitudinale sous radiographie par rayons X. Ces tests ont par la suite été modélisés par éléments finis. La résistance au cisaillement entre les lamelles a été quantifiée grâce à des méthodes inverses afin de comprendre comment une fissure intimale, et éventuellement médiale, change de direction afin de se propager entre les couches. Les propriétés matériau et la résistance au mode I ont été identifiées grâce à des tests de traction et de pelage, respectivement. La rupture a été modélisée grâce à des interfaces cohésives. La grande résistance au cisaillement des échantillons aortiques dans la direction longitudinale comparé à la direction circonférentielle est surprenante, malgré la concordance avec la littérature, car en clinique la propagation se fait principalement dans la direction longitudinale dans la majorité des cas. La faible délamination lors des tests sur des échantillons longitudinaux montre que la tension de l'échantillon n'est pas un facteur déterminant dans la propagation interlamellaire de la fissure, au contraire des échantillons circonférentiels. Ces résultats peuvent expliquer pourquoi certaines études [85, 65] parviennent à obtenir une propagation de fissure dans la direction circonférentielle avec principalement du mode II.

Ces différentes études numériques sur des essais expérimentaux uniaxiaux ont permis une

meilleure compréhension de la dissection aortique, ainsi qu'une quantification des modes I et II de rupture. Cependant, un test mécanique plus proche des conditions *in vivo* est nécessaire afin de mieux comprendre par quels mécanismes la dissection se propage le long de l'aorte dans la direction longitudinale. Ainsi, un modèle numérique reproduisant l'initiation et la propagation d'une dissection aortique lors d'un test de traction-gonflement a été développé afin d'être au plus proche des conditions physiologiques et d'étudier les principaux facteurs contribuant à cette maladie. Les résultats obtenus par le modèle sont conformes à la littérature. Une dégénérescence de la media semble nécessaire pour atteindre une pression critique physiologique ainsi que pour propager la fissure dans le plan circonférentiel-longitudinal. La morphologie de la déchirure semble aussi être un facteur important dans le déclenchement de la dissection aortique, ainsi une déchirure initiale plus importante et plus profonde augmente le risque de dissection aortique. L'influence de la résistance au cisaillement et du stress résiduel semble limité, cependant, les limites du modèle, comme l'hypothèse d'un matériau homogène, peuvent expliquer le faible impact de ces paramètres. Ces résultats nécessitent encore une validation expérimentale, mais apportent un classement relatif de l'influence de différents paramètres sur la dissection aortique et peut contribuer à la création de critères identifiant les patients à risques.

Le Chapitre IV a permis de modéliser la dissection aortique au plus proche des conditions *in vivo*, cependant, il n'existe aucune étude permettant de valider ce modèle. En effet, aucune information sur la géométrie de l'aorte avant, pendant, et après dissection n'est présente dans la littérature, d'après les connaissances de l'auteur. Ainsi, une nouvelle méthode permettant d'observer la propagation d'une dissection *in vitro* en 3D dans des carotides porcines avec un microtomographe à rayons X a été mise au point. Une machine de traction-gonflement s'adaptant à l'intérieur du tomographe, ainsi qu'une méthode pour créer une entaille à l'intérieur de l'artère ont été développées. Un agent de contraste est utilisé afin de visualiser l'artère grâce aux rayons X. Des scans à différentes pressions ont été effectués et une description quantitative de la morphologie de l'entaille au cours de son évolution avec la pression a été présentée. De plus, la présence de nombreux plans de délamination dans un échantillon disséqué a été mise en évidence. Ces résultats suggèrent la prévalence d'une forte contrainte de cisaillement dans la région du bout de la fissure comme un possible déclencheur de la propagation d'une dissection. Cependant, la fissure était longitudinale alors que dans plus de 80% des cas la fissure intimale est circonférentielle. Les mécanismes de propagation pouvant être différents en fonction de l'orientation de la fissure, une étude avec une fissure circonférentielle est nécessaire. De plus, les carotides de porc ont été identifiées comme étant grandement résistantes à la délamination, et la dissection ou la non-dissection des échantillons se produisait de façon aléatoire et non répétable.

Afin de mieux comprendre pourquoi les échantillons de carotides porcines était plus résistantes à la dissection que des échantillons aortiques, des tests de traction et de pelage ont été effectués dans les directions circonférentielle et longitudinale. Les tissus de carotide porcine ont révélé une anisotropie dans leurs propriétés mécaniques avec une plus grande rigidité dans la direction circonférentielle. De plus, la direction circonférentielle a montré une plus grande résistance à la traction, à l'inverse, la direction longitudinale a révélé une plus grande énergie de décohésion. Ces résultats sont conformes à la littérature. Cependant, les énergies de dissection trouvées pour les échantillons de carotide porcines sont bien supérieures à celle de tissu aortique humain ou même porcin. Ce résultat explique sans doute pourquoi les carotides porcines sont fortement résistantes à la dissection. Un autre

élément pouvant expliquer la plus grande propension de l'aorte a subir une dissection est lié à leur ratio rayon/diamètre qui est plus important que celui des carotides. Ceci indique qu'elles sont sujettes à une contrainte plus importante.

Afin d'obtenir une dissection répétable, les expériences en microtomographie à rayons X ont été refaites avec des échantillons aortiques de lapin dans lesquelles une dissection s'initie à une pression critique plus faible. Les aortes ont été prélevées quelques minutes après le sacrifice des lapins, les branches ont été suturées avec du fil de soie, puis les échantillons ont été congelés. Le jour du test, après avoir trempé 12 heures dans de l'agent de contraste, les tests de traction-gonflement ont été réalisés. La fissure à l'intérieur de l'artère a été effectuée en retournant l'échantillon avant de sectionner partiellement la paroi aortique. Ce type de tissu s'est révélé beaucoup moins résistant à la dissection que les carotides porcines. Les résultats ont montré que bien que la pression nécessaire pour provoquer la dissection aortique est en moyenne supra-physiologique, elle devient physiologique lorsque la profondeur ou la largeur de fissure est suffisamment grande. De plus, la pression critique s'est révélée corrélée à la profondeur, l'ouverture, et la largeur de fissure. Ces résultats sont conformes aux résultats obtenus grâce au modèle du Chapitre IV. Les images observées à différentes pressions sont très similaires aux images du Chapitre III. La propagation de la fissure montre que la présence de la pression exercée par le sang est un élément essentiel à la dissection telle qu'elle est observée en clinique. Une hypothèse pouvant expliquer cette observation serait que le fluide pousse les deux parois de la fissure, créant un fort cisaillement en bout de fissure. Une fois que la fissure a changé de direction et s'est engagée entre les lamelles, le fluide s'insère entre les couches et continue la séparation le long de l'aorte. Pendant cette étape, la rupture semble être un mélange entre mode I et II. Les observations des images d'échantillons disséqués ont montré, comme dans la littérature, que la fissure se propage principalement dans la direction longitudinale et implique la moitié de la circonférence de l'aorte dans la majorité des cas. La dissection aortique a aussi été observée en temps réel par images radiographiques. Ces images ont montré la présence d'un renflement en bout de fissure avant la dissection. Ce changement de morphologie de l'aorte est une conséquence de la diminution de l'épaisseur de la paroi non-disséquée, la couche extérieure se déforme afin de maintenir l'équilibre en pression. Ce phénomène accroît les contraintes en bout de fissure et favorise la propagation longitudinale. De plus, un retour élastique du flap compris entre 5.3% and 12.3% a été observé. Ce mécanisme semble contribuer aussi à la propagation de la dissection dans la direction longitudinale. Cette étude vient combler un manque de la littérature concernant les données géométriques d'aorte disséquée avant et après rupture afin de valider des modèles numériques. Enfin, les mécanismes de rupture mis en évidence dans cette étude sont un pas en avant dans la compréhension et la découverte de nouveaux traitements pour la dissection aortique.

Limites

Dans la première partie de ce travail doctoral, des modèles numériques ont été utilisés pour étudier les différents modes de rupture impliqués dans la dissection aortique ainsi que les paramètres susceptibles d'affecter cette maladie. Plusieurs limites s'appliquent à ces études. Les hypothèses faites sur les comportements matériaux sont critiquables. Par exemple, dans le Chapitre II, le matériau a été défini comme isotrope car dans Helfenstein-Didier et al. [89] aucune différence significative entre les directions circonférentielle et longitudinale n'a été trouvée. De nombreuses études de la littérature ont cependant montré

une anisotropie du tissu aortique [52, 199, 171, 246] ce qui met à mal cette hypothèse. L'anisotropie du matériau a été prise en compte dans les chapitres suivants.

Une autre limite est l'hypothèse d'un matériau homogène alors que dans la réalité il est hétérogène. La microstructure joue un rôle essentiel dans le comportement mécanique de l'aorte ainsi que dans l'initiation [190, 189] et la propagation de la dissection aortique. Par exemple, la structure en couches de la média participe à cette maladie en orientant la fissure vers une propagation dans le plan circonférentiel-longitudinal. Dans le Chapitre IV, le fait que la résistance au cisaillement n'ait que peu d'effet sur l'initiation et la propagation aortique peut s'expliquer par la non prise en compte de la microstructure. Haslach et al. [84] a démontré la présence de glissements entre les couches médiales, créant du cisaillement et facilitant la dissection de l'aorte. Ainsi, l'aorte peut être modélisée à l'échelle lamellaire, avec des couches médiales indépendantes et ayant des propriétés mécaniques différentes les unes des autres, comme dans Gültekin et al. [81]. Une autre solution afin de tenir compte de la microstructure est de modéliser le tissu aortique avec un modèle multi-échelle. Ce type de modèle numérique permet de simuler le comportement global de l'aorte par rapport aux micro-mécanismes régissant les structures d'intérêt (fibres de collagène et d'élastine) [199, 246].

Dans la deuxième partie de ce travail doctoral, des tests mécaniques reproduisant une dissection aortique *in situ* ont été réalisés sur des carotides porcines et des aortes de lapin. Une limitation importante de ces études est le choix de faire les tests de gonflement à pression quasi-statique alors que la pression artérielle physiologique est dynamique. Plusieurs études [175, 11] pointent vers une influence de $(\frac{dP}{dt})_{\max}$ plutôt que de la pression artérielle moyenne sur la pression critique déclenchant une dissection aortique. De plus, l'effet de la fatigue sur l'initiation de l'entaille n'est pas non plus étudié. Ces phénomènes n'ont pas été inclus dans ce travail afin de permettre une évaluation de l'influence de chaque mécanisme indépendamment. Ainsi, maintenant que des données relatives à la dissection en gonflement quasi-statique ont été présentées, des tests incluant ces mécanismes pourront être réalisé et leur influence quantifiée.

Une autre limitation peut être la trempe dans l'agent de contraste qui agit certainement sur les propriétés mécaniques. L'agent de contraste en lui-même [89] n'a pas d'effet, mais le fait de garder un échantillon pendant 12 à 24 heures à 4°C [209] peut affecter le comportement mécanique. C'est pour cette raison que dans le Chapitre VI nous avons diminué le temps d'incubation de moitié. Cependant, la proximité des résultats en termes de pression critique par rapport à d'autres études de la littérature [28, 220, 185] tend à nuancer cette limite.

Des limitations relatives à la tomographie à rayons X doivent être relevées. La principale limite est la résolution temporelle. Un scan dure plusieurs minutes au minimum, durant cette période l'échantillon observé n'est pas parfaitement statique et des micro-mouvements peuvent survenir. Cela a pour conséquence de créer des artefacts sur les images obtenues et ainsi affecter les mesures prises. La qualité des images s'est néanmoins avérée satisfaisante pour les mesures effectuées, mais pourrait limiter l'application d'éventuelles mesures volumétriques type corrélation d'image volumique (DVC).

Enfin, de l'histologie aurait pu être faite dans le Chapitre VI afin d'étudier le profil de rupture et de quantifier de manière exacte différentes valeurs d'intérêts comme le nombre de lamelles cassées. Afin de palier à ce défaut, une étude histologique est prévue dans les travaux qui suivront cette thèse doctorale.

Contributions

Les contributions originales de ce travail doctoral par rapport à la littérature sont listées dans cette section.

- Un modèle cohésif a été développé et les propriétés élastique et de rupture en mode I d'échantillons artériels ont été identifiées.
- La faiblesse de la résistance à la délamination en mode II due au retour élastique après la rupture en mode I des couches médiales a été mise en évidence.
- Des tests de traction sur des échantillons avec fissure ont démontré qu'une délamination apparaissait due à la structure laminaire de la paroi aortique.
- Ces tests ont aussi démontré que la direction circonférentielle était plus fragile face à la délamination induite par la traction.
- La résistance au cisaillement des échantillons aortique a été quantifiée dans les directions circonférentielle et longitudinale.
- Il a été démontré que le cisaillement induit par la traction dans la direction longitudinale ne suffit pas a expliquer la dissection aortique et que d'autres mécanismes sont en jeu.
- Un modèle anisotrope d'aorte au plus proche des conditions *in vivo* a été développé. Des critères d'initiation d'endommagement ont été créé à partir de valeurs de la littérature. L'initiation et la propagation de la dissection ont été simulé grâce à la méthode des éléments finis étendue.
- L'influence de différents facteurs reflétant la géométrie de la fissures et la mécanique de la paroi sur la pression critique et la direction de propagation a été quantifiée.
- Une méthode combinant un test de traction-gonflement sur des échantillons entaillés avec de la tomographie à rayon X a été développée.
- Le comportement général de la carotide porcine ainsi que la morphologie de la fissure de l'échantillon a été quantifié à différentes pressions.
- Un échantillon disséqué a été présenté permettant la mise en évidence de nombreux plans de délamination comme identifié par Helfenstein-Didier et al. [89].
- La méthode *in situ* de traction-gonflement appliquée a des aortes de lapin a permis d'obtenir une dissection de manière répétable
- Des images à différentes pressions ont permis de quantifier l'évolution de la géométrie de l'aorte ainsi que celle de la fissure jusqu'à dissection de l'échantillon.
- Des images de dissection similaires à ce que l'on peut observer en clinique sur des patients atteints de dissection aortique ont pu être observées.
- La dissection des échantillons a pu être observée en temps réel, il a ainsi été montré que ce processus se déroulait de manière quasi-instantané (moins d'une seconde).
- Des corrélations entre la morphologie de la fissure et la pression critique ont été démontrées.
- Un retour élastique du flap, participant à la dissection, a été quantifié.
- La présence d'un renflement en bout de fissure lors de la dissection a été démontré.

Perspectives

Les perspectives pour ce travail doctoral sont nombreuses. Tout d'abord, pour la partie numérique, un couplage du modèle numérique avec les tests de traction-gonflement du Chapitre VI permettrait une études des mécanismes décrits lors de ces expériences, ainsi qu'une identification et une quantification des modes de rupture présents lors de l'initiation et la propagation de la dissection aortique. Pour cela, plusieurs approches sont possibles. La méthode des éléments finis étendue et le modèle utilisé dans le chapitre IV pourraient être utilisés pour reproduire les phénomènes observés, cependant, des problèmes de convergence importants ont été observés pendant la propagation de la fissure. Une méthode explicite pour résoudre la simulation pourrait résoudre ce problème [243]. Un modèle "phase-field" pourrait également être utilisé pour simuler la dissection aortique comme dans l'étude de Gültekin et al. [81]. Avec ces deux méthodes, il n'est pas nécessaire de définir au préalable la trajectoire de la fissure. Ainsi, les observations du Chapitre VI pourraient être utilisées pour valider ces modèles. Enfin, un modèle par éléments finis utilisant des interfaces cohésives, comme dans les chapitres II et III, pourrait également être utilisé pour modéliser l'initiation et la propagation de la dissection. La trajectoire de la fissure est déjà définie par les observations du Chapitre VI. Cette méthode peut être utilisée pour quantifier les modes de fracture à la pointe de l'entaille et la proportion des modes I et II au cours des différentes étapes de la délamination. En outre, les mécanismes observés, comme le renflement en bout de fissure, pourraient également être étudiés, et l'importance du rôle de la pression quantifiée.

Par la suite, une étude clinique rétrospective pourrait être effectuée en faisant évoluer le modèle aortique du Chapitre IV vers des géométries réelles de patient avant dissection afin de comparer le résultat des simulations avec les géométries après dissection. Cela apporterait certainement de nombreuses informations qualitatives et quantitatives sur les facteurs conduisant à cette maladie et ferait progresser les modèle numériques vers une utilisation clinique pour la détection de patients à risque.

Une prise en compte de la microstructure semble indispensable à la détection de patients à risque [106, 153]. Une étude expérimentale pourrait chercher une corrélation entre la proportion des différents composants microstructurels (comme l'élastine, le collagène, ou les cellules musculaires lisses) avec la pression critique. Ces informations pourraient être intégrées dans un modèle numérique afin d'étudier plus en détail l'influence de ces composants sur l'initiation et la propagation de la dissection aortique. Les modèles multi-échelles [199, 246] ou "constrained mixture" [149] semblent être les meilleures façons de lier la microstructure à la macrostructure tout en gardant un modèle continu. Ainsi, une étude numérique pourrait quantifier la capacité de prédiction du modèle sur des cas réel et ainsi valider une approche par jumeau numérique dans le suivi des patients à haut risque de maladie vasculaire.

Les études expérimentales présentées dans cette thèse de doctorat ouvrent de nombreuses voies de recherches. La première étape serait de refaire les tests de traction-gonflement avec des tissus humains afin de quantifier les modes de rupture présents lors d'une dissection aortique chez l'humain. Dans le Chapitre V, il est explicité que les tissus porcins sont plus résistants que les tissus humains, certainement car les tissus sont obtenus chez des porcs souvent jeunes. Un modèle de dissection aortique avec des tissus humains permettrait d'être au plus proche des conditions *in vivo*.

La dissection aortique se produit majoritairement chez des personnes âgées avec des fac-

teurs aggravant comme l'hypertension. Ainsi, il semble que les modifications des propriétés mécaniques de l'aorte dues à l'âge, comme l'augmentation de la rigidité ou la diminution du pré-étirement, conduisent à une plus grande faiblesse de l'aorte face à cette maladie. La principale cause de ces changements est la dégradation de l'élastine [106, 242] causant une diminution de l'élasticité de l'aorte et la diminution de la cohésion interlamellaire. De plus, il a été observé une réduction marquée des fibres élastiques interlamellaires chez les patients présentant une dissection aortique [153]. Afin d'étudier ces phénomènes et leur influence sur la dissection aortique une étude expérimentale comparant des échantillons sains et des échantillons avec une élastine dégradée pourrait être menée. Pour dégrader l'élastine dans les tissus, de l'élastase ou des souris génétiquement modifiées peuvent être utilisées. De la même facon l'influence du collagène pourrait être étudiée en comparant des échantillons sains et d'autres avec le collagène dégradé en utilisant de la collagénase.

L'étude de l'initiation de la dissection aortique *in vivo* grâce à des souris génétiquement modifiées semble être une piste de recherche prometteuse. Cela permettrait de répondre à l'une des questions essentielles sur cette maladie : comment se forment les fissures intimales ? Cette réponse donnerait les clés pour comprendre ce qui initie ce processus de dissection aortique, ainsi que pour identifier les patients les plus à risques.

L'influence de $(\frac{dP}{dt})_{\max}$ pourrait aussi être étudiée afin de confirmer ou d'infirmer la prévalence de ce facteur sur la pression moyenne. Cette étude serait aussi l'occasion d'étudier l'impact de la fatigue sur l'initiation de la fissure. Dans les conditions *in vivo* la fatigue joue certainement un rôle prépondérant dans l'initiation de la dissection aortique en créant un processus d'endommagement et de réparation de la paroi [106]. Le dispositif expérimental *in situ* pourrait être modifié pour générer ce type de sollicitation.

Une autre piste possible pourrait être de faire de la DVC sur les images de tomographie à rayons X. La DVC apporterait une cartographie des déformations durant les étapes précédant la dissection. Cette technique permettrait aussi, en connaissant le champ de déformation, de faire une identification locale des propriétés de cohésion [191]. Ces résultats permettraient de mieux mettre en lumière et de quantifier les mécanismes menant à la dissection aortique. Cela permettrait aussi de valider des modèles numériques de façon précise. Le contraste présent dans les images de tomographie n'est pour l'instant pas suffisant mais avec de la tomographie en contraste de phase ou en collant des billes de titane sur la paroi aortique il serait possible de réaliser cette étude.

Chaque méthode d'imagerie possède des avantages mais aussi des limitations comme relevé dans le Chapitre I. Ainsi, d'autre techniques d'imageries combinées avec des tests mécaniques peuvent être employées en complément de la tomographie à rayons X afin de compléter les observations réalisées dans cette étude.

- **La tomographie en contraste de phase** est une méthode permettant, grâce à un synchrotron, de se passer d'agent de contraste pour observer les tissus mous, ce qui éviterait l'incubation de l'échantillon avant le test de traction-gonflement. De plus, le contraste et la résolution obtenues avec cette technique d'imagerie sont bien meilleurs qu'avec de la tomographie à rayon X classique. Ainsi, il serait possible de descendre à l'échelle lamellaire comme fait par Trachet et al. [225], ce qui permettrait une analyse des processus menant à la dissection aortique extrêmement poussée et aboutirait certainement à la découverte ou la confirmation de nouveaux mécanismes dans l'initiation et la propagation de cette maladie.
- **La microscopie multiphotonique** a été utilisée par notre laboratoire pour étudier

le comportement des fibres de collagène dans l'adventice lors de tests mécaniques. De nombreuses études ont été menées en couplant cette technique d'imagerie avec des tests de traction [119], de gonflement [29], et de traction-gonflement [120]. Ces études ne concernent pas directement la dissection aortique mais la compréhension du comportement mécanique de l'adventice et de l'aorte en général est une nécessité afin de mieux caractériser la dissection aortique. De plus, dans le Chapitre VI il a été montré que l'adventice se déforme avant et pendant la dissection aortique et participe à celle-ci.

- **La tomographie en cohérence optique** combinée avec des tests mécaniques est aussi une piste suivie par notre laboratoire. Cette technique d'imagerie a notamment été utilisé par Brooks Lane pour observer des tests de traction sur des échantillons entaillés afin de comprendre comment une fissure se propage dans la paroi aortique. Ces expériences ont ensuite été modélisées dans le Chapitre III.

La principale limitation à l'utilisation clinique des données présentes dans cette thèse doctorale est la faible résolution des techniques actuelles d'imagerie clinique (entre 1 et 2 mm) qui empêche l'évaluation de l'état de la paroi aortique du patient. Svensson et al. [211] ont montré que sur 181 cas de réparation de l'arche aortique, 9 patients (5%) avaient développé une dissection aortique limitée non détectée avant opération, malgré le fait d'avoir subi ≥ 3 techniques d'imagerie. De nouveaux dispositifs émergent comme l'OCT endoscopiques, qui permettent une résolution dix fois supérieure aux techniques d'imagerie classiques [76, 115]. Le désavantage de cette technique est qu'elle nécessite une intervention semi-invasive sur le patient. À terme, ce travail doctoral pourrait permettre une amélioration de la détection de risque pour le patient. Pour cela, de la prévention pour les patients à haut risque (hypertension, syndrome de marphan) pourrait être fait en scannant leur paroi artérielle à la recherche de défauts intimals ou de marqueurs de la dissection aortique comme une altération des cellules muscullaires lisses [106] ou une diminution des fibres élastiques interlamellaires [153]. Ces informations pourraient être intégrées dans des modèles numériques multi-échelles intégrant des méthodes de remodelage, ce qui donnerait lieu à un indice de risque donné pour le patient. Des méthodes d'intelligence artificielle pourraient être utilisées afin de se passer de modèle numérique et de déterminer un risque pour le patient avec les informations disponibles. Ainsi, un jumeau numérique du patient à risque serait utilisé tout le long de son suivi afin de déterminer si des mesures préventives étaient nécessaires afin d'éviter une maladie vasculaire. Un degré de certitude serait associé avec chaque prédiction. Ce pourcentage serait déterminé par le nombre de données disponibles sur le patient et pourrait évoluer, en augmentant ou diminuant, en fonction des examens réalisés et de leur espacement dans le temps.

Bibliography

[1] Víctor A Acosta Santamaría, María Flechas García, Jérôme Molimard, and Stephane Avril. "Three-Dimensional Full-Field Strain Measurements across a Whole Porcine Aorta Subjected to Tensile Loading Using Optical Coherence Tomography–Digital Volume Correlation". In: *Front. Mech. Eng.* 4 (2018), p. 3.

[2] Åsa Rydén Ahlgren, Magnus Cinthio, Stig Steen, Tobias Nilsson, Trygve Sjöberg, Hans W Persson, and Kjell Lindström. "Longitudinal displacement and intramural shear strain of the porcine carotid artery undergo profound changes in response to catecholamines". In: *American Journal of Physiology-Heart and Circulatory Physiology* 302.5 (2012), H1102–H1115.

[3] H Ahmadzadeh, MK Rausch, and JD Humphrey. "Particle-based computational modelling of arterial disease". In: *J. R. Soc. Interface.* 15.149 (2018), p. 20180616.

[4] Mona Alimohammadi, Joseph M Sherwood, Morad Karimpour, Obiekezie Agu, Stavroula Balabani, and Vanessa Díaz-Zuccarini. "Aortic dissection simulation models for clinical support: fluid-structure interaction vs. rigid wall models". In: *Biomed. Eng. Online* 14.1 (2015), p. 34.

[5] Marcus Ang, Aris Konstantopoulos, Gwendoline Goh, Hla M Htoon, Xinyi Seah, Nyein Chan Lwin, Xinyu Liu, Si Chen, Linbo Liu, and Jodhbir S Mehta. "Evaluation of a micro-optical coherence tomography for the corneal endothelium in an animal model". In: *Sci. Rep.* 6 (2016), p. 29769.

[6] Dimitrios C Angouras, Eleftherios P Kritharis, and Dimitrios P Sokolis. "Regional distribution of delamination strength in ascending thoracic aortic aneurysms". In: *J. Mech. Behav. Biomed. Mater.* (2019).

[7] Dimitrios Angouras, Dimitrios P. Sokolis, Theodosios Dosios, Nikolaos Kostomitsopoulos, Harisios Boudoulas, Gregorios Skalkeas, and Panagiotis E. Karayannacos. "Effect of impaired vasa vasorum flow on the structure and mechanics of the thoracic aorta: implications for the pathogenesis of aortic dissection". In: *Eur. J. Cardiothorac. Surg.* 17.4 (2000), pp. 468–473.

[8] Georgia Southern University - Armstrong. *Heart and vessels.* URL: https://www.studyblue.com/notes/note/n/heart-and-vessels/deck/6409908 (visited on 09/20/2020).

[9] DJ Aronberg, HS Glazer, K Madsen, and SS Sagel. "Normal thoracic aortic diameters by computed tomography." In: *J. Comput. Assist. Tomogr.* 8.2 (1984), pp. 247–250.

[10] Stéphane Avril, Pierre Badel, Mohamed Gabr, Michael A Sutton, and Susan M Lessner. "Biomechanics of porcine renal arteries and role of axial stretch". In: *J. Biomech. Eng.* 135.8 (2013).

[11] Charles van Baardwijk and Margot R Roach. "Factors in the propagation of aortic dissections in canine thoracic aortas". In: *J. Biomech.* 20.1 (1987), pp. 67–73.

[12] Charles van Baardwijk and Margot R Roach. "Factors in the propagation of aortic dissections in canine thoracic aortas". In: *J. Biomech.* 20.1 (1987), pp. 67–73.

[13] Pierre Badel, Stéphane Avril, Michael A. Sutton, and Susan M. Lessner. "Numerical simulation of arterial dissection during balloon angioplasty of atherosclerotic coronary arteries". In: *J. Biomech.* 47.4 (2014), pp. 878–889.

[14] Zhixuan Bai, Jun Gu, Yingkang Shi, and Wei Meng. "Effect of inflammation on the biomechanical strength of involved aorta in type A aortic dissection and ascending thoracic aortic aneurysm: an initial research". In: *Anatol. J. Cardiol.* 20.2 (2018), pp. 85–92.

[15] John D Bancroft and Marilyn Gamble. *Theory and practice of histological techniques*. Elsevier health sciences, 2008.

[16] Grigory Isaakovich Barenblatt et al. "The mathematical theory of equilibrium cracks in brittle fracture". In: *Adv. Appl. Mech.* 7.1 (1962), pp. 55–129.

[17] Alex J Barker, Craig Lanning, and Robin Shandas. "Quantification of hemodynamic wall shear stress in patients with bicuspid aortic valve using phase-contrast MRI". In: *Annals of biomedical engineering* 38.3 (2010), pp. 788–800.

[18] José Baruchel, Jean-Yves Buffiere, and Eric Maire. *X-ray tomography in material science*. Hermes science publications, 2000.

[19] Yuri Bazilevs, Kenji Takizawa, and Tayfun E. Tezduyar. "Challenges and directions in computational fluid-structure interaction". In: *Math. Models Methods Appl. Sci.* 23.02 (2013), pp. 215–221.

[20] C. J. Beller, M. R. Labrosse, M. J. Thubrikar, and F. Robicsek. "Finite element modeling of the thoracic aorta: including aortic root motion to evaluate the risk of aortic dissection". In: *J. Med. Eng. Technol.* 32.2 (2008), pp. 167–170.

[21] Ted Belytschko and Tom Black. "Elastic crack growth in finite elements with minimal remeshing". In: *Int. J. Numer. Methods Eng.* 45.5 (1999), pp. 601–620.

[22] Renate W Boekhoven, Mathijs FJ Peters, Marcel CM Rutten, Marc R van Sambeek, Frans N van de Vosse, and Richard GP Lopata. "Inflation and bi-axial tensile testing of healthy porcine carotid arteries". In: *Ultrasound Med. Biol.* 42.2 (2016), pp. 574–585.

[23] Stephan A Boppart, Brett E Bouma, Costas Pitris, James F Southern, Mark E Brezinski, and James G Fujimoto. "In vivo cellular optical coherence tomography imaging". In: *Nat. Med.* 4.7 (1998), pp. 861–865.

[24] J Brunet, B Pierrat, J Adrien, E Maire, N Curt, and P Badel. "A Novel Method for In Vitro 3D Imaging of Dissecting Pressurized Arterial Segments Using X-Ray Microtomography". In: *Exp. Mech.* (2020), pp. 1–11.

[25] J Brunet, B Pierrat, E Maire, J Adrien, and P Badel. "A combined experimental-numerical lamellar-scale approach of tensile rupture in arterial medial tissue using X-ray tomography". In: *J. Mech. Behav. Biomed. Mater.* 95 (2019), pp. 116–123.

[26] Joseph Brunet, Baptiste Pierrat, and Pierre Badel. "Review of current advances in the mechanical description and quantification of aortic dissection mechanisms". In: *IEEE Rev. Biomed. Eng.* (2020).

[27] L Cardamone, A Valentin, JF Eberth, and JD Humphrey. "Origin of axial prestretch and residual stress in arteries". In: *Biomech. Model. Mechanobiol.* 8.6 (2009), p. 431.

[28] Michael W Carson and Margot R Roach. "The strength of the aortic media and its role in the propagation of aortic dissection". In: *J. Biomech.* 23.6 (1990), pp. 579–588.

[29] Cristina Cavinato, Clementine Helfenstein-Didier, Thomas Olivier, Sabine Rolland Du Roscoat, Norbert Laroche, and Pierre Badel. "Biaxial loading of arterial tissues with 3D in situ observations of adventitia fibrous microstructure: a method coupling multi-photon confocal microscopy and bulge inflation test". In: *J. Mech. Behav. Biomed. Mater.* 74 (2017), pp. 488–498.

[30] Cristina Cavinato, Jerome Molimard, Nicolas Curt, Salvatore Campisi, Laurent Orgéas, and Pierre Badel. "Does the knowledge of the local thickness of human ascending thoracic aneurysm walls improve their mechanical analysis?" In: *Front. bioeng. biotechnol.* 7 (2019), p. 169.

[31] Z. Cheng, F. P. P. Tan, C. V. Riga, C. D. Bicknell, M. S. Hamady, R. G. J. Gibbs, N. B. Wood, and X. Y. Xu. "Analysis of flow patterns in a patient-specific aortic dissection model". In: *J. Biomech. Eng.* 132.5 (2010), p. 051007.

[32] Qingzhuo Chi, Ying He, Yong Luan, Kairong Qin, and Lizhong Mu. "Numerical analysis of wall shear stress in ascending aorta before tearing in type A aortic dissection". In: *Comput. Biol. Med.* 89 (2017), pp. 236–247.

[33] Anne S Chin, Martin J Willemink, Aya Kino, Virginia Hinostroza, Anna M Sailer, Michael P Fischbein, R Scott Mitchell, Gerald J Berry, D Craig Miller, and Dominik Fleischmann. "Acute limited intimal tears of the thoracic aorta". In: *Journal of the American College of Cardiology* 71.24 (2018), pp. 2773–2785.

[34] Ming-Jay Chow, Raphaël Turcotte, Charles P Lin, and Yanhang Zhang. "Arterial extracellular matrix: a mechanobiological study of the contributions and interactions of elastin and collagen". In: *Biophys. J.* 106.12 (2014), pp. 2684–2692.

[35] Jin Wook Chung, Christopher Elkins, Toyohiko Sakai, Noriyuki Kato, Thomas Vestring, Charles P. Semba, Suzanne M. Slonim, and Michael D. Dake. "True-lumen collapse in aortic dissection". In: *Radiology* 214.1 (2000), pp. 87–98.

[36] Cheng-Jen Chuong and Yuan-Cheng Fung. "Residual stress in arteries". In: *Front. Biomech.* Springer, 1986, pp. 117–129.

[37] John M Clark and S Glagov. "Structural integration of the arterial wall. I. Relationships and attachments of medial smooth muscle cells in normally distended and hyperdistended aortas". In: *Lab. Invest.* 40.5 (1979), pp. 587–602.

[38] John M Clark and Seymour Glagov. "Transmural organization of the arterial media. The lamellar unit revisited." In: *Arterioscler Thromb Vasc Biol* 5.1 (1985), pp. 19–34.

[39] Michael J Collins, Varun Dev, Bradley H Strauss, Paul WM Fedak, and Jagdish Butany. "Variation in the histopathological features of patients with ascending aortic aneurysms: a study of 111 surgically excised cases". In: *J. Clin. Pathol.* 61.4 (2008), pp. 519–523.

[40] Matthew I Converse, Raymond G Walther, Justin T Ingram, Yang Li, S Michael Yu, and Kenneth L Monson. "Detection and characterization of molecular-level collagen damage in overstretched cerebral arteries". In: *Acta Biomater.* 67 (2018), pp. 307–318.

[41] Irene Costantini, Riccardo Cicchi, Ludovico Silvestri, Francesco Vanzi, and Francesco Saverio Pavone. "In-vivo and ex-vivo optical clearing methods for biological tissues". In: *Biomed. Opt. Express* 10.10 (2019), pp. 5251–5267.

[42] Felisa Berenguer de la Cuesta, Richard J Bean, Catriona McCallion, Kris Wallace, Laurent Bozec, Jen C Hiller, Nicholas J Terrill, and Ian K Robinson. "Collagen imaged by Coherent X-ray Diffraction: towards a complementary tool to conventional scanning SAXS". In: *J. Phys. Conf. Ser.* 247.1 (2010), p. 012004.

[43] A. Daugherty and L. A. Cassis. "Mouse Models of Abdominal Aortic Aneurysms". In: *Arterioscler. Thromb. Vasc. Biol.* 24.3 (2004), pp. 429–434.

[44] Jorge O Virues Delgadillo, Sebastien Delorme, Rouwayda El-Ayoubi, Robert DiRaddo, Savvas G Hatzikiriakos, et al. "Effect of freezing on the passive mechanical properties of arterial samples". In: *Journal of Biomedical Science and Engineering* 3.07 (2010), p. 645.

[45] Koert P Dingemans, Norien Jansen, and Anton E Becker. "Ultrastructure of the normal human aortic media". In: *Virchows Arch. A Pathol. Anat. Histol.* 392.2 (1981), pp. 199–216.

[46] CM Disney, PD Lee, JA Hoyland, MJ Sherratt, and BK Bay. "A review of techniques for visualising soft tissue microstructure deformation and quantifying strain Ex Vivo". In: *J. Microsc.* (2018).

[47] Robert M Doroghazi and Eve Elizabeth Slater. *Aortic dissection*. McGraw-Hill Companies, 1983.

[48] Barry J Doyle and Paul E Norman. "Computational biomechanics in thoracic aortic dissection: today's approaches and tomorrow's opportunities". In: *Ann. Biomed. Eng.* 44.1 (2016), pp. 71–83.

[49] Wolfgang Drexler, U Morgner, FX Kärtner, C Pitris, SA Boppart, XD Li, EP Ippen, and JG Fujimoto. "In vivo ultrahigh-resolution optical coherence tomography". In: *Opt. Lett.* 24.17 (1999), pp. 1221–1223.

[50] Donald S Dugdale. "Yielding of steel sheets containing slits". In: *J. Mech. Phys. Solids* 8.2 (1960), pp. 100–104.

[51] Dennis W. Dunning, Joel K. Kahn, Earl T. Hawkins, and William W. O'Neill. "Iatrogenic coronary artery dissections extending into and involving the aortic root". In: *Catheter. Cardiovasc. Interv.* 51.4 (2000), pp. 387–393.

[52] Ambroise Duprey, Khalil Khanafer, Marty Schlicht, Stéphane Avril, David Williams, and Ramon Berguer. "In vitro characterisation of physiological and maximum elastic modulus of ascending thoracic aortic aneurysms using uniaxial tensile testing". In: *European Journal of Vascular and Endovascular Surgery* 39.6 (2010), pp. 700–707.

[53] Tomasz Dziodzio, Andrzej Juraszek, David Reineke, Hansjörg Jenni, Etienne Zermatten, Daniel Zimpfer, Martin Stoiber, Verena Scheikl, Heinrich Schima, Michael Grimm, et al. "Experimental acute type B aortic dissection: different sites of primary entry tears cause different ways of propagation". In: *Ann. Thorac. Surg.* 91.3 (2011), pp. 724–727.

[54] Alexander Emmott, Ismaïl El-Hamamsy, and Richard L. Leask. "Histopathological and biomechanical properties of the aortic wall in 2 patients with chronic type A aortic dissection". In: *Cardiovasc. Pathol.* 29 (2017), pp. 48–52.

[55] R Erbel, F Alfonso, C Boileau, O Dirsch, B Eber, A Haverich, H Rakowski, J Struyven, K Radegran, U Sechtem, et al. "Diagnosis and management of aortic dissection: task force on aortic dissection, European society of cardiology". In: *European heart journal* 22.18 (2001), pp. 1642–1681.

[56] Raimund Erbel, Hellmut Oelert, Jürgen Meyer, Maria Puth, Susanne Mohr-Katoly, Dirk Hausmann, Werner Daniel, Stefano Maffei, Aurelio Caruso, and FE Covino. "Effect of medical and surgical therapy on aortic dissection evaluated by transesophageal echocardiography. Implications for prognosis and therapy. The European Cooperative Study Group on Echocardiography." In: *Circulation* 87.5 (1993), pp. 1604–1615.

[57] Elsa Madeleine Faure, Ludovic Canaud, Philippe Cathala, Isabelle Serres, Charles Marty-Ané, and Pierre Alric. "Human ex-vivo model of Stanford type B aortic dissection". In: *J. Vasc. Surg.* 60.3 (2014), pp. 767–775.

[58] Andriy Fedorov, Reinhard Beichel, Jayashree Kalpathy-Cramer, Julien Finet, Jean-Christophe Fillion-Robin, Sonia Pujol, Christian Bauer, Dominique Jennings, Fiona Fennessy, Milan Sonka, et al. "3D Slicer as an image computing platform for the Quantitative Imaging Network". In: *Magnetic resonance imaging* 30.9 (2012), pp. 1323–1341.

[59] Emer M Feerick, Xiangyi Cheryl Liu, and Patrick McGarry. "Anisotropic mode-dependent damage of cortical bone using the extended finite element method (XFEM)". In: *J. Mech. Behav. Biomed. Mater.* 20 (2013), pp. 77–89.

[60] A Ferrara and A Pandolfi. "A numerical study of arterial media dissection processes". In: *Int. J. Fract.* 166.1-2 (2010), pp. 21–33.

[61] Anna Ferrara and ANNA Pandolfi. "Numerical modelling of fracture in human arteries". In: *Computer Methods in Biomechanics and Biomedical Engineering* 11.5 (2008), pp. 553–567.

[62] Jacopo Ferruzzi, Sae-Il Murtada, Guangxin Li, Yang Jiao, Selen Uman, Magdalene YL Ting, iae Tellides, and Jay D Humphrey. "Pharmacologically improved contractility protects against aortic dissection in mice with disrupted transforming growth factor-β signaling despite compromised extracellular matrix properties". In: *Arterioscler. Thromb. Vasc. Biol.* (2016), ATVBAHA–116.

[63] Erwan Filoux, Jonathan Mamou, Orlando Aristizábal, and Jeffrey A Ketterling. "Characterization of the spatial resolution of different high-frequency imaging systems using a novel anechoic-sphere phantom". In: *IEEE Trans. Ultrason. Ferroelectr. Freq. Control* 58.5 (2011).

[64] Brian FitzGibbon, Behrooz Fereidoonnezhad, Jamie Concannon, Niamh Hynes, Sherif Sultan, Kevin Mattheus Moerman, and Patrick McGarry. "A numerical investigation of the initiation of aortic dissection". In: (2020).

[65] Brian FitzGibbon and Patrick McGarry. "Development of a test method to investigate mode II fracture and dissection of arteries". In: *Acta Biomaterialia* (2020).

[66] Jiawei Fu, Fabrice Pierron, and Pablo D Ruiz. "Elastic stiffness characterization using three-dimensional full-field deformation obtained with optical coherence tomography and digital volume correlation". In: *J. Biomed. Opt.* 18.12 (2013), p. 121512.

[67] Y. C Fung. *Biomechanics: mechanical properties of living tissues*. New York: Springer-Verlag, 1993.

[68] Feng Gao, Zhihong Guo, Makoto Sakamoto, and Teruo Matsuzawa. "Fluid-structure interaction within a layered aortic arch model". In: *J. Biol. Phys.* 32.5 (2006), pp. 435–454.

[69] Claudio M García-Herrera, José M Atienza, FJ Rojo, Els Claes, GV Guinea, Diego J Celentano, Carlos García-Montero, and Raúl L Burgos. "Mechanical behaviour and rupture of normal and pathological human ascending aortic wall". In: *Medical & biological engineering & computing* 50.6 (2012), pp. 559–566.

[70] Stefano Gasperini, Valerio Zacà, and Sergio Mondillo. "Real-time imaging of dissection of the ascending aorta". In: *Eur. J. Echocardiogr.* 9.1 (2007), pp. 97–98.

[71] T Christian Gasser, Ray W Ogden, and Gerhard A Holzapfel. "Hyperelastic modelling of arterial layers with distributed collagen fibre orientations". In: *J. R. Soc. Interface* 3.6 (2006), pp. 15–35.

[72] T. Christian Gasser and Gerhard A. Holzapfel. "Modeling the propagation of arterial dissection". In: *Eur. J. Mech. A. Solids* 25.4 (2006), pp. 617–633.

[73] Daniel Thomas Ginat and Rajiv Gupta. "Advances in computed tomography imaging technology". In: *Annu. Rev. Biomed. Eng.* 16 (2014), pp. 431–453.

[74] Audrey M Glauert. "The high voltage electron microscope in biology". In: *J. Cell Biol.* 63.3 (1974), p. 717.

[75] Silvia Gómez-Moreno, Manel Sabaté, Pilar Jiménez-Quevedo, Paul Vázquez, Fernando Alfonso, Dominick J. Angiolillo, Rosana Hernández-Antolín, Raúl Moreno, Camino Bañuelos, Javier Escaned, and Carlos Macaya. "Iatrogenic dissection of the ascending aorta following heart catheterisation: incidence, management and outcome". In: *EuroIntervention* 2.2 (2006), pp. 197–202.

[76] Michalina J Gora, Melissa J Suter, Guillermo J Tearney, and Xingde Li. "Endoscopic optical coherence tomography: technologies and clinical applications". In: *Biomedical optics express* 8.5 (2017), pp. 2405–2444.

[77] I Gore. "Pathogenesis of dissecting aneurysm of the aorta". In: *Arch. Pathol.* 53.2 (1952), pp. 142–153.

[78] Will Goth, John Lesicko, Michael S. Sacks, and James W. Tunnell. "Optical-Based Analysis of Soft Tissue Structures". In: *Annu. Rev. Biomed. Eng.* 18.1 (2016), pp. 357–385.

[79] Hayit Greenspan. "Super-resolution in medical imaging". In: *The Computer Journal* 52.1 (2008), pp. 43–63.

[80] Osman Gültekin, Hüsnü Dal, and Gerhard A Holzapfel. "Numerical aspects of anisotropic failure in soft biological tissues favor energy-based criteria: A rate-dependent anisotropic crack phase-field model". In: *Computer methods in applied mechanics and engineering* 331 (2018), pp. 23–52.

[81] Osman Gültekin, Sandra Priska Hager, Hüsnü Dal, and Gerhard A Holzapfel. "Computational modeling of progressive damage and rupture in fibrous biological tissues: application to aortic dissection". In: *Biomech. Model. Mechanobiol.* (2019), pp. 1–22.

[82] Alfred Hager, Harald Kaemmerer, Ulrike Rapp-Bernhardt, Sebastian Blücher, Karl Rapp, Thomas M Bernhardt, Michael Galanski, and John Hess. "Diameters of the thoracic aorta throughout life as measured with helical computed tomography". In: *J. Thorac. Cardiovasc. Surg.* 123.6 (2002), pp. 1060–1066.

[83] Zvi Hashin. "Failure criteria for unidirectional fiber composites". In: *J. Appl. Mech.* 47.2 (1980), pp. 329–334.

[84] Henry W Haslach Jr, Lauren N Leahy, Parinaz Fathi, Joshua M Barrett, Amanda E Heyes, Thomas A Dumsha, and Eileen L McMahon. "Crack propagation and its shear mechanisms in the bovine descending aorta". In: *Cardiovasc. Eng. Technol.* 6.4 (2015), pp. 501–518.

[85] Henry W Haslach Jr, Ahmed Siddiqui, Amanda Weerasooriya, Ryan Nguyen, Jacob Roshgadol, Noel Monforte, and Eileen McMahon. "Fracture mechanics of shear crack propagation and dissection in the healthy bovine descending aortic media". In: *Acta Biomater.* 68 (2018), pp. 53–66.

[86] Henry W. Haslach, Peter Riley, and Aviva Molotsky. "The influence of medial substructures on rupture in bovine aortas". In: *Cardiovasc. Eng. Technol.* 2.4 (2011), pp. 372–387.

[87] I Hatzaras, M Tranquilli, M Coady, PM Barrett, Jesse Bible, and JA Elefteriades. "Weight lifting and aortic dissection: more evidence for a connection". In: *Cardiology* 107.2 (2007), pp. 103–106.

[88] Michael R Hee, Joseph A Izatt, Eric A Swanson, David Huang, Joel S Schuman, Charles P Lin, Carmen A Puliafito, and James G Fujimoto. "Optical coherence tomography of the human retina". In: *Arch. Ophthalmol.* 113.3 (1995), pp. 325–332.

[89] Clémentine Helfenstein-Didier, Damien Taïnoff, Julien Viville, Jérôme Adrien, Eric Maire, and Pierre Badel. "Tensile rupture of medial arterial tissue studied by X-ray micro-tomography on stained samples". In: *J. Mech. Behav. Biomed. Mater.* 78 (2018), pp. 362–368.

[90] LF Hiratzka, GL Bakris, JA Beckman, RM Bersin, VF Carr, DE Casey, KA Eagle, LK Hermann, EM Isselbacher, EA Kazerooni, et al. "Guidelines for the diagnosis and management of patients with thoracic aortic disease: a report of the american college of cardiology foundation/american heart association task force on practice guidelines, american association for thoracic surgery, american college of radiology, american stroke association, society of cardiovascular anesthesiologists, society for cardiovascular angiography and interventions, society of interventional radiology, society of thoracic surgeons, and society for vascular medicine". In: *Circulation* 121.3 (2010), e266–e369.

[91] Albert E Hirst Jr and Varner J Johns Jr. "Experimental dissection of media of aorta by pressure: its relation to spontaneous dissecting aneurysm". In: *Circ. Res.* 10.6 (1962), pp. 897–903.

[92] Albert E Hirst, Varner J Johns, and S Wesley Kime. "Dissecting aneurysm of the aorta: a review of 505 cases". In: *Medicine (Baltimore)* 37.3 (1958), p. 217.

[93] A Gerhard Holzapfel. *Nonlinear solid mechanics II*. John Wiley & Sons, Inc., 2000.

[94] Gerhard A. Holzapfel, Gerhard Sommer, Christian T. Gasser, and Peter Regitnig. "Determination of layer-specific mechanical properties of human coronary arteries with nonatherosclerotic intimal thickening and related constitutive modeling". In: *Am. J. Physiol. Heart Circ. Physiol.* 289.5 (2005), H2048–H2058.

[95] Gerhard A Holzapfel, Thomas C Gasser, and Ray W Ogden. "A new constitutive framework for arterial wall mechanics and a comparative study of material models". In: *J. Elast.* 61.1-3 (2000), pp. 1–48.

[96] Gerhard A Holzapfel, Gerhard Sommer, Martin Auer, Peter Regitnig, and Ray W Ogden. "Layer-specific 3D residual deformations of human aortas with non-atherosclerotic intimal thickening". In: *Ann. Biomed. Eng.* 35.4 (2007), pp. 530–545.

[97] Lukas Horny, Jakub Kronek, Hynek Chlup, Rudolf Zitny, Jan Vesely, and Martin Hulan. "Orientations of collagen fibers in aortic histological section". In: *Bulletin of applied mechanics* 6.22 (2010), pp. 25–29.

[98] Lukáš Horný, Marek Netušil, and Tereza Voňavková. "Axial prestretch and circumferential distensibility in biomechanics of abdominal aorta". In: *Biomechanics and modeling in mechanobiology* 13.4 (2014), pp. 783–799.

[99] Chih-Chung Huang, Pei-Yu Chen, Po-Hsun Peng, and Po-Yang Lee. "40 MH z high-frequency ultrafast ultrasound imaging". In: *Med. Phys.* 44.6 (2017), pp. 2185–2195.

[100] Walter Huda and R Brad Abrahams. "X-ray-based medical imaging and resolution". In: *Am. J. Roentgenol.* 204.4 (2015), W393–W397.

[101] J. D. Humphrey. "Possible mechanical roles of glycosaminoglycans in thoracic aortic dissection and associations with dysregulated transforming growth factor-β". In: *J. Vasc. Res.* 50.1 (2013), pp. 1–10.

[102] Jay D Humphrey. *Cardiovascular solid mechanics: cells, tissues, and organs*. Springer Science & Business Media, 2013.

[103] Jay D Humphrey and Gerhard A Holzapfel. "Mechanics, mechanobiology, and modeling of human abdominal aorta and aneurysms". In: *J. Biomech.* 45.5 (2012), pp. 805–814.

[104] JD Humphrey, JF Eberth, WW Dye, and RL Gleason. "Fundamental role of axial stress in compensatory adaptations by arteries". In: *Journal of biomechanics* 42.1 (2009), pp. 1–8.

[105] Janne MJ Huttunen, Leo Kärkkäinen, and Harri Lindholm. "Pulse transit time estimation of aortic pulse wave velocity and blood pressure using machine learning and simulated training data". In: *PLoS Comput. Biol* 15.8 (2019), e1007259.

[106] Toshiharu Ishii and Noriko Asuwa. "Collagen and elastin degradation by matrix metalloproteinases and tissue inhibitors of matrix metalloproteinase in aortic dissection". In: *Human pathology* 31.6 (2000), pp. 640–646.

[107] Ding-Sheng Jiang, Xin Yi, Xue-Hai Zhu, and Xiang Wei. "Experimental in vivo and ex vivo models for the study of human aortic dissection: promises and challenges". In: *Am. J. Transl. Res.* 8.12 (2016), pp. 5125–5140.

[108] FHW Jonker, H Mojibian, FJV Schlösser, DM Botta, JE Indes, FL Moll, and BE Muhs. "The impact of hypovolaemic shock on the aortic diameter in a porcine model". In: *European Journal of Vascular and Endovascular Surgery* 40.5 (2010), pp. 564–571.

[109] C. Karmonik, J. Bismuth, D. J. Shah, M. G. Davies, D. Purdy, and A. B. Lumsden. "Computational study of haemodynamic effects of entry- and exit-tear coverage in a DeBakey type III aortic dissection: technical report". In: *Eur. J. Vasc. Endovasc. Surg.* 42.2 (2011), pp. 172–177.

[110] Dennis Kasper, Anthony Fauci, Stephen Hauser, Dan Longo, J Jameson, and Joseph Loscalzo. *Harrison's principles of internal medicine, 19e*. Vol. 1. 2. Mcgraw-hill, 2015.

[111] VA Kasyanov, BA Purinya, and EE Tseders. "Determination of the shear modulus of human blood-vessel walls". In: *Polymer Mechanics* 14.5 (1978), pp. 753–755.

[112] NS Khamin. "The strength properties of the human iliac and carotid arteries and their changes with age". In: *Polymer Mechanics* 14.5 (1978), pp. 715–718.

[113] Khalil Khanafer and Ramon Berguer. "Fluid-structure interaction analysis of turbulent pulsatile flow within a layered aortic wall as related to aortic dissection". In: *J. Biomech.* 42.16 (2009), pp. 2642–2648.

[114] Armen R Kherlopian, Ting Song, Qi Duan, Mathew A Neimark, Ming J Po, John K Gohagan, and Andrew F Laine. "A review of imaging techniques for systems biology". In: *BMC Syst. Biol.* 2.1 (2008), p. 74.

[115] Junyoung Kim, Sunwon Kim, Joon Woo Song, Hyun Jung Kim, Min Woo Lee, Jeongmoo Han, Jin Won Kim, and Hongki Yoo. "Flexible endoscopic micro-optical coherence tomography for three-dimensional imaging of the arterial microstructure". In: *Scientific Reports* 10.1 (2020), pp. 1–11.

[116] Yskert von Kodolitsch, Susanne K Csösz, Dietmar H Koschyk, Ilka Schalwat, Roger Loose, Matthias Karck, Christoph Dieckmann, Rossella Fattori, Axel Haverich, Jürgen Berger, et al. "Intramural hematoma of the aorta: predictors of progression to dissection and rupture". In: *Circulation* 107.8 (2003), pp. 1158–1163.

[117] Nicholas T. Kouchoukos and Dimitrios Dougenis. "Surgery of the thoracic aorta". In: *N. Engl. J. Med.* 336.26 (1997), pp. 1876–1889.

[118] Marta Kozuń. "Delamination properties of the human thoracic arterial wall with early stage of atherosclerosis lesions". In: *Journal of Theoretical and Applied Mechanics* 54 (2016).

[119] Witold Krasny, Hélène Magoariec, Claire Morin, and Stéphane Avril. "Kinematics of collagen fibers in carotid arteries under tension-inflation loading". In: *Journal of the Mechanical Behavior of Biomedical Materials* 77 (2018), pp. 718–726.

[120] Witold Krasny, Claire Morin, Hélène Magoariec, and Stéphane Avril. "A comprehensive study of layer-specific morphological changes in the microstructure of carotid arteries under uniaxial load". In: *Acta Biomater.* 57 (2017), pp. 342–351.

[121] Michel R Labrosse, Eleanor R Gerson, John P Veinot, and Carsten J Beller. "Mechanical characterization of human aortas from pressurization testing and a paradigm shift for circumferential residual stress". In: *J. Mech. Behav. Biomed. Mater.* 17 (2013), pp. 44–55.

[122] Jeffrey C Lagarias, James A Reeds, Margaret H Wright, and Paul E Wright. "Convergence properties of the Nelder–Mead simplex method in low dimensions". In: *SIAM J. Optim.* 9.1 (1998), pp. 112–147.

[123] Xiaochang Leng, Boran Zhou, Xiaomin Deng, Lindsey Davis, Susan M Lessner, Michael A Sutton, and Tarek Shazly. "Experimental and numerical studies of two arterial wall delamination modes". In: *J. Mech. Behav. Biomed. Mater.* 77 (2018), pp. 321–330.

[124] Eugene Lin and Adam Alessio. "What are the basic concepts of temporal, contrast, and spatial resolution in cardiac CT?" In: *J. Cardiovasc. Comput. Tomogr.* 3.6 (2009), pp. 403–408.

[125] Linbo Liu, Joseph A Gardecki, Seemantini K Nadkarni, Jimmy D Toussaint, Yukako Yagi, Brett E Bouma, and Guillermo J Tearney. "Imaging the subcellular structure of human coronary atherosclerosis using micro–optical coherence tomography". In: *Nat. Med.* 17.8 (2011), p. 1010.

[126] Gerlinde Logghe, Bram Trachet, Lydia Aslanidou, Pablo Villaneuva-erez, Julie De Backer, Nikolaos Stergiopulos, Marco Stampanoni, Hiroki Aoki, and Patrick Segers. "Propagation-based phase-contrast synchrotron imaging of aortic dissection in mice: from individual elastic lamella to 3D analysis". In: *Scientific Reports* 8.1 (2018), pp. 1–11.

[127] Júlia López-Guimet, Jordi Andilla, Pablo Loza-Alvarez, and Gustavo Egea. "High-Resolution Morphological Approach to Analyse Elastic Laminae Injuries of the Ascending Aorta in a Murine Model of Marfan Syndrome". In: *Sci. Rep.* 7 (2017).

[128] X. Lu, J. Yang, J. B. Zhao, H. Gregersen, and G. S. Kassab. "Shear modulus of porcine coronary artery: contributions of media and adventitia". In: *Am. J. Physiol. Heart Circ. Physiol.* 285.5 (2003), H1966–H1975.

[129] Fang Luo, Xian-Liang Zhou, Jian-Jun Li, and Ru-Tai Hui. "Inflammatory response is associated with aortic dissection". In: *Ageing Res. Rev.* 8.1 (2009), pp. 31–35.

[130] Neil F MacLean, Nancy L Dudek, and Margot R Roach. "The role of radial elastic properties in the development of aortic dissections". In: *J. Vasc. Surg.* 29.4 (1999), pp. 703–710.

[131] Michele Marino, Matthew I Converse, Kenneth L Monson, and Peter Wriggers. "Molecular-level collagen damage explains softening and failure of arterial tissues: A quantitative interpretation of CHP data with a novel elasto-damage model". In: *J. Mech. Behav. Biomed. Mater.* 97 (2019), pp. 254–271.

[132] K. von der Mark. "Localization of collagen types in tissues". In: *Int. Rev. Connect. Tissue Res.* 9 (1981), pp. 265–324.

[133] Baby Martin-McNulty, Jon Vincelette, Ronald Vergona, Mark E Sullivan, and Yi-Xin Wang. "Noninvasive measurement of abdominal aortic aneurysms in intact mice by a high-frequency ultrasound imaging system". In: *Ultrasound Med. Biol.* 31.6 (2005), pp. 745–749.

[134] Caitlin Martin, Thuy Pham, and Wei Sun. "Significant differences in the material properties between aged human and porcine aortic tissues". In: *Eur. J. Cardiothorac. Surg.* 40.1 (2011), pp. 28–34.

[135] Charles-Henri Marty-Ané, Olivier SerreCousiné, Jean-Claude Laborde, Valérie Costes, Henry Mary, and Jean-Paul Senac. "Use of a Balloon-expandable Intravascular Graft in the Management of Type B Aortic Dissection in an Animal Model". In: *J. Vasc. Interv. Radiol.* 6.1 (1995), pp. 97–103.

[136] C Mayerick, F Carré, and J Elefteriades. "Aortic dissection and sport: physiologic and clinical understanding provide an opportunity to save young lives." In: *J. Card. Surg.* 51.5 (2010), pp. 669–681.

[137] E Louise Meredith and Navroz D Masani. "Echocardiography in the emergency assessment of acute aortic syndromes". In: *Eur. J. Echocardiogr.* 10.1 (2009), pp. i31–i39.

[138] Istvan Meszaros, Jozsef Morocz, Jozsef Szlavi, Janos Schmidt, Laszlo Tornoci, Laszlo Nagy, and Laszlo Szép. "Epidemiology and clinicopathology of aortic dissection". In: *Chest* 117.5 (2000), pp. 1271–1278.

[139] Ting Miao, Liqiong Tian, Xiaochang Leng, Zhangmu Miao, Jingjing Wang, Chengjun Xu, and Lisheng Liu. "A comparative study of cohesive zone models for predicting delamination fracture behaviors of arterial wall". In: *Open Phys.* 18.1 (2020), pp. 467–477.

[140] Dianna M Milewicz, Dong-Chuan Guo, Van Tran-Fadulu, Andrea L Lafont, Christina L Papke, Sakiko Inamoto, Carrie S Kwartler, and Hariyadarshi Pannu. "Genetic basis of thoracic aortic aneurysms and dissections: focus on smooth muscle cell contractile dysfunction". In: *Annu. Rev. Genomics Hum. Genet.* 9 (2008), pp. 283–302.

[141] Dianna M Milewicz, Siddharth K Prakash, and Francesco Ramirez. "Therapeutics targeting drivers of thoracic aortic aneurysms and acute aortic dissections: insights from predisposing genes and mouse models". In: *Annu. Rev. Med.* 68 (2017), pp. 51–67.

[142] Dianna M Milewicz and Francesco Ramirez. *Therapies for thoracic aortic aneurysms and acute aortic dissections: old controversies and new opportunities.* 2019.

[143] Hideya Mitsui, Hatsuzo Uchida, and Shigeru Teramoto. "Correlation between the layer of an intimal tear and the progression of aortic dissection." In: *Acta Med. Okayama* 48.2 (1994), pp. 93–99.

[144] Ryuta Mizutani and Yoshio Suzuki. "X-ray microtomography in biology". In: *Micron* 43.2-3 (2012), pp. 104–115.

[145] Susanne Mohr-Kahaly, Raimund Epbel, Peter Kearney, Maria Puth, and Jürgen Meyer. "Aortic intramural hemorrhage visualized by transesophageal echocardiography: findings and prognostic implication". In: *J. Am. Coll. Cardiol.* 23.3 (1994), pp. 658–664.

[146] David L. S Morales, Jacquelyn A Quin, John H Braxton, Graeme L Hammond, Richard J Gusberg, and John A Elefteriades. "Experimental confirmation of effectiveness of fenestration in acute aortic dissection". In: *Ann. Thorac. Surg.* 66.5 (1998), pp. 1679–1683.

[147] Carmel M Moran, Stephen D Pye, William Ellis, Anna Janeczko, Keith D Morris, Alan S McNeilly, and Hamish M Fraser. "A comparison of the imaging performance of high resolution ultrasound scanners for preclinical imaging". In: *Ultrasound Med. Biol.* 37.3 (2011), pp. 493–501.

[148] Paul D Morris, Andrew Narracott, Hendrik von Tengg-Kobligk, Daniel Alejandro Silva Soto, Sarah Hsiao, Angela Lungu, Paul Evans, Neil W Bressloff, Patricia V Lawford, D Rodney Hose, and Julian P Gunn. "Computational fluid dynamics modelling in cardiovascular medicine". In: *Heart* 102.1 (2016), pp. 18–28.

[149] S Jamaleddin Mousavi, Solmaz Farzaneh, and Stéphane Avril. "Computational predictions of damage propagation preceding dissection of ascending thoracic aortic aneurysms". In: *Int. j. numer. method. biomed. eng.* 34.4 (2018), e2944.

[150] Charles A Murray and Jesse E Edwards. "Spontaneous laceration of ascending aorta". In: *Circulation* 47.4 (1973), pp. 848–858.

[151] Manoj Myneni, Akshay Rao, Mingliang Jiang, Michael R Moreno, KR Rajagopal, and Chandler C Benjamin. "Segmental Variations in the Peel Characteristics of the Porcine Thoracic Aorta". In: *Annals of Biomedical Engineering* (2020), pp. 1–17.

[152] Masaki Nakashima, Shuichiro Kaji, Ryosuke Murai, Yasuhiro Sasaki, Mitsuhiko Ota, Kitae Kim, Takafumi Yamane, Takeshi Kitai, Atsushi Kobori, Natsuhiko Ehara, et al. "Detection of Micro Intimal Tear at a Very Early Stage in Patients With Acute Aortic Intramural Hematoma". In: *Circulation* 134.suppl_1 (2016), A13989–A13989.

[153] Yutaka Nakashima. "Pathogenesis of aortic dissection: elastic fiber abnormalities and aortic medial weakness". In: *Annals of vascular diseases* 3.1 (2010), pp. 28–36.

[154] Derek P. Nathan, Chun Xu, Joseph H. Gorman, Ron M. Fairman, Joseph E. Bavaria, Robert C. Gorman, Krishnan B. Chandran, and Benjamin M. Jackson. "Pathogenesis of acute aortic dissection: a finite element stress analysis". In: *Ann. Thorac. Surg.* 91.2 (2011), pp. 458–463.

[155] Christoph A Nienaber and Rachel E Clough. "Management of acute aortic dissection". In: *The Lancet* 385.9970 (2015), pp. 800–811.

[156] Christoph A Nienaber, Rachel E Clough, Natzi Sakalihasan, Toru Suzuki, Richard Gibbs, Firas Mussa, Michael P Jenkins, Matt M Thompson, Arturo Evangelista, James SM Yeh, et al. "Aortic dissection". In: *Nat. Rev. Dis. Primers.* 2.1 (2016), pp. 1–18.

[157] Christoph A Nienaber, Yskert von Kodolitsch, Ben Petersen, Roger Loose, Udo Helmchen, Axel Haverich, and Rolf P Spielmann. "Intramural hemorrhage of the thoracic aorta: diagnostic and therapeutic implications". In: *Circulation* 92.6 (1995), pp. 1465–1472.

[158] Mathieu Nierenberger, Yves Rémond, Saïd Ahzi, and Philippe Choquet. "Assessing the three-dimensional collagen network in soft tissues using contrast agents and high resolution micro-CT: application to porcine iliac veins". In: *C.R. Biol.* 338.7 (2015), pp. 425–433.

[159] Christopher Noble, Nicole Smulders, Roger Lewis, Matt J Carré, Steve E Franklin, Sheila MacNeil, and Zeike A Taylor. "Controlled peel testing of a model tissue for diseased aorta". In: *J. Biomech.* 49.15 (2016), pp. 3667–3675.

[160] Mary K O'Connell, Sushila Murthy, Samson Phan, Chengpei Xu, JoAnn Buchanan, Ryan Spilker, Ronald L Dalman, Christopher K Zarins, Winfried Denk, and Charles A Taylor. "The three-dimensional micro-and nanostructure of the aortic medial lamellar unit measured using 3D confocal and electron microscopy imaging". In: *Matrix Biol.* 27.3 (2008), pp. 171–181.

[161] Patrick T O'Gara and Roman W DeSanctis. "Acute aortic dissection and its variants: toward a common diagnostic and therapeutic approach". In: *Circulation* 92.6 (1995), pp. 1376–1378.

[162] Siobhan A O'Leary, Barry J Doyle, and Tim M McGloughlin. "The impact of long term freezing on the mechanical properties of porcine aortic tissue". In: *Journal of the mechanical behavior of biomedical materials* 37 (2014), pp. 165–173.

[163] Teruaki Okuno, Masato Yamaguchi, Takuya Okada, Takuya Takahashi, Noriaki Sakamoto, Eisuke Ueshima, Kazuro Sugimura, and Koji Sugimoto. "Endovascular creation of aortic dissection in a swine model with technical considerations". In: *J. Vasc. Surg.* 55.5 (2012), pp. 1410–1418.

[164] Hiroaki Osada, Masahisa Kyogoku, Motonori Ishidou, Manabu Morishima, and Hiroyuki Nakajima. "Aortic dissection in the outer third of the media: what is the role of the vasa vasorum in the triggering process?" In: *Eur. J. Cardio-Thorac. Surg.* 43.3 (2012), e82–e88.

[165] Hiroaki Osada, Masahisa Kyogoku, Motonori Ishidou, Manabu Morishima, and Hiroyuki Nakajima. "Aortic dissection in the outer third of the media: what is the role of the vasa vasorum in the triggering process?" In: *Eur. J. Cardiothorac. Surg.* 43.3 (2013), e82–e88.

[166] Siladitya Pal, Alkiviadis Tsamis, Salvatore Pasta, Antonio D'Amore, Thomas G Gleason, David A Vorp, and Spandan Maiti. "A mechanistic model on the role of radially-running collagen fibers on dissection properties of human ascending thoracic aorta". In: *J. Biomech.* 47.5 (2014), pp. 981–988.

[167] Salvatore Pasta, Julie A. Phillippi, Alkiviadis Tsamis, Antonio D'Amore, Giuseppe M. Raffa, Michele Pilato, Cesare Scardulla, Simon C. Watkins, William R. Wagner, Thomas G. Gleason, and David A. Vorp. "Constitutive modeling of ascending thoracic aortic aneurysms using microstructural parameters". In: *Med. Eng. Phys.* 38.2 (2016), pp. 121–130.

[168] Salvatore Pasta, Julie A Phillippi, Thomas G Gleason, and David A Vorp. "Effect of aneurysm on the mechanical dissection properties of the human ascending thoracic aorta". In: *J. Thorac. Cardiovasc. Surg.* 143.2 (2012), pp. 460–467.

[169] Srikara V Peelukhana, Yanmin Wang, Zachary Berwick, Jarin Kratzberg, Joshua Krieger, Blayne Roeder, Rachel E Cloughs, Albert Hsiao, Sean Chambers, and Ghassan S Kassab. "Role of pulse pressure and geometry of primary entry tear in acute type B dissection propagation". In: *Ann. Biomed. Eng.* 45.3 (2017), pp. 592–603.

[170] Juan A Peña, Miguel A Martínez, and Estefanía Peña. "Failure damage mechanical properties of thoracic and abdominal porcine aorta layers and related constitutive modeling: phenomenological and microstructural approach". In: *Biomechanics and Modeling in Mechanobiology* 18.6 (2019), pp. 1709–1730.

[171] Juan A Peña, Miguel A Martínez, and Estefanía Peña. "Layer-specific residual deformations and uniaxial and biaxial mechanical properties of thoracic porcine aorta". In: *Journal of the Mechanical Behavior of Biomedical Materials* 50 (2015), pp. 55–69.

[172] Jop Perrée, Ton G van Leeuwen, Raphaella Kerindongo, Jos AE Spaan, and Ed VanBavel. "Function and structure of pressurized and perfused porcine carotid arteries: effects of in vitro balloon angioplasty". In: *Am. J. Pathol.* 163.5 (2003), pp. 1743–1750.

[173] Julie A Phillippi, Benjamin R Green, Michael A Eskay, Mary P Kotlarczyk, Michael R Hill, Anne M Robertson, Simon C Watkins, David A Vorp, and Thomas G Gleason. "Mechanism of aortic medial matrix remodeling is distinct in patients with bicuspid aortic valve". In: *J. Thorac. Cardiovasc. Surg.* 147.3 (2014), pp. 1056–1064.

[174] Joseph E Pichamuthu, Julie A Phillippi, Deborah A Cleary, Douglas W Chew, John Hempel, David A Vorp, and Thomas G Gleason. "Differential tensile strength and collagen composition in ascending aortic aneurysms by aortic valve phenotype". In: *Ann. Thorac. Surg.* 96.6 (2013), pp. 2147–2154.

[175] Edward K Prokop, Roger F Palmer, and Myron W Wheat Jr. "Hydrodynamic forces in dissecting aneurysms: in-vitro studies in a tygon model and in dog aortas". In: *Circ. Res.* 27.1 (1970), pp. 121–127.

[176] Peter P Purslow. "Positional variations in fracture toughness, stiffness and strength of descending thoracic pig aorta". In: *J. Biomech.* 16.11 (1983), pp. 947–953.

[177] Chuan Qin and Dai-Shi Tian. "Acute ischemic stroke due to painless long-segmental aortic dissection". In: *Neurology* 92.10 (2019), pp. 484–485.

[178] Leslie E Quint, Joel F Platt, Seema S Sonnad, G Michael Deeb, and David M Williams. "Aortic intimal tears: detection with spiral computed tomography". In: *J. Endovasc. Ther.* 10.3 (2003), pp. 505–510.

[179] Keshava Rajagopal, Craig Bridges, and K. R. Rajagopal. "Towards an understanding of the mechanics underlying aortic dissection". In: *Biomech. Model. Mechanobiol.* 6.5 (2007), pp. 345–359.

[180] Mahmood K. Razavi, Earl Nishimura, Suzanne Slonim, Werner Zeigler, Stephen Kee, Heidi L. Witherall, Charles P. Semba, and Michael D. Dake. "Percutaneous creation of acute type-B aortic dissection: an experimental model for endoluminal therapy". In: *J. Vasc. Interv. Radiol.* 9.4 (1998), pp. 626–632.

[181] Weihong Ren, Yan Liu, Xuerui Wang, Lixin Jia, Chunmei Piao, Feng Lan, and Jie Du. "β-Aminopropionitrile monofumarate induces thoracic aortic dissection in C57BL/6 mice". In: *Sci. Rep.* 6 (2016), p. 28149.

[182] Johannes A. G. Rhodin. "Architecture of the vessel wall". In: *Comprehensive Physiology*. Ed. by Ronald Terjung. John Wiley & Sons, Inc., 1980, pp. 1–31.

[183] Erik L Ritman. "Current status of developments and applications of micro-CT". In: *Annu. Rev. Biomed. Eng.* 13 (2011), pp. 531–552.

[184] RS Rivlin. "Large elastic deformations of isotropic materials IV. Further developments of the general theory". In: *Philos. Trans. Royal Soc. A* 241.835 (1948), pp. 379–397.

[185] Margot R Roach and SH Song. "Variations in strength of the porcine aorta as a function of location". In: *Clin. Invest. Med.* 17.4 (1994), p. 308.

[186] Charles S Roberts and William C Roberts. "Aortic dissection with the entrance tear in the descending thoracic aorta. Analysis of 40 necropsy patients." In: *Annals of surgery* 213.4 (1991), p. 356.

[187] William C Roberts. "Aortic dissection: anatomy, consequences, and causes". In: *American heart journal* 101.2 (1981), pp. 195–214.

[188] Francis Robicsek and Mano J Thubrikar. “Hemodynamic considerations regarding the mechanism and prevention of aortic dissection”. In: *Ann. Thorac. Surg.* 58.4 (1994), pp. 1247–1253.

[189] S Roccabianca, C Bellini, and JD Humphrey. “Computational modelling suggests good, bad and ugly roles of glycosaminoglycans in arterial wall mechanics and mechanobiology”. In: *J. R. Soc. Interface* 11.97 (2014), p. 20140397.

[190] Sara Roccabianca, Gerard A Ateshian, and Jay D Humphrey. “Biomechanical roles of medial pooling of glycosaminoglycans in thoracic aortic dissection”. In: *Biomech. Model. Mechanobiol.* 13.1 (2014), pp. 13–25.

[191] Stéphane Roux, Julien Réthoré, and François Hild. “Digital image correlation and fracture: an advanced technique for estimating stress intensity factors of 2D and 3D cracks”. In: *Journal of Physics D: Applied Physics* 42.21 (2009), p. 214004.

[192] Curtis T Rueden, Johannes Schindelin, Mark C Hiner, Barry E DeZonia, Alison E Walter, Ellen T Arena, and Kevin W Eliceiri. “ImageJ2: ImageJ for the next generation of scientific image data”. In: *BMC bioinformatics* 18.1 (2017), p. 529.

[193] P Sáez, A García, Estefanía Peña, Thomas Christian Gasser, and MA Martínez. “Microstructural quantification of collagen fiber orientations and its integration in constitutive modeling of the porcine carotid artery”. In: *Acta biomaterialia* 33 (2016), pp. 183–193.

[194] Ashish Saini, Colin Berry, and Stephen Greenwald. “Effect of age and sex on residual stress in the aorta”. In: *J. Vasc. Res.* 32.6 (1995), pp. 398–405.

[195] M Catherine Sapp. *A Mathematical Model to Describe Aortic Dissections*. Faculty of Graduate Studies, University of Western Ontario, 1997.

[196] Johannes Schindelin, Ignacio Arganda-Carreras, Erwin Frise, Verena Kaynig, Mark Longair, Tobias Pietzsch, Stephan Preibisch, Curtis Rueden, Stephan Saalfeld, Benjamin Schmid, et al. “Fiji: an open-source platform for biological-image analysis”. In: *Nature methods* 9.7 (2012), pp. 676–682.

[197] JTC Schrauwen, A Vilanova, R Rezakhaniha, N Stergiopulos, FN Van De Vosse, and PHM Bovendeerd. “A method for the quantification of the pressure dependent 3D collagen configuration in the arterial adventitia”. In: *J. Struct. Biol.* 180.2 (2012), pp. 335–342.

[198] Andreas J Schriefl, Heimo Wolinski, Peter Regitnig, Sepp D Kohlwein, and Gerhard A Holzapfel. “An automated approach for three-dimensional quantification of fibrillar structures in optically cleared soft biological tissues”. In: *J. R. Soc. Interface* 10.80 (2013), p. 20120760.

[199] Sachin B. Shah, Colleen Witzenburg, Mohammad F. Hadi, Hallie P. Wagner, Janna M. Goodrich, Patrick W. Alford, and Victor H. Barocas. “Prefailure and failure mechanics of the porcine ascending thoracic aorta: experiments and a multiscale model”. In: *J. Biomech. Eng.* 136.2 (2014), p. 021028.

[200] Selda Sherifova, Gerhard Sommer, Christian Viertler, Peter Regitnig, Thomas Caranasos, Margaret Anne Smith, Boyce E Griffith, Ray W Ogden, and Gerhard A Holzapfel. “Failure properties and microstructure of healthy and aneurysmatic human thoracic aortas subjected to uniaxial extension with a focus on the media”. In: *Acta Biomater.* (2019).

[201] Hisashi Shimizu, Hideaki Yoshino, Hiroshi Udagawa, Atsushi Watanuki, Kohei Yano, Hirofumi Ide, Kenichi Sudo, and Kyozo Ishikawa. "Prognosis of aortic intramural hemorrhage compared with classic aortic dissection." In: *Am. J. Cardiol.* 85.6 (2000), pp. 792–5.

[202] Balraj Singh, Jennifer M Treece, Ghulam Murtaza, Samit Bhatheja, Steven J Lavine, and Timir K Paul. "Aortic dissection in a healthy male athlete: a unique case with comprehensive literature review". In: *Case Rep. Cardiol.* 2016 (2016).

[203] Gerhard Sommer, T Christian Gasser, Peter Regitnig, Martin Auer, and Gerhard A Holzapfel. "Dissection properties of the human aortic media: an experimental study". In: *J. Biomech. Eng.* 130.2 (2008), p. 021007.

[204] Gerhard Sommer, Selda Sherifova, Peter J Oberwalder, Otto E Dapunt, Patricia A Ursomanno, Abe DeAnda, Boyce E Griffith, and Gerhard A Holzapfel. "Mechanical strength of aneurysmatic and dissected human thoracic aortas at different shear loading modes". In: *J. Biomech.* 49.12 (2016), pp. 2374–2382.

[205] Jae-Kwan Song. "Update in acute aortic syndrome: intramural hematoma and incomplete dissection as new disease entities". In: *Journal of Cardiology* 64.3 (2014), pp. 153–161.

[206] Amy Henderson Squillacote, James Ahrens, Charles Law, Berk Geveci, Kenneth Moreland, and Brad King. *The paraview guide*. Vol. 366. Kitware Clifton Park, NY, 2007.

[207] Zoran Stankovic, Bradley D Allen, Julio Garcia, Kelly B Jarvis, and Michael Markl. "4D flow imaging with MRI". In: *Cardiovasc. Diagn. Ther.* 4.2 (2014), p. 173.

[208] Christodoulos I Stefanadis, Panagiotis E Karayannacos, Harisios K Boudoulas, Costas G Stratos, Charalambos V Vlachopoulos, Ismene A Dontas, and Pavlos K Toutouzas. "Medial necrosis and acute alterations in aortic distensibility following removal of the vasa vasorum of canine ascending aorta". In: *Cardiovasc. Res.* 27.6 (1993), pp. 951–956.

[209] Brian D Stemper, Narayan Yoganandan, Michael R Stineman, Thomas A Gennarelli, Jamie L Baisden, and Frank A Pintar. "Mechanics of fresh, refrigerated, and frozen arterial tissue". In: *Journal of Surgical Research* 139.2 (2007), pp. 236–242.

[210] Zhonghua Sun and Thanapong Chaichana. "A systematic review of computational fluid dynamics in type B aortic dissection". In: *Int. J. Cardiol.* 210 (2016), pp. 28–31.

[211] Lars G Svensson, Sherif B Labib, Andrew C Eisenhauer, and John R Butterly. "Intimal tear without hematoma: an important variant of aortic dissection that can elude current imaging techniques". In: *Circulation* 99.10 (1999), pp. 1331–1336.

[212] Jeremy Szajer and Kevin Ho-Shon. "A comparison of 4D flow MRI-derived wall shear stress with computational fluid dynamics methods for intracranial aneurysms and carotid bifurcations - A review". In: *Magn. Reson. Imaging* 48 (2018), pp. 62–69.

[213] Amy SM Tam, M Catherine Sapp, and Margot R Roach. "The effect of tear depth on the propagation of aortic dissections in isolated porcine thoracic aorta". In: *J. Biomech.* 31.7 (1998), pp. 673–676.

[214] Zhongzhao Teng, Dalin Tang, Jie Zheng, Pamela K Woodard, and Allen H Hoffman. "An experimental study on the ultimate strength of the adventitia and media of human atherosclerotic carotid arteries in circumferential and axial directions". In: *J. Biomech.* 42.15 (2009), pp. 2535–2539.

[215] Hiromu Terai, Nobushige Tamura, Sadatoshi Yuasa, Tatsuo Nakamura, Yasuhiko Shimizu, and Masashi Komeda. "An experimental model of Stanford type B aortic dissection". In: *J. Vasc. Interv. Radiol.* 16.4 (2005), pp. 515–519.

[216] Mano J Thubrikar. *Vascular mechanics and pathology.* Vol. 494. Springer, 2007.

[217] MJ Thubrikar, P Agali, and F Robicsek. "Wall stress as a possible mechanism for the development of transverse intimal tears in aortic dissections". In: *J. Med. Eng. Technol.* 23.4 (1999), pp. 127–134.

[218] James R. Thunes, Siladitya Pal, Ronald N. Fortunato, Julie A. Phillippi, Thomas G. Gleason, David A. Vorp, and Spandan Maiti. "A structural finite element model for lamellar unit of aortic media indicates heterogeneous stress field after collagen recruitment". In: *J. Biomech.* 49.9 (2016), pp. 1562–1569.

[219] James R. Thunes, Julie A. Phillippi, Thomas G. Gleason, David A. Vorp, and Spandan Maiti. "Structural modeling reveals microstructure-strength relationship for human ascending thoracic aorta". In: *J. Biomech.* 71 (2018), pp. 84–93.

[220] IM Tiessen and MR Roach. "Factors in the initiation and propagation of aortic dissections in human autopsy aortas". In: *J. Biomech. Eng.* 115.1 (1993), pp. 123–125.

[221] Jianhua Tong, Yu Cheng, and Gerhard A. Holzapfel. "Mechanical assessment of arterial dissection in health and disease: advancements and challenges". In: *J. Biomech.* 49.12 (2016), pp. 2366–2373.

[222] Jianhua Tong, T Cohnert, Peter Regitnig, Julia Kohlbacher, Ruth Birner-Grünberger, Andreas Jörg Schriefl, Gerhard Sommer, and Gerhard A Holzapfel. "Variations of dissection properties and mass fractions with thrombus age in human abdominal aortic aneurysms". In: *Journal of biomechanics* 47.1 (2014), pp. 14–23.

[223] Jianhua Tong, Gerhard Sommer, Peter Regitnig, and Gerhard A Holzapfel. "Dissection properties and mechanical strength of tissue components in human carotid bifurcations". In: *Ann. Biomed. Eng.* 39.6 (2011), pp. 1703–1719.

[224] Bram Trachet, Lydia Aslanidou, Alessandra Piersigilli, Rodrigo A. Fraga-Silva, Jessica Sordet-Dessimoz, Pablo Villanueva-Perez, Marco F.M. Stampanoni, Nikolaos Stergiopulos, and Patrick Segers. "Angiotensin II infusion into ApoE-/- mice: a model for aortic dissection rather than abdominal aortic aneurysm?" In: *Cardiovasc. Res.* 113.10 (2017), pp. 1230–1242.

[225] Bram Trachet, Mauro Ferraro, Goran Lovric, Lydia Aslanidou, Gerlinde Logghe, Patrick Segers, and Nikolaos Stergiopulos. "Synchrotron-based visualization and segmentation of elastic lamellae in the mouse carotid artery during quasi-static pressure inflation". In: *J. R. Soc. Interface* 16.155 (2019), p. 20190179.

[226] Bram Trachet, Rodrigo A Fraga-Silva, Francisco J Londono, Abigaíl Swillens, Nikolaos Stergiopulos, and Patrick Segers. "Performance comparison of ultrasound-based methods to assess aortic diameter and stiffness in normal and aneurysmal mice". In: *PLoS One* 10.5 (2015), e0129007.

[227] Bram Trachet, Alessandra Piersigilli, Rodrigo A. Fraga-Silva, Lydia Aslanidou, Jessica Sordet-Dessimoz, Alberto Astolfo, Marco F. M. Stampanoni, Patrick Segers, and Nikolaos Stergiopulos. "Ascending aortic aneurysm in angiotensin II-infused mice: formation, progression, and the role of focal dissections". In: *Arterioscler. Thromb. Vasc. Biol.* 36.4 (2016), pp. 673–681.

[228] Thomas T Tsai, Marty S Schlicht, Khalil Khanafer, Joseph L Bull, Doug T Valassis, David M Williams, Ramon Berguer, and Kim A Eagle. "Tear size and location impacts false lumen pressure in an ex vivo model of chronic type B aortic dissection". In: *J. Vasc. Surg.* 47.4 (2008), pp. 844–851.

[229] Kwong Ming Tse, Peixuan Chiu, Heow Pueh Lee, and Pei Ho. "Investigation of hemodynamics in the development of dissecting aneurysm within patient-specific dissecting aneurismal aortas using computational fluid dynamics (CFD) simulations". In: *J. Biomech.* 44.5 (2011), pp. 827–836.

[230] I. Vilacosta. "Acute aortic syndrome". In: *Heart* 85.4 (2001), pp. 365–368.

[231] Isidre Vilacosta, José Alberto San Román, Joaquin Ferreirós, Paloma Aragoncillo, Ramiro Méndez, Juan Antonio Castillo, Maria Jesus Rollán, Elena Batlle, Vicente Peral, and Luis Sánchez-Harguindey. "Natural history and serial morphology of aortic intramural hematoma: a novel variant of aortic dissection". In: *Am. Heart J.* 134.3 (1997), pp. 495–507.

[232] David A Vorp, Brian J Schiro, Marek P Ehrlich, Tatu S Juvonen, M Arisan Ergin, and Bartley P Griffith. "Effect of aneurysm on the tensile strength and biomechanical behavior of the ascending thoracic aorta". In: *The Annals of thoracic surgery* 75.4 (2003), pp. 1210–1214.

[233] J. Vossoughi and A. Tozeren. "Determination of an effective shear modulus of aorta". In: *Russian J. Biomech* 1-2 (1998), pp. 20–35.

[234] Jan Vychytil, Fanny Moravec, Petra Kochovà, Jitka Kuncovà, and Jitka Svíglerová. "Modelling of the mechanical behaviour of porcine carotid artery undergoing inflation-deflation test". In: *Appl. Comput. Mech.* 4.2 (2010), pp. 251–262.

[235] Lucy A Walton, Robert S Bradley, Philip J Withers, Victoria L Newton, Rachel EB Watson, Clare Austin, and Michael J Sherratt. "Morphological characterisation of unstained and intact tissue micro-architecture by X-ray computed micro-and nano-tomography". In: *Sci. Rep.* 5 (2015), p. 10074.

[236] Hui Wang and Amir A Amini. "Cardiac motion and deformation recovery from MRI: a review". In: *IEEE Trans. Med. Imaging* 31.2 (2011), pp. 487–503.

[237] Lei Wang, Nicholas A Hill, Steven M Roper, and Xiaoyu Luo. "Modelling peeling- and pressure-driven propagation of arterial dissection". In: *J. Eng. Math.* 109.1 (2018), pp. 227–238.

[238] Lei Wang, Steven M. Roper, X. Y. Luo, and N. A. Hill. "Modelling of tear propagation and arrest in fibre-reinforced soft tissue subject to internal pressure". In: *J. Eng. Math.* 95.1 (2015), pp. 249–265.

[239] Lei Wang, Steven M Roper, Nicholas A Hill, and Xiaoyu Luo. "Propagation of dissection in a residually-stressed artery model". In: *Biomech. Model. Mechanobiol.* 16.1 (2017), pp. 139–149.

[240] Ruoya Wang, Luke P Brewster, and Rudolph L Gleason Jr. "In-situ characterization of the uncrimping process of arterial collagen fibers using two-photon confocal microscopy and digital image correlation". In: *J. Biomech.* 46.15 (2013), pp. 2726–2729.

[241] Hannah Weisbecker, David M Pierce, Peter Regitnig, and Gerhard A Holzapfel. "Layer-specific damage experiments and modeling of human thoracic and abdominal aortas with non-atherosclerotic intimal thickening". In: *J. Mech. Behav. Biomed. Mater.* 12 (2012), pp. 93–106.

[242] Dan Wen, Xian-Liang Zhou, Jian-Jun Li, and Ru-Tai Hui. "Biomarkers in aortic dissection". In: *Clinica chimica acta* 412.9-10 (2011), pp. 688–695.

[243] Longfei Wen and Rong Tian. "Improved XFEM: Accurate and robust dynamic crack growth simulation". In: *Computer Methods in Applied Mechanics and Engineering* 308 (2016), pp. 256–285.

[244] Andrew L Wentland, Thomas M Grist, and Oliver Wieben. "Review of MRI-based measurements of pulse wave velocity: a biomarker of arterial stiffness". In: *Cardiovasc. Diagn. Ther.* 4.2 (2014), p. 193.

[245] David M Williams, Mark A LePage, and Do Yun Lee. "The dissected aorta: part I. Early anatomic changes in an in vitro model." In: *Radiology* 203.1 (1997), pp. 23–31.

[246] Colleen M Witzenburg, Rohit Y Dhume, Sachin B Shah, Christopher E Korenczuk, Hallie P Wagner, Patrick W Alford, and Victor H Barocas. "Failure of the porcine ascending aorta: multidirectional experiments and a unifying microstructural model". In: *J. Biomech. Eng.* 139.3 (2017).

[247] Harvey Wolinsky and Seymour Glagov. "A lamellar unit of aortic medial structure and function in mammals". In: *Circ. Res.* 20.1 (1967), pp. 99–111.

[248] Wen Yang, Vincent R Sherman, Bernd Gludovatz, Eric Schaible, Polite Stewart, Robert O Ritchie, and Marc A Meyers. "On the tear resistance of skin". In: *Nature communications* 6.1 (2015), pp. 1–10.

[249] Jared L Zitnay, Yang Li, Zhao Qin, Boi Hoa San, Baptiste Depalle, Shawn P Reese, Markus J Buehler, S Michael Yu, and Jeffrey A Weiss. "Molecular level detection and localization of mechanical damage in collagen enabled by collagen hybridizing peptides". In: *Nat. Commun.* 8 (2017), p. 14913.

[250] Rainer J Zotz, Raimund Erbel, and Jürgen Meyer. "Noncommunicating intramural hematoma: an indication of developing aortic dissection?" In: *J. Am. Soc. Echocardiogr.* 4.6 (1991), pp. 636–638.

Appendix A

Appendix to chapter 3

Contents of the chapter

A.1 Convergence study

In FE modelling, it is necessary to perform a convergence study to investigate the effect of the mesh size on the result. A simulation with the elastic and failure parameters presented in Table A.1 was run with different mesh size. The outcome is presented Figure A.1. The different mesh sizes are presented Figure A.2. A mesh size of 0.1 mm was chosen for this study.

μ (kPa)	k_1 (kPa)	k_2	α (°)	κ	σ_n^0 (kPa)	G_c^n (N/mm)	σ_t^0 (kPa)	G_c^t (N/mm)
10.0	19.9	15.0	44	0.1	220	0.12	100	0.1

Table A.1 – Parameters used for the mesh analysis

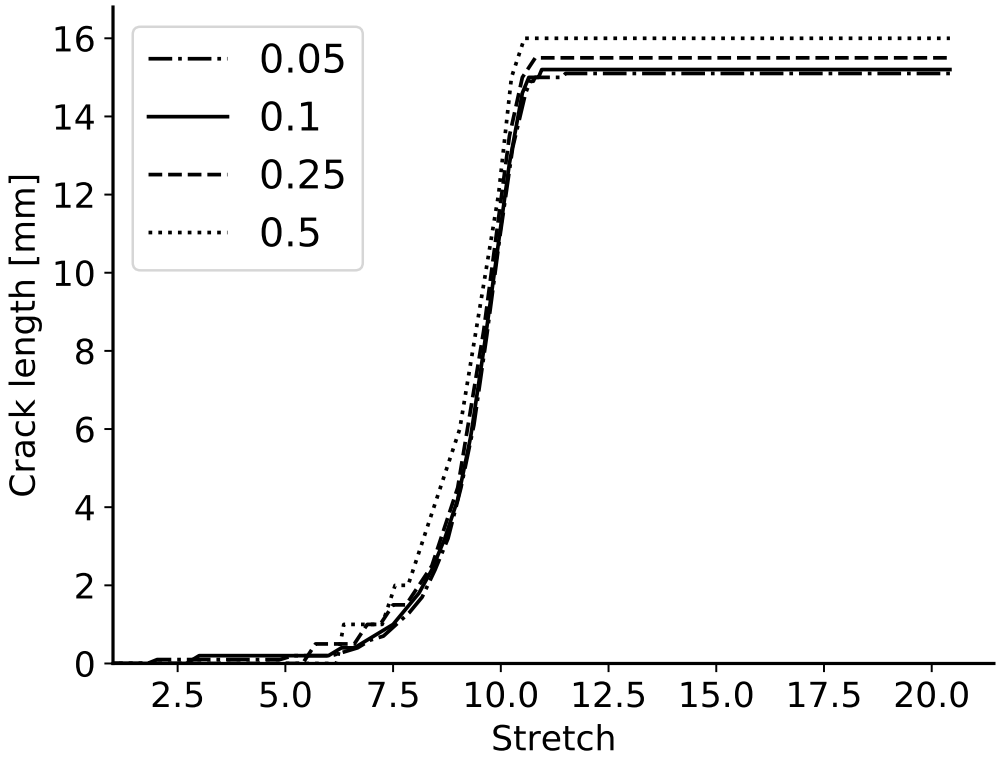

Figure A.1 – Result of the mesh convergence study. The different curves represent the crack length as a function of the stretch for different mesh sizes. The mesh size are in millimetre.

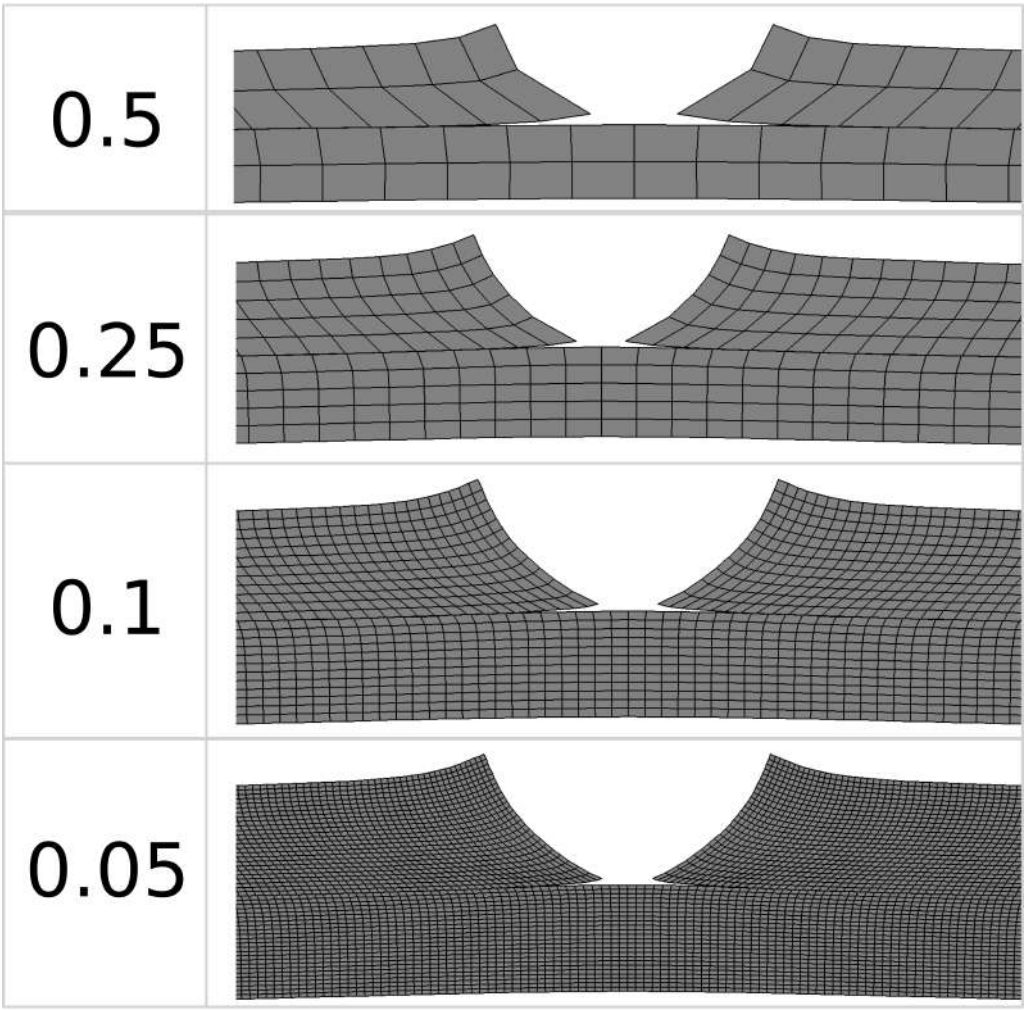

Figure A.2 – Comparison of the different mesh sizes. The mesh size are in millimetre.

Appendix B

Appendix to chapter 4

Contents of the chapter

B.1 Convergence study

When using the finite element method, a convergence study is always necessary to ensure that the mesh does not affect the simulation result, especially with XFEM. Therefore, multiple simulations with different mesh size were performed. The r-θ tear configuration with a standard set of parameters was chosen (Table B.1). The critical pressure for each simulation is presented in Figure B.1. According to the result, we chose a number of elements of 58500 as the error is lower than 0.11% with respect to the most refined model. Moreover, in all simulations, the first criterion to be reached was the circumferential criterion, thus the crack always propagated in the r-z plane regardless of the number of elements.

Parameter	Value
Crack depth (mm)	0.3
Crack width (°)	30
Crack position (mm)	0
Tensile strength (kPa)	T
Shear strength (kPa)	S
Opening angle (°)	0
Initial stretch (-)	1.0

Table B.1 – Set of parameters used for the study of mesh convergence. T and S are the tensile and shear strengths presented in Table IV.2 for each direction.

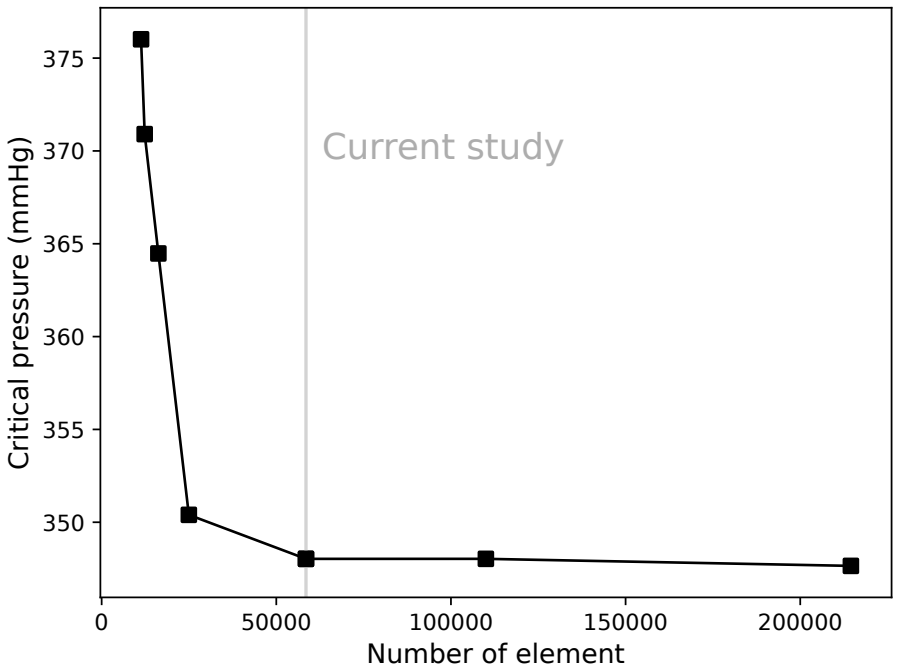

Figure B.1 – Result of the mesh convergence study. The grey vertical bar shows the number of elements used in the current study.

B.2 First-order and interactions polynomial coefficients with the critical pressure as output

Parameters	Crack length	Crack width	Crack position	Tensile strength	Shear strength	Opening angle	Initial stretch
Crack length	-71.1 ***	-13.6 *	-4.9	-53.4 ***	0.8	-17.0 *	15.8 *
Crack width	-	-30.1 ***	-14.4 *	-26.1 ***	-1.0	5.4	11.1
Crack position	-	-	-31.9 ***	-22.7	0.2	7.7	18.0 **
Tensile strength	-	-	-	161.3 ***	0.8	19.1 **	1.2
Shear strength	-	-	-	-	1.6	0.3	-0.3
Opening angle	-	-	-	-	-	22.1 ***	-10.1
Initial stretch	-	-	-	-	-	-	5.5

Table B.2 – First-order and interactions polynomial coefficients for the θ-z tear configuration with the critical pressure as output. $*\ 0.01 < p < 0.05$, $**\ 0.001 < p \leqslant 0.01$, $*** \leqslant 0.001$, with p standing for significance. F-test probability <0.001. r^2=0.90.

Parameters	Crack depth	Crack length	Crack position	Tensile strength	Shear strength	Opening angle	Initial stretch
Crack depth	-14.2 ***	-9.0 **	-4.1	6.7 *	-1.7	-4.1	2.9
Crack length	-	-30.0 ***	7.9 *	-21.9 ***	2.2	-11.9 ***	5.7
Crack position	-	-	18.6 ***	22.2 ***	-0.3	-9.9 **	-14.0 ***
Tensile strength	-	-	-	132.6 ***	8.0 *	4.7	-30.8 ***
Shear strength	-	-	-	-	7.1 *	5.4	-1.7
Opening angle	-	-	-	-	-	9.7 **	0
Initial stretch	-	-	-	-	-	-	-20.9 ***

Table B.3 – First-order and interactions polynomial coefficients for the r-z tear configuration with the critical pressure as output. $*\ 0.01 < p < 0.05$, $**\ 0.001 < p \leqslant 0.01$, $*** \leqslant 0.001$, with p standing for significance. F-test probability <0.001. for all tear configurations. r^2=0.95.

Parameters	Crack depth	Crack width	Crack position	Tensile strength	Shear strength	Opening angle	Initial stretch
Crack depth	-36.0 ***	-9.8 *	4.5	-0.4	1.3	-6.8	8.6 *
Crack width	-	-18.5 ***	9.6 *	-16.4 ***	-1.3	-8.3 *	0.3
Crack position	-	-	16.1 ***	31.8 ***	-0.4	-3.6	-8.8 *
Tensile strength	-	-	-	124.5 ***	9.4 *	-1.2	-36.2 ***
Shear strength	-	-	-	-	10.3 **	3.0	-5.1
Opening angle	-	-	-	-	-	-7.9 *	-1.4
Initial stretch	-	-	-	-	-	-	-36.0 ***

Table B.4 – First-order and interactions polynomial coefficients for the r-θ tear configuration with the critical pressure as output. $*\ 0.01 < p < 0.05$, $**\ 0.001 < p \leqslant 0.01$, $*** \leqslant 0.001$, with p standing for significance. F-test probability <0.001. r^2=0.93.

B.3 First-order and interactions polynomial coefficients with the direction of propagation as output

Parameters	Crack length	Crack width	Crack position	Tensile strength	Shear strength	Opening angle	Initial stretch
Crack length	0.109 ***	0.016	-0.047 *	0.109 ***	0	0.047 *	-0.016
Crack width	-	0.016	-0.016	0.016	0	0.016	0.016
Crack position	-	-	0.141 ***	0.141 ***	0	-0.047 *	0.016
Tensile strength	-	-	-	-0.203 ***	0	-0.016 ***	-0.078
Shear strength	-	-	-	-	0	0	0
Opening angle	-	-	-	-	-	-0.016	-0.016
Initial stretch	-	-	-	-	-	-	-0.078 ***

TABLE B.5 – First-order and interactions polynomial coefficients for the θ-z tear configuration with the θ-z propagation as output. $*\,0.01 < p < 0.05$, $**\,0.001 < p \leqslant 0.01$, $*** \leqslant 0.001$, with p standing for significance. F-test probability <0.001. r^2=0.79.

Parameters	Crack length	Crack width	Crack position	Tensile strength	Shear strength	Opening angle	Initial stretch
Crack length	-0.062***	0	0.063 ***	-0.062 ***	0	0	0.062 ***
Crack width	-	0	0	0	0	0	0
Crack position	-	-	-0.062 ***	-0.063 ***	0	0	0.063 ***
Tensile strength	-	-	-	0.062 ***	0	0	-0.062 ***
Shear strength	-	-	-	-	0	0	0
Opening angle	-	-	-	-	-	0	0
Initial stretch	-	-	-	-	-	-	-0.062 ***

TABLE B.6 – First-order and interactions polynomial coefficients for the θ-z tear configuration with the r-z propagation as output. $*\,0.01 < p < 0.05$, $**\,0.001 < p \leqslant 0.01$, $*** \leqslant 0.001$, with p standing for significance. F-test probability <0.001. r^2=0.67.

Parameters	Crack length	Crack width	Crack position	Tensile strength	Shear strength	Opening angle	Initial stretch
Crack length	-0.047 ***	-0.016	-0.016	-0.047 **	0	-0.047 **	-0.047 **
Crack width	-	-0.016	0.016	-0.016	0	-0.016	-0.016
Crack position	-	-	-0.078 ***	-0.078 ***	0	0.047 **	-0.078 ***
Tensile strength	-	-	-	0.141 ***	0	0.016	0.141 ***
Shear strength	-	-	-	-	0	0	0
Opening angle	-	-	-	-	-	0.016	0.016
Initial stretch	-	-	-	-	-	-	0.141 ***

TABLE B.7 – First-order and interactions polynomial coefficients for the θ-z tear configuration with the r-θ propagation as output. $*\,0.01 < p < 0.05$, $**\,0.001 < p \leqslant 0.01$, $*** \leqslant 0.001$, with p standing for significance. F-test probability <0.001. r^2=0.75.

Parameters	Crack depth	Crack length	Crack position	Tensile strength	Shear strength	Opening angle	Initial stretch
Crack depth	0	0	0	0	0	0	0
Crack length	-	0	0	0	0	0	0
Crack position	-	-	0	0	0	0	0
Tensile strength	-	-	-	-0.5 ***	0	0	0
Shear strength	-	-	-	-	0	0	0
Opening angle	-	-	-	-	-	0	0
Initial stretch	-	-	-	-	-	-	0

TABLE B.8 – First-order and interactions polynomial coefficients for the r-z tear configuration with the θ-z propagation as output. $*\,0.01 < p < 0.05$, $**\,0.001 < p \leqslant 0.01$, $*** \leqslant 0.001$, with p standing for significance. F-test probability <0.001. r^2=0.99.

Parameters	Crack depth	Crack length	Crack position	Tensile strength	Shear strength	Opening angle	Initial stretch
Crack depth	0	0	0	0	0	0	0
Crack length	-	0	0.031	0	-0.031	0	0
Crack position	-	-	-0.031	-0.031	0	0.031	-0.031
Tensile strength	-	-	-	0.375 ***	-0.094 ***	0	-0.125 ***
Shear strength	-	-	-	-	-0.094 ***	-0.031	-0.094 ***
Opening angle	-	-	-	-	-	0	0
Initial stretch	-	-	-	-	-	-	-0.125 ***

Table B.9 – First-order and interactions polynomial coefficients for the r-z tear configuration with the r-z propagation as output. $*\,0.01 < p < 0.05$, $**\,0.001 < p \leqslant 0.01$, $*** \leqslant 0.001$, with p standing for significance. F-test probability <0.001. r^2=0.86.

Parameters	Crack depth	Crack length	Crack position	Tensile strength	Shear strength	Opening angle	Initial stretch
Crack depth	0	0	0	0	0	0	0
Crack length	-	0	-0.031	0	0.031	0	0
Crack position	-	-	0.031	0.031	0	-0.031	0.031
Tensile strength	-	-	-	0.125 ***	0.094 ***	0	0.125 ***
Shear strength	-	-	-	-	0.094 ***	0.031	0.094 ***
Opening angle	-	-	-	-	-	0	0
Initial stretch	-	-	-	-	-	-	0.125 ***

Table B.10 – First-order and interactions polynomial coefficients for the r-z tear configuration with the r-θ propagation as output. $*\,0.01 < p < 0.05$, $**\,0.001 < p \leqslant 0.01$, $*** \leqslant 0.001$, with p standing for significance. F-test probability <0.001. r^2=0.73.

Parameters	Crack depth	Crack width	Crack position	Tensile strength	Shear strength	Opening angle	Initial stretch
Crack depth	0.078 ***	0	-0.063 ***	-0.047 *	-0.016	0.016	0.047 *
Crack width	-	0	-0.016 ***	0	0	0	0
Crack position	-	-	0.062 ***	-0.062 ***	0	0	0.062 ***
Tensile strength	-	-	-	-0.422 ***	-0.016	0.016	0.047
Shear strength	-	-	-	-	-0.016	-0.016	0.016
Opening angle	-	-	-	-	-	0.016	-0.016
Initial stretch	-	-	-	-	-	-	-0.078 ***

Table B.11 – First-order and interactions polynomial coefficients for the r-θ tear configuration with the θ-z propagation as output. $*\,0.01 < p < 0.05$, $**\,0.001 < p \leqslant 0.01$, $*** \leqslant 0.001$, with p standing for significance. F-test probability <0.001. r^2=0.86

Parameters	Crack depth	Crack width	Crack position	Tensile strength	Shear strength	Opening angle	Initial stretch
Crack depth	-0.008	-0.008	-0.008	-0.008	-0.008	0.008	0.008
Crack width	-	-0.023	0.008	-0.023	0.008	-0.008	0.023
Crack position	-	-	-0.023	-0.023	0.039 *	0.023	0.023
Tensile strength	-	-	-	0.164 ***	0.07 ***	-0.039 *	-0.164 ***
Shear strength	-	-	-	-	0.07 ***	0.023	-0.07 ***
Opening angle	-	-	-	-	-	-0.039 *	0.039 *
Initial stretch	-	-	-	-	-	-	-0.164 ***

Table B.12 – First-order and interactions polynomial coefficients for the r-θ tear configuration with the r-z propagation as output. $*\,0.01 < p < 0.05$, $**\,0.001 < p \leqslant 0.01$, $*** \leqslant 0.001$, with p standing for significance. F-test probability <0.001. r^2=0.79

Parameters	Crack depth	Crack width	Crack position	Tensile strength	Shear strength	Opening angle	Initial stretch
Crack depth	-0.07 **	0.008	0.07 **	0.055 *	0.023	-0.023	-0.055 *
Crack width	-	0.023	0.008	0.023	-0.008	0.008	-0.023
Crack position	-	-	-0.039	0.086 ***	-0.039	-0.023	-0.086 ***
Tensile strength	-	-	-	0.258 ***	-0.055 *	0.023	0.117 ***
Shear strength	-	-	-	-	-0.055 *	-0.008	0.055 *
Opening angle	-	-	-	-	-	0.023	-0.023
Initial stretch	-	-	-	-	-	-	0.242 ***

Table B.13 – First-order and interactions polynomial coefficients for the r-θ tear configuration with the r-θ propagation as output. $*\,0.01 < p < 0.05$, $**\,0.001 < p \leqslant 0.01$, $*** \leqslant 0.001$, with p standing for significance. F-test probability <0.001. r^2=0.78

Appendix C

Appendix to chapter 6

Contents of the chapter

C.1 Aortic dissection followed by radiographic images

Radiographic images were taken between 300 mmHg to the propagation of the dissection inside the aortic specimen at a rate of 5 frames per second. X-ray images at different time steps are displayed in Figure C.1. Only the specimens with a circumferential notch were imaged with this method as the orientation of the longitudinal notch hindered the observation with this type of technique. Before the first image and after the last image, the aortic sample was in a quasi-static state and almost no movement could be observed on the X-ray images. The propagation of the dissection along the specimens was quasi instantaneous; however, we can observe a local delamination around the tear before the failure of the samples. The images showed that the tear propagated first in the anterograde direction in both samples and then in the retrograde direction.

Radiographic images are a projection of a 3D cylinder on a 2D plane, thus they are difficult to interpret and geometric quantification is challenging compared to tomographic images. Consequently, only qualitative results were extracted from these images.

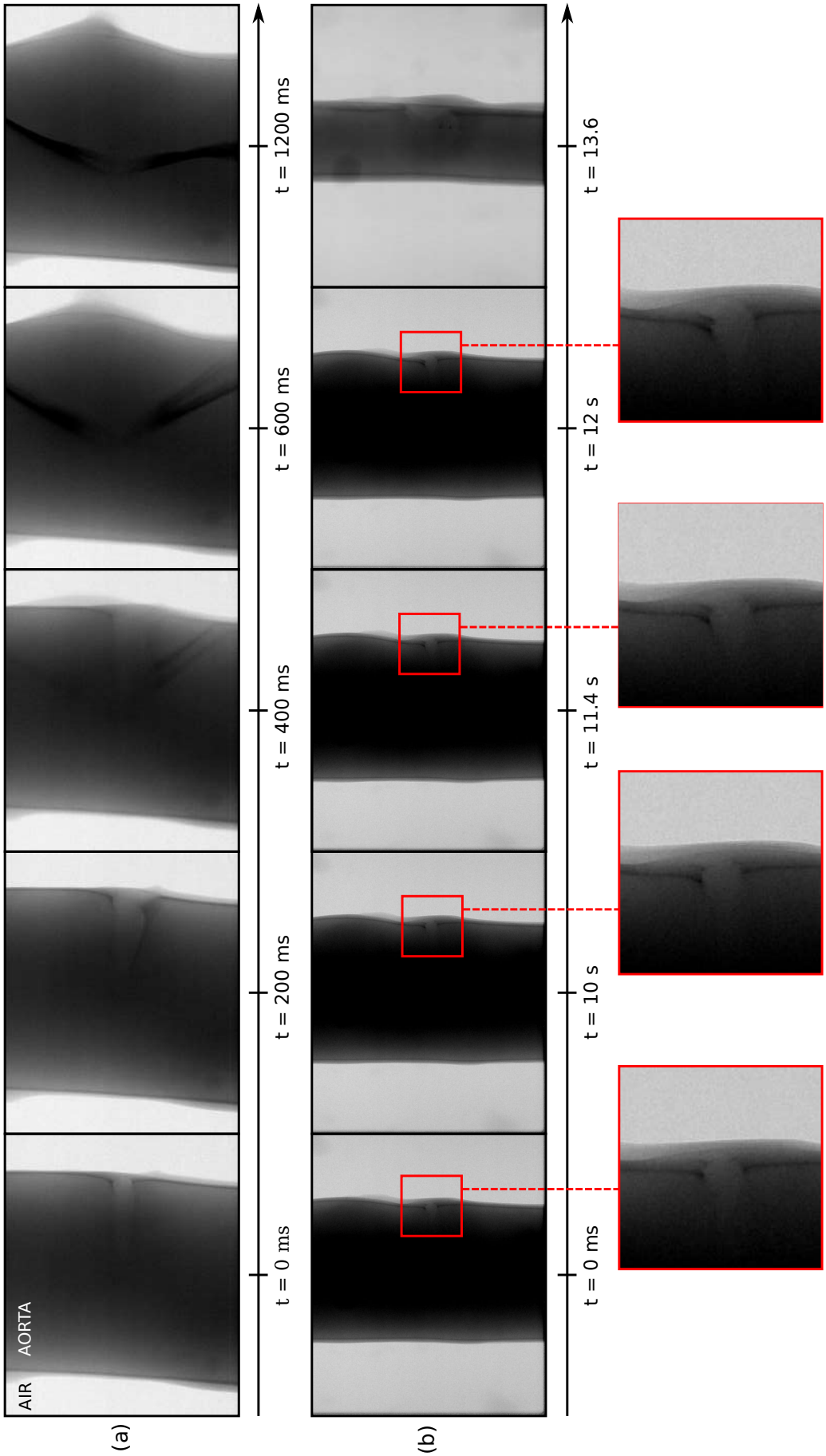

Figure C.1 – Radiographic images of two aortic specimens, (a) and (b), during the inflation at different time steps. The blacker pixels represent the aorta whereas the whiter pixels are the air. The first image was taken as a reference in term of time. The second specimen experienced a failure of the wall after the dissection which is why the diameter decreased drastically.

C.2 Real-time measurement

The issue with the scan measurements is that the pressure steps were quite large. To complete these lacks a sample was followed with radiographic images at 5 frames per seconds to measure the specimen diameter in real time during the inflation. The maximum pressure was limited to 300 mmHg. The circumferential stretch and stress were calculated with the method presented in Section VI.1.2.5. The results are presented in Figure C.2

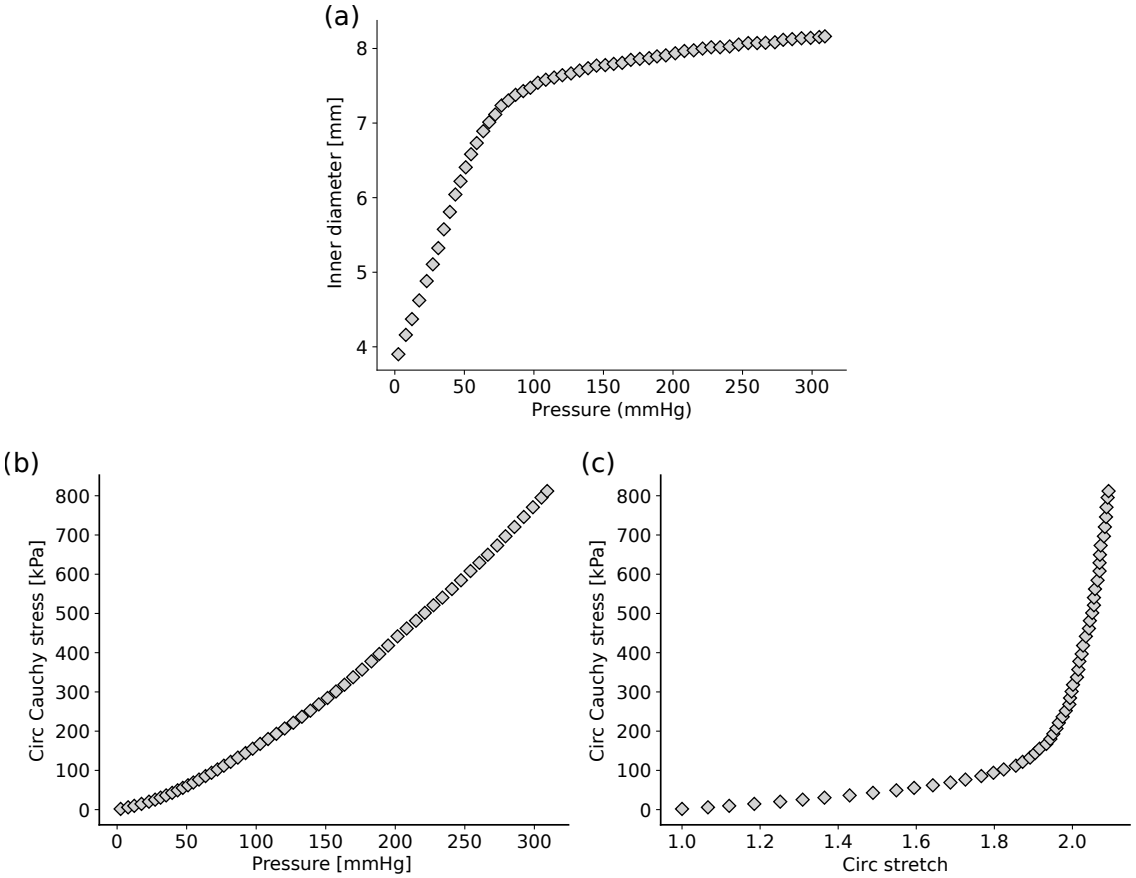

FIGURE C.2 – (a) Inner diameter of the specimen in function of the pressure, (b) circumferential Cauchy stress in function of the pressure, and (c) circumferential Cauchy stress in function of the circumferential stretch.

École Nationale Supérieure des Mines
de Saint-Étienne

NNT: 2021LYSEM010

Author: Joseph Brunet

Title: Understanding the mechanisms of aortic dissection: finite element modeling and in situ experimentation with X-ray tomography

Speciality: Mechanics and Engineering

Keywords: Aortic dissection, Failure, X-ray microtomography, Inverse method, XFEM

Abstract

Aortic dissection is a serious vascular disease characterised by a separation of the layers of the arterial wall and the creation of a second lumen. Mortality due to this disease is particularly high and requires surgery as soon as possible. Although widely documented clinically, the phenomena behind this condition are largely unknown and many questions remain unanswered. Thus, the objective of this thesis is to better understand the mechanisms triggering aortic dissection and the parameters influencing its propagation. Initially, two studies combining tensile tests with finite element models allowed the mechanical properties and fracture modes I and II of the aortic wall to be identified using inverse methods. Subsequently, an aortic dissection model using the extended finite element method was developed in order to quantify the impact of geometric and mechanical factors on the rupture pressure and the direction of propagation of the aortic dissection. In order to validate this model, a new experimental method combining a mechanical tension-inflation test with X-ray microtomography has been developed. This in-situ test made it possible to observe the 3D evolution of the delamination profile during the propagation of a dissection in the aortic wall. These observations and modelling have led to a better understanding of the mechanisms of propagation of the dissection, and open perspectives on the development of personalised diagnostic tools.

ÉCOLE DES MINES DE SAINT-ÉTIENNE
158, cours Fauriel – CS 62362
42023 Saint-Étienne Cedex 2 – France
Tél. +33(0)4 77 42 01 23
www.mines-stetienne.fr

École Nationale Supérieure des Mines
de Saint-Étienne

NNT: 2021LYSEM010

Auteur: Joseph Brunet

Titre: Comprendre les mécanismes de dissection aortique: modélisation éléments finis et expérimentation in situ sous tomographie RX

Spécialité: Mécanique et Ingénierie

Mots-Clefs: Dissection aortique, Rupture, Microtomographie aux rayons X, Méthode inverse, XFEM, traction-gonflement

Résumé

La dissection aortique est une maladie vasculaire grave caractérisée par un décollement des couches de la paroi artérielle et la création d'un chaux chenal. La mortalité due à cette affection est particulièrement élevée et demande une intervention chirurgicale dans les délais les plus brefs. Bien que largement documentés cliniquement, les phénomènes à l'origine de cette condition sont peu connus et de nombreuses questions demeurent sans réponses. Ainsi, l'objectif de cette thèse est de mieux comprendre les mécanismes déclenchant la dissection aortique et les paramètres influençant sa propagation. Dans un premier temps, deux études combinant des tests mécaniques de traction avec des modèles éléments finis ont permis d'identifier les propriétés mécaniques et les modes de rupture I et II de la paroi aortique grâce à des méthodes inverses. Par la suite, un modèle de dissection aortique utilisant la méthode des éléments finis étendus à été développé afin de quantifier l'impact de facteurs géométriques et mécaniques sur la pression de rupture ainsi que sur la direction de propagation de la dissection aortique. Afin de valider ce modèle, une nouvelle méthode expérimentale combinant un essai mécanique de traction-gonflement avec de la microtomographie à rayons X a été mise au point. Ce test in situ a permis d'observer l'évolution 3D du profil de délamination lors de la propagation d'une dissection dans la paroi. Ces observations et modélisations ont permis une meilleure compréhension des mécanismes de propagation de la dissection, et ouvrent des perspectives sur le développement d'outils de diagnostic personnalisés.

ÉCOLE DES MINES DE SAINT-ÉTIENNE
158, cours Fauriel – CS 62362
42023 Saint-Étienne Cedex 2 – France
Tél. +33(0)4 77 42 01 23
www.mines-stetienne.fr